Magma mixing and sulfide production in the lower crust: insights into arc metallogenesis

A thesis submitted in total fulfillment of the requirements for the degree
Doctor of Philosophy

by

Kyle Charles Rebryna
Bachelor of Science (First Class Honours)

School of Geosciences, Faculty of Science
Monash University, Melbourne, Australia

August 2009

Long days, still office
A thesis is a journey
Never quite finished

Table of Contents

Abstract

The location and distribution of metal sources for felsic-magma related ore deposits in continental and island arcs (porphyry Cu-Au-Mo, epithermal Au-Ag, and skarn) is contentious. Crustal and mantle sources may both contribute to the metal budgets of these types of deposits, with a chemical signature that is set early. Mixing between mantle-sourced magmas and crustal partial melts in Mixing, Assimilation, Storage, and Homogenisation (MASH) zones, at or near the base of the Earth's crust, is a possible mechanism to generate fertile magmas for ore development. Magma mixing of this sort may have an important role in sulfur solubility and thus sulfide mineral stability. Sulfide minerals partition Cu, Au, Ag, Mo, platinum group elements, and other chalcophile metals, which are key components in felsic magma-related ore deposits. This study investigates the role of magma mixing in the production of sulfide melts in the lower crust and the role that these sulfide melts have in ore generation in the upper crust. Geochemical data from samples collected in the lower crustal Opirarukaomappu Gabbroic Complex (OGC), southeastern Hokkaido, Japan suggest that sulfide occurrences are associated with magma compositions produced by mixing ~80% gabbro with ~20% tonalite. High temperature, high pressure piston cylinder experiments are used to simulate this mixing and the consequent saturation and exsolution of sulfide melt. A new, redox-controlled, model for sulfide saturation, called the "sulfur fence", describes a sudden reduction in sulfur solubility caused by the mixing of oxidised, sulfate-rich magmas with magmas containing a strongly reducing component (i.e. graphite). In this model, reduction from sulfate-stable to sulfide-stable decreases sulfur solubility by an order of magnitude (from ~1 wt. % to ~0.1 wt. %). Resulting large scale sulfur oversaturation may allow the generation of pervasive and voluminous sulfide melts in mixing magmas. The greater density of sulfide melts causes them to settle through lower density silicate magmas. Small globules (<0.1 cm radius) are able to be entrained in migrating liquidus magmas of OGC compositions. However, to entrain sulfide globules similar in size to those observed in the OGC (~0.1 cm – 0.25 cm radius), about 20% w/v crystallisation of these magmas must occur. Controlling the settling out of sulfide melts generated during mixing may determine the deposit type generated in MASH zone-affected arc settings. Felsic magma-related ore deposits may occur in arcs where sulfide saturation is prevented both during mixing of magmas at depth and during migration from their source regions to emplacement. These types of deposits may also develop from magmas that are able to continuously entrain sulfides after sulfide saturation. Conversely, sulfide saturation, followed by settling out of the sulfide melt, may result in the accumulation of massive sulfides and the formation of magmatic Ni-Cu deposits. Hence, felsic magma-related ore deposits and massive sulfide deposits may represent endmembers of an ore deposit spectrum: porphyry Cu-Au-Mo, epithermal Au-Ag, and skarn deposits where sulfides were not generated or were kept entrained when they were; magmatic Ni-Cu where sulfides were generated and settled out.

General Declaration for thesis

Monash University
Monash Research Graduate School

In accordance with Monash University Doctorate Regulation 19/Doctor of Philosophy and Master of Philosophy (MPhil) regulations the following declarations are made:

I hereby declare that this thesis contains no material which has been accepted for the award of any other degree or diploma at any university or equivalent institution and that, to the best of my knowledge and belief, this thesis contains no material previously published or written by another person, except where due reference is made in the text of the thesis.

This thesis includes six original chapters. The core theme of the thesis is the geochemistry and rheology of mixing magmas and the role that this plays in ore deposit genesis. The ideas, development and writing up of all the chapters in the thesis were the principal responsibility of myself, the candidate, working within the School of Geosciences under the supervision of Dr Andy Tomkins and Dr Roberto Weinberg.

Signed:  **……**

Date: **4 August 2009**

eThesis Copyright Information

Notice 1

Under the Copyright Act 1968, this thesis must be used only under the normal conditions of scholarly fair dealing. In particular no results or conclusions should be extracted from it, nor should it be copied or closely paraphrased in whole or in part without the written consent of the author. Proper written acknowledgment should be made for any assistance obtained from this thesis.

Notice 2

I certify that I have made all reasonable efforts to secure copyright permissions for third-party content included in this thesis and have not knowingly added copyright content to my work without the owner's permission.

Acknowledgements

For my growth as a scientist, I have to thank my supervisors Andy and Roberto, without whom I doubt that I should ever have gone beyond undergraduate geology. Indeed, the very foundations of this entire project came from the space between these two minds. Watching them in scientific discussion was a singular and inspiring experience. They deserve my sincere gratitude for putting up with my many reservations, personal crises, and general academic moodiness, while still keeping me on track and encouraging me to always perform better. Two others also played a significant role in this production: Ian Nicholls and Bruce Schaefer. Their knowledge of geochemistry and isotopes made Chapter 3 far more than a meaningless collection of numbers and laid the foundation for the rest of the thesis. Thank you to the AusIMM Bicentennial Gold 88 Endowment, which funded important analyses for Chapter 3. Thank you also to David Clark, Dean Scott, and the experimental petrology gang at ANU. Chapter 4 would not have happened without such a great piston cylinder lab.

The one and absolutely necessary rock collecting adventure in Japan would have ground to a spectacular halt were it not for two not only brilliantly helpful, but just plain brilliant, locals: Ryo Anma and Hiroyuki Kamiyama. Had it not been for their profoundly friendly and comprehensive help, the field work would have been hard, hard yakka. For his understanding and patience with broken mauls and scientific reservations, I will always be grateful to Anma-san. I learned from him the Japanese for 'good night' – *oi-ya su-men na-sai*. Something in his intonation made the rest of the trip less immense.

The Japanese are not just friendly, but helpful in the extreme. Although I'm sure I was coddled because of my very western quaintness, I do wish to thank many people in Samani town for being so utterly selfless in helping me. I am very fond of Hokkaido in particular and Japan in general because of my time amongst you. Thank you Gallagher-san for translating everything and opening your home to me. Thank you Masatoshi Kodama for rescuing Andy and I from the train station when even my phasebook couldn't help us. To the whole crew from the Ministry of Education goes my deepest gratitude for the many times I showed up beaten from a day of field work to find them waiting with what seemed like bottomless cans of Sapporo lager and a hot teppanyaki grill surrounded by food. Kampai! For the woman I met outside my onsen after the Day From Hell on Tick Mountain: you filled my empty insides when I needed it most, thank you.

Standing behind this document are three of the most enlightening years of my life; enlightenment that shines far beyond this little field of science. These years have taught me to look closer, to see the beauty beyond the science, and to see that it would be meaningless without people to make the endeavour worthwhile. Pat, Megan, Wendy, Chris F, Chris C, Heather, Matty (thanks for the Friday Beers Songs), Benni, Max, Leonor, Augustin (I'll never forget the proper way to eat ribs), Bec (sorry I never showed you my knitting), Geeza, Jess,

and Lucy: I will forever search for a more authentic, friendly, trancendant, and wonderful group of people, I'm certain. Special mentions for my officemates Michiel and Dean. An extra special mention to Henning, who's been with me from the start. Thanks for not paying special attention to the stream of expletives directed at my long-suffering computer and thanks for being a point of constancy in the whirlwind of post-graduate life. Special gratitude goes to Fran and Nick, fast friends extraordinaire. Without you two, Canberra would have been the lesser.

If I could, I would make a series called 'Conversations with Patricia Vickers-Rich and Jeff Stilwell'. Thank you for our conversations about life and science. I always left somehow feeling better for them and will probably forever regret not doing something in palaeontology. Marion, without whom I never would have discovered Firefly and learned more Mars stuff than I can shake a stick at; for being quite possibly the most flexible employer I have ever and will ever meet; for proofreading so professionally: thank you. I promise to collect a Mars rock for you, by hand, should I get the opportunity. That is, unless you beat me to it. Gail, Florita, Caroline, Ana, Robert, Chris, Massimo, and Meagan: you are the beating heart that keeps the department functioning. Geoscience just wouldn't be as good without you.

I have been truly blessed with Australians who have adopted me in my time as an itinerant. Family in all but blood, to Helen and Bruce I must give a dear, deep, and loving thank you. Words just aren't enough: you are my Aussie parents. To the Trews, thanks for all the evenings' breaks. You made my life better.

To Adele: indeed, I'm gonna go eat cake. Wanna join me? From a tortured soul never exposed to the proper meaning of 'marathon', to a seasoned veteran with season upon season of Stargate gracing my memory, an enormous thank you. Thank you, of course, for more than Stargate. You are extraordinary. To Luke and the Bear clan, I'd have been lucky to be born into such a family. Thank you for sharing your life with me.

Georgina, Georgina. I'm not moving away, just changing houses. Besides, I'm only, at most, 0.7 seconds away and that's not long, relativity speaking. Thank you for everything. Thank you also to Kirsten for volunteering to proofread and Andrea for collating. What a chore.

To my long suffering friends and family in Canada: thank you for sticking with me through this whole thing. You say that you live vicariously through me, but I am you, reflected. You gave me the opportunity and tools to succeed in a fantastically diverse array of environments; if words fail from time to time, this is one of those times. Without you, my life would be a barren place, dry and dusty. Mom: how you can put up with my foulness and still love me as much as you do is a lesson in tolerance and unconditional love. You are stoic and joyfull and optimistic and strong and tender and precious. I hope I have even a teaspoon of your gumption, of your spirit, somewhere in me. Bob, Dad, Judy, Kristin, Quinn, A.C.T.R.S., Kim, Donnie, Clint, Rhonda, and the Kuin gang: sincere apologies. I'm not much of a son/

brother/uncle/great-uncle. Your love and support have meant more than you can possibly imagine. And to Grant, because you are with me still.

To Louise, the light of my life. You have shown me a very singular world. Your proofing, understanding, patience, encouragement, tolerance, and love mean the world to me. You are beautiful. I love you. I'll be with you always.

List of Figures

List of Tables

Chapter 1: Project introduction, aims, scope, and thesis structure

Project Introduction and Aims

Many of our most important ore deposits form in continental and island arcs (porphyry Cu-Au-Mo, epithermal Au-Ag, and skarn) and it is the goal of this project to illuminate the source processes that influence the generation of intermediate arc magmas. This will allow an analysis of the processes that control the metal budgets of these magmas in their source(s) and, ultimately, the genesis of felsic intrusion-related ore deposits in the upper arc crust. These deposit types are well understood in terms of near-surface and late-stage processes, but little is known about the location of their source regions or the distribution of metals there. Even less is known of metal behaviour during transport of migrating silicate melts. Moreover, the role of deep crustal magmatism in the development of intrusion-related ore deposits in the upper crust is not constrained in the current literature. In particular, the source of metals involved in ore development often remains undefined. This project posits that magma mixing in the deep crust plays a significant role in the development of ore deposits in the upper crust. To address this statement, this thesis investigates mixing and geochemical evolution of magmas at the base of arcs. The understanding of deep crustal magmatism gained through this investigation is then applied to the genesis of the Earth's most important Cu-Au-Mo-Ag resources.

The study of the implications of deep crustal magma mixing for ore genesis is a new line of research. A key process detailed in this thesis is that of magma mixing causing sulfide saturation. The existing paradigm in porphyry-Cu research is that sulfide saturation in the source region, and the resulting exsolution of sulfide melts, inhibits ore formation (e.g. Mungall, 2002). This project will show that although chalcophile-element depletion often follows sulfide saturation, there are mechanisms by which metal content can be retained in these types of systems through entrainment of sulfide melt. This is consistent with the observations of sulfide melt inclusions in intrusions near porphyry Cu-Au deposits (e.g. Halter et al., 2005; Stavast et al., 2006). However, sulfur solubility in magmas is affected by oxidation state and most porphyry-Cu systems are found to be oxidised (see Richards, 2009). Therefore, since the porphyry-Cu literature is a rich database of sulfur behaviour in oxidised systems, this thesis investigates the behaviour and role of sulfides in equivalent, but reduced, systems. These investigations will provide insights into why, in some settings, magmas that remain oxidised may be better suited to ore formation.

The source of metals in felsic magma-related ore deposits is the subject of much discussion. In arcs, metals may come from a variety of sources, such as subducted slab or metasomatised mantle wedge material (Sillitoe, 1997; Mungall, 2002), from mantle metallogenic heterogeneities (Sillitoe, 1972), from adjacent intruded crust (Krauskopf, 1967), or in anatectic

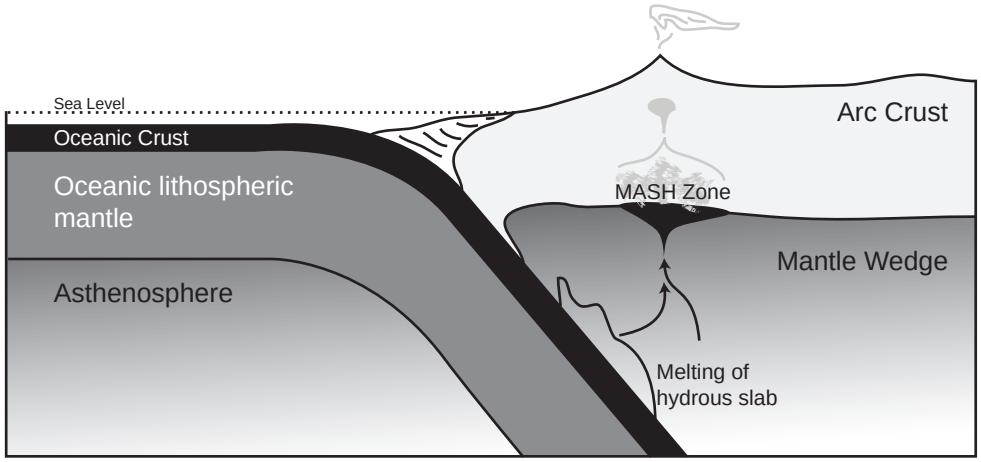

Figure 1.1: MASH zone schematic diagram. Simplified from Richards (2003).

melts from the lower crust (Hedenquist and Lowenstern, 1994; Tomkins and Mavrogenes, 2003). Currently, there are few constraints on the relative contributions from these potential sources. The existing hypothesis for porphyry-Cu and epithermal-Au genesis is that chlorine- and sulfur-rich hydrothermal fluids exsolve from cooling, water-saturated magmas in the shallow upper crust. These fluids scavenge chalcophile elements from the cooling magma body, precipitating them in sulfide phases throughout a fracture stockwork overlying the intrusion (e.g. Sillitoe and Hedenquist, 2003). The fertile arc magmas associated with these deposit types are thought to be generated by partial melting of the lithospheric mantle wedge, followed by ascent through, and interaction (hybridisation) with, the intervening crust. It is currently thought that sulfide saturation must be avoided in these melts to prevent the loss of chalcophile and siderophile elements to a sulfide phase that settles out of the system (Richards, 2003, 2009). Evidence from the lower crust, presented in this thesis, indicates that the mantle may be the primary source for the metals found in these types of felsic-magma related deposits, but perhaps not the only source.

The intermediate magmas associated with porphyry and epithermal deposits are thought to be generated, in arcs, as a result of mixing between mantle-derived basaltic melt and crust-derived granitic melt in MASH zones at 30 to 45 km depth (Hildreth and Moorbath, 1988). A MASH zone is a zone of active magma modification at the base of the Earth's crust, typically of deep arc crust, where (M)ixing, (A)ssimilation, (S)torage, and (H)omogenisation of magmas occurs (Fig. 1.1; Hildreth and Moorbath, 1988; Richards, 2003; Annen et al., 2006). This study focuses on the role of these zones in the evolution of metalliferous arc magmas. The metal content of mantle-derived magmas is often taken to be fixed at the site of generation; therefore, processes that affect the metal content of ascending mantle-derived magmas are not well constrained. The role of the intervening country rock between source and emplacement is often minimised, with translithospheric extensional pathways (Richards, 2003) hypothesised to allow for minimal interaction during rapid magma ascent to upper crustal levels. However, the core thesis presented here is that MASH processes affect the generation, sequestration, transport, and emplacement of metal-rich immiscible sulfide melts within silicate magmas by influencing sulfide solubility. For example, mixing of sulfide undersaturated granitic melt with primitive basaltic melt is thought to be a

mechanism involved in the formation of magmatic Ni deposits (Li and Naldrett, 1993; Li et al., 2001; Naldrett, 2004). The role of immiscible sulfide-silicate melts during near-surface emplacement and subsequent ore body mineralisation has been thoroughly addressed (e.g. Candela and Holland, 1986; Hattori, 1993; Ebel and Naldrett, 1997; Hattori and Keith, 2001; Richards, 2003; Halter et al., 2004, 2005; Core et al., 2006). However, these studies typically focus on the intricacies of formation of single ore bodies, or on the near-deposit geology. They leave the questions of metal source, and transport from that source, to speculation.

This thesis presents the idea that magma mixing in MASH zones is the primary cause of sulfide oversaturation (resulting in sulfide melt generation) in hybrid magmas and that this process may significantly influence the metal content of magmas that escape to the upper crust. The role of the sulfide melts generated through MASH zone magma mixing, and their interaction with the hybridised magma, has never been addressed before, but some previous workers have investigated interaction between sulfide melts and felsic magmas. For example, some have suggested that immiscible sulfide liquids (which form at an unspecified depth) sequester metals, later releasing these metals to late-stage, volatile-rich hydrothermal fluids evolved from the hybrid in the upper crust (Hattori and Keith, 2001; Halter et al., 2002). It has also been suggested that during partial melting of the lower crust, pre-existing gold deposits may be preferentially melted, leading to localised escape of metal-enriched felsic magmas (Tomkins and Mavrogenes, 2003; Tomkins et al., 2009), although it may be difficult to form pre-peak metamorphic gold deposits in an arc setting. However, many questions remain regarding metallogenic processes in the roots of arcs. In deep crustal mixing chambers, it is unknown whether sulfide liquids will typically exsolve in the magma and settle, or whether they typically remain suspended, available for later upward transport with an escaping intermediate magma. Is additional sulfur required or available from external sources to cause sulfide saturation in hybrid magmas in this setting? Addressing these questions requires detailed knowledge of the factors affecting sulfur solubility in silicate magmas.

The temperature, pressure, iron content, oxygen fugacity (fO_2), sulfur fugacity (fS_2), and composition all affect the solubility of sulfur in silicate magmas (Naldrett, 2004; Jugo et al., 2005). Sulfur solubility, referred to as Sulfur Content at Sulfur Saturation (SCSS), is influenced by a complex interplay of these parameters. Several authors have found that iron content exerts the dominant control on SCSS, with less agreement on the importance of the other factors (Mavrogenes and O'Neill, 1999; Li et al., 2001; Mungall, 2002; O'Neill and Mavrogenes, 2002; Naldrett, 2004). Several authors have found that the change in oxidation state between sulfide (reduced species) and sulphate (oxidised species) stability exerts a significant control on SCSS; oxidised magmas contain up to several times the sulfur as relatively oxidised mineral phases (e.g. sulphate) than as sulfide (Carroll and Rutherford, 1987; Audetat et al., 2004; Jugo et al., 2005). Widespread devolatilisation through degassing of a magma body causes sulfur loss and allows important metals such as copper to redissolve into the silicate melt (Keith et al., 1997). However, lithostatic pressures at the depths that MASH zone processes occur (~30 – 40 km) (Annen et al., 2006) prevent degassing. As a

result, the most important outcome of this study is its establishment of constraints on the saturation behaviour of sulfide in mixing magmas at depth.

Project Scope

Since a myriad of physical and chemical factors affect the metallogeny and sulfide/sulfate evolution of magmas, an appropriate field site was required where relevant magmatic processes in the deep crust are observable. The southern part of the Hidaka Metamorphic Belt in south-eastern Hokkaido, Japan (Fig. 1.2), features evidence of magma mixing in outcrop within a mid- to deep-crustal arc setting. Fieldwork undertaken at this location provides the observational framework to constrain the theoretical ideas generated in this project to the real world. Specifically, the Opirarukaomappu Gabbroic Complex was chosen for detailed sampling because it contains sub-economic massive and disseminated sulfide deposits. The location of these sulfides in the lower crust and the mixed nature of the rock units in the gabbroic complex enabled observation, in an almost unique natural laboratory, of large-scale magmatic processes at depth. After developing an understanding of magma mixing processes and their influence on metal distribution at this locality, the resulting theories are extrapolated and applied to those operating in MASH zones in general.

Several methods of investigation were employed to fully characterise lower crustal magma mixing and the consequent evolution of sulfide melts. These investigations have resulted in significant advances in understanding not only relating to the genesis of porphyry-Cu deposits, but also intrusion-related ore deposit metallogeny in general. Samples collected during fieldwork in Japan provide the petrological and geochemical framework for the project. Mathematical modelling was used to produce a quantitative estimate of mixing to account for the major sulfide-bearing compositions in the field area. High pressure experimental petrology (using piston cylinders) was undertaken at the Australian National University to provide physical validation of the project's thesis of mixing being an important driver of sulfide oversaturation. Finally, a cohesive model addressing the mobility of metal-rich sulfide melts in migrating silicate melts is presented to link the lower crustal site of sulfide melt generation with upper crustal magma emplacement and possible ore deposition. A synthesis of the conclusions is presented at the end, with some speculation about the ultimate role of lower crustal processes in the enrichment and generation of sulfide deposits in the upper crust.

Fieldwork

A field site was chosen in the Opirarukaomappu Gabbroic Complex, a major gabbroic complex located near the southern end of the Hidaka Metamorphic Belt in south-eastern Hokkaido,

Figure 1.2 (facing page): (a) Overview tectonic map of Japan showing relative locations of intersecting plates in the western Pacific. (b) Overview geological map of Hidaka Metamorphic Belt in southeastern Hokkaido, Japan. Adapted from Honma (1997).

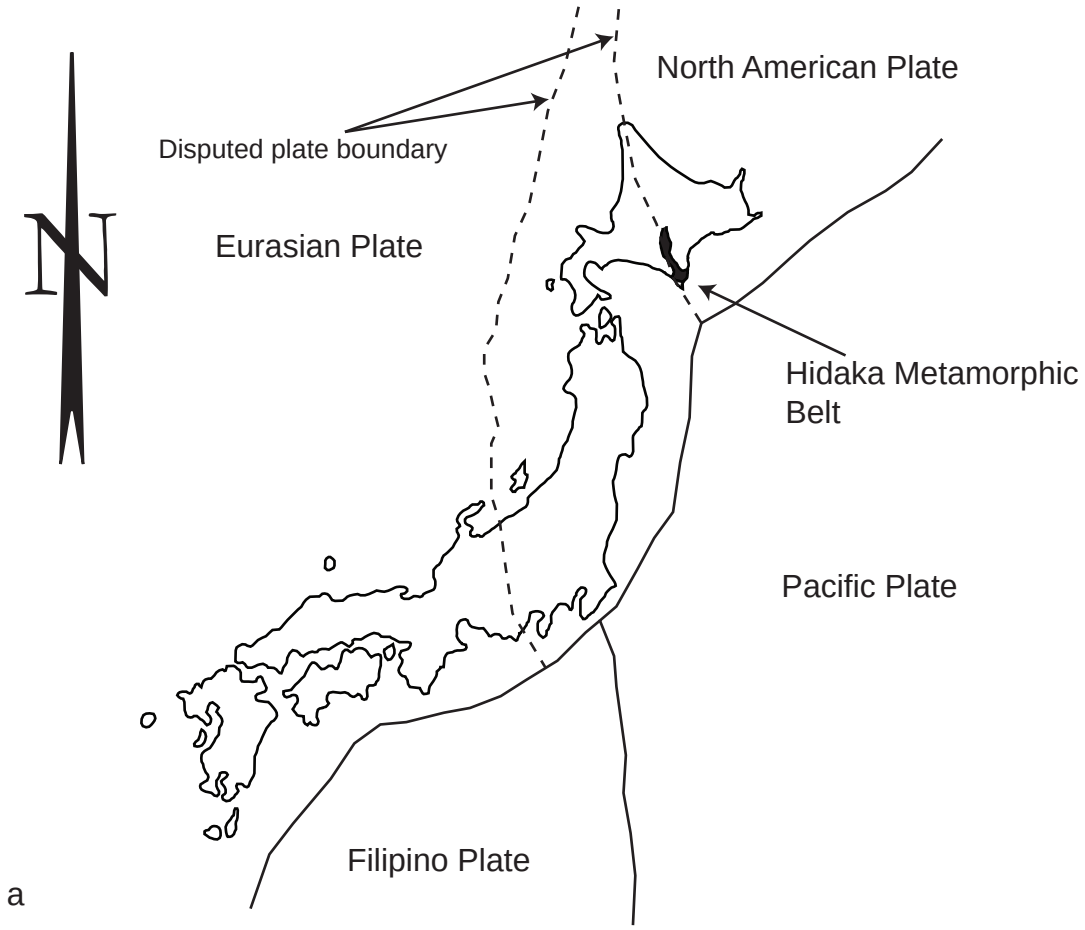
North American Plate
Disputed plate boundary
Eurasian Plate
Hidaka Metamorphic Belt
Pacific Plate
Filipino Plate
a

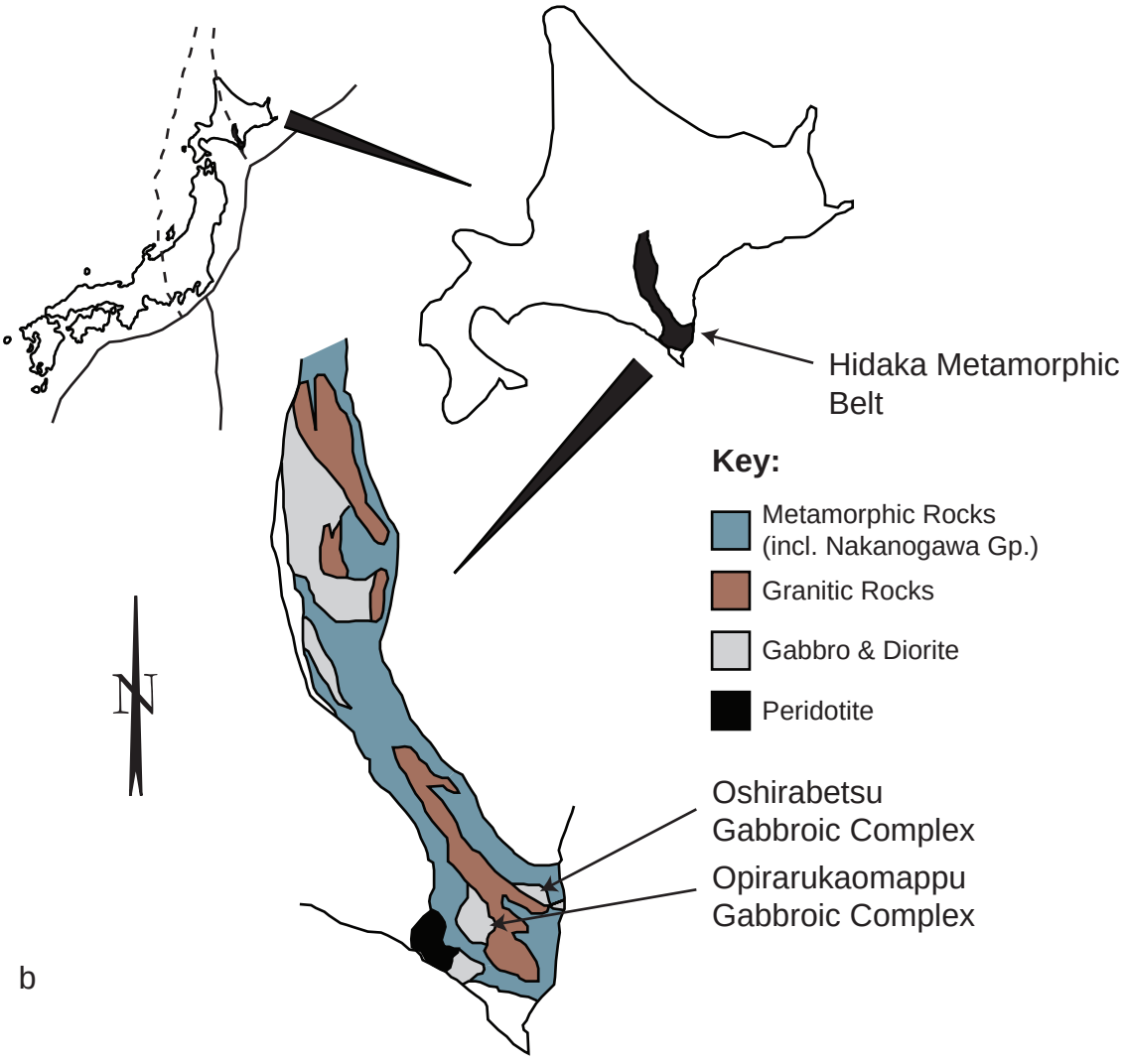
Hidaka Metamorphic Belt
Key:
Metamorphic Rocks (incl. Nakanogawa Gp.)
Granitic Rocks
Gabbro & Diorite
Peridotite
Oshirabetsu Gabbroic Complex
Opirarukaomappu Gabbroic Complex
b

Japan. Textures consistent with magma mingling between felsic and mafic magmas, which outcrop within the gabbroic complex, suggest interaction between mantle- and crust-derived magmas. The southern part of the Hidaka Metamorphic Belt has been interpreted to be an east-dipping arc crustal sequence, with a complete section from the mid-lower to upper crust exposed (Maeda and Kagami, 1996; Tsumura et al., 1999). The succession, from west to east, contains basal peridotite complexes and ophiolites in fault contact with gneisses, granulites, migmatites, and gabbroic complexes through to greenschist-grade metasediments and overlying granites. Disused Cu and Ni mines exist in the middle and upper parts of this sequence, implying that sulfide melts were developed at depth under the paleo-Japan arc. This site therefore provides a unique opportunity to observe and describe sulfide and silicate interaction in the deep crust.

Sample numbers and locations

All samples were collected during a single field season in July – August of 2006 at locations throughout and around the Opirarukaomappu Gabbroic Complex. GPS coordinates of the locations of all samples used in this study are provided in Appendix A, with an accompanying topographic map marking the sample localities. There are extra samples listed in the appendix so that all points on the map are accounted for with rock type observations and extra samples collected but not used.

Geochemistry

Samples collected during the fieldwork were thin sectioned for petrographic analysis and processed into powders. Standard transmitted-light optical microscopy was used for textural and silicate mineralogy interpretation; reflected-light optical microscopy and energy dispersive spectroscopy was used on polished thin sections to qualitatively determine the identity of certain opaque and sulfide minerals. Bulk rock powders and sulfide separates, where appropriate, were analysed by XRF, ICP-MS-AES, MC-ICP-MS, elemental analyser-continuous flow isotope ratio mass spectrometry, and Ni-S fire assay for almost the entire set of major and trace elements, including PGE, Nd isotopes, and S isotopes. Interpretations of these data are based on element ratios and trending behaviour. The data are used throughout the following chapters in different ways and are appropriately introduced where required.

Mathematical modelling

Two methods of mathematical modelling were used to constrain the theoretical limits of mixing in the gabbroic system. The first is the assimilation and fractional crystallisation equations of DePaolo (1981). The second is the hyperbolic mixing relationship equations of Albarède (1995). These two methods are used to bracket the amount of mixing between the supposed mafic and felsic endmembers with DePaolo's equations accounting for fractional crystallisation as well as mixing and Albarède's equations giving an upper limit on pure

mixing. Model considerations are again later used to address sulfide-globule settling through silicate melts. The resulting discussion relies on the modelling of silicate melt rheology using new equations presented by (Giordano et al., 2008) on compositional data modelled by the MELTS software package (Ghiorso and Sack, 1995).

Experimental petrology: end-loaded piston cylinder

A significant portion of the project focuses on experimentally demonstrating mixing-induced sulfide exsolution. An endloaded piston cylinder apparatus was used to run these experiments. Specific felsic and mafic bulk rock powders were selected, for reasons outlined in Chapter 4, and mixed at varying proportions. The mixed powders were then individually packed into platinum capsules, welded shut, inserted in the piston cylinder, and run in succession. Following each run, the metal-encased experimental charge was sectioned lengthwise, polished, and analysed for sulfide melts by reflected-light microscopy of the quench glasses from the experimental runs. The experiments were run for varying periods of less than 24 hours at pressures and temperatures reflective of those interpreted for the gabbroic complex in the field area from which they were sampled.

Thesis Organisation

This thesis is organised largely in a traditional format. None of the chapters is constructed to have the internal components that would allow for straight publication and therefore each necessarily relies on the information presented in previous sections. As each chapter covers a distinct area, there is only small overlap in the references required for each. To ease the reader's search for references of interest, each chapter's reference list comes after the chapter conclusion. The chapters, and the role that each plays in the overall arc of the thesis, are as follows:

Chapter 2: Geologic and tectonic setting of the Opirarukaomappu Gabbroic Complex, southeastern Hokkaido, Japan

This chapter focuses on modernising the terminology that is used in the current survey maps, introducing the tectonic framework of the northeast Japan Arc, introducing the geology of the field area, and describing the petrology and mineralogy of the main units that make up the Opirarukaomappu Gabbroic Complex. This information forms the geological foundation for the subsequent chapters.

Chapter 3: Magma mixing models

The specifics of mixing and the control it exerts on sulfide exsolution in Opirarukaomappu Gabbroic Complex magmas are calculated and described in this chapter. Bulk rock geochemistry and isotope data are used extensively with the equations of DePaolo (1981)

and Albarède (1995). The equations are presented, in simplified form, to help the reader understand the mathematical basis on which the element concentrations are modelled.

Chapter 4: The Sulfur Fence - a new model for magmatic sulfide formation

This chapter shows that mixing of graphitic metasediments with sulfate-rich mafic melts can lower the redox state of the melt to sulfide-stable conditions. This causes sudden, and significant, sulfide oversaturation. These observations are made using experiments designed to resemble the mixing conditions in the Opirarukaomappu Gabbroic Complex. Since the primary focus of this thesis is that mixing between felsic and mafic magmas at the base of the crust in arc regions is a primary driver of sulfide saturation and the generation of sulfide melts, this is a critical finding.

Chapter 5: Magma chamber dynamics – sulfide melt formation and settling behaviour

This chapter brings together the topics and findings presented in the previous chapters into a cohesive model characterising magmatic sulfide retention and entrainment in migrating silicate melts. This provides a conceptual link between sulfide generation and metal enrichment at depth in MASH zones with ore deposit formation and mineralisation near surface. Modelling of sulfide entrainment in silicate melt is performed with the silicate melt viscosity equations of Giordano (2008) and sulfide settling velocities determined using the Hadamard-Rybczynski equation. This approach shows that liquidus magmas similar to those in the Opirarukaomappu Gabbroic Complex are incapable of entraining sulfide melts. Some crystallisation is required to increase melt viscosity enough to allow migrating silicate magmas to entrain sulfide melts.

Chapter 6: Synthesis and conclusions – New models for magmatic Ni-Cu and porphyry-Cu genesis

This chapter restates the main findings of each previous chapter and synthesises them into a new ore formation model. In this model, the ultimate and fundamental role of the lower crust in the generation and enrichment of sulfides at depth is highlighted. It is speculated that these sulfides play a role in the mineralisation of two previously unrelated ore deposit types: porphyry-Cu and other shallow intrusion-related ore systems are linked with magmatic Ni-Cu deposits through a sulfide retention model. Magmas that are able to entrain metal-enriched sulfide globules from the lower crust to the upper crust, or those in which sulfide oversaturation is avoided, are responsible for contributing metals to porphyry systems. Magmas that are unable to entrain this metal-rich sulfide phase allow it to settle out, which accumulates as a massive sulfide, magmatic Ni-Cu deposit. Lastly, this chapter provides guidance and some suggestions for the direction of future research to address the enduring unknowns of deep crustal magmatism.

References

Albarède F. (1995) *Introduction to Geochemical Modeling*. University Press, Cambridge.

Annen C., Blundy J. D. and Sparks R. S. J. (2006) The genesis of intermediate and silicic magmas in deep crustal hot zones. *Journal of Petrology* **47**(3), 505-539.

Audetat A., Pettke T. and Dolejs D. (2004) Magmatic anhydrite and calcite in the ore-forming quartz-monzodiorite magma at Santa Rita, New Mexico (USA): genetic constraints on porphyry-Cu mineralization. *Lithos* **72**(3-4), 147-161.

Candela P. A. and Holland H. D. (1986) A mass transfer model for copper and molybdenum in magmatic hydrothermal systems; the origin of porphyry-type ore deposits. *Economic Geology* **81**(1), 1-19.

Carroll M. R. and Rutherford M. J. (1987) The stability of igneous anhydrite: experimental results and implications for sulfur behavior in the 1982 El Chichon trachyandesite and other evolved magmas. *Journal of Petrology* **28**(5), 781-801.

Core D. P., Kesler S. E. and Essene E. J. (2006) Unusually Cu-rich magmas associated with giant porphyry copper deposits: Evidence from Bingham, Utah. *Geology* **34**(1), 41-44.

DePaolo D. J. (1981) Trace element and isotopic effects of combined wallrock assimilation and fractional crystallisation. *Earth and Planetary Science Letters* **53**, 189-202.

Ebel D. S. and Naldrett A. J. (1997) Crystallization of sulfide liquids and the interpretation of ore composition. *Canadian Journal of Earth Sciences* **34**(4), 352-365.

Ghiorso M. S. and Sack R. O. (1995) Chemical mass transfer in magmatic processes IV. A revised and internally consistent thermodynamic model for the interpolation and extrapolation of liquid-solid equilibria in magmatic systems at elevated temperatures and pressures. *Contributions to Mineralogy and Petrology* **119**(2), 197-212.

Giordano D., Russell J. K. and Dingwell D. B. (2008) Viscosity of magmatic liquids: A model. *Earth and Planetary Science Letters* **271**(1-4), 123-134.

Halter W. E., Heinrich C. A. and Pettke T. (2004) Laser-ablation ICP-MS analysis of silicate and sulfide melt inclusions in an andesitic complex II: evidence for magma mixing and magma chamber evolution. *Contributions to Mineralogy and Petrology* **147**(4), 397-412.

Halter W. E., Heinrich C. A. and Pettke T. (2005) Magma evolution and the formation of porphyry Cu-Au ore fluids: evidence from silicate and sulfide melt inclusions. *Mineralium Deposita* **39**(8), 845-863.

Halter W. E., Pettke T. and Heinrich C. A. (2002) The Origin of Cu/Au Ratios in Porphyry-Type Ore Deposits. *Science* **296**(5574), 1844-1846.

Hattori K. (1993) High-sulfur magma, a product of fluid discharge from underlying mafic magma: Evidence from Mount Pinatubo, Philippines. *Geology* **21**(12), 1083-1086.

Hattori K. and Keith J. (2001) Contribution of mafic melt to porphyry copper mineralization: evidence from Mount Pinatubo, Philippines, and Bingham Canyon, Utah, USA. *Mineralium Deposita* **36**(8), 799-806.

Hedenquist J. W. and Lowenstern J. B. (1994) The role of magmas in the formation of hydrothermal ore deposits. *Nature* **370**(6490), 519-527.

Hildreth W. and Moorbath S. (1988) Crustal contributions to arc magmatism in the Andes of Central Chile. *Contributions to Mineralogy and Petrology* **98**(4), 455-489.

Honma H. (1997) Petrological characteristics of Opirarukaomappu Plutonic Complex in the southern Hidaka Metamorphic Belt, Hokkaido, Japan. *Memoirs of the Geological Society of Japan* **47**, 43-55.

Jugo P. J., Luth R. W. and Richards J. P. (2005) An experimental study of the sulfur content in basaltic melts saturated with immiscible sulfide or sulfate liquids at 1300°C and 1.0 GPa. *Journal of Petrology* **46**(4), 783-798.

Keith J. D., Whitney J. A., Hattori K., Ballantyne G. H., Christiansen E. H., Barr D. L., Cannan T. M. and Hook C. J. (1997) The role of magmatic sulfides and mafic alkaline magmas in the Bingham and Tintic mining districts, Utah. *Journal of Petrology* **38**(12), 1679 - 1690.

Krauskopf K. B. (1967) Source rocks for metal bearing fluids. In *Geochemistry of Hydrothermal Ore Deposits* (ed. H. L. Barnes), pp. 1-33. Holt, Rinehart, and Winston Inc.

Li C., Maier W. D. and de Waal S. A. (2001) The role of magma mixing in the genesis of PGE mineralization of the Bushveld Complex; thermodynamic calculation and new interpretations. *Economic Geology* **96**(3), 653-662.

Li C. and Naldrett A. J. (1993) Sulfide capacity of magma: a quantitative model and its application to the formation of sulfide ores at Sudbury, Ontario. *Economic Geology* **88**(5), 1253-1260.

Maeda J. i. and Kagami H. (1996) Interaction of a spreading ridge and an accretionary prism: Implications from MORB magmatism in the Hidaka magmatic zone, Hokkaido, Japan. *Geology* **24**(1), 31-34.

Mavrogenes J. A. and O'Neill H. S. C. (1999) The relative effects of pressure, temperature and oxygen fugacity on the solubility of sulfide in mafic magmas. *Geochimica et Cosmochimica Acta* **63**(7-8), 1173-1180.

Mungall J. E. (2002) Roasting the mantle: Slab melting and the genesis of major Au and Au-rich Cu deposits. *Geology* **30**(10), 915-918.

Naldrett A. J. (2004) *Magmatic Sulfide Deposits: Geology, Geochemistry, and Exploration*. Springer, Berlin. pp. 727.

O'Neill H. S. C. and Mavrogenes J. A. (2002) The sulfide capacity and the sulfur content at sulfide saturation of silicate melts at 1400°C and 1 bar. *Journal of Petrology* **43**(6), 1049-1087.

Richards J. P. (2003) Tectono-magmatic precursors for porphyry Cu-(Mo-Au) deposit formation. *Economic Geology* **98**(8), 1515-1533.

Richards J. P. (2009) Postsubduction porphyry Cu-Au and epithermal Au deposits: Products of remelting of subduction-modified lithosphere. *Geology* **37**(3), 247-250.

Sillitoe R. H. (1972) Relation of Metal Provinces in Western America to Subduction of Oceanic Lithosphere. *Geological Society of America Bulletin* **83**(3), 813-818.

Sillitoe R. H. (1997) Characteristics and controls of the largest porphyry copper-gold and epithermal gold deposits in the circum-Pacific region. *Australian Journal of Earth Sciences* **44**(3), 373 - 388.

Sillitoe R. H. and Hedenquist J. W. (2003) Linkages between volcanotectonic settings, ore-fluid compositions, and epithermal precious metal deposits. In *Volcanic, geothermal, and ore-forming fluids: Rulers and witnesses of precesses within the Earth: Special Publication 10* (eds. S. F. Simmons and I. Grapham), pp. 315-343. Society of Economic Geologists.

Stavast W. J. A., Keith J. D., Christiansen E. H., Dorais M. J., Tingey D., Larocque A. and Evans N. (2006) The fate of magmatic sulfides during intrusion or eruption, Bingham and Tintic districts, Utah. *Economic Geology* **101**(2), 329-345.

Tomkins A., Weinberg R. and McFarlane C. (2009) Preferential magma extraction from K- and metal-enriched source regions in the crust. *Mineralium Deposita* **44**(2), 171-181.

Tomkins A. G. and Mavrogenes J. A. (2003) Generation of metal-rich felsic magmas during crustal anatexis. *Geology* **31**(9), 765-768.

Tsumura N., Ikawa H., Ikawa T., Shinohara M., Ito T., Arita K., Moriya T., Kimura G. and Ikawa T. (1999) Delamination-wedge structure beneath the Hidaka collision zone, Central Hokkaido, Japan inferred from seismic reflection profiling. *Geophysical Research Letters* **26**(8), 1057-1060.

Chapter 2: Geologic and tectonic setting of the Opirarukaomappu Gabbroic Complex, southeastern Hokkaido, Japan

Introduction

The Opirarukaomappu Gabbroic Complex (OGC) in southeastern Hokkaido, Japan is a mafic to intermediate polytypic igneous body containing several graphite-bearing massive sulfide bodies, which in the past were mined for Ni and Cu. It is situated in the southern Hidaka Metamorphic Belt (HMB), which forms part of the Hidaka Mountains, extending 150 km from southeastern to central Hokkaido. The Hidaka Metamorphic Belt is striking because it represents a 23 km thick, easterly dipping cross-section of island arc crust, with lower to middle crust exposed in the west, and uppermost crust in the east. It therefore contains a rare example of exposed deep arc crust, preserving the petrological, geochemical, and physical relationships between intrusive units and metasediments that form the deep foundations of continental arcs. There are only two other similarly well-described sections known worldwide: the Talkeetna arc section in south-central Alaska and the Kohistan sequence in the Pakistani Himalayas.

The OGC is situated near the bottom of the HMB succession, in the lower to middle crust. Massive and disseminated sulfides are present within the OGC. In Chapter 3, these occurrences are discussed with a view to elucidating the role of magma mixing in the generation of magmatic sulfides. In Chapters 4 and 5, they are discussed with regard to their role in porphyry Cu-Mo-Au (hereafter called porphyry Cu) and magmatic Ni-Cu-(PGE) deposit genesis. However, this chapter firstly describes the tectonics of the Japan Arc and the major components of the arc involved in development of the OGC within the HMB, and the evidence for involvement of mantle magmas in lower crustal magmatic processes represented by the OGC. Secondly, this chapter updates the original, and slightly out-of-date, Geological Survey of Japan information on Hidakan geology. Thirdly, this chapter provides descriptions of samples collected during fieldwork and classifies these samples into major unit types consistent with the present body of literature on Hidakan geology.

Tectonics and Geology of the Northern Japan Arc: Framework for the OGC

Global occurrence of arc sections

This thesis posits significant constraints on magmatic processes operating in the lower crust of island and continental arcs. Real-world validation of these constraints necessitates quality exposures of deep arc crust; however, few of these are known. The Tertiary Hidaka Metamorphic Belt in Japan (Komatsu et al., 1989), the Cretaceous Kohistan Sequence in Afghanistan (Treloar et al., 1996), and the Jurassic Talkeetna Arc Section in Alaska (Greene

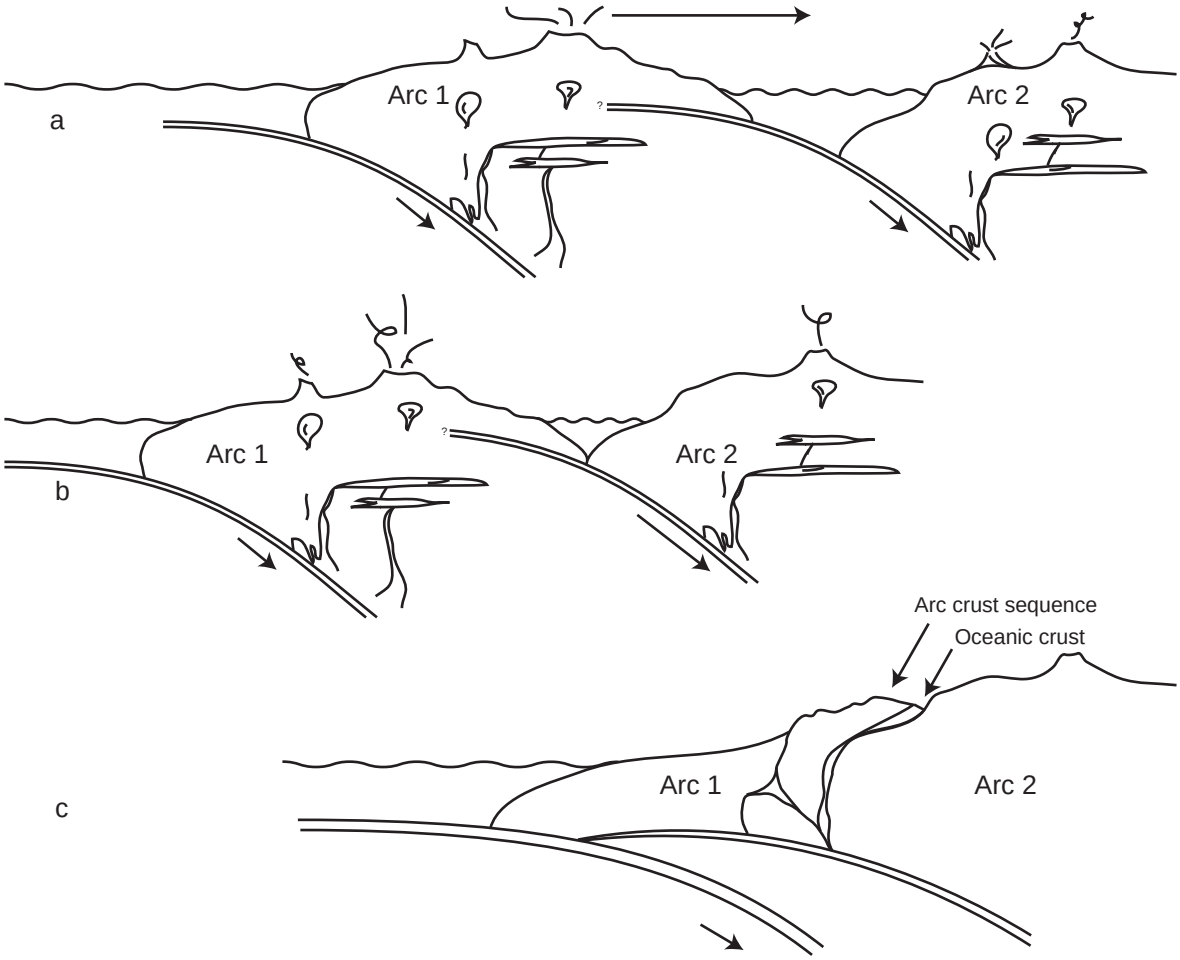

Figure 2.1: Schematic tectonic progression of an arc-arc collision showing one possible arrangement that can result in the obduction of arc crustal sequences onto the mainland of a neighbouring arc: (a) the two arcs are separated by oceanic crust, but are moving toward one another with independent magmatic plumbing systems; (b) the oceanic crust separating the two arcs has been completely consumed by subduction under arc 2. The crust of the arcs first makes contact during this stage; (c) collision continues (driven by subduction on the far side of arc 1), causing obduction of oceanic and arc crust onto arc 2. This cuts off subduction under arc 2, but subduction continues on the oceanward side of the combined arc-arc complex. Outcrop of an arc crustal section could occur as indicated in (c).

et al., 2006) are the only known and well characterised arc crust sequences. The Darb Zubaydah ophiolite in Saudi Arabia (Quick, 1990) and the Tilemsi Belt in Mali (Dostal et al., 1994) have been interpreted as parts of arc sections, but are not thought to represent entire sequences. Arc sections are thus rare, implying that their emplacement processes must also be uncommon. The intrinsic buoyancy of arc sequences (Malavieille, 1998; Greene et al., 2006), coupled with deep-seated thrusting (Atkinson, 1976) driven by subduction of neighbouring plates, are important geodynamic forces driving obduction of arc crust sections onto continental crust. Obduction of arc crust sections requires the accretion of island arc terranes at plate boundaries and fortuitous faulting through to the deeper parts of the arc crust sequence (Moho, or near-Moho depths), the latter presumably accounting for the rarity of these sequences (Fig. 2.1). Magmatic interactions observed in the intrusions of the Hidaka Metamorphic Belt are therefore almost unique in their exposure, providing an important natural library of deep-crustal magmatic processes.

Tectonics of the Hidaka Metamorphic Belt

Japan is affected by the tectonic activity of four plates: the Eurasian, North American, Pacific, and Filipino. Hokkaido, the northernmost of the four major islands of Japan, is situated between the North American, Eurasian, and Pacific plates (Fig. 2.2). Much previous research has focused on the tectonic evolution of this area, with the HMB being of particular interest (e.g. Komatsu et al., 1994; Arita et al., 1998; Moriya et al., 1998; Tsumura et al., 1999; Ito et al., 2001). Collision between the paleo-Japan arc-trench system and the paleo-Kuril arc-trench system (on the Eurasian plate and North American palaeo-plate margins, respectively) is thought to have resulted in the formation of the HMB, which runs NW-SE from central to southeastern Hokkaido in the Hidaka Collision Zone (Fig. 2.2; Komatsu et al., 1989). The HMB is thought to have once been part of the Kuril Arc (Tsumura et al., 1999). Uplift of the HMB occurred along the crustal-scale Hidaka Main Thrust (HMT), which borders the western margin of the HMB. Intrusive bodies in the south of the HMB have calc-alkaline major element trends and abundant hydrous mineral phases, consistent with arc-related genesis (e.g. Chapter 3; Komatsu et al., 1989). However, some intrusions also exhibit MORB-like geochemical signatures which Maeda and Kagami (1996) attribute to subduction of the Kula Pacific Ridge during Paleogene ridge-trench collision. Alternatively, Kemp et al. (2007) suggest that the MORBs result from mantle upwelling and decompression magmatism related to back-arc extension due to rollback of the Japan and Kuril arc systems.

The ridge subduction-rollback argument notwithstanding, magmatism associated firstly with arc development and finally with arc accretion clusters into two ages: ~50 Ma and 23–18 Ma. The data for these ranges come from a number of sources in the HMB. Kemp et al. (2007) presented zircon U-Pb ages from granulites, amphibolites, gabbros, tonalites, and granites; Maeda and Kagami (1996) estimate the age of the mafic part of the suite through comparison with whole-rock Rb-Sr ages of associated felsic anatectic melts (Owada et al., 1991); Owada et al. (1997) present whole rock and mineral Rb-Sr ages of metaluminous (I-type) tonalites. The older age is not as well defined: zircon data from Kemp et al. (2007) indicate an older pulse of magmatism at 37 Ma, significantly younger than previously published; Rb-Sr dating from Owada et al. (1997) suggests older magmatism at 51 Ma. In any case, the age data of the MORB gabbros, which must be most closely associated with either the purported ridge subduction event or the initiation of rollback magmatism, cluster in the 23–18 Ma range. The most metamorphosed domains of the HMB (granulites) share the same age range as the MORBs, implying that the arc had not yet been obducted from the Kuril Arc side onto the Japan Arc by 18 Ma. However, sediments surrounding the HMB clearly show that the HMB arc sequence was obducted in the Miocene (Kimura, 1986), which implies that the major phases of activity associated with the collision, accretion, and uplift of the HMB started and ended in the Mid to Late Miocene. The Eurasian-North American-Pacific plate triple junction has since migrated south, with a current disputed location in the eastern Sea of Japan (Chapman and Solomon, 1976; Kato et al., 2004).

Intracontinental plate margins are often ambiguous. The Eurasian-North American plate boundary in northeast Asia is particularly difficult to define. Chapman (1976) uses earthquake

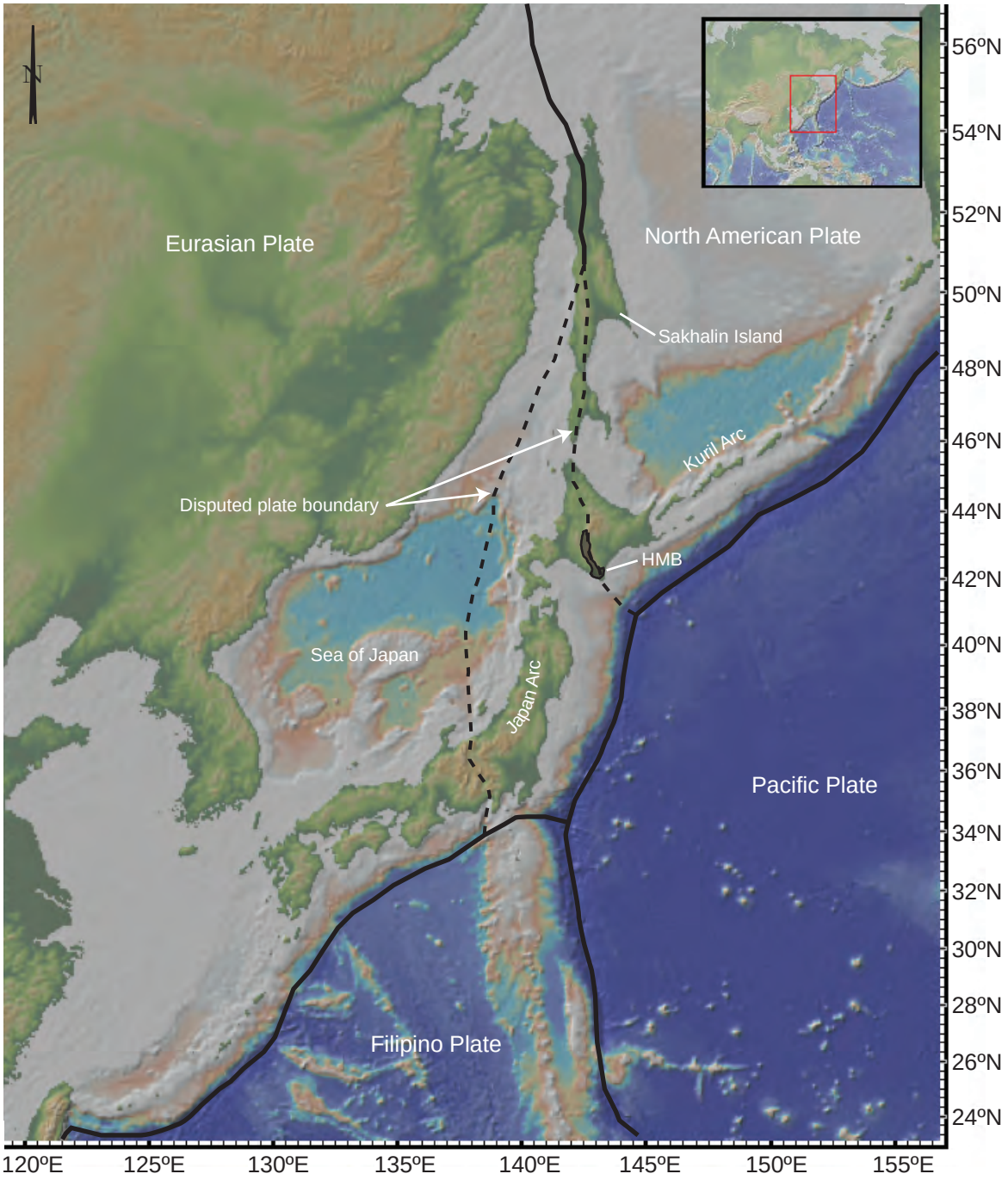

Figure 2.2: Tectonic map of the northwest Pacific, Japan Arc, and Kuril Arc. The Pacific plate subducts northwest under the Eurasian and North American plates. The Eurasian – North American plate boundary is unclear between the Pacific margin and Sakhalin Island. The Hidaka Metamorphic Belt (HMB) lies along this disputed plate boundary. There is probably a broad zone of tectonism between the Eurasian and North American plates in this region (see text for discussion).

data to hypothesize that the Eurasian-North American Plate margin around Japan propagates through a wide band of tectonically active continental crust around the Sea of Okhotsk in eastern Asia, along the spine of Sakhalin Island, and south through central Hokkaido ending at the Japan Arc-Kuril Arc triple junction (Fig. 2.2). Late Cenozoic reverse faulting in the eastern Sea of Japan documented by Okamura (2000), as well as co-located higher seismicity, recent shallow tectonic depressions and valleys interpreted from Sea of Japan bathymetry, and folding of Quaternary strata (Nakamura, 1984; Kato et al., 2004), led Kato et al. (2004) to propose that the plate boundary has shifted to the eastern Sea of Japan within the last ~1 Ma. Their analysis, using high-resolution seismic reflection data, suggests that the slip rate

along the HMT is 4 mm/yr and that it has not slowed during the Quaternary. As a result, the 7–9 mm/yr convergence rate of the Eurasian and North American plates in the Hokkaido region (Kato et al., 2004) cannot be localised to movement along a single fault line running through central Hokkaido. The balance of the convergence is thought by Kato et al. (2004) to be taken up by the deformation in the eastern Sea of Japan, implying that the Eurasian-North American plate margin in the northern Japan Arc is a diffuse zone of tectonism rather than a single focused zone.

Several remnant deep crustal structures are thought to remain from the arc-arc collision. One such structure has been described as a delamination-wedge (Tsumura et al., 1999), based on seismic analysis (Fig. 2.3), to account for the complex separation and thrusting behaviour interpreted to exist along and under the Hidaka Collision Zone. This seismic interpretation suggests that the Kuril Arc crust has, in its lower reaches, delaminated into upper and lower slabs with the upper part of the lower Kuril Arc crust thrusting up along the HMT onto the Japan Arc, and the lower part of the lower Kuril Arc crust thrusting down under the Japan Arc. A wedge of Japan Arc material occupies the space between the two opposing slabs. Deep crustal intrusive complexes are also common features in the arc sequence. The Tottabetsu Pluton is one such intrusion. It is located in the northern reaches of the HMB and has been interpreted as a ~10 km cross-section of a frozen mafic to felsic magma chamber. Kamiyama et al. (2007) use the Tottabetsu Pluton to assess the magmato-dynamic history of pluton construction. They show that roof collapse, large-scale convection, replenishment, fractional crystallisation, and magma mixing operate on long time scales, affecting the evolution of felsic intrusions in the deep crustal environment.

The HMB itself is interpreted to be an easterly dipping island arc cross-section exposing a lower to upper crustal section, from ~23 km depth to surface (Komatsu et al., 1994; Maeda and Kagami, 1996). The delamination-wedge hypothesis implies, however, that the sequence has been truncated and therefore there are parts of the sequence that are missing. The succession from west to east, bottom to top, respectively, gradually decreases in metamorphic grade from granulite grade at the bottom to greenschist grade near the top and is situated conformably below nearly unmetamorphosed Nakanogawa Group sediments lying atop the sequence. The sequence is not, however, entirely conformable, with shearing and thrust fault truncation reducing the outcropping thickness of the HMB to 16 km (Komatsu et al., 1989). The stratigraphic succession, in order from west to east, contains fault bound basal peridotite complexes, such as the Horoman Peridotite (representing a portion of ancient lithospheric mantle, see Malaviarachchi et al., 2008), ultramafic to mafic gabbros, gneisses, granulites, and migmatites through to greenschist-grade metasediments, tonalite dikes, and granites. Situated to the west and stratigraphically below, but fault-separated from, the HMB arc sequence is an internally faulted and overturned ophiolite unit (Komatsu et al., 1989).

What is missing from the HMB arc section?

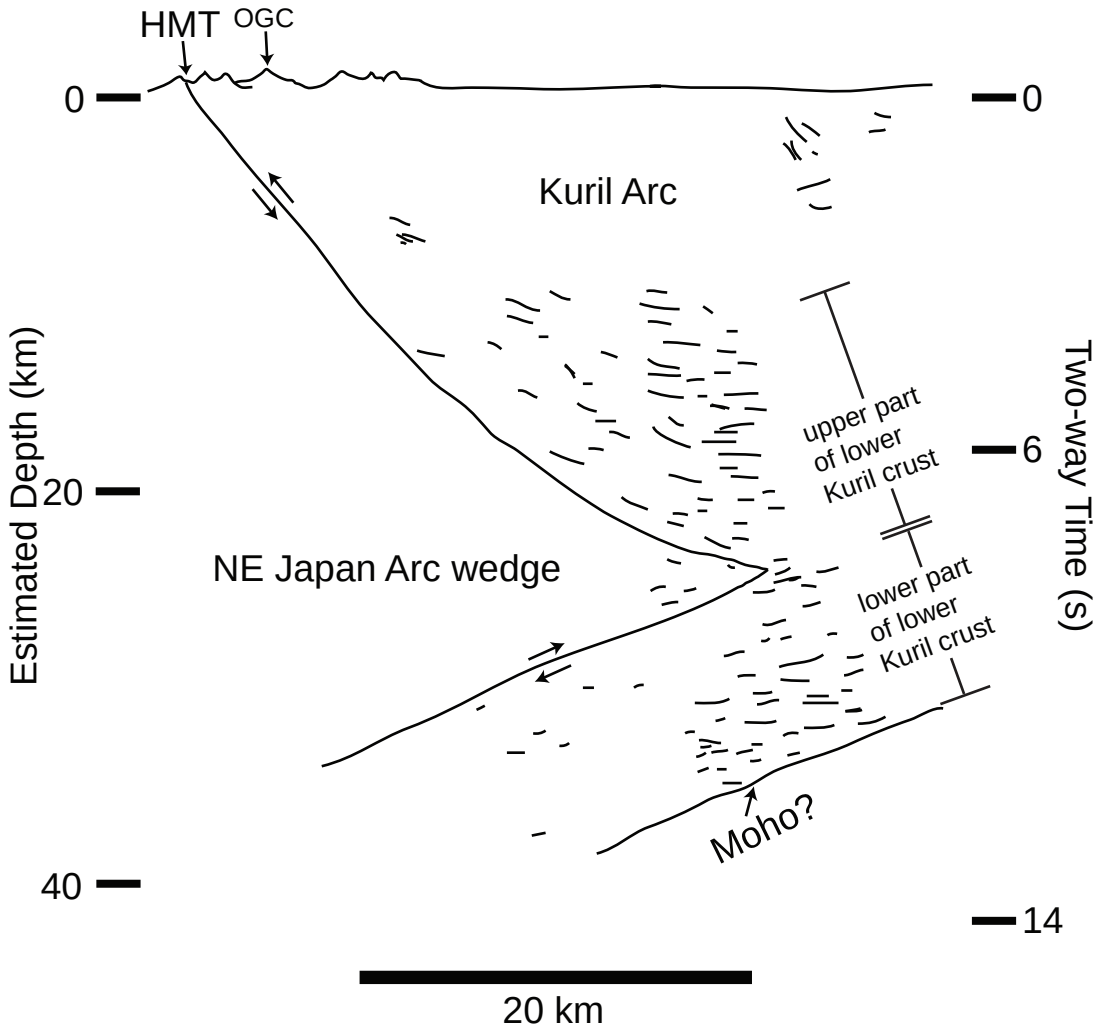

Figure 2.3: Schematic seismic interpretation showing delamination of the lower Kuril Arc crust upon collision with NE Japan Arc. Kuril Arc crust features abundant reflectors, while Japan Arc materials are relatively reflectorless. Seismic velocity of 2.9 km/s used to estimate depth. HMT = Hidaka Main Thrust; OGC = Opirarukaomappu Gabbroic Complex. Adapted from figure 4 of Tsumura et al. (1999). Reproduced/modified by permission of American Geophysical Union.

The interpretation that the lowermost crust of the HMB sequence has delaminated (Tsumura et al., 1999) is consistent with the lack of extensive cumulate piles or layered mafic intrusions in the HMB sequence, as one would expect at the base of an arc section. The Talkeetna arc section in Alaska is a more complete sequence, continuous from peridotitic upper mantle to layered gabbroic intrusions to upper crustal volcanic rocks (Greene et al., 2006). The Kohistan sequence in Pakistan includes at its base a series of layered mafic and ultramafic intrusions (Treloar et al., 1996), but is without a mantle peridotite sequence as in the Talkeetna and HMB. The HMB sequence does have many components similar to those of the Talkeetna section, but not in such an uninterrupted sequence. It has fault-bound mantle peridotites and faulted ophiolites present, but these are not conformable with the bottom of the sequence. It is therefore apparent that in most instances, some truncation is to be expected and that an entirely uninterrupted conformable sequence from upper mantle to upper crust is exceptionally rare. Even in the otherwise complete Talkeetna section, delamination in the lower crust is invoked to account for an apparent volumetric lack of pyroxenite (Greene et al., 2006). Truncation may therefore be common in obducted arc sequences, which may also explain the rarity of these sequences in the rock record globally.

Accretionary complexes in arc obduction

There is clear evidence for the involvement of accretionary complexes in arc sequence obduction. The Talkeetna and HMB sequences both have extensive metasediment accretionary domains associated with the arc section: the Chugach Terrane with the Talkeetna arc, and the Hidaka Supergroup with the HMB. This is a critical observation since magmatism in and through the surrounding crust could assimilate the sediments from the accretionary complexes or partial melting of the crust could involve these domains. In the HMB, mafic magmas are thought to have underplated the crust, causing tonalite magma generation by partial melting of the accretionary sediments of the Hidaka Supergroup; this study has found evidence of mixing in the HMB involving tonalitic melts and gabbroic melts (Chapter 3). Early plate tectonic models explaining porphyry Cu genesis included oceanic sediments as metal sources (e.g. Sillitoe, 1972). Furthermore, in many porphyry Cu deposits around the world, remnants of crustal material – such as old cores in zircons – are found in ore-associated intrusions (e.g. Harris et al., 2004), indicating that mixing between mantle- and crust-derived magmas in arcs is a global phenomenon. The chemistry of accretionary complexes may thus be important in controlling metal source and enrichment processes. The development of metalliferous magmas incubated in the lower crust of arcs and their roles in later ore deposit formation is discussed further in later chapters.

Ore deposits and island arcs

A central goal of this project is to conceptually link lower crustal magma mixing with upper crustal ore deposits, with particular attention on intrusion-related systems, such as porphyry Cu and magmatic Ni-Cu-(PGE) deposits. All of the tectonic and magmatic ingredients favouring porphyry Cu deposit formation are present in the HMB sequence (cf. Richards, 2003): hydrous, metalliferous, sulfur-rich magmas; mixing of mantle and crustal melts; and a regime of high tectonic stress. However, even though Komatsu et al. (1989), Kamiyama et al. (2007), and this study found many felsic intrusives in the upper arc sequence, the HMB does not contain any known occurrences of porphyry-type mineralisation. Other modern arcs, such as Papua New Guinea and the Andes, feature gigantic porphyry ore deposits. The development of massive sulfides near the base of the HMB sequence may indicate a key difference between well-developed porphyry systems and barren ones. The presence of different types of ore deposits in the upper crust may be related to the ability of metalliferous magmas to ascend quickly to the upper crust. Brown (1994) and Weinberg (1999) indicate that magmas will buoyantly ascend through fracture-controlled pathways and that translithospheric strike-slip structures primarily control magma emplacement in many arcs. Fault geometries resulting in extensional domains within larger-scale compressional tectonic regimes will serve as focused magma ascent pathways. In the HMB, there is evidence for dextral strike-slip faulting (Kimura, 1986) and thrust faults penetrating at least to the lower crust (Tsumura et al., 1999). However, mineralisation seems to be restricted to the lower parts of the sequence. This perhaps reflects an unsuitable arrangement of ascent

pathways from the deep crust, even considering the deposit-favourable conditions under which the HMB sequence was obducted. In the Talkeetna arc, there is little evidence for magmatic ore deposits of any kind. However, in the upper half of the sequence, the volcanic and volcaniclastic Talkeetna Formation hosts rare occurrences of volcanogenic massive sulfide deposits (Newberry et al., 1986). In the Kohistan Sequence, disseminated sulfide mineralisation (~ 0.1–1vol%) occurs throughout the Jijal layered mafic-ultramafic intrusion with elevated concentrations of PGE in some of the sulfides (Miller et al., 1991). Therefore, an important consideration is whether or not the extraction of metals from the lower crust is a critical process controlling the metallogenic potential of the upper crust.

Geological setting of the field area, Northern Japan Arc

The Horoman Peridotite and the Opirarukaomappu Gabbroic Complex

A major basal peridotite complex in the HMB sequence that warrants mention is the Horoman Peridotite Complex. Several previous studies suggest that the Horoman Peridotite Complex represents an obducted wedge of mantle material (Komatsu et al., 1994; Ozawa and Takahashi, 1995; Takazawa et al., 1999; Saal et al., 2001; Morishita et al., 2004; Ozawa, 2004) showing strong evidence of mixing between intrusions, subducted slab components, and mantle material. Moreover, Pb, Nd, and Hf isotope ratios suggest that the Horoman Peridotite is an ancient mantle remnant that has escaped homogenisation with the modern mantle (Malaviarachchi et al., 2008). Ultramafic layering is a peculiarity of the Horoman Complex, the styles of which have been used to subdivide the complex into Upper and Lower Zones. The Lower Zone has cyclic layering, tens to hundreds of metres in thickness, with the sequence plagioclase lherzolite to spinel lherzolite to harzburgite to dunite (not always present) to harzburgite to spinel lherzolite to plagioclase lherzolite (Ozawa and Takahashi, 1995; Takazawa et al., 1999). The Upper Zone is characterised by centimetre-scale layering of plagioclase lherzolite, harzburgite, dunite, and gabbro (Takazawa et al., 1999). Equilibrium temperatures estimated from orthopyroxene cores were found to increase gradually from the Lower to Upper Zone (Ozawa and Takahashi, 1995). This temperature gradient was interpreted by these authors to reflect the temperature gradient inside an ascending mantle diapir. Takazawa et al. (1999) take this interpretation further, arguing that melt extraction from peridotite of this composition results in MORB magmatism. As mentioned, the cause of MORB magmatism in the HMB is contentious and the upwelling of mantle material through diapirism or through fault-mediated migration may affect structural-tectonic interpretations of this area. However, the fault-bound nature of the complex separates it physically and chemically from the rest of the sequence and it is argued here that slab delamination provided a mechanism for transporting the complex, as a single entity, onto the Japan arc.

The OGC (Fig. 2.4a) lies to the east of the Horoman Complex in the southern Hidaka Belt. It was emplaced into metasedimentary rocks of the Nakanogawa Group and has been uplifted from approximately 23 km depth (Komatsu et al., 1989; Komatsu et al., 1994; Maeda and

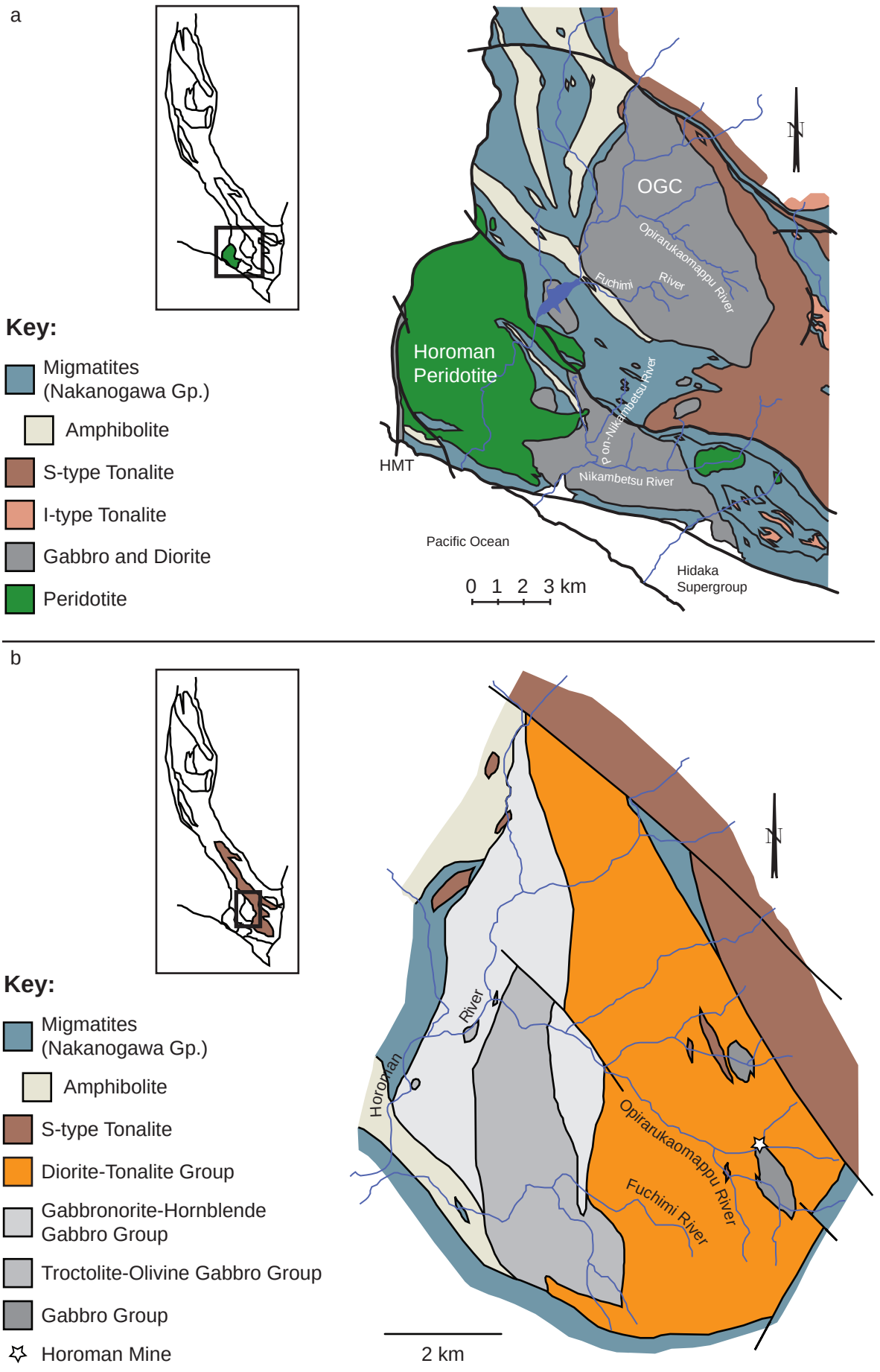

Figure 2.4: (a) Geological map showing location of simplified OGC with respect to Horoman Peridotite Complex. Adapted from Shiba and Morinaga (1998). (b) Detailed geological map of OGC. Note slight key colour difference between (a) and (b). Adapted from Honma (1997).

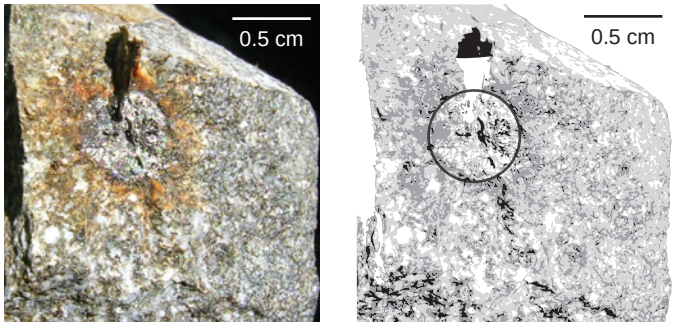

Figure 2.5: Magmatic sulfide globule (circled) in fresh gabbro from Opirarukaomappu River. Globules ranged in size between samples, but averaged ~0.5 cm in diameter. Spherical shape suggests magmatic origin. Sampled from creek bed just upstream from KR045 – see Appendix A for coordinates.

Kagami, 1996). S- and I-type tonalites intrude the OGC and mafic to intermediate composition rocks host disseminated spherical sulfide globules (Fig. 2.5), and in some localities, massive sulfide deposits.

Honma (1997) described six distinct igneous units within the OGC and the terms used to label these units will be used throughout this chapter: (1) a cumulate troctolite-olivine gabbro group, which is intruded by (2) fine-grained gabbronorite and (3) fine-grained olivine gabbronorite, (4) a gabbronorite-hornblende gabbro group, (5) a gabbro group, and (6) a diorite-tonalite group (Fig. 2.4b). Troctolite-olivine gabbros, gabbronorite-hornblende gabbros, gabbro group, and diorite-tonalite group rocks are the major units; fine-grained gabbronorite and fine-grained olivine gabbronorite outcrops are not of mappable scale and will not be further mentioned. Based on these units, the OGC may be broadly divided into halves: troctolite-olivine gabbro and gabbronorite-hornblende gabbro group in the western half, and diorite-tonalite group in the eastern half (Fig. 2.4b). The eastern half is the only area within the OGC with significant outcrops of gabbro group rocks.

Nakanogawa Group

The OGC is bounded to the west and south primarily by gneisses, mylonites, and migmatites of the metasedimentary Nakanogawa Group, and to the east by S-type tonalites (Fig. 2.4a). The Nakanogawa Group is part of the Hidaka Supergroup, a latest Cretaceous to Early Paleocene (Kiminami et al., 1992) accretionary wedge complex. The Nakanogawa Group itself is mainly a succession of Paleocene turbidites sourced from both the paleo-Kuril Arc and paleo-Japan Arc margins (Nanayama et al., 1993). Detrital clinopyroxene grains in the sediments of the southern and central parts of the Nakanogawa Group reflect the input of nearby calc-alkaline and tholeiitic volcanism; two populations of chrome spinel grains occur throughout the entire Nakanogawa stratigraphy, originating from upper mantle peridotite and from an unconfirmed paleo-Kuril fore-arc ophiolite sequence (Nanayama et al., 1993).

The part of the Nakanogawa Group envelope that is immediately to the south of the OGC is incised by the Pon-Nikambetsu River (Fig. 2.4a) where it contains localised areas of migmatisation. Bodies of gabbro are present in the Pon-Nikambetsu section and are, in

one locality, associated with a small massive sulfide occurrence. The migmatites in this area contain abundant graphite confined mostly to biotite-rich melanosomes. Leucosomes within the migmatite have andalusite porphyroblasts and lack any peritectic porphyroblasts, indicating that melting took place under water-saturated conditions at this locality. In other localities, such as in the Tottabetsu River to the north (see Kamiyama et al., 2007), migmatites containing peritectic garnet and orthopyroxene were found, indicating that in some areas the Nakanogawa Group underwent high temperature dehydration melting of the sort that produces tonalitic melt (e.g. Shimura et al., 1991; Singh and Johannes, 1996). Moreover, amphibolites in the southwest and northwest edges of the OGC (Fig. 2.4b) were observed to have undergone some minor dehydration melting, supporting the contention of high temperature metamorphism in the lower parts of the sequence. Shiba and Morinaga (1998) conducted a detailed structural examination of the shear movement associated with mylonite development in the Nakanogawa Group around the OGC, finding that southeast movement of the complex occurred under lower granulite to amphibolite facies metamorphic grade. Mylonisation is concentrated in biotite gneiss and S-type tonalite that surrounds the OGC.

Historical Map Terminology

Before going into the specifics of the geology of the HMB, a brief addressing of, and update to, the available map information covering the area of interest must be presented. The last major survey of the area was completed by the Geological Survey of Japan in 1951, before a modern understanding not only of many igneous rock types, but also of plate tectonic theory and the processes of migmatisation and mylonisation became widespread. These processes have generated textures that are widespread in and around the OGC and are therefore critical to understanding the geological and geochemical evolution of the area. Figure 2.6 is a digitised version of the original 1951 Survey map showing several of the previous rock names in the left-hand margin of the map: acidified metasomatic facies (aG), coarse-grained metasomatic facies (cG), normal dioritic gabbro (ndG), diabasic dioritic gabbro (ddG), shistose biotite hornfels (sh), and biotite gneiss (gb).

These historical classifications were not reconsidered until recently. Honma (1997) reinterpreted the rock types within the OGC, combining the acidified metasomatic facies, coarse-grained metasomatic facies, and normal dioritic gabbro units into a single rock unit called diorite-tonalite group. The diabasic dioritic gabbro was reduced simply to gabbro group. Other units were referred to by the Survey using slightly different, but still currently understandable, terminology. Surrounding the main body of the OGC, the shistose biotite hornfels and biotite gneiss units were reinterpreted by Shiba and Morinaga (1998) as belonging to a broader banded gneiss unit with lenses of biotite gneiss. The development of this igneous suite is clearly linked to Japan's aforementioned position within the global tectonic framework.

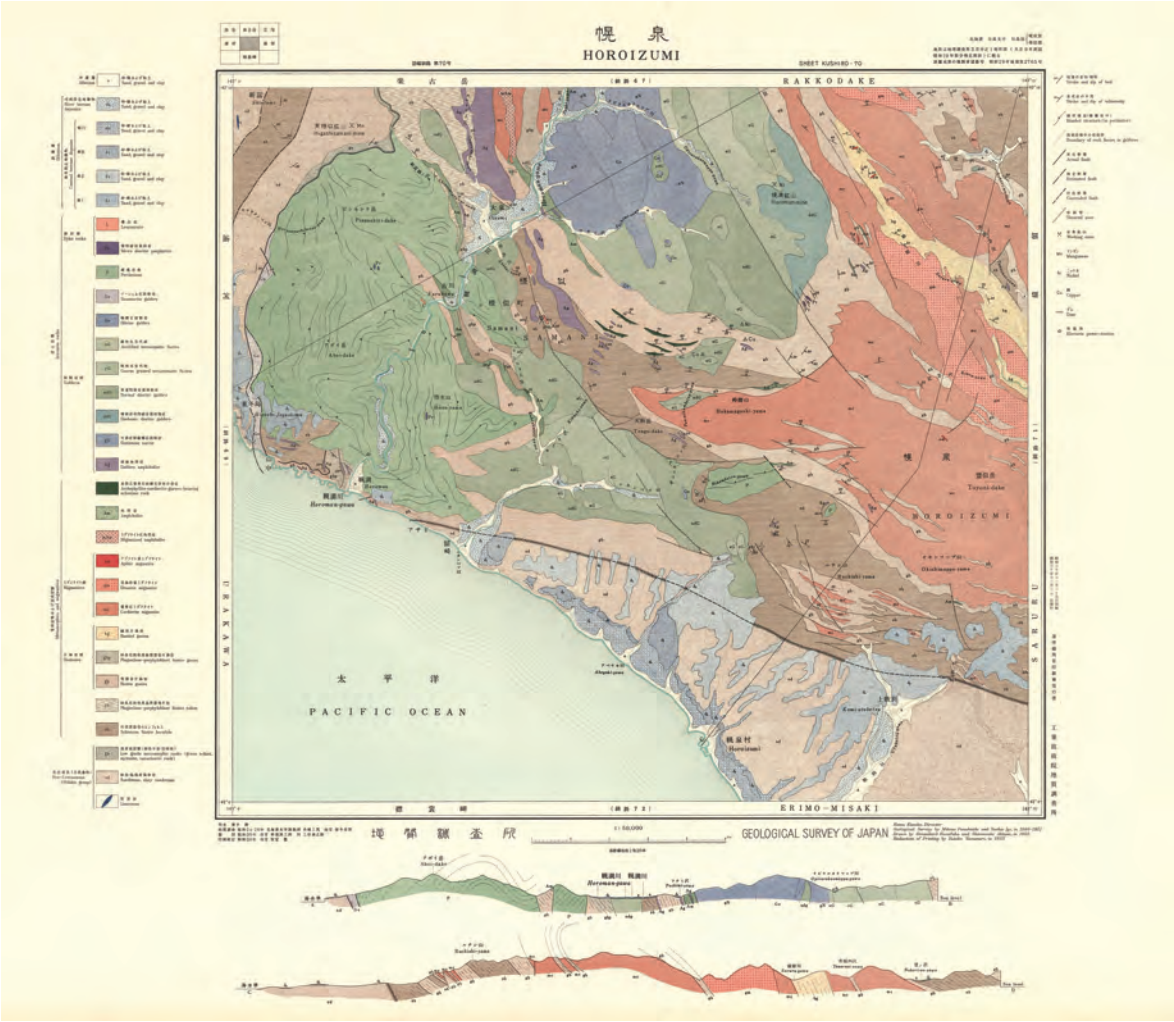

Figure 2.6: Original 1951 Geological survey map of the field area. Rock type legend is on the left-hand margin of the map image. This image © Geological Survey of Japan, used with permission. Geological Survey of Japan (ed.) (2003) Digital Geological Map of Japan 1:200,000, South Hokkaido. Digital Geoscience Map G20-2, Geological Survey of Japan, AIST.

Unit Descriptions

Troctolite-Olivine Gabbro Group

Troctolite-olivine gabbros constitute the most mafic compositions in the OGC (Fig. 2.4b). Rocks of this type comprise approximately equal proportions of olivine (~Fo_{75-80}) and plagioclase (~An_{70}). Olivine and plagioclase are typically coarsely crystalline, with sizes in excess of 1 mm, and cumulate in texture. Amphibole and pyroxene (orthopyroxene and/or clinopyroxene) occur in more coarsely crystalline (≈ 10 mm) samples, constituting up to 35% and 5%, respectively. Reaction rims occur between orthopyroxene and surrounding plagioclase and olivine and frequently between olivine and plagioclase where orthopyroxene is located nearby (Fig. 2.7a). Olivine is occasionally twinned. The plagioclase is not altered and possesses pervasive albite twinning with weak normal zoning (~An_{70} in cores to ~An_{35-40} in the rims). Opaque minerals form about 1% abundance and are primarily sulfides. Pyrrhotite and chalcopyrite often occur together with minor magnetite occurring elsewhere.

Gabbro Group

Gabbro group samples were not collected; however, Honma (1997, in Japanese) performed extensive petrography on this and the other types of rocks within the OGC. Based on his observations, gabbro group rocks comprise approximately 52% plagioclase and 33% clinopyroxene. The remaining proportions are unspecified. Significant sulfide mineralisation is not known to be hosted in Gabbro Group rocks.

MORB-like Gabbros

MORB-like gabbros have mineralogies and textures similar to olivine gabbros and the gabbro group unit. However, as will be shown in Chapter 3, their rare earth element patterns, platinum group element ratios, and Nd isotopic values share a strong affinity with MORB patterns. They are typically among the most mafic samples in the suite and are used as the mafic endmember for the mixing modelling in the next chapter.

Gabbronorite-Hornblende Gabbro Group

Rocks of the gabbronorite-hornblende gabbro group are shaded lightest grey in Fig. 2.4b. This is the main sulfide-rich unit in the OGC.

Gabbronorite

Gabbronorite gabbros comprise roughly equal proportions (45%) of plagioclase and orthopyroxene with some clinopyroxene, amphibole, and minor chlorite. Plagioclase (~An_{50}, 0.6 mm) has abundant internal sericitisation and typically has corroded crystal margins (Fig. 2.7b), implying chemical instability with the final crystallisation assemblage. Orthopyroxene is very inclusion-rich and corroded (Fig. 2.7c). Clinopyroxene has rare simple twins, is partially replaced by amphibole (Fig. 2.7d), is typically anhedral against plagioclase crystals, and exhibits reaction rims where it is in contact with included portions of plagioclase crystals. A reaction zone also often marks the boundary between amphibole and included plagioclase crystals. Chlorite partially pseudomorphs amphibole in some examples and is occasionally located in contact with sulfide globules. All phases in these samples are inclusion rich to the point of pervasive cloudiness.

The most sulfide-rich samples belong to the gabbronorite rock type. The opaque assemblage in the sulfide-rich gabbronorites constitutes approximately 10% of the rock and is dominantly pyrrhotite with accessory chalcopyrite and ilmenite. The sulfides are typically included in clinopyroxene, but less commonly in plagioclase, with the most common inclusionary phase being chalcopyrite. Pyrrhotite occurs interstially to the silicates. Chalcopyrite blebs tend to be found in plagioclase and not in clinopyroxene. Rocks of this type host the Horoman Mine (star in Fig. 2.4b), a massive to disseminated sulfide body that outcrops near the

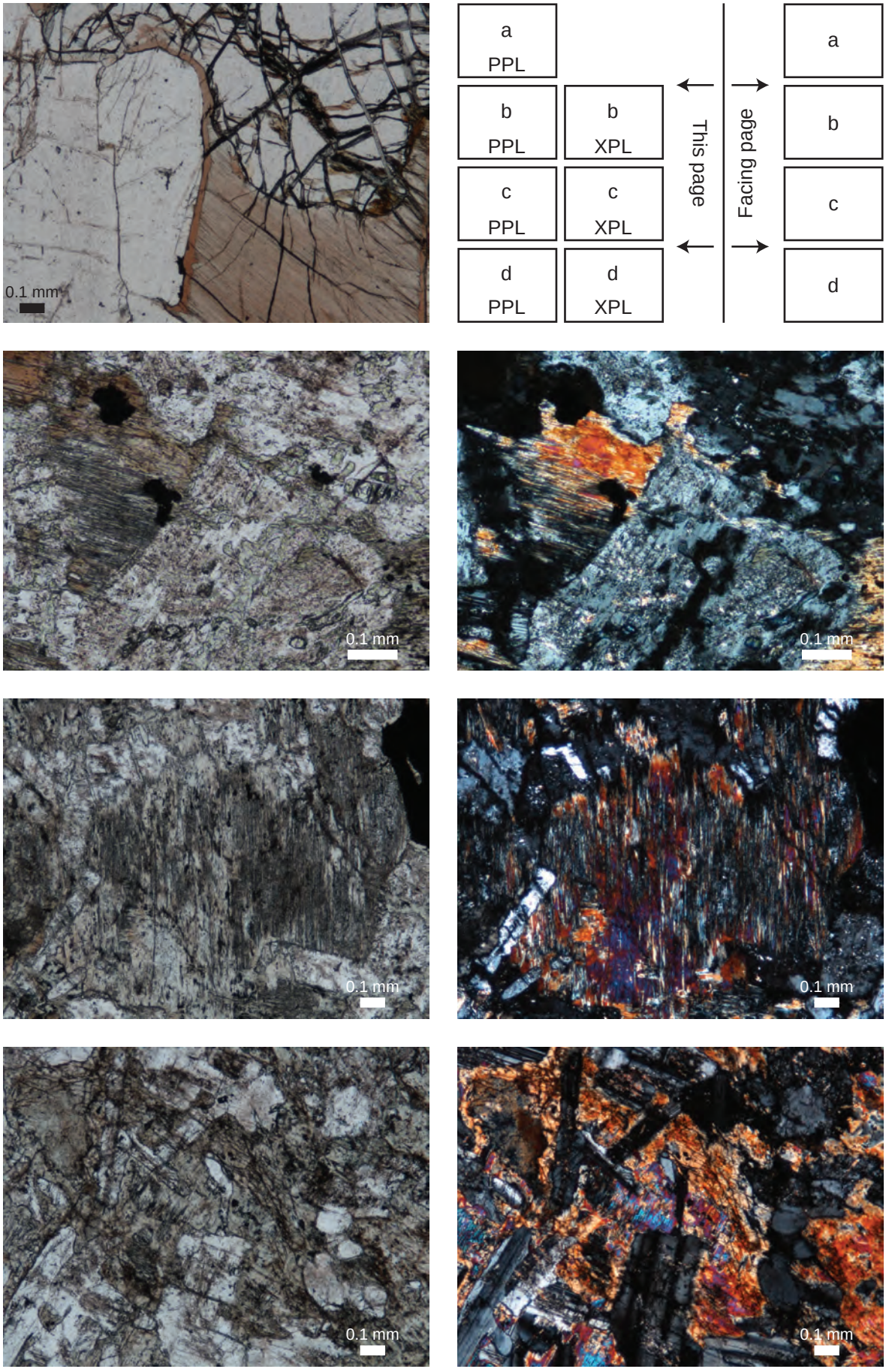

Figure 2.7: Thin section photomicrographs of rock textures in OGC samples. Each photomicrograph is presented three ways: firstly, the PPL photo is shown to allow the reader to see the minerals and textures without interpretation or annotation. Secondly, the XPL photo is shown as sometimes the crystal margins are not clear in PPL. Thirdly, a simplified, annotated, and interpreted schematic is shown to highlight

continued facing page...

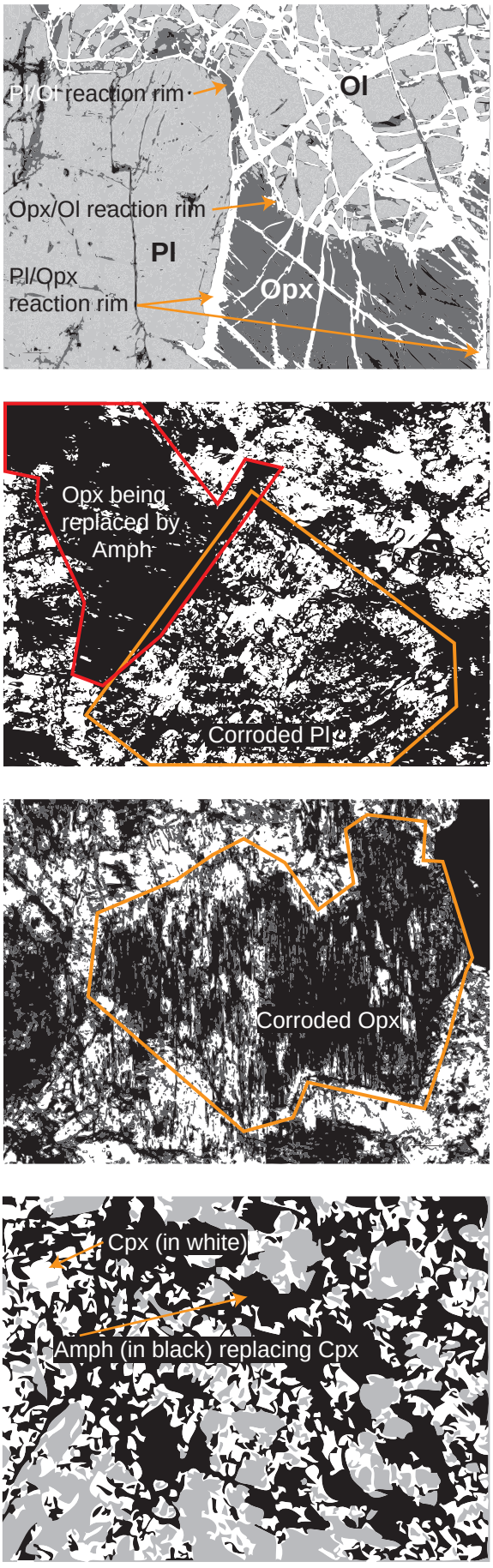

Fig. 2.7 (cont'd): the appropriate minerals and textures. See the navigation grid in the top right corner of the facing page of the figure to find the photomicrograph of interest. (a) Pl, Ol, and Opx reaction rims. (b) Corroded crystal margins and chloritisation of plagioclase; Opx being replaced by amphibole. (c) Unstable and corroded Opx crystal in gabbro. (d) Amphibole replacing Clinopyroxene in gabbro.

eastern fringes of the OGC. Leucogranite dikes cross-cut the gabbros in this region along fracture-controlled pathways. Structural control by brittle deformational features implies late emplacement of these dikes and they are not considered further.

Hornblende Gabbro

Hornblende + plagioclase gabbros of the GNHG group contain about 53% plagioclase (An_{45}) and 45% hornblende with minor biotite at various levels of chloritisation. The plagioclase features sieve texture (Fig. 2.8) and is slightly larger in size than the hornblende and biotite crystals (0.6 mm verus 0.4 mm). Alteration of the assemblage is concentrated along fractures running through the samples, but in general sericitisation is confined to the sieve-textured plagioclase. These samples tend to be much less inclusion-rich, unlike the sulfide-rich gabbronorite-hornblende gabbro group. In some samples, hornblende has been replaced, in varying degrees, by biotite, which itself is slightly chloritised.

The opaque assemblage in this rock type is almost entirely comprised of ilmenite with rare sulfides, forming less than 1% of the total. The opaques are small, typically $\leq$0.15 mm, with the largest present as inclusions in hornblende and the smallest as inclusions in plagioclase. In samples with more prevalent sulfides, the opaques are most often included in, or associated with, biotite and hornblende.

Diorite-Tonalite Group

Diorites and tonalites of this group constitute the eastern half of the OGC (orange in Fig. 2.4b). Hornblende diorites, Bt + Hbl (I-type) and Bt + Ms ± Grt ± Opx ± Crd ± Sil (S-type) tonalites are the major rock types in the diorite-tonalite group.

Diorites

Diorites of the OGC have plagioclase (~An_{38}) and amphibole as the dominant phases with biotite and quartz as minor phases. Plagioclase crystals range in size up to 1.1 mm, with amphibole, biotite, and quartz ranging in size up to 0.4 mm. Plagioclase is commonly sieve-textured, but is not as inclusion-rich as in the GNHG rocks described in the previous section. The amphibole appears unstable, having undergone varying degrees of replacement by biotite and is generally resorbed in appearance. Biotite has undergone limited chloritisation at most. Opaques are mostly ilmenite with little sulfide present, and are up to 1% in abundance. They occur mostly as inclusions in amphibole and biotite crystals.

Tonalites

I-type tonalites have albitic plagioclase (~An_{32}), quartz, biotite, and sometimes amphibole. Crystal sizes range up to ~3 mm for plagioclase and up to ~1 mm for quartz, biotite, and

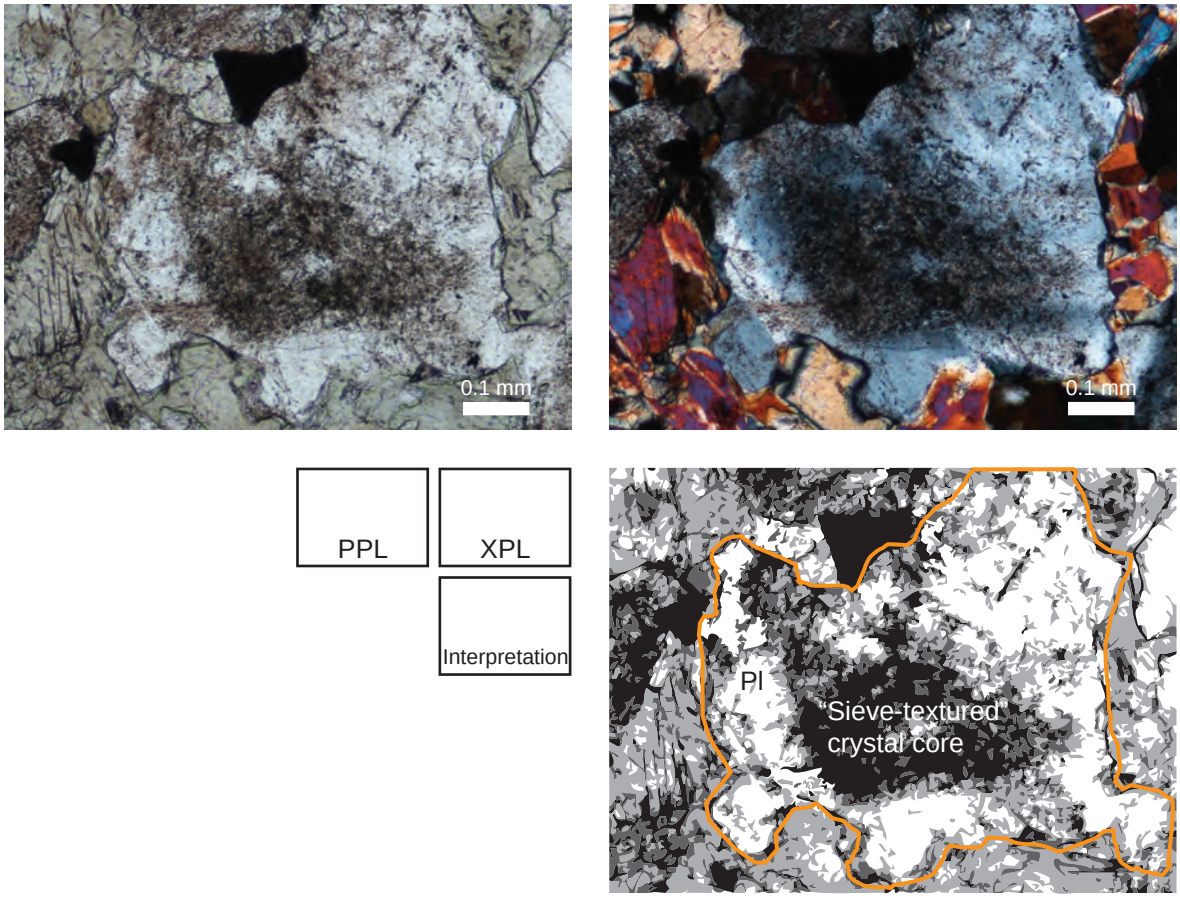

Figure 2.8: 'Sieve texture' in plagioclase crystal. See navigation grid at centre-left for orientation. Note embayed margins of the crystal.

amphibole. Plagioclase features normal zoning and mild sericitisation with abundant inclusions. Myrmekite occurs throughout. Amphibole is rare in most samples and is usually highly resorbed. S-type tonalites have Pl + Qz + Crd and/or Sil + Grt + Opx + Ms + Bt. Minor chlorite as a replacement of mica occurs occasionally. Quartz ranges in size up to 0.9 mm and plagioclase up to 1.9 mm, but typically 0.6 mm. The other phases range down in size from 0.4 mm.

The opaque phases in both types comprise pyrrhotite, chalcopyrite, and graphite, with a combined abundance of approximately 1%. The graphite and sulfide content are stressed here for later discussion in sulfide genesis when these tonalites are theoretically mixed with gabbros from elsewhere in the OGC.

Sulfide deposits

Broadly, the opaque mineral budget of the three main rock units comprises ilmenite, magnetite, pyrrhotite, chalcopyrite, and graphite with occasional cobaltite and pentlandite. The most sulfide-rich samples are almost pure sulfide (90% or greater) and are exemplified by the samples from the Horoman Mine, as well as minor sulfide mineralisation to the south of the OGC in the Pon-Nikambetsu valley.

The Horoman Mine sulfide mineralisation consists of pyrrhotite + chalcopyrite + pentlandite ± cobaltite. Ilmenite is common, magnetite is rare, and graphite occurs in some outcrops. Sulfides occur in both disseminated and massive varieties. Previous work in the area by the Geological Survey of Japan (Funahashi and Igi, 1956) described the deposit as a Sudbury-type deposit, consisting of several small pods dispersed throughout the area within gabbros. However, the genetic interpretation was made before the impact-related origin of Sudbury was known. This study observed pyrrhotite finely disseminated amongst the silicate minerals, having coalesced in some samples to form massive sulfide. Early published work on the deposit indicated that the main sulfide ore contained pentlandite and chalcopyrite in pyrrhotite with an associated trace of cobalt (Funahashi and Igi, 1956). This study found a sulfide suite consistent with the earlier study, identifying cobaltite amongst the dominant pyrrhotite-chalcopyrite-pentlandite assemblage. The Funahashi and Igi (1956) report indicated that hydrothermal alteration was always associated with major mineralisation. However, it is clear from the foregoing observations that although alteration is associated with the most sulfide-rich samples, in most cases the original mineralogy is preserved. It is therefore likely that the alteration is a by-product of, or later than, mineralisation, rather than a cause of it. Even in massive ores, reasonably fresh silicate minerals are preserved. Funahashi and Igi (1956) also found graphite in association with the sulfide mineralisation, which is supported by the observations made during this study. The Sudbury-type interpretation of the Horoman Mine deposit is not considered valid due to the lack of impact features such as shock deformation, large-scale heating or surficial crustal melting. The Pon-Nikambetsu valley mineralisation is very similar to the Horoman Deposit and consists of pyrrhotite + chalcopyrite + pentlandite + ilmenite. Funahashi and Igi (1956) describe this deposit as barren of nickel minerals; however, this study has found minor pentlandite in sulfide-rich samples. They found a higher proportion of chalcopyrite than in the Horoman sulfides, possibly reflecting less olivine fractionation from the parental magmas in the Pon-Nikambetsu region versus in the Horoman. Elsewhere throughout almost all rock types in the OGC, small sulfide globules (< 0.5 mm) are associated with biotite-rich intrusive rocks.

Rock types and classification

Figure 2.9 shows the QAPF classification types based on CIPW normative mineralogies for all samples used in this study. The CIPW normalisation incorrectly identifies many of the tonalites as granodiorites; Table 2.1 compares these classifications with those based on thin section petrography and field observation. Extensive trace element and isotope geochemical data was also collected and it is presented in the next chapter (tabulated in Appendix B2).

Summary

The position, history, geology, and tectonics of the HMB provide an almost unique natural laboratory to observe and interpret magmatic processes operating in the lower to middle crust. The appropriate mixture of silicate and sulfide mineralogies occurring within the lower

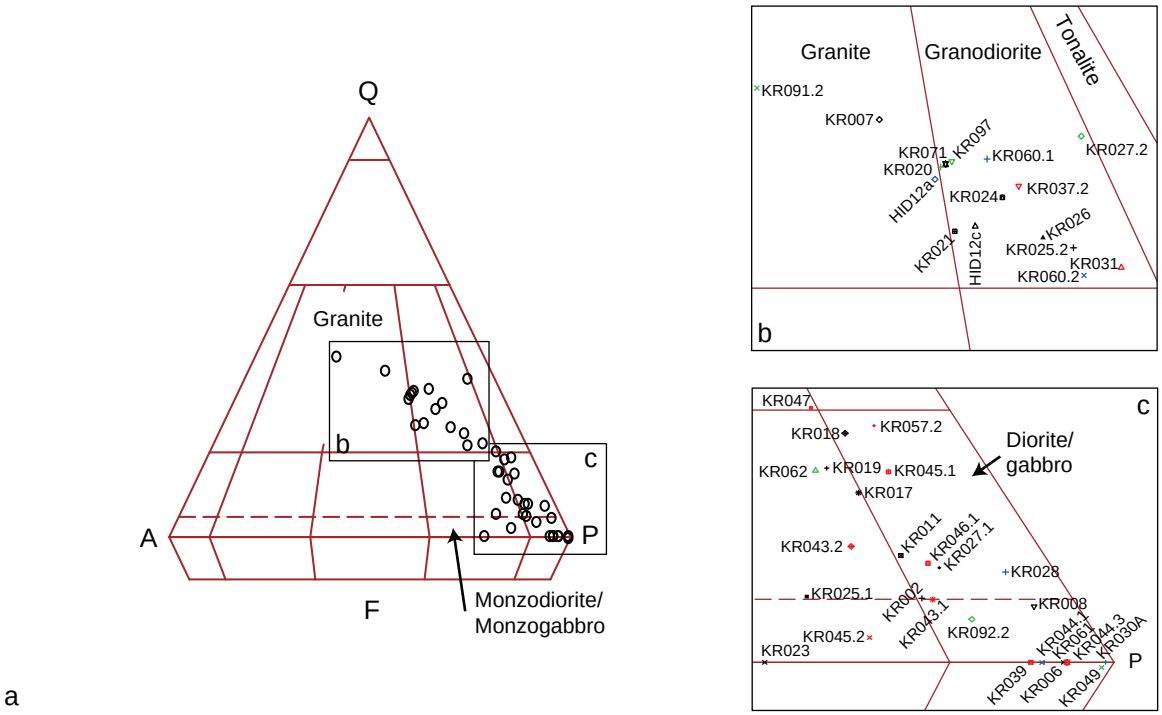

Figure 2.9: (a) QAPF classification of all samples examined in this study. These classifications are based on CIPW normative mineralogies calculated from major element analyses. Insets (b) and (c) provide sample number for each point.

crustal portion of the HMB allows a concise investigation into sulfide-silicate interaction at depth. The ore models developed from this investigation and discussed in the following chapters provide a new conceptual understanding of the link between the mineralogy and magmatism of the lower crust of arcs with the development of mineralisation in the upper crust.

TABLE 2.1
CIPW vs observational rock type classification

Sample	QAPF - CIPW Rock Type	Observation/Interpretation Rock Type
HID12a	Granite	S-Type Tonalite
HID12c	Granodiorite	S-Type Tonalite
OS1		Migmatite
KR002	Diorite/gabbro	Sulphide-bearing gabbro
KR005		Sulfide separate
KR006	Diorite/gabbro	MORB-like gabbro
KR007	Granite	Leucogranite
KR008	Diorite/gabbro	Sulphide-bearing gabbro
KR011	Diorite/gabbro	Gabbro
KR017	Monzodiorite/monzogabbro	Diorite
KR018	Diorite/gabbro	Diorite
KR019	Monzodiorite/monzogabbro	Sulphide-bearing gabbro
KR020	Granodiorite	Metasediment (?)
KR021	Granodiorite	Metasediment (?)
KR023	Monzodiorite/monzogabbro	MORB-like gabbro
KR024	Granodiorite	I-type Tonalite
KR025.1	Monzodiorite/monzogabbro	Sulphide-bearing gabbro
KR025.2	Granodiorite	I-type Tonalite
KR026	Granodiorite	I-type Tonalite
KR027.1	Diorite/gabbro	Sulphide-bearing gabbro
KR027.2	Granodiorite	Granite
KR028	Diorite/gabbro	Gabbro
KR030A	Diorite/gabbro	Troctolite-Olivine Gabbro
KR031	Granodiorite	I-type Tonalite
KR035		Migmatite
KR036		Migmatite
KR037.1		Migmatite
KR037.2	Granodiorite	I-type Tonalite
KR039	Diorite/gabbro	Sulphide-bearing gabbro
KR043.1	Diorite/gabbro	Gabbro
KR043.2	Monzodiorite/monzogabbro	Gabbro
KR044.1	Diorite/gabbro	Sulphide-bearing gabbro
KR044.2		Sulfide separate
KR044.3	Diorite/gabbro	Sulphide-bearing gabbro
KR045.1	Diorite/gabbro	Gabbro
KR045.2	Monzodiorite/monzogabbro	Sulphide-bearing gabbro
KR046.1	Diorite/gabbro	Sulphide-bearing gabbro
KR047	Granodiorite	Diorite
KR049	Foid-bearing diorite/gabbro	MORB-like gabbro
KR050		Migmatite
KR057.2	Diorite/gabbro	Diorite
KR060.1	Granodiorite	Granite
KR060.2	Granodiorite	Diorite
KR061	Diorite/gabbro	MORB-like gabbro
KR062	Monzodiorite/monzogabbro	Diorite
KR071	Granodiorite	S-Type Tonalite
KR091.2	Granite	Granite
KR092.2	Diorite/gabbro	Sulphide-bearing gabbro
KR097	Granodiorite	S-Type Tonalite

References

Arita K., Ikawa T., Ito T., Yamamoto A., Saito M., Nishida Y., Satoh H., Kimura G., Watanabe T., Ikawa T. and Kuroda T. (1998) Crustal structure and tectonics of the Hidaka Collision Zone, Hokkaido (Japan), revealed by vibroseis seismic reflection and gravity surveys. *Tectonophysics* **290**(3-4), 197-210.

Atkinson S. J. (1976) Ophiolite emplacement on to continental margins. *Nature* **264**(5582), 164-165.

Brown M. (1994) The generation, segregation, ascent and emplacement of granite magma: the migmatite-to-crustally-derived granite connection in thickened orogens. *Earth-Science Reviews* **36**(1-2), 83-130.

Chapman M. E. and Solomon S. C. (1976) North American-Eurasian Plate Boundary in Northeast Asia. *Journal of Geophysical Research* **81**(5), 921-930.

Dostal J., Dupuy C. and Caby R. (1994) Geochemistry of the Neoproterozoic Tilemsi belt of Iforas (Mali, Sahara): a crustal section of an oceanic island arc. *Precambrian Research* **65**(1-4), 55-69.

Funahashi M. and Igi S. (1956) Explanatory text of the geological map of Japan, Horoizumi, pp. 76. Geological Survey of Japan, Kawasaki, Japan.

Greene A. R., DeBari S. M., Kelemen P. B., Blusztajn J. and Clift P. D. (2006) A detailed geochemical study of island arc crust: the Talkeetna Arc Section, south-central Alaska. *Journal of Petrology* **47**(6), 1051-1093.

Harris A., Allen C., Bryan S., Campbell I., Holcombe R. and Palin J. (2004) ELA-ICP-MS U–Pb zircon geochronology of regional volcanism hosting the Bajo de la Alumbrera Cu–Au deposit: implications for porphyry-related mineralization. *Mineralium Deposita* **39**(1), 46-67.

Honma H. (1997) Petrological characteristics of Opirarukaomappu Plutonic Complex in the southern Hidaka Metamorphic Belt, Hokkaido, Japan. *Memoirs of the Geological Society of Japan* **47**, 43-55.

Ito T., Kazuka T. and Abe S. (2001) Delamination-wedge-subduction system in the Hidaka collision zone (HCZ) of arc-arc type, Hokkaido, Japan; a factory of continental crust. In *Geological Society of America, 2001 Annual Meeting*, pp. 327. Geological Society of America.

Kamiyama H., Nakajima T. and Kamioka H. (2007) Magmatic Stratigraphy of the Tilted Tottabetsu Plutonic Complex, Hokkaido, North Japan: Magma Chamber Dynamics and Pluton Construction. *The Journal of Geology* **115**, 295-314.

Kato N., Sato H., Orito M., Hirakawa K., Ikeda Y. and Ito T. (2004) Has the plate boundary shifted from central Hokkaido to the eastern part of the Sea of Japan? *Tectonophysics* **388**(1-4), 75-84.

Kemp A. I. S., Shimura T. and Hawkesworth C. J. (2007) Linking granulites, silicic magmatism, and crustal growth in arcs: Ion microprobe (zircon) U-Pb ages from the Hidaka metamorphic belt, Japan. *Geology* **35**(9), 807-810.

Kiminami K., Niida K., Ando H., Kito N., Iwata K., Miyashita S., Tajika J. and Sakakibara M. (1992) Cretaceous-Paleogene arc-trench systems in Hokkaido. In *29th IGC field trip guide book* (eds. M. Adachi and K. Suzuki), pp. 1-43. Nagoya University, Nagoya, Japan.

Kimura G. (1986) Oblique subduction and collision: Forearc tectonics of the Kuril arc. *Geology* **14**(5), 404-407.

Komatsu M., Osanai Y., Toyoshima T. and Miyashita S. (1989) Evolution of the Hidaka metamorphic belt, northern Japan. In *Evolution of metamorphic belts: proceedings of the 1987 joint meeting of the Metamorphic Studies Group and IGCP project 235.* (eds. J. S. Daly, R. A. Cliff and B. W. D. Yardley), pp. 487-493. Geological Society of London. London, United Kingdom.

Komatsu M., Toyoshima T., Osanai Y. and Arai M. (1994) Prograde and anatectic reactions in the deep arc crust exposed in the Hidaka metamorphic belt, Hokkaido, Japan. *Lithos* **33**(1-3), 31-49.

Maeda J. i. and Kagami H. (1996) Interaction of a spreading ridge and an accretionary prism: Implications from MORB magmatism in the Hidaka magmatic zone, Hokkaido, Japan. *Geology* **24**(1), 31-34.

Malaviarachchi S. P. K., Makishima A., Tanimoto M., Kuritani T. and Nakamura E. (2008) Highly unradiogenic lead isotope ratios from the Horoman peridotite in Japan. *Nature Geoscience* **1**(12), 859-863.

Malavieille C. L. (1998) Evolutionary model for Alpine Corsica: mechanism for ophiolite emplacement and exhumation of high-pressure rocks. *Terra Nova* **10**(6), 317-322.

Miller D. J., Loucks R. R. and Ashraf M. (1991) Platinum-group element mineralization in the Jijal layered ultramafic-mafic complex, Pakistani Himalayas. *Economic Geology* **86**(5), 1093-1102.

Morishita T., Arai S. and Green D. H. (2004) Possible non-melted remnants of subducted lithosphere: experimental and geochemical evidence from corundum-bearing mafic rocks in the Horoman Peridotite Complex, Japan. *Journal of Petrology* **45**(2), 235-252.

Moriya T., Okada H., Matsushima T., Asano S., Yoshii T. and Ikami A. (1998) Collision structure in the upper crust beneath the southwestern foot of the Hidaka Mountains, Hokkaido, Japan as derived from explosion seismic observations. *Tectonophysics* **290**(3-4), 181-196.

Nakamura K. (1984) Possible Nascent Trench along the Eastern Japan Sea as the Convergent Boundary between Eurasian and North American Plates. *Bulletin of the Earthquake Research Institute* **58**(3), 711-722.

Nanayama F., Kanamatsu T. and Fujiwara Y. (1993) Sedimentary petrology and paleotectonic analysis of the arc--arc junction: the Paleocene Nakanogawa Group in the Hidaka Belt, central Hokkaido, Japan. *Palaeogeography, Palaeoclimatology, Palaeoecology* **105**(1-2), 53-69.

Newberry R. J., Burns L. E. and Pessel G. H. (1986) Volcanogenic massive sulfide deposits and the "missing complement" to the calc-alkaline trend; evidence from the Jurassic Talkeetna island arc of southern Alaska. *Economic Geology* **81**(4), 951-960.

Okamura Y. (2000) Inversion tectonics along the eastern margin of the Japan Sea. *Journal of the Japanese Association for Petroleum Technology* **65**(1), 40-47.

Owada M., Osanai Y. and Kagami H. (1991) Timing of anatexis in the Hidaka metamorphic belt, Hokkaido, Japan. *Journal of the Geological Society of Japan* **97**(9), 751-754.

Owada M., Osanai Y. and Kagami H. (1997) Rb-Sr isochron ages for hornblende tonalite from the southeastern part of the Hidaka metamorphic belt, Hokkaido, Japan: Implication for timing of peak metamorphism. *Memoirs of the Geological Society of Japan* **47**, 21-27.

Ozawa K. (2004) Thermal history of the Horoman Peridotite Complex: a record of thermal perturbation in the lithospheric mantle. *Journal of Petrology* **45**(2), 253-273.

Ozawa K. and Takahashi N. (1995) P-T history of a mantle diapir: the Horoman peridotite complex, Hokkaido, northern Japan. *Contributions to Mineralogy and Petrology* **120**(3 - 4), 223-248.

Quick J. E. (1990) Geology and origin of the Late Proterozoic Darb Zubaydah ophiolite, Kingdom of Saudi Arabia. *Geological Society of America Bulletin* **102**(8), 1007-1020.

Richards J. P. (2003) Tectono-magmatic precursors for porphyry Cu-(Mo-Au) deposit formation. *Economic Geology* **98**(8), 1515-1533.

Saal A. E., Takazawa E., Frey F. A., Shimizu N. and Hart S. R. (2001) Re-Os isotopes in the Horoman Peridotite: evidence for refertilization? *Journal of Petrology* **42**(1), 25-37.

Shiba M. and Morinaga K. (1998) Shear movement which formed mylonites around the Opirarukaomappu Gabbro Complex in the southern part of the Hidaka Metamorphic Belt. *Bulletin of the Faculty of Science and Technology, Hirosaki University* **1**, 27-35.

Shimura T., Komatsu M. and Iiyama J. T. (1991) Genesis of the lower crustal garnet orthopyroxene tonalites (S-type) of the Hidaka Metamorphic Belt, Northern Japan. In *2nd Hutton Symposium on the Origin of Granites and Related Rocks*, pp. 259-268. Royal Society of Edinburgh - Earth Sciences, Canberra, Australia.

Sillitoe R. H. (1972) A plate tectonic model for the origin of porphyry copper deposits. *Economic Geology* **67**(2), 184-197.

Singh J. and Johannes W. (1996) Dehydration melting of tonalites. Part I: Beginning of melting. *Contributions to Mineralogy and Petrology* **125**(1), 16-25.

Takazawa E., Frey F. A., Shimizu N., Saal A. E. and Obata M. (1999) Polybaric petrogenesis of mafic layers in the Horoman peridotite complex, Japan. *Journal of Petrology* **40**(12), 1827-1851.

Treloar P. J., Petterson M. G., Jan M. Q. and Sullivan M. A. (1996) A re-evaluation of the stratigraphy and evolution of the Kohistan arc sequence, Pakistan Himalaya: implications for magmatic and tectonic arc-building processes. *Journal of the Geological Society* **153**(5), 681-693.

Tsumura N., Ikawa H., Ikawa T., Shinohara M., Ito T., Arita K., Moriya T., Kimura G. and Ikawa T. (1999) Delamination-wedge structure beneath the Hidaka collision zone, Central Hokkaido, Japan inferred from seismic reflection profiling. *Geophysical Research Letters* **26**(8), 1057-1060.

Weinberg R. F. (1999) Mesoscale pervasive felsic magma migration: alternatives to dyking. *Lithos* **46**(3), 393-410.

Chapter 3: Magma mixing models

Introduction

Lower to middle crustal magma mixing, as a controlling process in sulfide saturation affecting the early stages of porphyry magma genesis, has never been studied. Yet, the role of magma mixing in the genesis of intermediate-composition magmas is increasingly invoked to explain disequilibrium textures and mineralogies observed in intrusive and extrusive rocks in continental arcs (Pallister et al., 1996), such as those associated with many giant porphyry-Cu-Au deposits (e.g. Keith et al., 1997; Halter et al., 2004a). Studies in the Andes (Halter et al., 2002; Halter et al., 2004b, 2005) have investigated sulfur abundance and the role that it plays in metallogenic processes as magmas and fluids evolve during mixing in the upper crust, proximal to the final emplacement depth of mineralised porphyry magmas. These studies suggest that magmatic sulfides may have played a role in ore genesis and that it is likely they were generated by mixing between mafic and felsic magmas. Other authors have suggested that sulfide melts were present at upper crustal levels in the giant Bingham and Tintic deposits (Stavast et al., 2006). Sulfide melts have also been found in migmatites, which could provide a source of crustally derived metal (Tomkins and Mavrogenes, 2003).

Lower to middle crustal magma mixing and assimilation have also been suggested to play an important role in the genesis of intermediate arc magmas (Hildreth and Moorbath, 1988; Richards, 2003). In this model, crustal underplating, or intrusion, of large volumes of hot mafic magmas from the mantle drives partial melting of the lower crust. The resulting felsic melts eventually mix with the mafic magmas in a complex MASH zone (Mixing, Assimilation, Storage, and Homogenisation, see Hildreth and Moorbath, 1988), which generates intermediate magmas. Although metallogenic processes in the upper crust have received much attention, processes with the potential to influence metal distribution in lower to middle crustal MASH zones have not been investigated. In particular, the role of magmatic sulfides in these systems and the potential for magma mixing to generate sudden and widespread sulfide saturation and subsequent sulfide liquid generation have not been addressed.

The Hidaka Metamorphic Belt (HMB) in southeastern Hokkaido, Japan provides a rare opportunity to study the role of magma mixing in the generation of sulfide-related ore deposits in arc settings. It is a 23 km thick succession, interpreted to be a tilted cross section of island arc crust (see Chapter 2). Ophiolites, peridotites, gabbroic complexes, migmatites, tonalitic magmatism, and the youngest granulites on Earth (Kemp et al., 2007) are exposed within the belt. In the southern-most Hidaka Belt, occurrences of sub-economic massive sulfide deposits are hosted by the mafic to intermediate rocks of the Opirarukaomappu Gabbroic Complex (OGC, see Figs. 1.2b and 2.4). Magma mingling textures within the

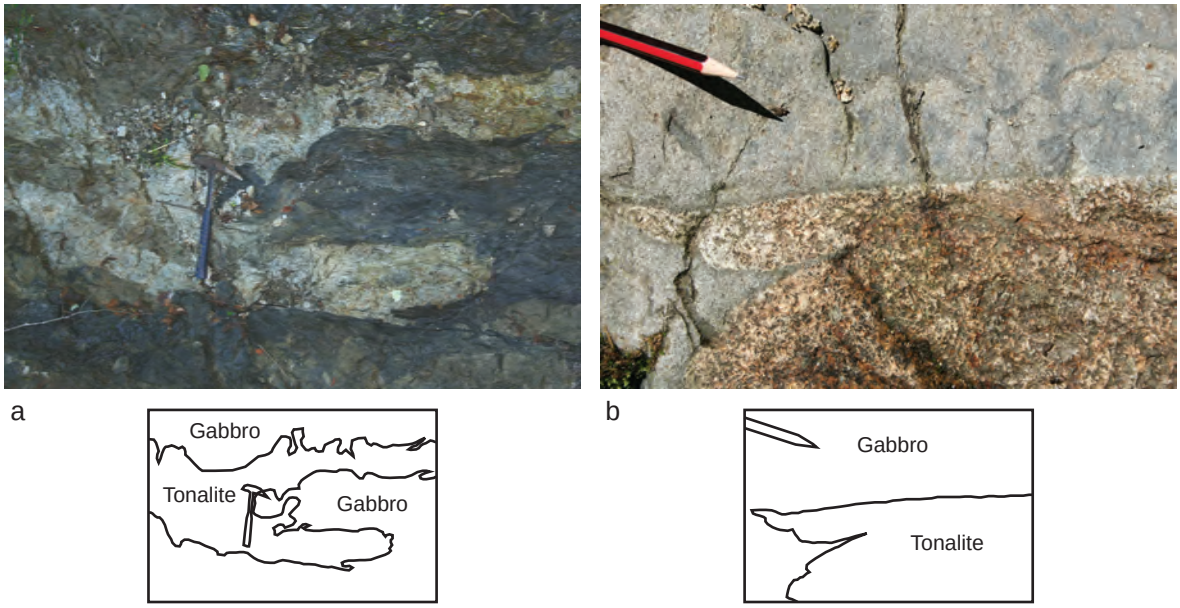

Figure 3.1: Examples of mingling textures in outcrop in the OGC. Darkly coloured rock in both (a) and (b) is gabbro, (a) lightly-coloured and (b) red-stained rock is tonalite.

OGC, developed between tonalite and gabbro (Fig. 3.1), suggest interaction between mantle- and crust-derived magmas.

This chapter aims to investigate the role of magma mixing in the generation of magmatic sulfides in the lower to middle crustal settings represented by the OGC through field-based observations, thin section petrography, geochemical analysis, and modelling of magma mixing using two different mathematical approaches. The results have implications for the role of magmatic sulfide liquids in the metallogenesis of chalcophile elements in intrusion-related ore deposits produced in these settings. Firstly, extensive geochemical data are presented to show evidence of mixing between mantle- and crust-derived melts in the OGC. Secondly, models of assimilation and fractional crystallisation (AFC) and then of simple ternary mixtures are used to estimate the amount of mixing that has occurred between the chosen endmembers. Finally, the data from these two approaches are combined to more fully characterise the role of mixing in sulfide generation in the lower crust.

The OGC comprises a significant lower-crustal mixed gabbroic body surrounded by migmatised metasedimentary rocks, intruded by tonalites, and containing massive sulfide ore bodies. It is therefore a prime target for studying the effects of mixing in the lower crust and the role that it plays in the development of sulfides in this environment. The common observation of sulfide accumulations in this lower crustal complex implies that sulfide saturation was reached at depth (20–23 km). The lack of hydrothermal alteration associated with many of the sulfide occurrences, the likely depth of formation, and platinum group element (PGE) ratios presented below, support a primary magmatic origin for these sulfides. In particular, the presence of spherical sulfide globules in an essentially unaltered silicate host is compelling evidence for the formation of magmatic sulfides in these rocks.

It is suggested here that partial melting of the deep crust resulted in production of tonalitic melt in this area of the HMB. Migmatites in the Pon-Nikambetsu River valley contain abundant andalusite porphyroblasts without peritectic mineral phases indicating that they formed through wet melting. This precludes the possibility that the tonalites represent melt extracted from these migmatites because (1) at mid-crustal pressure (~ 6 kbar) and temperatures of tonalite melt (here assumed to be ~950°C, see Shimura et al., 1991), sillimanite is the stable aluminosilicate polymorph, and (2) tonalites are the product of dehydration melting (e.g. Clemens and Vielzeuf, 1987), whereas andalusite-bearing migmatites can only form through wet melting. Therefore, it is likely that tonalites associated with the OGC (Fig. 2.4) were generated by melting of deeper crustal material, which remains unexposed. The significant outcrops of S-type tonalite surrounding the OGC, however, are not thought to be a critical component in the process of mixing-mediated sulfide production. Smaller, and typically unmappable, intrusions of I-type tonalite found within the diorite-tonalite eastern half of the OGC (Fig. 2.4b) are, for reasons discussed later, thought to be the key to understanding how mixing may have produced sulfides in the lower crust of the northern Japan arc.

Methods

Whole rock geochemistry forms the basis of the arguments presented in this chapter to characterise mixing. Major element, trace element, PGE, Nd isotope, and S isotope data, along with preparation methods, are presented in Appendix B. Opaque phases are not always definitively identifiable in thin section using reflected light microscopy; therefore energy dispersive spectroscopy (EDS) on in-house scanning electron microscope (SEM) equipment was used to determine the less obvious opaque phases. This electron microscopy work was performed on a JEOL 840A housed at the Monash Centre for Electron Microscopy.

Two main sections are used to present the main arguments of this chapter. The first is a geochemistry section, which sets the chemical framework for the mathematical models, which form the second section. The mineralogy and textures of the rocks comprising the troctolite-olivine gabbro group, MORB-like gabbros, sulfide/non-sulfide bearing gabbros, and diorite-tonalite group are described in detail in Chapter 2.

Results I: Geochemistry

Mineralogy and geochemistry

Magma mixing results in hybridisation of the chemical signatures of the magmas contributing to the mixture. However, fractional crystallisation also operates at the same time, complicating this otherwise simple relationship. Moreover, mixing often encourages fractional crystallisation by reducing the system temperature (DePaolo, 1981). Geochemical data of the OGC appear to show the effects of both mixing and of fractional crystallisation.

Careful examination of the behaviour of different element classes may provide a means of separating the role of each in the evolution of the OGC.

Major elements

Harker variation plots of major element oxides against SiO_2 (Fig. 3.2) are consistent with typical calc-alkaline fractionation trends. This is shown by elevated Al_2O_3 and increasing Fe_2O_3/MgO with increasing SiO_2. The sample with the lowest SiO_2 (43 wt%) is a forsterite-cumulate troctolite gabbro. This accounts for its elevated MgO content and positive Eu anomaly (discussed in next section, Fig. 3.3). It has depleted Na_2O, K_2O, P_2O_5, CaO, Al_2O_3, and TiO_2 contents, compared with the rest of the OGC suite (see Appendix B). The increasing Na_2O, K_2O, and P_2O_5, and decreasing CaO, Fe_2O_3, MgO, and MnO with increasing SiO_2 are commonly associated with calc-alkaline fractionation trends. This implies fractionation of olivine, pyroxene, and calcic plagioclase from the OGC magmas. S- and I-type tonalites from within the OGC (which are part of the diorite-tonalite group), and other S-type tonalites surrounding the OGC, are indistinguishable from each other on the basis of major elements. All samples with bulk SiO_2 > 70 wt% are late-stage leucogranite dikes unrelated to mixing in the rest of the suite.

Trace elements

The curvilinear trends in many of the major elements between mafic (~49 wt% SiO_2) and felsic (~65 wt% SiO_2) endmembers, consistent with fractional crystallisation, obscure the role of mixing in the overall development of the igneous suite. Trace element data may be used to see through this mineral fractionation obfuscation.

Figure 3.3a shows the REE pattern for the troctolite-olivine gabbros, normalised to primitive mantle (Hofmann, 1988). The large positive Eu anomaly is consistent with the cumulate nature of these gabbros. Other gabbros present in the OGC have two distinct REE profiles: (i) MORB-like with relatively flat chondrite-normalised REE values of around 10 and (ii) sloping light REE (LREE), flat heavy REE (HREE) non-sulfide and sulfide-bearing gabbros (Fig. 3.3b).

Tonalite (63–70 wt% SiO_2) is the dominant felsic member of the OGC igneous suite. Two distinct generations exist: a Bt ± Hbl tonalite, here referred to as 'I-type', and a Bt + Ms ± Grt ± Opx ± Crd ± Sil tonalite, here referred to as 'S-type'. The S- and I-type tonalites are clearly delineated in terms of their REE patterns. S-type tonalites have negatively sloped chondrite-normalised profiles. The lightest REE values of these are mostly above 50 and the heaviest REE values are ~2.5. La/Yb ratios range from 26.9 to 48.3. The S-type tonalite profiles have a continuous negative slope from the start of the LREE through the HREE (Fig. 3.3c). Conversely, the I-type tonalites have more variable chondrite-normalised concentrations with profiles sloping negatively from 30 – 100 in the LREE to 6 – 10 in the HREE (Fig. 3.3c).

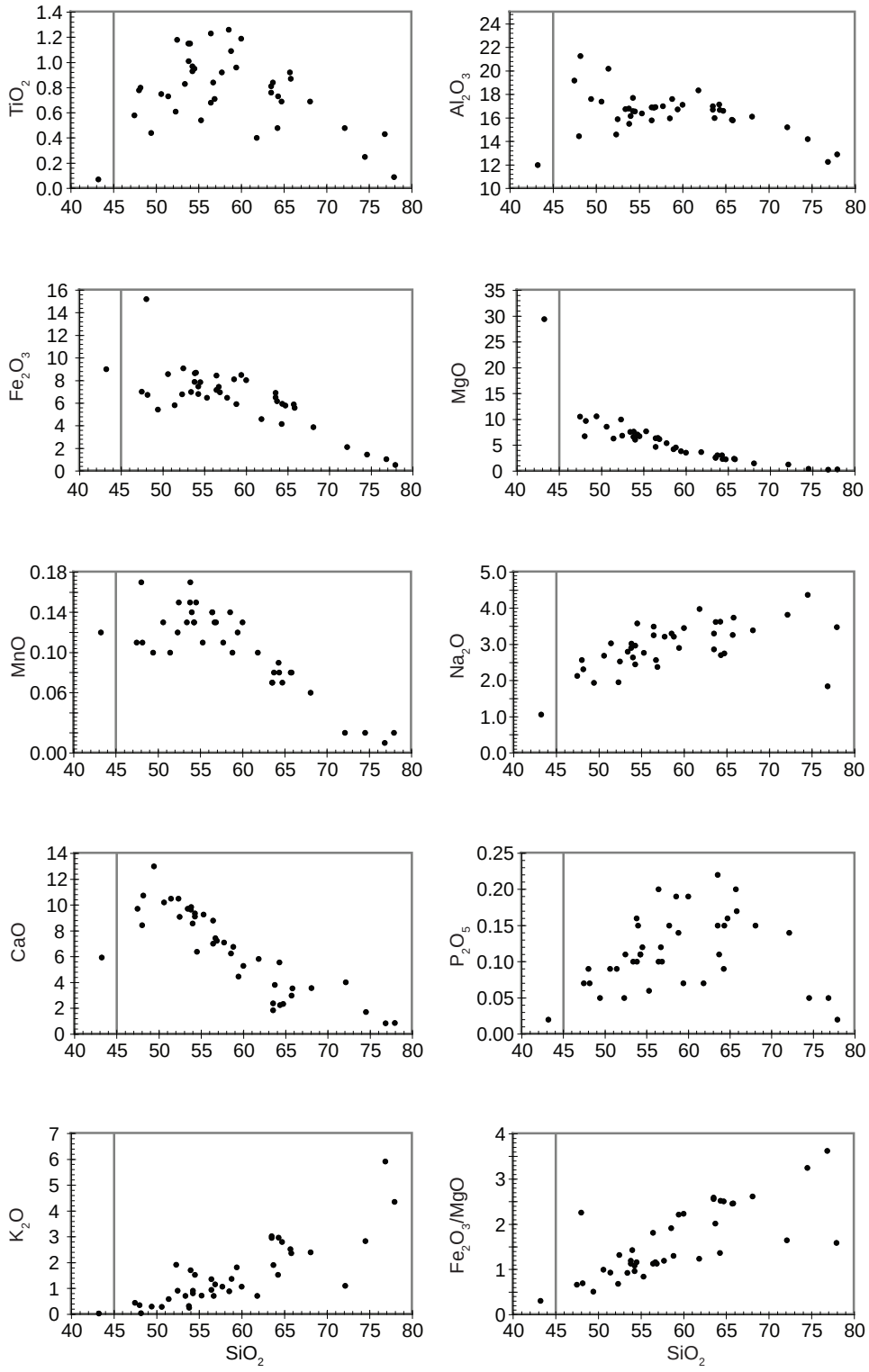

Figure 3.2: Major element Harker variation plots in wt. % element vs. wt. % SiO_2. Troctolite gabbro is to left of vertical grey line through 45% SiO_2. Increasing Na_2O, K_2O, and to some extent P_2O_5, and decreasing CaO, Fe_2O_3, MgO, and MnO with increasing SiO_2 are commonly related to the fractionation of olivine, plagioclase, and clinopyroxene and are distinctly calcalkaline trends. However, the linearity particularly apparent in the CaO vs SiO_2 plot and also in the Fe_2O_3, MgO, MnO, Na_2O, and K_2O vs. SiO_2 plots is likely due to mixing between gabbroic and tonalitic endmembers for reasons discussed in the text. Everything with SiO_2 greater than 45% is non-troctolitic, and the line at this composition is drawn to help the reader.

La/Yb ratios range from 3.7 to 17.3. The I-type profiles feature negatively-sloping LREE as in the S-types, but the HREE flatten at ~10. The most distinctive feature separating S- and I-types is the relative HREE enrichment in the I-types. This is also reflected in Y content, an element chemically similar to the HREE, which in I-type rocks is 1.1 to 3 times greater than in

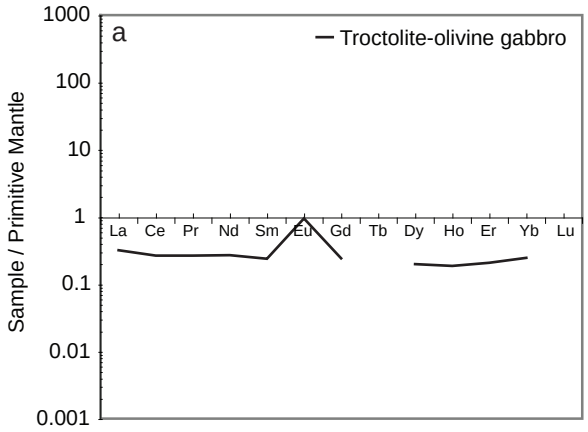

Figure 3.3 (above and facing page): (a) Primitive mantle-normalised spider plot of troctolite-olivine gabbro cumulate from OGC. Facing page: extended spiderplots normalised to McDonough and Sun (1995) CI chondrite values: (b) MORB-like and sulphide-bearing gabbros; (c) S- and I-type tonalites; and (d) Diorites. Element groupings are based on siderophile/chalcophile vs lithophile behaviour as determined by McDonough and Sun (1995).

S-type rocks. This may indicate the presence of residual garnet in the source region of the S-type tonalites, whilst I-type tonalites may have been extracted from a garnet-free source. The aluminous assemblage of the S-type tonalites, containing garnet, orthopyroxene, cordierite, and sillimanite, is consistent with dehydration melting of metapelites. These minerals may represent peritectic phases that were entrained as the magma escaped its source. In contrast, the hornblende-bearing I-type tonalites may have been produced by dehydration melting of intermediate to mafic meta-igneous rocks (this is consistent with observation of partially melted amphibolites on the southwestern margin of the OGC, see Fig. 3.3b). Trace amounts of sulfide minerals (~1 vol%) associated with graphite and ilmenite occur throughout both types of tonalite (Fig. 3.4). In the nearby Oshirabetsu Gabbroic Complex, which is similar to the OGC, graphite is abundant and is isotopically similar to that found in Nakanogawa Group sediments (Tsuchiya et al., 1991). This suggests that the graphite in the OGC tonalites may also be sourced from Nakanogawa Group sediments. Both types of tonalite have a positive Pb anomaly relative to CI chondrite and primitive mantle. This is probably related to the presence of sulfides in the system because Pb is mildly chalcophile.

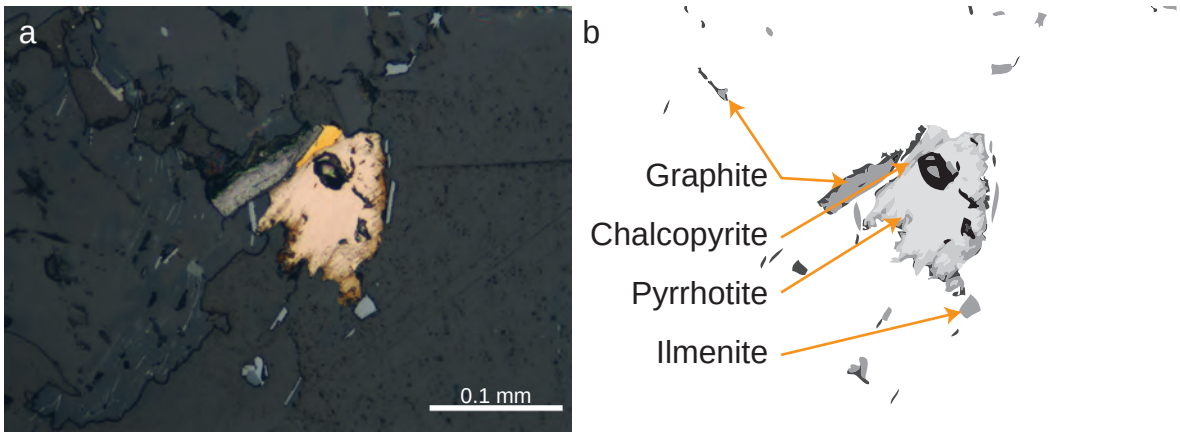

Figure 3.4: (a) Reflected light photomicrograph from polished section showing pyrrhotite (labels in b) surrounded by graphite in tonalite host. Note presence of ilmenite associated with the sulfide occurrence. Graphite is a common mineral phase in rocks of the OGC and surrounding gabbroic complexes.

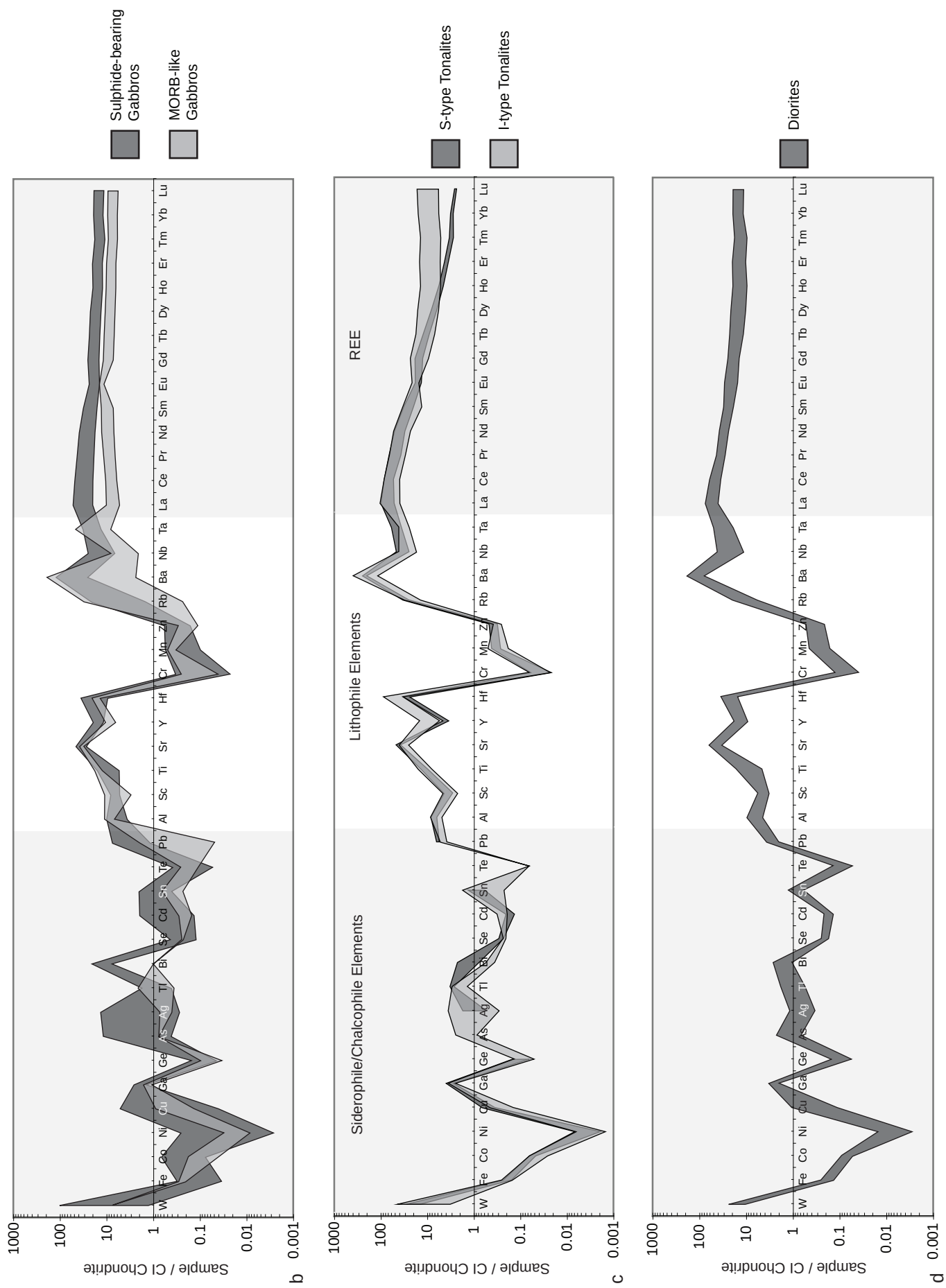
Sulphide-bearing Gabbros
MORB-like Gabbros
S-type Tonalites
I-type Tonalites
Diorites
Lithophile Elements
Siderophile/Chalcophile Elements
REE
Sample / CI Chondrite
1000
100
10
1
0.1
0.01
0.001
W Fe Co Ni Cu Ga Ge As Ag Tl Bi Se Cd Sn Te Pb Al Sc Ti Sr Y Hf Cr Mn Zn Rb Ba Nb Ta La Ce Pr Nd Sm Eu Gd Tb Dy Ho Er Tm Yb Lu
b
c
d

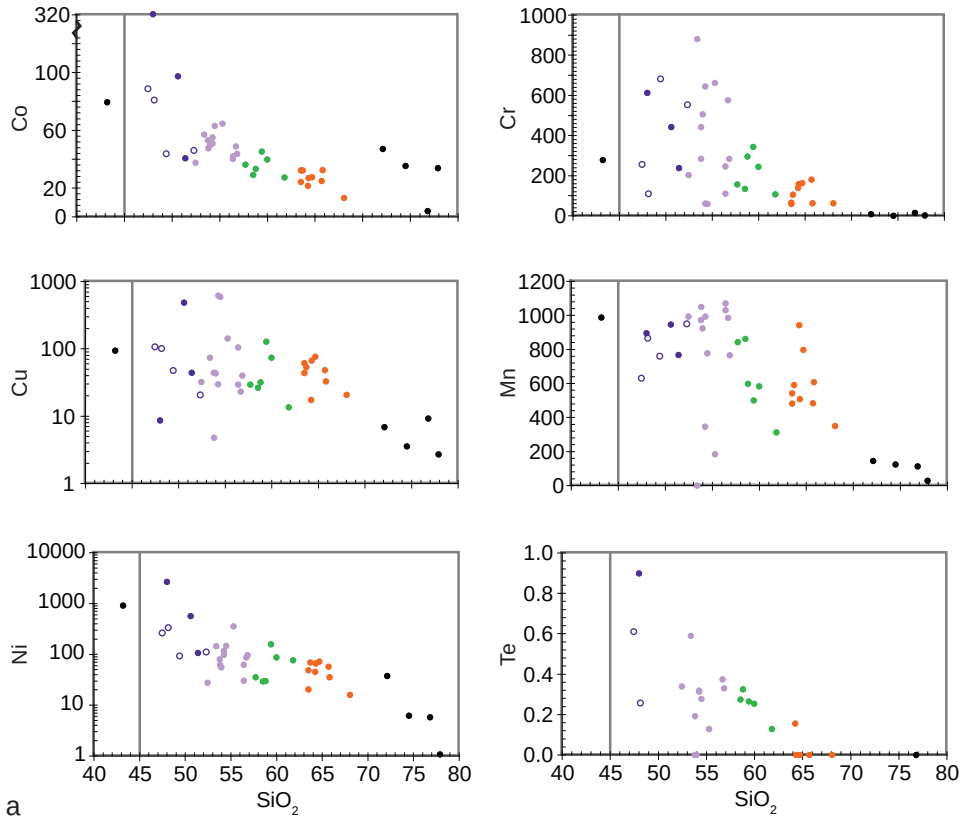

Figure 3.5 (above and facing page): Harker variation plots of ppm trace metal vs. wt. % SiO_2. Troctolite gabbro to left of vertical grey line through 45% SiO_2. Linear trends indicate mixing. Two distinct slope profiles are apparent: (a) negative with increased abundance in mafic types and reduced abundance in felsic types; and (b) positive with decreased abundance in mafic types and increased abundance in felsic types. The elevated abundances of Co, Cr, Cu, Mn, Ni, and Te (part a) in mafic rocks indicate a mantle source for these metals, whereas the elevated abundances of Ba, Ga, Hf, Nb, Pb, Rb, Sn, Sr, Ta, Tl, and Zn (part b) in felsic rocks indicate a crust source for these metals.

Diorites (57–63 wt% SiO_2) are intermediate between the non-troctolite gabbros and the tonalites in terms of major element, trace element, and REE chemistry. Diorite REE profiles (Fig. 3.3d) follow the gabbroic trends, with enriched sloping LREE and, importantly, flat HREE trends. However normalised values are above the gabbro values (Fig. 3.3b). Trace element Harker variation plots (Fig. 3.5) show that the diorites lie on broadly linear trends between mafic and felsic endmembers, indicating a possible bimodal mixing signature with non-troctolite gabbros as the mafic endmember and tonalites as the felsic endmember.

Relative to felsic rocks, mafic rocks are enriched in Co, Cr, Cu, Fe, Mn, Ni, and Te and depleted in Ba, Ga, Hf, Nb, Pb, Rb, Sn, Sr, Ta, Tl, and Zn (Fig. 3.5). Although these are common features of fractional crystallisation trends, if mixing is the dominant process operating in the OGC, these observations may have significant implications for the source of metals in magmatic ore deposits.

Chalcophile elements including PGE

Chalcophile and platinum group element abundances are indicators of sulfide segregation (e.g. Keays and Lightfoot, 2007). In this study, all samples from which sulfides have been removed are depleted in Cu and Ni relative to CI chondrite. Depletions range from 10^{-1} to

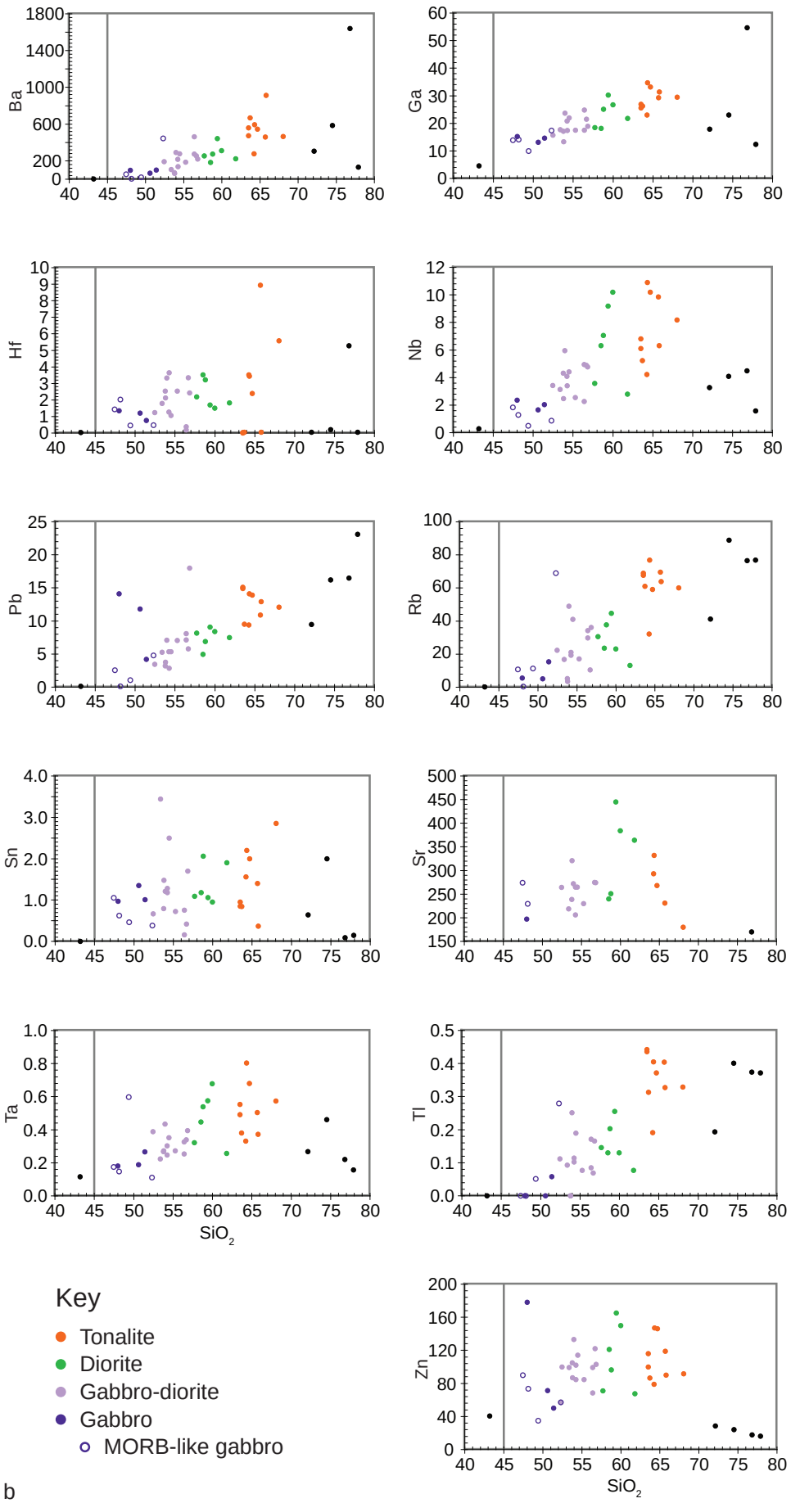
Ba
Ga
Hf
Nb
Pb
Rb
Sn
Sr
Ta
Tl
Zn
SiO2
SiO2
Key
Tonalite
Diorite
Gabbro-diorite
Gabbro
MORB-like gabbro

b

10^{-4} in Ni and 1 to 10^{-2} in Cu relative to CI chondrite (Fig. 3.3). Some of the variability may result from a 'nugget' effect where some blocks milled for analysis contained sulfides, but others did not. Alternatively, if the variability in Cu and Ni content is real, it may reflect disequilibrium partitioning into the sulfides.

Appendix B gives PGE abundances and Table 3.1 shows Pd/Ir ratios of several representative rock types from the OGC suite. Figure 3.6 shows mantle normalised (Barnes et al., 1987) PGE spider plots. Sulfide separates, which were extracted from massive sulfide samples in the OGC, are enriched in all PGE except Pt; gabbros, diorites, and tonalites are depleted in all PGE. The variable depletion relative to mantle (Barnes et al., 1987) in the S- and non-S-bearing gabbros is likely due to a nugget effect in the analysed sample powder. However, it is clear that all the gabbros are depleted in PGE relative to the sulfide separates. An in-depth discussion of PGE enrichment, depletion, and sequestration is beyond the scope of this chapter, but the use of a small selection of ratios highlights some significant trends pertinent to the aims of this chapter.

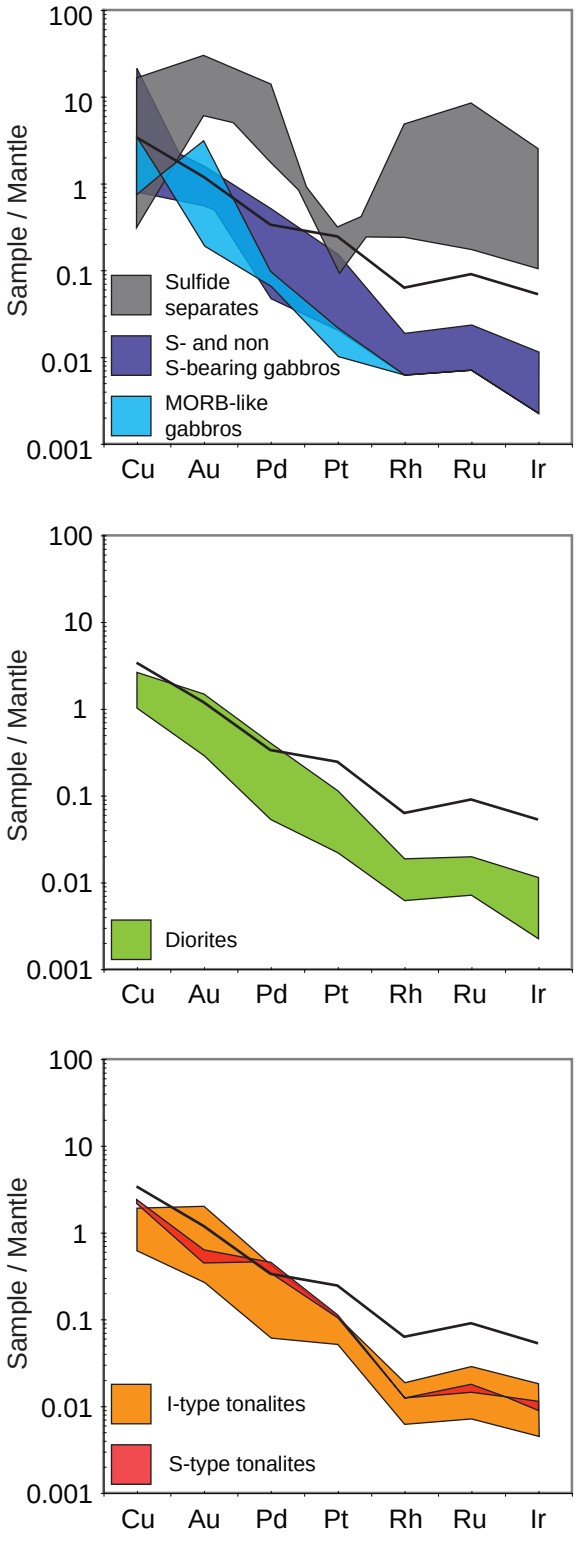

Figure 3.6: Mantle normalised (Barnes et al. 1987) PGE spider diagrams of the range of samples taken in the OGC. Note PGE depletion in all rocks relative to sulfide separates. Dark line on each plot is troctolite-olivine gabbro trace for reference.

The Pd/Ir ratio is thought to be a key discriminant between hydrothermal and magmatic sulfides, a result of the relative fluid immobility of Ir with respect to Pd in hydrothermal fluids (Keays et al., 1982). In the sample set from the OGC, the average Pd/Ir ratio of sulfide separates and sulfide-bearing gabbros is 22.7. This value is consistent with those measured in magmatic sulfides from primitive magmas; hydrothermally mediated ore deposits have Pd/Ir one or more orders of magnitude greater than this (Pd/Ir $\geq$ 100 - see Keays and Davison, 1976; Keays et al., 1982). There is no significant difference between

the range of values for sulfide-separates and those from whole-rock sulfide-bearing gabbro analyses (Table 3.1).

TABLE 3.1
Pd/Ir ratios

Sample		Pd/Ir
HID12c		50.50
KR005	ss	23.11
KR011		45.20
KR017		24.00
KR023		43.00
KR025.2		23.50
KR026		35.67
KR030A		6.35
KR031		13.50
KR044.1	ss	13.49
KR044.2	ss	1.57
KR044.3	ss	38.71
KR045.1		23.00
KR045.2		38.50
KR047		35.40
KR049		29.00
KR071		40.20
KR092.2		21.00

"ss" indicates sulfide separate.

Plots of Cu against Pd are used as an indicator of sulfur saturation. $D_{Pd}^{sul\text{-}sil}$ (~35000) is two orders of magnitude greater than $D_{Cu}^{sul\text{-}sil}$ (~700). Therefore, during sulfide saturation and exsolution, the silicate liquid becomes more depleted in Pd relative to Cu. It follows that Cu-Pd ratios can be used to distinguish systems that have experienced sulfide saturation and segregation from those that have not (Keays and Lightfoot, 2007). Even with very limited sulfide melt generation and segregation, the difference in partition coefficients will cause Pd to be strongly depleted relative to Cu. Figure 3.7 shows that all the analysed samples from the OGC suite, independent of rock type, are either very near to the sulfur saturation line or fully within the sulfur saturated field. This means that these magmas have all undergone sulfide saturation and segregation; those points further from the saturation line have also undergone more extensive fractionation. However, given the possible range in D values, the data points near to the saturation line may not have undergone either segregation or saturation.

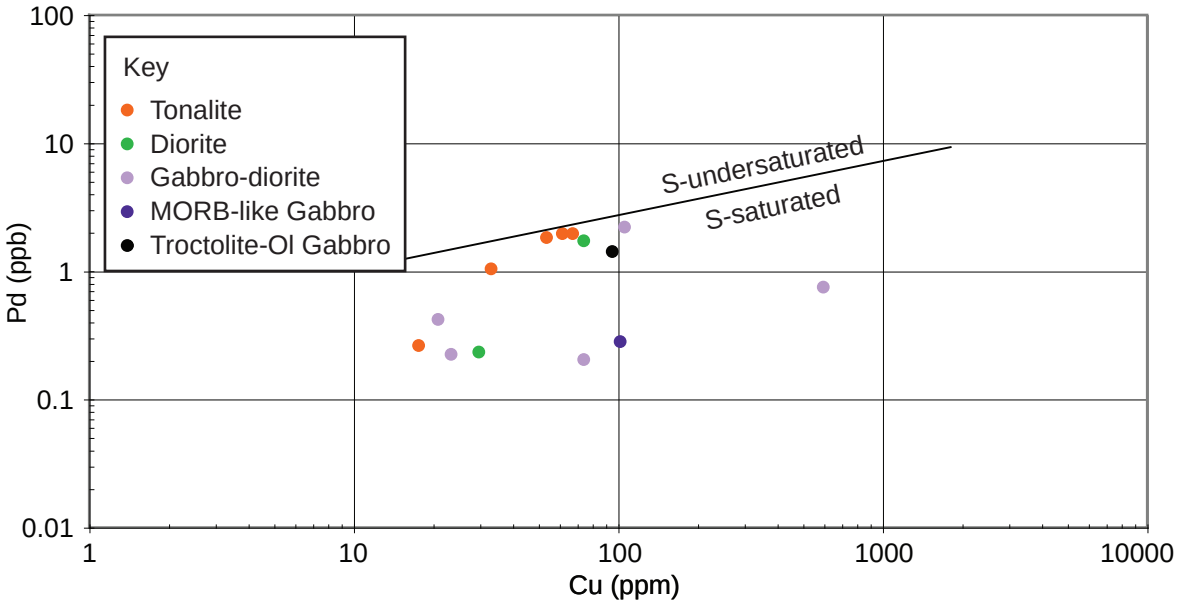

Figure 3.7: Pd (ppb) vs Cu (ppm) plot of whole rock samples. Sulfur saturation line inferred from Keays and Lightfoot (2007). MORB-like gabbros in purple; gabbro-diorites, including sulfide-bearing gabbros, in light purple; diorites in green; and tonalites in orange. Note that all samples from OGC plot in the S-saturated field and many are near the saturation line.

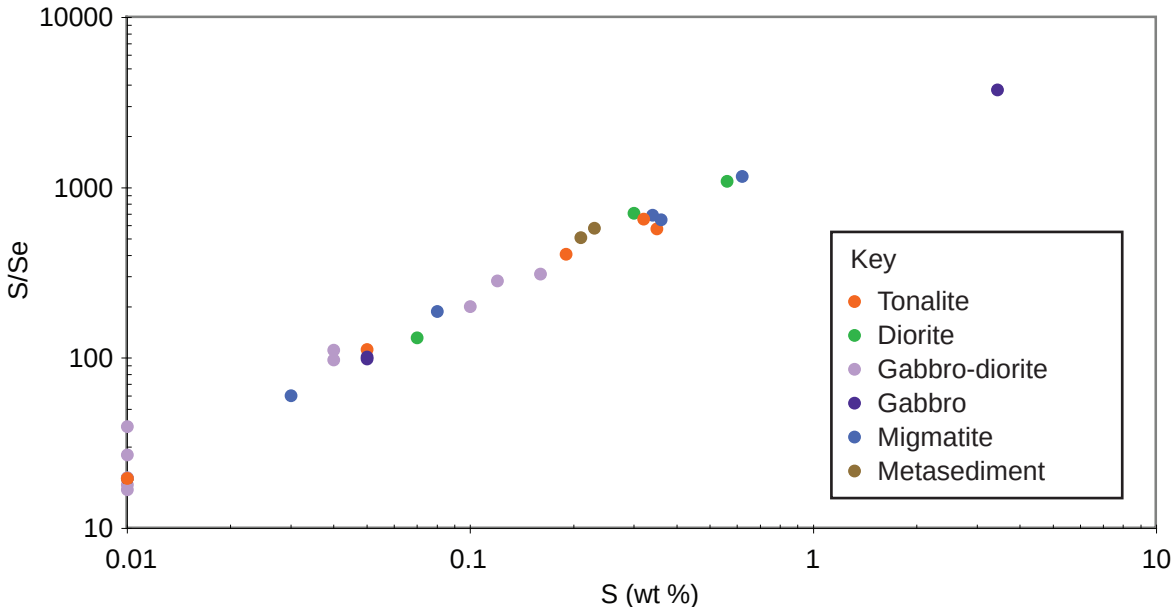

Figure 3.8: S/Se vs S plot. The exceptional linearity of this trend may indicate mixing. Metasediments in this sample set are of the Nakanogawa Group.

S/Se ratios

Sulfur/selenium ratios are used to discriminate between crustal and mantle sourced sulfur in magmatic ore deposits. In this element pair, S is considerably more mobile. Se is a compatible element and is left behind when melts are extracted from the mantle, such that S/Se ratios of typical mantle-derived magmas range up to 3500 (Hattori et al., 2002). Addition of mobile sulfur from crustal sources raises the S/Se ratio such that magmatic sulfide deposits with a significant crustal signature can have values on the order of 10^6 (Reid Keays, pers comm). S/Se values in this study, including tonalites, range from 17 to 3927 with an average of 410 (Fig. 3.8 and Table 3.2), all within the accepted range of mantle values. Two analyses of Nakanogawa Group metasediments have S/Se of 577 and 508, which is in the middle of the S/Se spread of the samples (Fig. 3.8). Since tonalites are crustally-derived melts, their curiously low S/Se values imply that significant Se is present in the tonalite source region. If the tonalites are partial melts of Nakanogawa Group sediments, peridotite detritus present in the sediments (Nanayama et al., 1993) would impart mantle-like geochemistry, such as high Se, in the resulting melts.

An intriguing relationship between S/Se ratio and S content is present in Fig. 3.8. There is a very tight positive linear mixing relationship of S/Se with increasing S content. The reasons for this relationship are unclear; however, the linearity of this trend is highly suggestive of mixing given that the migmatite and metasediment samples also plot on this trend. Fractional crystallisation processes are unlikely to exert such control on the behaviour of Se in relation to S and there are no compositional trends in S/Se ratios, which would be expected if S/Se were affected by fractional crystallisation. Therefore, these data cannot discriminate whether crust-derived sulfur has been added via assimilation of the metasediments because they have the same S/Se signature as the magmas.

Nd isotopes

Figure 3.9 shows εNd_i vs. 1/Nd for a subset of samples between the endmember MORB-like gabbros and S- and I-type tonalites, with sulfide-bearing gabbros plotting between the mafic and felsic endmembers. The positive εNd_i mantle signature of the MORB-like gabbros (+10 – +12) contrasts with the near-zero crustal signature of the tonalites, with I-types approximately 2.5 epsilon units above the S-types (Fig. 3.9). The sulfide-bearing gabbros have intermediate values, with the most sulfide-rich occurrences closer to the mantle values. The data points in Fig. 3.9 appear to form an isochron, but this is an illusory relationship caused by mixing between the endmembers. The Sm/Nd isotopic system is resistant to weathering and alteration due to the elevated electronegativities of REEs (Faure and Mensing, 2005). The stronger ionic bonds formed by these elements reduce the ability of post-crystallisation geochemical processes to alter the initial Sm/Nd ratio, providing a robust tool to describe or check for magma mixing relationships independent of non-magmatic processes. The maximum age of the magmatism in the southern Hidaka is ~51 ma (Owada et al., 1997). In this relatively short period, the range in Nd isotope values found within the suite could not have internally evolved and therefore must represent a mixing relationship.

TABLE 3.2
S/Se Ratios

Sample	S/Se
OS1	649.82
KR002	39.53
KR008	29.94
KR018	27.03
KR019	111.42
KR020	508.47
KR021	577.89
KR024	407.73
KR025.1	311.89
KR027.1	283.69
KR028	18.02
KR031	19.65
KR035.2	187.79
KR036	60.24
KR037.1	1206.23
KR037.2	112.36
KR043.1	19.65
KR044.1	3926.94
KR045.1	97.56
KR045.2	200.80
KR046.1	19.88
KR047	707.55
KR049	99.00
KR050	689.66
KR057.2	22.62
KR060.2	1131.31
KR061	101.63
KR062	131.58
KR071	654.40
KR091.2	21.46
KR092.2	16.89
KR097	574.71

The mixing hyperbola is plotted on Fig. 3.9 as a straight line due to the 1/Nd value for the x-axis. Each hash represents 10% mixing between endmembers using the lever rule. The choice of the MORB-like gabbro and tonalite as the endmembers is subjective. In this system, the choice of endmembers is based on two factors: (1) the widest possible εNd_i margin between the most felsic and the most mafic composition and (2) the coalescence into a linear array of the intermediate εNd_i values between the endmembers. Under these assumptions, the sulfide-rich gabbros occur at mixing percentages between ~20% and 57%.

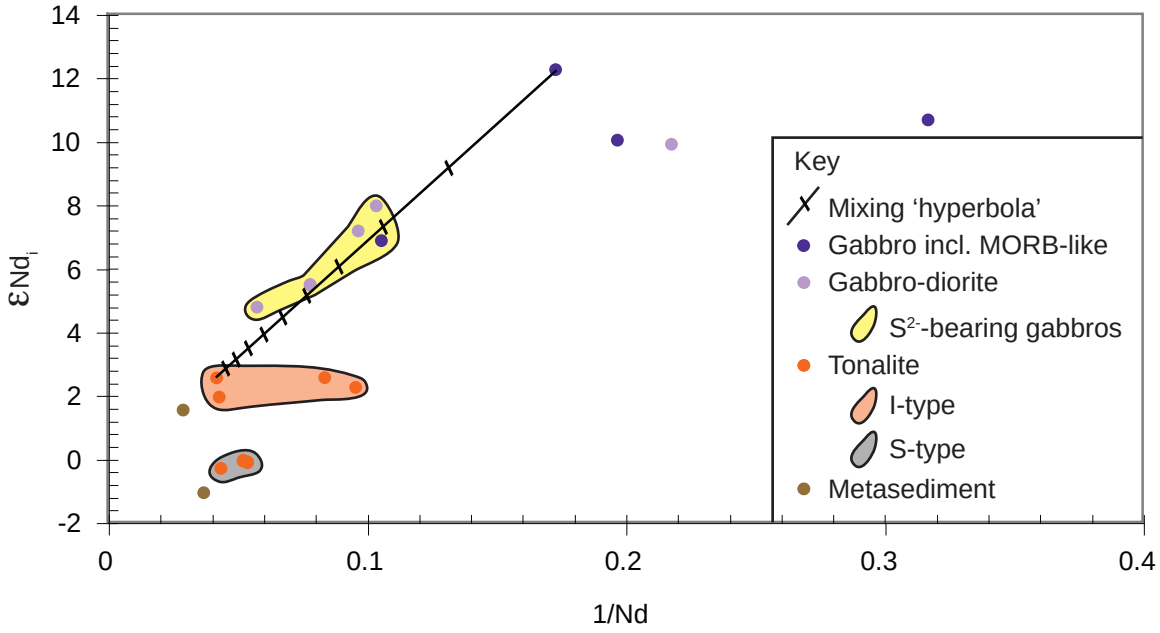

Figure 3.9: εNd_i vs. 1/Nd (ppm) showing a hyperbolic mixing relationship, which is made linear by using 1/Nd for the x-axis. Each hash represents 10% mixing, based on the lever rule, of tonalite into MORB-type gabbro with gabbros on the upper right and tonalites on the lower left. Sulphide-bearing gabbros occur between ~20% and 67% tonalite. vs. 1/Nd (ppm) showing a hyperbolic mixing relationship, which is made linear by using 1/Nd for the x-axis.

Sulfur isotopes

The constant flow elemental analyser method of performing sulfur isotope analyses produces erratic results due to matrix effects where pyroxene, amphibole, and biotite are present in the whole rock matrix (Studley et al., 2002). A few silicate samples did show erratic results, but the sulfide separates produced reasonably consistent values (Fig. 3.10). Sulfur isotopes of sulfide separates from non-troctolite gabbros (SiO_2 > 45%, see Figs. 3.2 and 3.5), relative to Vienna Cañon Diablo Troilite (VCDT), cluster at $\delta^{34}S_{VCDT}$ = -5.46 ± 1.16(1σ)‰ (n = 20, error reported as ± 1 standard deviation). Mantle sulfur is characterised by $\delta^{34}S_{VCDT}$ values of 0 ± 2‰, implying that much of the sulfur in the sulfides is not mantle derived. Takahashi and Sasaki (1983) reported similar sulfur isotope data for sulfides in the nearby Oshirabetsu Gabbroic Complex ($\delta^{34}S_{VCDT}$ = -5.91 ± 0.92‰; see Fig. 1.2b for location relative to OGC), positing that their data reflect magmatic assimilation of country rock sedimentary sulfur ranging in $\delta^{34}S_{VCDT}$ between -12.3‰ and -5.3‰. Therefore, mixing/assimilation of crustal melts, containing a component of crustal sulfur, is likely to have occurred in both instances.

Results II: Modelling Magma Mixing

Two methods were used to characterise the mixing of tonalites and MORB-like gabbros. The first method accounts for assimilation/mixing and fractional crystallisation processes. The second method attempts to independently produce the same geochemical signatures using mixing alone.

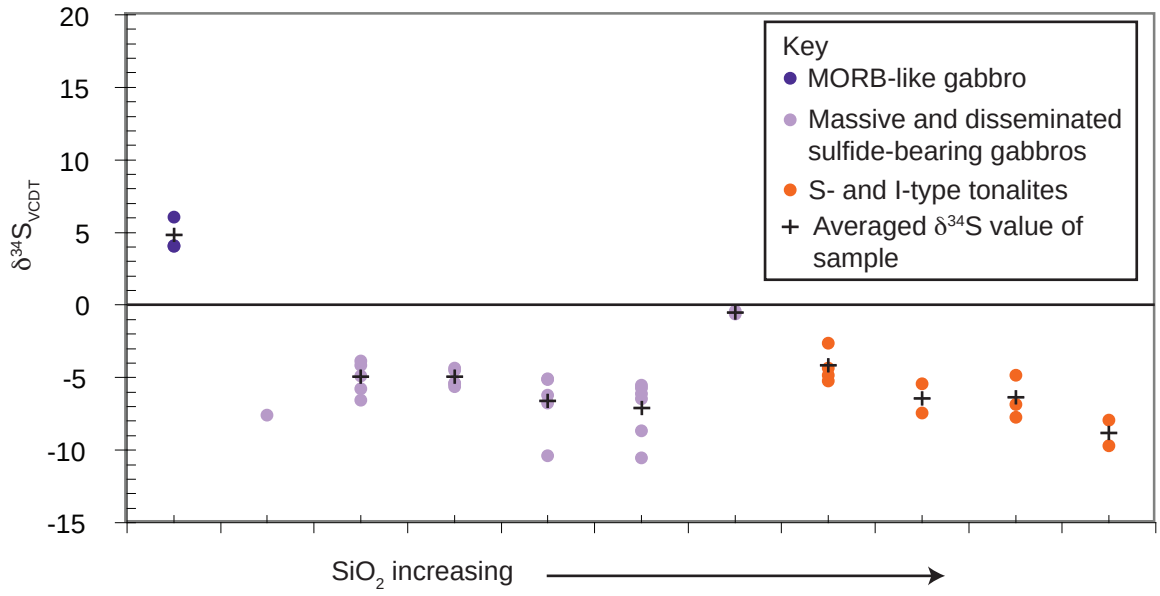

Figure 3.10: $\delta^{34}S_{VCDT}$ of sulfide separates vs. increasing SiO_2 of silicate host rock. SiO_2 content increases to the right from MORB-like gabbros in purple on the left, sulfide-bearing gabbros in the middle in light purple, and tonalites in orange on the right. Vertical trends are repeat analyses of the same sample. Averages of the plotted data for each sample line are shown as black crosses. Analyses where significant interference from silicate phases interfered with isotope determinations are not included on the plot. Isotope values for the sulfide-bearing samples were determined on purified sulfide separates. Samples that contained a significant volume of sulfide minerals plot with light average values around -5‰ implying some, but limited, crustal input of sulfur. One sample where sulfide only occurred as isolated globules within the silicate matrix plots very near 0‰, implying mantle sulfur only.

AFC modelling

The Nd and sulfur isotope values and REE patterns presented here contradict the existing hypothesis for closely related, nearby gabbroic complexes that the mafic to intermediate suite results from differentiation of a calc-alkaline magma (Takahashi, 1983). The calc-alkaline differentiation affinities are apparent in the major element Harker variation plots (Fig. 3.2), but the sloping LREE-enriched, flat HREE signature of the sulfide-bearing gabbros and diorites (Fig. 3.3) cannot be produced through simple fractional crystallisation of any of the gabbros because these elements do not fractionate in this way. Nd and sulfur isotope plots are also incompatible with a differentiation origin for the OGC igneous suite, again because crystallisation does not fractionate isotopes of Nd or S. To constrain the magmatic processes operating in the OGC, an assimilation-fractional crystallisation (AFC) model (after DePaolo, 1981) was constructed to model assimilation (mixing) and fractional crystallisation effects within the Hidaka suite.

AFC modelling provides the means to quantify the combined effects of assimilation, here synonymous with mixing, and fractional crystallisation on REE distribution in silicate magmas. Assembling an array of partition coefficients (D) for common silicate minerals crystallising from an assumed mafic parent magma, chondrite-normalised REE profiles resulting from differing relative proportions of mixing and fractionation allow the chemical effects of these magmatic processes to be quantified. A mixing proportion term, r, refers to a

ratio of rate of assimilation ($\dot{M}_a$) over rate of crystallisation ($\dot{M}_c$), both in units of mass per unit time, such that:

$$r = \frac{\dot{M}_a}{\dot{M}_c} \qquad (1).$$

A second quantity, F, refers to the mass of magma remaining after mixing and fractionation as a fraction of the original mass of magma. It can be taken as a crystallisation index with large values at large melt fractions and small values at small melt fractions as the melt nears complete freezing. To calculate the concentrations of REEs at each model r and F state, C_m/C_m^0 is calculated thus:

$$\frac{C_m}{C_m^0} = F^{-z} + \left(\frac{r}{r-1}\right)\frac{C_a}{zC_m^0}\left(1 - F^{-z}\right) \qquad (2),$$

where for each element, C_m is the concentration in the evolving magma, C_m^0 is the concentration in the original magma, C_a is the concentration in the assimilant, *F* is the ratio of evolved magma mass to initial magma mass (or amount of melt remaining), *z* is an equation relating r to the element bulk partition coefficient in all crystallising phases.

In this model, REE concentrations in ppm were modelled at each F value inclusively between 0.05 to 1.0 in steps of 0.05 and for r values of 0 to 0.9 in steps of 0.1 (the term "r-value" used here should not be confused with "r-factor", which describes the relative volume of silicate magma "seen" by sulfide droplets in ore deposit studies). The case of pure fractional crystallisation is where r = 0; r = 1 is not calculable (see equation 2 and DePaolo, 1981). It was decided to restrict *r* to values less than one (i.e. where the rate of crystallisation exceeds the rate of assimilation) because inflections in major element Harker variation plots clearly show that fractional crystallisation is a dominant process; enrichment in highly incompatible trace elements also suggests that the total system mass decreases during magma evolution (Figs. 3.2 and 3.5). Indeed, if the model is applied using $r > 1$, observed trends cannot be replicated.

AFC model results

A MORB-like gabbro was assumed to be the parental mafic magma. S- and I-type tonalites were then mixed with the mafic parent to produce REE profiles at different proportions and degrees of mixing and fractionation. The goal of the model was to produce a REE profile of a mixed gabbro and tonalite composition that matched the REE profile of the S-bearing gabbros. The negatively sloping, enriched LREE, flat HREE of the sulfide-bearing gabbros (Fig. 3.3) is a key feature that cannot be brought about by fractionation alone. Based on D values, none of the major silicate minerals crystallising from typical gabbroic intrusions fractionate the REEs in such a way.

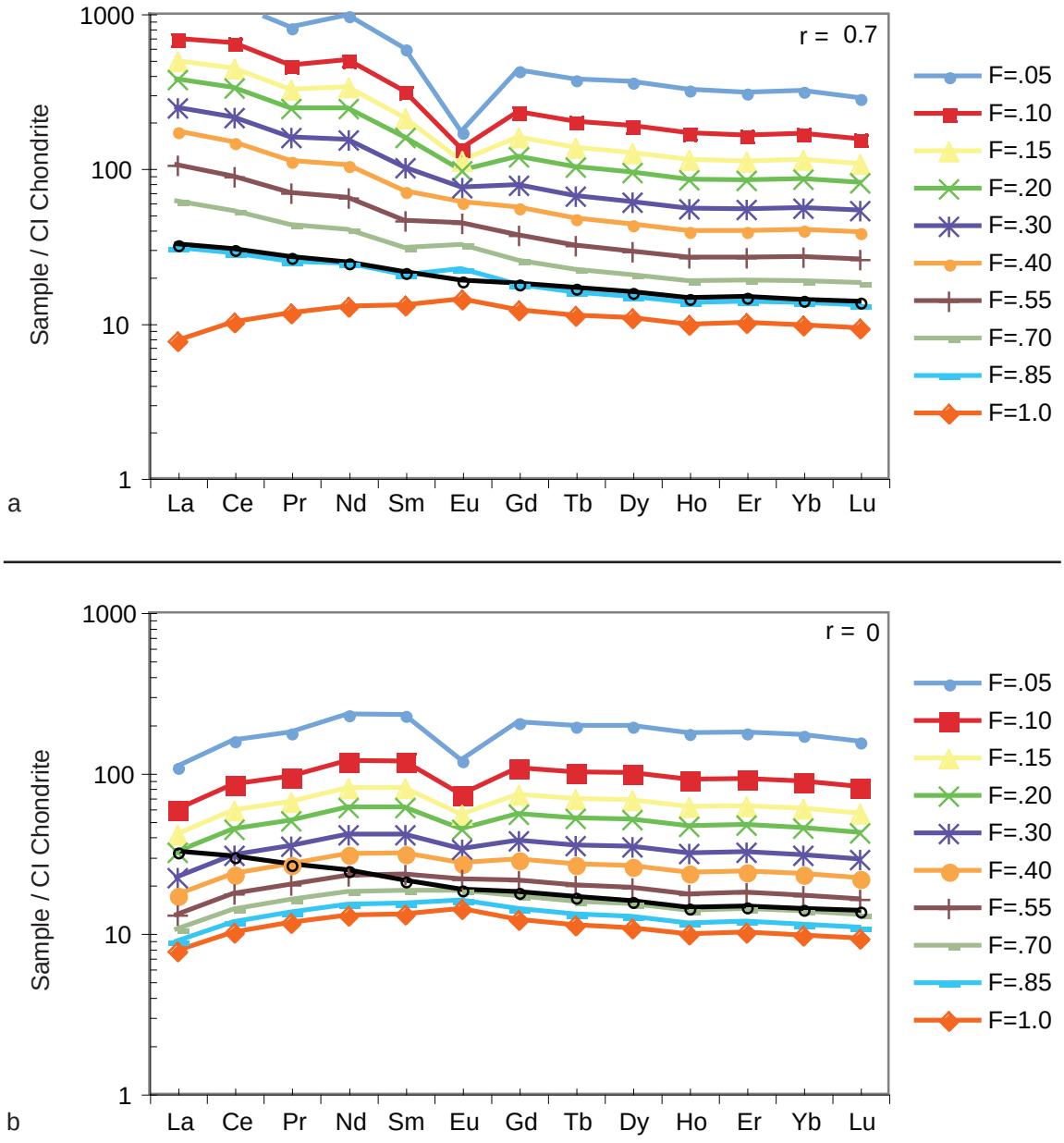

Figure 3.11: (a) AFC model output at r = 0.7. The black curve is the averaged sulphide-bearing gabbro trace; coloured curves represent the REE chemistry of the system at varying F values. Linear-regressed best-fit is at F=0.85. Only selected REE model curves are shown to reduce clutter. (b) AFC model output at r = 0 or the case of differentiation only. CI Chondrite normalisation values are taken from McDonough and Sun (1995).

The best fit between the averaged chondrite-normalised sulfide-bearing gabbro REE profile and the modelled REE profiles (Fig. 3.11a) occurs at an r-value of 0.7 and F = 0.85. The best fit was determined by least-squares linear regression. The modelled REE profiles at r = 0 (Fig. 3.11b) show the fractionation-only condition, showing only upward translation of the REE profile rather than a change in profile shape to the negatively sloping, enriched LREE profile. Addition of melt containing LREE to the gabbroic mass is one possible mechanism in the OGC through which this enrichment can occur.

An r value of 0.7 at F = 0.85 implies that the original magma underwent a comparable amount of assimilation relative to fractionation. A combination of approximately 10.5 wt% mixing and 15 wt% fractional crystallisation result in the REE abundances of the average chondrite-normalised sulfide-bearing gabbro shown in Fig. 3.11. This estimate is based on an assumed

constant crystallising phase assemblage of plagioclase + olivine + clinopyroxene ± ilmenite. An iterative model accounting for changes in phase stability with progressing crystallisation would refine this estimate; however, at such small mixing and fractionation proportions, the bulk chemistry of the evolving magma changes little and therefore the stable crystallising assemblage would not change significantly.

A sensitivity analysis on the D values of the REE in each crystallising phase showed that increases and decreases by one order of magnitude have little effect on the relative proportions of mixing and fractionation estimated by the model. In the 'plagioclase Ds x 10' case, excepting Eu, the REE profile of best fit became r = 0.7, F = 0.75, which increased the mixing and fractionation estimates to 17.5 wt% and 25 wt%, respectively. However, based on linear regression, this best-fit curve departs from the averaged sulfide-gabbro trace with five times the regression error of the original best-fitted profile at r = 0.7, F = 0.85. Based on thin section petrography, MORB-like gabbros are approximately 85% plagioclase, so changes in D value in this mineral would intuitively have a strong effect on the curve shapes. In the 'clinopyroxene Ds x 10' case, the profile of best fit is at r = 0.5, F = 0.7. However, most of the change in REE profile shape is due to wholesale compatibility changes in HREE D values. Nominally, these values are all incompatible, but close enough to 1 (D = 0.32 to 0.63) that a change by an order of magnitude causes them to become compatible. It is unlikely that previous experiments (e.g. Frey, 1969) have incorrectly interpreted compatible REE behaviour as incompatible. Interestingly, however, the proportion of mixing at the associated *r* and *F* values is essentially the same as in the original case: 15 wt% vs. 10.5 wt%, respectively. In the 'olivine Ds x 10' case, there was no change in r or F value for the best fit profile. Reverse cases for plagioclase, clinopyroxene, and olivine Ds divided by 10 showed no change in best fit profile at r = 0.7, F = 0.85. This means that the model is somewhat insensitive to the input parameters and that the output, therefore, is necessarily limited in scope. However, since the mixing estimates produced by the AFC model are used broadly (i.e. the exact abundances of REE in calculated mixtures are not under scrutiny), these estimates are still useful.

Albarède simple ternary mixing based on element ratios

Ratios of trace element concentrations are far more robust indicators of differentiation and mixing processes than concentrations alone. However, ratios do not respond linearly to such processes and therefore must be treated carefully.

Albarède's (1995) equations describe hyperbolic mixing curves between magmas with differing element and isotopic ratios. For example, the La/Yb ratio of a hybrid magma produced through mixing of a MORB-like gabbro and an I-type tonalite endmember each with a different La/Yb ratio is calculated using an equation of the form:

$$\left(\frac{La}{Yb}\right)_{hybrid} = \left(\frac{La}{Yb}\right)_{MORB} \varphi^{Yb}_{MORB} + \left(\frac{La}{Yb}\right)_{I-ton.} \varphi^{Yb}_{I-ton.}$$

where $\varphi^{Yb}_{I-ton.}$ is the mass fraction of Yb contributed by the I-type tonalite endmember to the hybrid magma and φ^{Yb}_{MORB} is similarly so for the MORB-like endmember.

The ratios La/Yb and Dy/Yb show the distinction between LREE and HREE contents of three chosen mixing components in the OGC. MORB-like gabbros have similar La/Yb and Dy/Yb averaging 1.4 and 1.7, respectively. I-type tonalites have La/Yb and Dy/Yb averaging 9.4 and 2.0, respectively. S-type tonalites have La/Yb and Dy/Yb averaging 36.8 and 3.7, respectively (see Table 3.3 for all data). The plot of La/Yb vs. Dy/Yb differentiates the tonalites, sulphide gabbros, and MORB-like gabbros into separate reservoirs (Fig. 3.12a). The range of compositions suggest a three endmember mixing system with the two tonalite types as well as the MORB-like gabbros (Fig. 3.12a). "Pure" I-type tonalites plot along Dy/Yb = 1, "pure" S-types at Dy/Yb ≈ 2.5 and La/Yb ≈ 20 and mixed tonalites in between. MORB-like gabbros plot near La/Yb and Dy/Yb ≈ 1. Sulphide-bearing gabbros plot in a field bounded by pure I-types, pure S-types, and MORB-like gabbros.

The low and high Dy/Yb distinction between the tonalites is also apparent in Harker plots of REE against wt% SiO_2 (Fig. 3.12b) where the S-type tonalites are HREE-depleted relative to the I-types. One I-type tonalite is very like the S-types in terms of HREE abundance (see Fig. 3.12b), but is otherwise I-type in mineralogy. There is no systematic difference between S- and I-types in LREE chemistry. The bimodal relationship on the La vs. SiO_2 plot, with sulfide-bearing gabbros plotting

TABLE 3.3
La/Yb ratios

Sample	La/Yb
HID12a	26.9
HID12c	33.7
OS1	32.7
KR002	2.49
KR006	1.33
KR007	21.9
KR008	1.94
KR011	3.49
KR017	4.8
KR018	4.0
KR019	6.4
KR020	7.8
KR021	40.9
KR023	1.23
KR024	14.0
KR025.1	4.1
KR025.2	14.4
KR026	17.3
KR027.1	3.97
KR027.2	5.90
KR028	2.79
KR030A	1.913
KR031	3.65
KR035.2	8.4
KR036	58.0
KR037.1	25.5
KR037.2	7.0
KR039	2.53
KR043.1	3.31
KR043.2	4.4
KR044.1	2.86
KR044.3	2.5
KR045.1	4.3
KR045.2	3.82
KR046.1	3.58
KR047	7.1
KR049	1.17
KR050	36.8
KR057.2	4.93
KR060.1	13.4
KR060.2	9.8
KR061	1.96
KR062	5.4
KR071	48.3
KR091.2	19.94
KR092.2	3.02
KR097	38.5

Figure 3.12 (facing page): (a) Hyperbolic mixing triangle between three proposed mixing endmembers: an S-type tonalite, an I-type tonalite, and a MORB-like gabbro. Three mixing curves are shown: between MORB and S-type in red, between MORB and I-type in blue, and between S- and I-types in green. Coeval mixing between a felsic endmember of 20% I-type and 80% S-type with MORB-like gabbro is shown in purple. Using log-log plots accentuates the curvature of the mixing hyperbolae. Hash marks indicate 5% mixing such that the sulphide-bearing gabbros occur between 15 and 30% mixing. The gabbro near 50% mixing possibly indicates another generation of sulfides or suggests different endmembers.
(b) REE (ppm) vs. SiO_2 (wt. %) showing tonalite fractionation of HREEs (Dy and Yb) from LREE (La). In LREE content, there is no distinction between the tonalite types with both S- and I-types plotting throughout the range. In HREE content, the tonalite types become distinct, except with one I-type sample, which seems to be more S-type in HREE, but is I-type in mineralogy. S-types are relatively HREE depleted, whereas I-types plot within the broader trend of decreasing abundance with increasing SiO_2. This suggests that the I-types are more dominant in mixing than the S-types; otherwise, the intermediate samples would plot on a line between S-type and MORB-like endmembers, rather than between I-type and MORB-like endmembers, as is evident here.
(c) An alternative explanation for the lack of clear bimodal mixing in the HREE Harker plots is to invoke fractionation of MORB-like gabbros first, which is followed by bimodal mixing of the more evolved magma. AFC calculations state that a small amount of fractionation is required in the model.

between tonalitic and gabbroic endmembers, is lost on the HREE plots of Fig. 3.12b. The sulfide-bearing gabbros do not lie on a simple linear trend between the previously given endmembers, hence the usage of element ratios in this case as a more robust tool to determine mixing. Figure 3.12 clearly shows that despite HREE vs. SiO_2 plots (Fig. 3.12b) not showing a linear mixing relationship, REE ratios (Fig. 3.12a) do. The lack of a linear mixing relationship between MORB-like gabbros and tonalites through the sulfide-bearing compositions could alternatively be explained by fractionation. Since the REE tend to be incompatible (Best, 2003), fractionation would increase REE concentration in the melts. If the MORB-like gabbros were extracted from a garnet-stable source, HREE depletion would result. Later fractionation outside the garnet stable region would increase the residual HREE concentration along the trajectory shown in Fig. 3.12c. Garnet does not strongly partition the LREE, therefore the same depletion signature would not be evident in LREE. An evolved endmember elevated in HREE concentrations would be the result, which would be more compatible with a bimodal mixing line interpretation, as shown in Fig. 3.12c. Since the AFC model does require some fractionation to explain the sulfide-bearing compositions, the REE Harker plots merely reflect this behaviour in elemental abundances.

Based on REEs, two possible mixing scenarios to explain the range in geochemical signatures of the mixed OGC magmas are (i) coeval mixing of two separate tonalite magmas with a MORB-like gabbro – the case of three individual endmembers, which produces a field of possible mixtures bounded by the mixing hyperbola between each endmember – and (ii) a single felsic component, itself a mixture of the S- and I-type tonalites, subsequently mixing with the MORB-like gabbro endmember. An example of a possible mixing scenario of type (i) is presented in Fig. 3.12a, in which specific pure I-type tonalite, pure S-type tonalite, and MORB-like gabbro endmembers were chosen. The field of possible mixtures from this selection of mutually mixing endmembers is bounded by the blue, red, and light green curves in Fig. 3.12a. The sulfide-bearing gabbros, however, plot on a more confined trend, and an example of a mixing scenario of type (ii) is shown as the purple curve in Fig. 3.12a to account for this trend. The purple mixing curve is calculated between a single tonalite endmember of

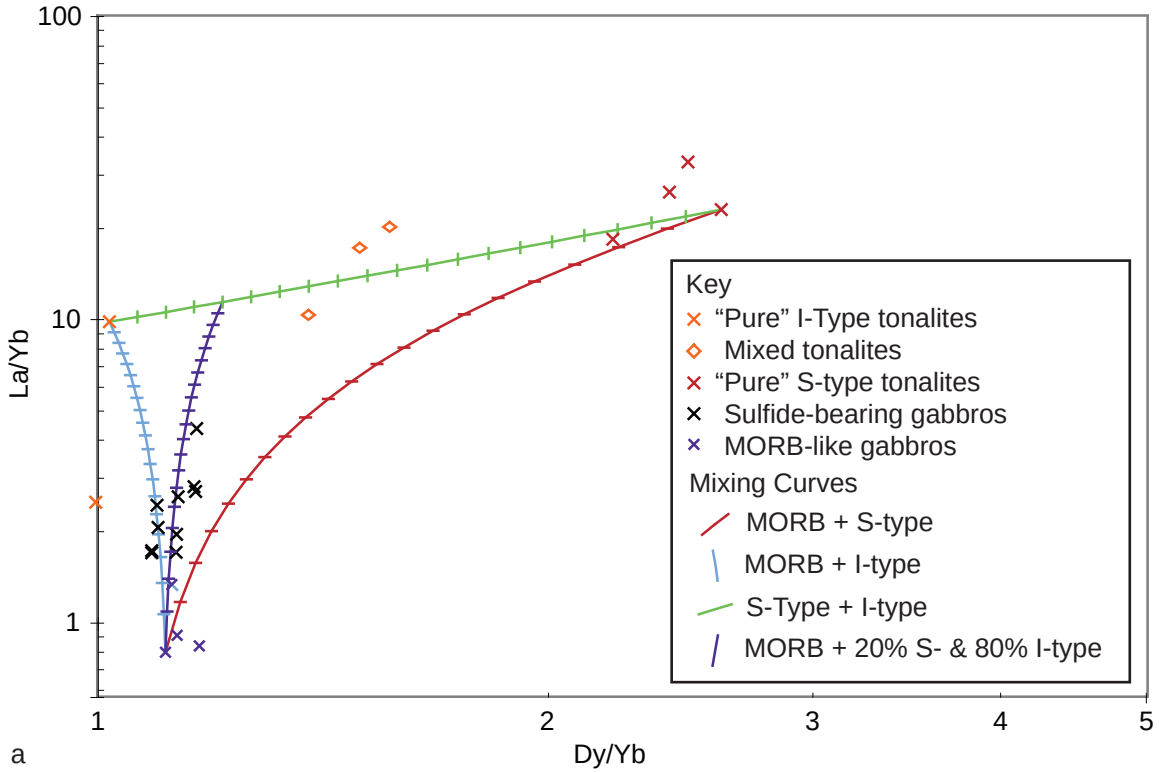
100
10
1
La/Yb
1
2
3
4
5
Dy/Yb
Key
"Pure" I-Type tonalites
Mixed tonalites
"Pure" S-type tonalites
Sulfide-bearing gabbros
MORB-like gabbros
Mixing Curves
MORB + S-type
MORB + I-type
S-Type + I-type
MORB + 20% S- & 80% I-type

a

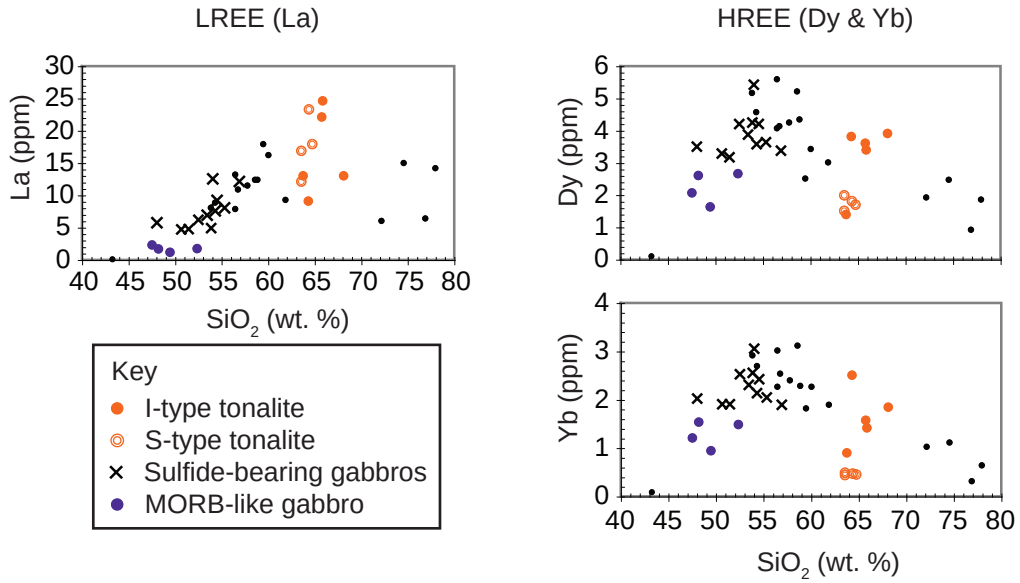
LREE (La)
HREE (Dy & Yb)
La (ppm)
Dy (ppm)
Yb (ppm)
SiO2 (wt. %)
Key
I-type tonalite
S-type tonalite
Sulfide-bearing gabbros
MORB-like gabbro

b

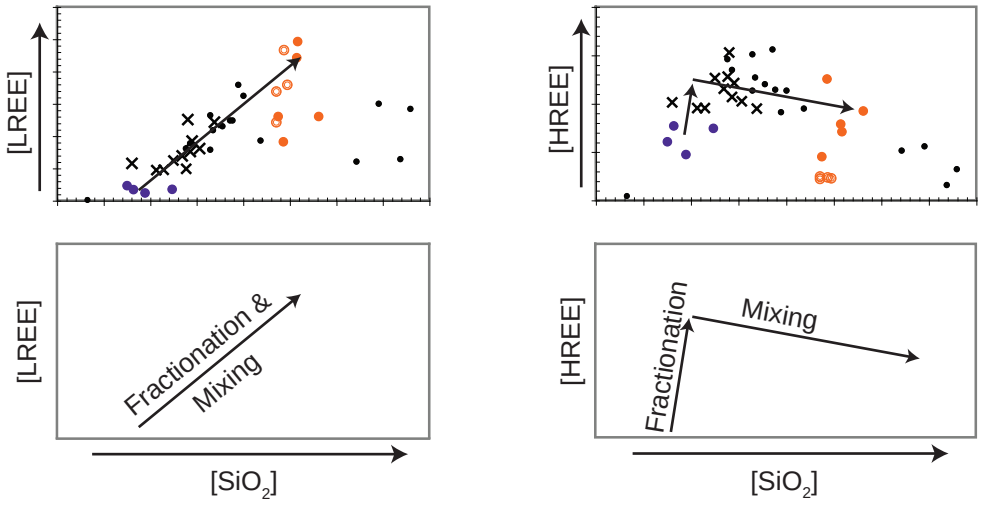
[LREE]
[HREE]
Fractionation &
Mixing
Mixing
Fractionation
[SiO2]

c

20% pure S-type and 80% pure I-type tonalite mixing with a MORB-like gabbro. In either case, the net geochemical result is the same with sulfide-rich compositions occurring at mixing fractions of 15 to 30% with a maximum value of 50% mixing between MORB-like gabbros and tonalite (hash marks, Fig. 3.12a). The maximum value likely reflects either a second generation of sulfides unrelated to the magmatic sulfides or an improper choice of endmember. A different endmember, either a felsic one with higher La/Yb or a mafic one with higher La/Yb would reduce the overall mixing estimates, shifting them towards those predicted by the AFC models. A felsic endmember with lower La/Yb or a mafic endmember with lower La/Yb would increase the mixing estimates further away from the AFC values. The spread of values between the MORB-like gabbros suggests that a mafic endmember with higher La/Yb than the selected one is more likely than one with lower La/Yb.

Discussion

Origin of mafic-intermediate magmas in the OGC

The lower range of the values estimated by the Albarède equations agree with the AFC values: 15% mixing compared to 10.5% mixing, respectively. AFC modelling accounts for differentiation, which is the key difference between the AFC model and the models strictly using hyperbolic mixing curves. The AFC values show that fractional crystallisation is needed to account for the geochemical signatures of the sulfide-rich compositions of the OGC, but that mixing is also an important process operating in the OGC.

The most compelling geochemical evidence for mixing is the array of εNd_i values (Fig. 3.9). Mixing relationships in εNd_i versus 1/Nd space plot as straight lines and therefore one is forced to choose distinct endmembers, and not coevally mixing endmembers as discussed above. Variations in mixing estimates notwithstanding, the conclusion supported by all the foregoing geochemical and mathematical methods is that mixing is an important process controlling the sulfide-bearing, mafic-intermediate rock types in the OGC.

Role of magma mixing in sulfide generation

The chalcophile elements Ni, Cu, and Au have $D^{sul}_{sil} \approx 5.0–9.0 \times 10^2$, 1.3×10^3, and $1.5–1.9 \times 10^4$, respectively, for coexisting sulfide and mafic silicate melts (Peach et al., 1990). Similarly, the platinum group elements Pd, Ir, and Pt have sulfide/mafic silicate $D \approx 3.5 \times 10^4$, $1.2–1.6 \times 10^4$, and 2.4×10^3, respectively (Peach et al., 1990). Although Ds have not been measured for coexisting sulfide and felsic silicate melts, they are expected to be similar to those for mafic melts. Magmatic sulfides formed in the lower crust therefore are able to sequester these ore-forming metals from silicate magmas. Gravitational segregation of these sulfides is then capable of forming metal-depleted and metal-enriched batches of silicate magma. Therefore, whether magmas exsolve and subsequently retain or lose metal-rich sulfide melts

may be a critical factor controlling the ore-forming potential of magmas that escape to the upper crust.

The OGC, having formed at ~23 km depth, is a lower- to mid-crustal magma chamber and the presence of massive Ni-Cu-bearing sulfides implies that sulfide saturation was reached at depth. There are a number of ways in which sulfide saturation may be reached during magma evolution. Decreasing temperature, increasing pressure, decreasing Fe^{2+} content, and increasing Si content (O'Neill and Mavrogenes, 2002), all reduce the sulfur content needed to cause sulfide saturation. Each of these mechanisms can individually induce sulfide exsolution. In contrast to changing the amount of sulfur needed to cause sulfide saturation, simply adding externally sourced sulfur to the magma is commonly implicated in the formation of magmatic nickel sulfide deposits (Naldrett, 2004). Indeed, coupling these mechanisms is a more effective way of inducing sulfide melt exsolution. In the middle crust, assuming isobaric conditions, limited conductive heat losses to country rock and enthalpic losses to crystallising phases, changes in Fe^{2+} and Si content and addition of external sulfur are likely to be the dominating chemical controls on sulfur saturation. Magma mixing and assimilation are ideal processes to mediate changes in Fe, Si, and S content.

In the southern Hidaka Belt, textural, chemical, isotopic, and model arguments support mixing of mantle-derived OGC gabbros and crust-derived tonalites. Major element data indicate that mixing between these gabbros and tonalites would cause a net reduction in Fe content due to the lower Fe content in the tonalites relative to the gabbros (Appendix B). Optical and electron microscopy indicate that most sulfur is present as pyrrhotite with minor chalcopyrite and pentlandite, and sulfur isotope data, discussed further below, suggests that a uniform mantle-dominated sulfur reservoir was the major contributor to the massive and disseminated sulfide mineralisation. The change in bulk Si content brought about through the mixing, as presented in models above, is small. Using the AFC mixing and fractionation estimates, a complete mixture of 10.5 wt% tonalite with a parent MORB-like gabbro increases the Si content of the resulting hybrid melt from 48 wt% SiO_2 to only 50 wt%.

Particularly important in the study of sulfide ore deposits is the source of sulfur in the sulfide minerals. Sulfur isotopes and S/Se ratios provide a means of fingerprinting sulfur involved in lower crustal magma mixing chambers such as the OGC. Mantle sulfur averages $\delta^{34}S_{VCDT}$ = 0‰ with little variability (up to ± 2‰, e.g. Ripley et al., 2002), while crustal sulfur can range from -34‰ to -10‰ in bacterially mediated reservoirs (Johnston et al., 2007) to +10 to +30‰ in evaporites (Faure and Mensing, 2005) with high variability beween different reservoirs. Alirezaei and Cameron (2001) showed that high-grade metamorphism has little effect on the sulfur isotope signatures of metasedimentary and meta-igneous rocks. Melts extracted from the mantle inherit similar isotopic signatures to their source regions, implying that partial melting does not fractionate sulfur isotopes more than 1–2‰ (Faure and Mensing, 2005).

In this study, the average sulfide-mineral separate isotopic value is $\delta^{34}S_{VCDT}$ = -5.47 ± 1.16(1σ)‰. This depleted value implies an isotopically light source of external, crustally-derived S, though with a signal that is still dominated by the mantle. S/Se ratios (presented above) also suggest that the sulfur is mantle-sourced, although the S/Se values are ambiguous. Sulfur addition with the tonalites as they mixed with gabbros of the OGC would have influenced the $\delta^{34}S$ signature. Recent studies (e.g. Liu et al., 2007) confirm that the solubility of sulfur in felsic melts is low compared to that in mafic melts, suggesting that the mixing of even sulfur-rich tonalites with OGC gabbros is an inefficient means of transferring enough sulfur to produce the observed mineralisation. However, many tonalites in the OGC have anomalously high sulfur content, up to 4000 ppm (Appendix B), which suggests a reason for the development of massive sulfides in the OGC. Therefore, observations suggest that tonalites may sometimes harbour surprisingly large amounts of sulfur and that felsic melts may indeed be significant sources of sulfur.

Many OGC tonalites have obviously assimilated migmatites (Fig. 3.13). The migmatites result from metamorphism of the surrounding sediments and if they are sulfur rich, which analyses suggest is the case, they will be a rich source of sulfur to oversaturate a tonalite-gabbro mixture that is already near saturation. Assimilation of the sulfur-rich metasediments themselves, from which some of the tonalites were extracted, is perhaps an efficient means of transferring crustal sulfur. Nakanogawa Group sediments and metasediments from the nearby Oshirabetsu gabbroic complex have a depleted signature encompassing the ore-sulfide values reported above ($\delta^{34}S_{VCDT}$ = -5 to -11‰, see Takahashi, 1983). Mixing of gabbros and tonalites has been observed chemically and texturally, but this does not preclude coincident assimilation of sulfur-rich metasediments ultimately of the same crustal reservoir as the tonalites. However, with both mixing of tonalites and assimilation of sulfur-rich sediments occurring, and with both having the same isotopic signature, the relative influence of each process is difficult to separate. Alternatively, the addition of a ^{34}S-depleted fluid during the mixing process could also result in the observed light $\delta^{34}S$ signature. These possibilities are constrained by the mantle S/Se signature, which implies that the magmas associated with any of these processes would had to have been fairly primitive at the time of mixing.

Sulfur saturation state

The sulfide saturation state of the gabbros is of considerable importance. The low proportion of mixing indicated by the AFC model (~10.5%) and the low SiO_2 content of the sulfide-hosting gabbros imply that, metasediment assimilation and fluid addition aside, little tonalite was added to the mixing system. Given that felsic melts typically contain less than 200 ppm dissolved sulfur (Li and Ripley, 2005), it is likely that the mafic magma was already close to sulfide saturation. Figure 3.7 shows that most of the rocks from the OGC plot in the S-saturated field; however, considering the uncertainty in the sulfide/silicate D values of Pd and Cu, the Pd/Cu ratio criterion of sulfide saturation is ambiguous and must be used with caution.

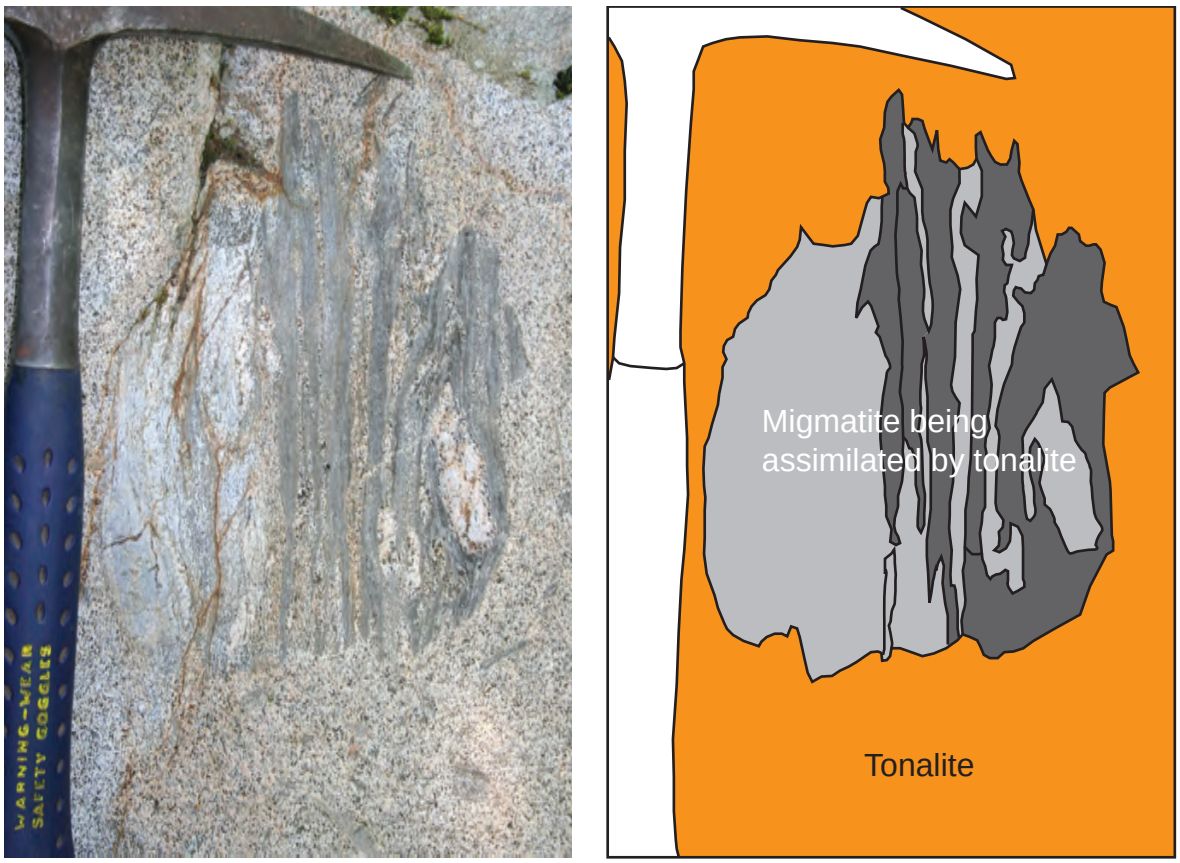

Figure 3.13: Partially assimlated migmatite within OGC tonalite. Close examination reveals that the felsic layers within the migmatite are in continuity with the main body of tonalite. This is evidence for the sediment-serived origin of the tonalites in the OGC. The S-type tonalites tend to be very inclusion-rich with many different xenoliths present.

The addition o f a small amount of sulfur from the tonalites, combined with a net reduction in Fe^{2+} content and a drop in sulfur solubility due to an increase in SiO_2 content, caused the mixed system to surpass the sulfide saturation limit and exsolve a sulfide liquid. The S/Se data does not provide a significant constraint on sulfur source. In light of the fact that the Nakanogawa Group sediments have some geochemically primitive sources (i.e. peridotite, see Chapter 2), the assumption of high S/Se in crustal material is not valid in the HMB and cannot be used to discriminate between crustal and mantle sources. However, Pd/Ir ratios suggest that magmatic sulfur, already present in the gabbros before mixing, retained control on the sulfur budget. Extrinsic forcing not related to significant sulfur addition, but effected by mixing, drove the system to sulfide saturation.

Nd isotopes

The isotopic mixing hyperbola in Fig. 3.9 suggests that mixing between MORB-like gabbro and tonalite endmembers involved 20–57% tonalite. The largest value is highly inconsistent with the estimates through the AFC and binary mixing models, whereas lower values (20–37%) are roughly coincident with the binary mixing estimates.

The Nd isotope signatures of the sulfide-bearing gabbros lie along a mixing line between the MORB-like gabbros and I-type tonalites. This is consistent with the observations from REE chemistry that the sulfide-bearing gabbros resulted from the mixing of MORB and I-type tonalites. Isotopically, the S-type tonalites do not have an influence, as in the hyperbolic mixing estimates, which were based on the elevated HREE content of the sulfide-gabbros relative to the HREE-depleted S-type tonalites and comparatively HREE-enriched I-type tonalites. Isotope ratios are probably the most robust of all methods employed in this study and therefore S-type tonalites are excluded from the mixing events that generated the sulfide-bearing gabbros. I-type tonalites could still inherit the crustal sulfur discussed previously by assimilating migmatites while migrating through the crust.

Metal reservoirs and the significance of MASH zones in arc metallogenesis

Sulfide saturation in a MASH zone at or near the base of the crust would have a controlling influence on the distribution of chalcophile metals in melts extracted from such a reservoir. The exact role of mixing in chalcophile element enrichment is discussed in later chapters. However, it is argued here that magmas in arcs that contain significant porphyry-Cu deposits could have been affected by these processes during incubation in the lower to middle crust. In the OGC, the evidence suggests that mixing caused sulfide saturation. The resulting sulfide magma, on separating from the silicate melt, depleted most of the silicate melt of chalcophile elements (Figs. 3.3 and 3.6), although some phases of silicate magma are demonstrably enriched in disseminated sulfide and therefore have elevated metal content (Fig. 3.6).

The negatively sloping trends of Co, Cr, Cu, Mn, Ni, and Te in Fig. 3.5a show that these metals are more abundant in the troctolite, MORB-like, and sulfide-bearing gabbros (43–55 wt% SiO_2); hence, they are mantle-sourced metals. The positively sloping trends of Ga, Pb, ± Sn, Ta, Tl, and Zn in Fig. 3.5b show that these metals are more abundant in tonalites (up to 68 wt% SiO_2); hence, they are crustally sourced metals. This dichotomy of elemental abundances reflects variations in silicate compatibility with compatible trace metals remaining in the mantle and incompatible trace metals being extracted to the crust during partial melting. Crustal material would therefore be a source of incompatible trace metals and mantle material a source of compatible trace metals in a MASH zone.

Sedimentary rocks, particularly shales, are sources of the low melting-point chalcophile elements (LMCE) As, Bi, and Sb (Turekian and Wedepohl, 1961; Marowsky and Wedepohl, 1971). The LMCE; crustal metals Ga, Pb, Sn, Tl, and Zn; and mantle metals Co, Cr, Cu, Ni, and Te are chalcophile (Goldschmidt, 1937) and so would partition into a sulfide magma. Therefore, since mantle and crustal magmas mix together in MASH zones, the metal budget of magmatic sulfides exsolved in a MASH zone should be a blend of crustal and mantle metals.

The terms "complex" and "simple" are here introduced to describe the relative importance of mixing-induced sulfide saturation in island arcs. Simple island arcs are those without accretionary wedge material in the deep arc, which are thus unlikely to experience a protracted history of mixing between crust- and mantle-derived magmas. An example of a simple island arc is the Tonga-Kermadec arc. Complex arcs have mixing of crustal material with upwelling mantle-sourced magmas, as in the example described here. Another example of a complex arc is Papua New Guinea, which has similarities with continental arcs in terms of the materials available for magma mixing. Complex arcs can have significant intermediate-felsic magma throughput due to the excess heat provided by mantle magmas in a setting with an abundant supply of felsic crust-derived melt. Intermediate–felsic magmas generated in complex island arcs are most likely to contain crust-derived metals, and to experience sulfide saturation through processes described in a new model presented in Chapter 4. It should be noted that within a single arc, there are likely to be areas of "simple" and areas of "complex" behaviour and that it may not be possible to assign a single type to an entire arc.

Conclusions

The development of magmatic sulfides associated with mixing gabbros and tonalites in the OGC is a window on a new line of research into the effects of mixing on the generation of magmatic sulfides in the igneous feeder systems of the lower to middle crust in arc settings. Relatively small amounts of tonalite mixing are required to reach and exceed sulfide saturation in mafic melts under favourable conditions at depth in arcs, particularly where the assimilant adds sulfur.

Estimates by AFC modelling, ternary mixing, and Nd isotope systematics generally offer similar mixing percentages. The ternary mixing and Nd isotope estimates place mixing at 15–30% and 20–37%, respectively. AFC modelling estimates combined mixing and fractional crystallisation at 25%.

The potential of magmatic sulfides to strip or enrich extracted melts in chalcophile metal content may be a controlling factor in the development of significant ore bodies following final emplacement in the upper crust. Many giant world-class porphyry Cu-Au deposits (Alumbrera, Bingham, etc.) are related to continental arcs and contain signatures of crustal contamination of mantle magmas. It is suggested that in some arcs, mixing between mafic and felsic melts in MASH zones plays a key role in influencing the genesis of porphyry-Cu deposits by causing sulfide saturation and the production of sulfide melts at depth. The resulting sequestration of chalcophile metals into these sulfide phases creates both chalcophile-metal depleted silicate domains and metal-enriched domains. Whether magmas escaping from MASH zones can entrain metal-rich sulfide melts may control ore formation in the upper crust. Those able to entrain sulfides carry metals that later contribute to mineralisation, whereas those unable to entrain sulfides will have no mineralisation potential at emplacement. This is considered further in Chapter 5.

Acknowledgements

The author wishes to thank the Bicentennial Gold 88 Endowment for their generous financial support of analyses for PGE content and Nd isotopes.

References

Albarède F. (1995) *Introduction to Geochemical Modeling*. University Press, Cambridge.

Alirezaei S. and Cameron E. M. (2001) Variations of sulfur isotopes in metamorphic rocks from Bamble Sector, southern Norway: a laser probe study. *Chemical Geology* **181**(1-4), 23-45.

Barnes S.-J., Boyd R., Korneliussen A., Nilsson L.-P., Often M., Pedersen R. B. and Robins B. (1987) The use of mantle normalisation and metal ratios in discriminating between the effects of partial melting, crystal fractionation and sulphide segregation on platinum-group elements, gold, nickel, and copper: Examples from Norway. In *Geo-Platinum 87* (eds. H. M. Prichard, P. J. Potts, J. F. W. Bowles and S. J. Cribb), pp. 113-143. Elsevier Science Publishers Ltd. U.K.

Best M. G. (2003) *Igneous and Metamorphic Petrology*. Blackwell Science, Oxford, UK. pp. 552.

Clemens J. D. and Vielzeuf D. (1987) Constraints on melting and magma production in the crust. *Earth and Planetary Science Letters* **86**(2-4), 287-306.

DePaolo D. J. (1981) Trace element and isotopic effects of combined wallrock assimilation and fractional crystallisation. *Earth and Planetary Science Letters* **53**, 189-202.

Faure G. and Mensing T. M. (2005) *Isotopes: Principles and Applications*. John Wiley & Sons, Hoboken, New Jersey. pp. 897.

Frey F. A. (1969) Rare earth abundances in a high-temperature peridotite intrusion. *Geochimica et Cosmochimica Acta* **33**(11), 1429-1447.

Goldschmidt V. M. (1937) The principles of distribution of chemical elements in minerals and rocks. *Journal of the Chemical Society*, 655-673.

Halter W. E., Bain N., Becker K., Heinrich C. A., Landtwing M., VonQuadt A., Clark A. H., Sasso A. M., Bissig T. and Tosdal R. M. (2004a) From andesitic volcanism to the formation of a porphyry Cu-Au mineralizing magma chamber: the Farallon Negro Volcanic Complex, northwestern Argentina. *Journal of Volcanology and Geothermal Research* **136**(1-2), 1-30.

Halter W. E., Heinrich C. A. and Pettke T. (2004b) Laser-ablation ICP-MS analysis of silicate and sulfide melt inclusions in an andesitic complex II: evidence for magma mixing and magma chamber evolution. *Contributions to Mineralogy and Petrology* **147**(4), 397-412.

Halter W. E., Heinrich C. A. and Pettke T. (2005) Magma evolution and the formation of porphyry Cu-Au ore fluids: evidence from silicate and sulfide melt inclusions. *Mineralium Deposita* **39**(8), 845-863.

Halter W. E., Pettke T. and Heinrich C. A. (2002) The Origin of Cu/Au Ratios in Porphyry-Type Ore Deposits. *Science* **296**(5574), 1844-1846.

Hattori K. H., Arai S. and Clarke D. B. (2002) Selenium, Tellurium, Arsenic, and Antimony Contents of Primary Mantle Sulfides. *The Canadian Mineralogist* **40**(2), 637-650.

Hildreth W. and Moorbath S. (1988) Crustal contributions to arc magmatism in the Andes of Central Chile. *Contributions to Mineralogy and Petrology* **98**(4), 455-489.

Hofmann A. W. (1988) Chemical differentiation of the Earth: the relationship between mantle, continental crust, and oceanic crust. *Earth and Planetary Science Letters* **90**(3), 297-314.

Johnston D. T., Farquhar J. and Canfield D. E. (2007) Sulfur isotope insights into microbial sulfate reduction: When microbes meet models. *Geochimica et Cosmochimica Acta* **71**(16), 3929-3947.

Keays R. R. and Davison R. M. (1976) Palladium, iridium, and gold in the ores and host rocks of nickel sulfide deposits in Western Australia. *Economic Geology* **71**(7), 1214-1228.

Keays R. R. and Lightfoot P. C. (2007) Siderophile and chalcophile metal variations in Tertiary picrites and basalts from West Greenland with implications for the sulphide saturation history of continental flood basalt magmas. *Mineralium Deposita* **42**(4), 319-336.

Keays R. R., Nickel E. H., Groves D. I. and McGoldrick P. J. (1982) Iridium and Palladium as Discriminants of Volcanic-Exhalative, Hydrothermal, and Magmatic Nickel Sulfide Mineralization. *Economic Geology* **77**(6), 1535-1547.

Keith J. D., Whitney J. A., Hattori K., Ballantyne G. H., Christiansen E. H., Barr D. L., Cannan T. M. and Hook C. J. (1997) The role of magmatic sulfides and mafic alkaline magmas in the Bingham and Tintic mining districts, Utah. *Journal of Petrology* **38**(12), 1679 - 1690.

Kemp A. I. S., Shimura T. and Hawkesworth C. J. (2007) Linking granulites, silicic magmatism, and crustal growth in arcs: Ion microprobe (zircon) U-Pb ages from the Hidaka metamorphic belt, Japan. *Geology* **35**(9), 807-810.

Li C. and Ripley E. M. (2005) Empirical equations to predict the sulfur content of mafic magmas at sulfide saturation and applications to magmatic sulfide deposits. *Mineralium Deposita* **40**, 218-230.

Liu Y., Samaha N.-T. and Baker D. R. (2007) Sulfur concentration at sulfide saturation (SCSS) in magmatic silicate melts. *Geochimica et Cosmochimica Acta* **71**(7), 1783-1799.

Marowsky G. and Wedepohl K. H. (1971) General trends in the behavior of Cd, Hg, Tl and Bi in some major rock forming processes. *Geochimica et Cosmochimica Acta* **35**(12), 1255-1267.

McDonough W. F. and Sun, S.-s (1995) The composition of the Earth. *Chemical Geology* **120**(3-4), 223-253.

Naldrett A. J. (2004) *Magmatic Sulfide Deposits: Geology, Geochemistry, and Exploration*. Springer, Berlin. pp. 727.

Nanayama F., Kanamatsu T. and Fujiwara Y. (1993) Sedimentary petrology and paleotectonic analysis of the arc--arc junction: the Paleocene Nakanogawa Group in the Hidaka Belt, central Hokkaido, Japan. *Palaeogeography, Palaeoclimatology, Palaeoecology* **105**(1-2), 53-69.

O'Neill H. S. C. and Mavrogenes J. A. (2002) The sulfide capacity and the sulfur content at sulfide saturation of silicate melts at 1400°C and 1 bar. *Journal of Petrology* **43**(6), 1049-1087.

Owada M., Osanai Y. and Kagami H. (1997) Rb-Sr isochron ages for hornblende tonalite from the southeastern part of the Hidaka metamorphic belt, Hokkaido, Japan: Implication for timing of peak metamorphism. *Memoirs of the Geological Society of Japan* **47**, 21-27.

Pallister J. S., Hoblitt R. P., Meeker G. P., Knight R. J. and Siems D. F. (1996) Magma mixing at Mount Pinatubo: Petrographic and chemical evidence from the 1991 deposits. In *Fire and mud: Eruptions and lahars of Mount Pinatubo, Philippines* (eds. C. G. Newhall and R. S. Punongbayan), pp. 687-731. University of Washington Press, United States, Quezon City, Philippines.

Peach C. L., Mathez E. A. and Keays R. R. (1990) Sulfide melt-silicate melt distribution coefficients for noble metals and other chalcophile elements as deduced from MORB: Implications for partial melting. *Geochimica et Cosmochimica Acta* **54**(12), 3379-3389.

Richards J. P. (2003) Tectono-magmatic precursors for porphyry Cu-(Mo-Au) deposit formation. *Economic Geology* **98**(8), 1515-1533.

Ripley E. M., Li C. and Shin D. (2002) Paragneiss assimilation in the genesis of magmatic N-Cu-Co sulfide mineralization at Voisey's Bay, Labrador: $\delta^{34}S$, $\delta^{13}C$, and Se/S evidence. *Economic Geology* **97**, 1307-1318.

Shimura T., Komatsu M. and Iiyama J. T. (1991) Genesis of the lower crustal garnet orthopyroxene tonalites (S-type) of the Hidaka Metamorphic Belt, Northern Japan. In *2nd Hutton Symposium on the Origin of Granites and Related Rocks*, pp. 259-268. Royal Society of Edinburgh - Earth Sciences, Canberra, Australia.

Stavast W. J. A., Keith J. D., Christiansen E. H., Dorais M. J., Tingey D., Larocque A. and Evans N. (2006) The fate of magmatic sulfides during intrusion or eruption, Bingham and Tintic districts, Utah. *Economic Geology* **101**(2), 329-345.

Studley S. A., Ripley E. M., Elswick E. R., Dorais M. J., Fong J., Finkelstein D. and Pratt L. M. (2002) Analysis of sulfides in whole rock matrices by elemental analyzer-continuous flow isotope ratio mass spectrometry. *Chemical Geology* **192**(1-2), 141-148.

Takahashi T. (1983) The Oshirabetsu gabbroic mass in the southeastern part of the Hidaka Metamorphic Belt, Hokkaido, Japan. *Journal of the Faculty of Science, Hokkaido University, Series IV* **20**(2-3), 203-224.

Tomkins A. G. and Mavrogenes J. A. (2003) Generation of metal-rich felsic magmas during crustal anatexis. *Geology* **31**(9), 765-768.

Tsuchiya N., Suzuki S. and Chida T. (1991) Origin of graphite in the Oshirabetsu gabbroic body, Hokkaido, Japan. *Journal of Mineralogy, Petrology and Economic Geology* **86**(6), 264-272.

Turekian K. K. and Wedepohl K. H. (1961) Distribution of the elements in some major units of the Earth's crust. *Geological Society of America Bulletin* **72**(2), 175-191.

Chapter 4: The Sulfur Fence - a new model for magmatic sulfide formation

Introduction

Magmatic Ni-Cu-(PGE) ore deposits form through exsolution and segregation of FeS-rich sulfide melt from mafic-ultramafic magmas (e.g. Wagner, 1929; Keays and Davison, 1976; Naldrett, 1992; Keays, 1995; Keays and Lightfoot, 2007). More recently, sulfide melts have been implicated in the genesis of porphyry Cu ore systems (e.g. Halter et al., 2002; Halter et al., 2004, 2005; Stavast et al., 2006). In general, sulfur oversaturation in silicate magmas causes exsolution of immiscible sulfide melts (Naldrett, 2004), which partition and concentrate chalcophile elements as segregation progresses (e.g. Goldschmidt, 1937; Peach et al., 1990). The greater the amount of sulfur oversaturation, the more pervasive the consequent sulfide globule nucleation (Mungall, 2002a). High sulfur oversaturation leads to a high number density of sulfide melt globules (Mungall, 2002a), which is likely to be a key factor encouraging efficient metal concentration from the silicate melt. The R-factor describes the volume of silicate melt that is seen chemically by a given sulfide globule(see Campbell and Naldrett, 1979; Mungall, 2002a). A high R-factor globule interacts with a large volume of silicate melt relative to its own volume, allowing it to scavenge more chalcophile elements from the silicate melt; therefore, high R-factor sulfide melts become metal enriched (high tenor). On the other hand, a high number density of sulfide globules may actually result in a reduced overall R-factor because the ratio of sulfide volume to silicate volume could be higher. This may result in a more efficient and complete scavenging of metals, as the entire volume of silicate melt would have some sulfide melt globules present (Fig. 4.1). Since ore deposits are extreme concentrations of otherwise uncommon metals, efficient sequestration of metals from large volumes of silicate magma is a critical process in their development.

Many intrinsic melt properties affect sulfur solubility in silicate melts: temperature, pressure, SiO_2 content, and Fe^{2+} content are among the most well characterised (Haughton et al., 1974; Li et al., 2001; O'Neill and Mavrogenes, 2002; Naldrett, 2004). Oxygen fugacity (fO_2) also has the potential to affect sulfur solubility, but has not yet received the same attention. MacLean (1969) intimated that oxygen fugacity might have a limited role in controlling sulfur solubility, although O'Neill and Mavrogenes (2002) questioned the validity of this idea. However, it has since been found by Jugo et al. (2005) that for a given silicate magma composition, the solubility of sulfur in silicate melt changes from ~0.15% to ~1.5% (an order of magnitude) between melts with $fO_2 \leq$ FMQ + 1 and those with $fO_2 \geq$ FMQ + 1, respectively (where FMQ is the fayalite-magnetite-quartz oxygen buffer). This solubility gap is thought to represent the change from sulfide to sulfate mineral stability, with sulfate more soluble than sulfide (Jugo et al., 2005). As many economically important metals are chalcophile (see Chapter 3), the formation of sulfides at any time during the evolution of a metalliferous silicate melt will have a critical control on metal distribution in the magma.

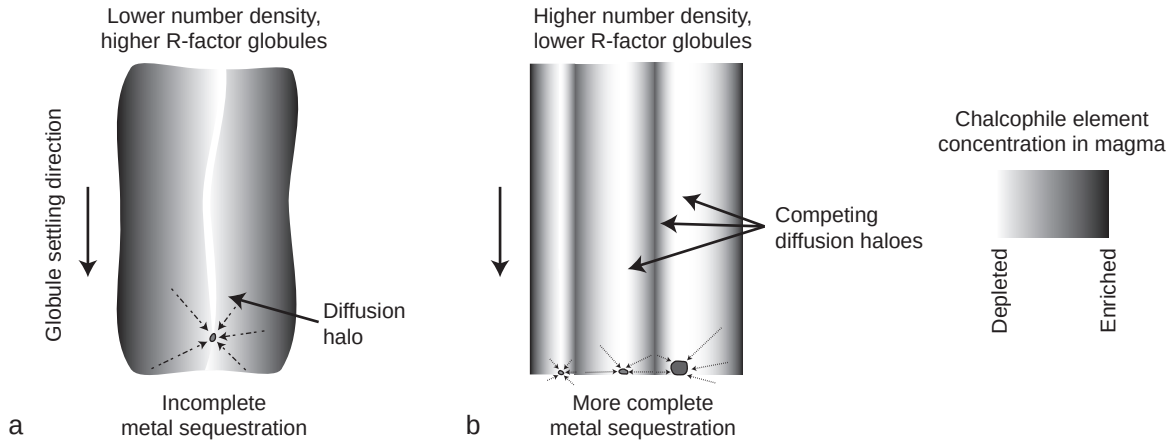

Figure 4.1: Schematic showing the chalcophile element depletion haloes around sulphide globules settling through a given volume of silicate magma: (a) low number density allows single globules to sequester metals from the entire surrounding volume of magma without diffusive competition from nearby globules; (b) higher number density of globules means that one globule will compete with other nearby globules for the same chalcophile elements.

Therefore, oxygen fugacity may be important in the evolution of sulfide ore deposits in areas with the potential for large fluctuations in fO_2, such as at the base of arcs.

Arc basalts have the potential to be oxidised and sulfur-rich (e.g. Carroll and Rutherford, 1987; Kress, 1997). The 1991 Pinatubo eruption, for example, discharged the largest SO_2 gas cloud ever measured and the sulfur in this eruption has been linked to highly oxidised magmatic sources (Kress, 1997). Conversely, consider that accretionary wedge complexes are commonly associated with arc sections and that graphite is a common component in metamorphosed accretionary wedges (Chapter 2). In this case, high-grade metamorphic rocks from the lower crust in these settings may typically be reduced, with many containing graphite. With graphite exerting redox control, this chapter investigates the idea that if a silicate melt changes redox state from sulfate stable to sulfide stable, sulfur will become highly oversaturated. It is under these conditions that high concentrations of immiscible sulfide melt will form; this would play a significant role in arc ore deposit formation.

Chapter 3 presented arguments supporting the role of MASH zone magma mixing in mediating changes in Fe, Si, and S content. It is also probable that magma mixing exerts a similar control on fO_2 when the mixing phases have elevated concentrations of elements or minerals that can exert strong redox control, such as graphite (see Mungall, 2002b). In this chapter, piston cylinder experiments are used to investigate the sulfur solubility of magma mixes, showing that fO_2 alone can alter the sulfur solubility of any given composition by an order of magnitude. This evidence is used in conjunction with a mass balance approach to argue that mixing of oxidised, sulfate-stable mantle-derived gabbroic melts with reduced, graphitic crust-derived felsic melts in MASH zones can result in hybrids with reduced redox states in which sulfides are stable. The term ‘sulfur fence’ is used to describe the step in sulfur solubility that occurs at the point of this redox transition. The resulting sudden and large oversaturation of sulfur is presented as a key process affecting the development of

sulfide ore deposits. The genesis of both magmatic Ni-Cu-(PGE) and porphyry Cu deposits may be affected by this process.

Sulfur Content and Mixing

In Chapter 3, evidence was presented from the Opirarukaomappu Gabbroic Complex (OGC) showing magma mixing and abundant sulfide production in the lower crust to mid-crust of the paleo-Kuril Arc. This was then used to propose a link between mixing in a MASH zone and the production of sulfide melts in arcs. It is clear that the primary chemical mechanisms controlling sulfur solubility (temperature, pressure, SiO_2 content, and Fe^{2+} content; see O'Neill and Mavrogenes, 2002) are modified during magma mixing; however, the processes driving a magma to become reducing and sulfide stable from it initially being oxidising and sulfate stable must rely on the addition of components into the system that have a strong effect on oxygen fugacity. One such component is graphite, which can result from metamorphism of organic-rich sediments (e.g. Pattison, 2006). If mixing of felsic, crust-derived partial melts and mantle-derived gabbros in MASH zones is widely associated with arc development, the question becomes two-fold: how common is graphite or carbon in arc settings and how may it become entrained in the MASH zone?

Exposed island arc sequences, though rare, are commonly associated with accretionary wedge complexes (see Chapter 2). Accretionary wedge complexes are mostly accumulations of oceanic floor sediments scraped off the downgoing slab at a subduction margin (e.g. Moore et al., 1982; Brown and Spadea, 1999).

Total carbon in oceanic floor sediments is highly variable. Factors that favour high carbon content in deep-sea sediments are high organic productivity in overlying waters (e.g. along coasts and at upwelling sites), high input of terrigenous organic matter (e.g. at fluvial deltas), and rapid burial rate (e.g. in turbidites) (Stein, 1990). These conditions are fundamentally related to arcs, which plate tectonic theory states are exclusively associated with subduction margins. Where accretionary wedge sediments form part of the stratigraphy of accreted arc sequences, such as in the Hidaka Metamorphic Belt, Talkeetna Arc, and Kohistan Sequence (see Chapter 2), there is much potential for partial melting of graphitic accretionary wedge sediments in a MASH zone setting. Along the margin of the paleo-Japan arc, for example, it is likely that all of these conditions were met: a coastal environment, terrigenous sediment input from erosion of the arc, and the formation of turbidites (Nanayama et al., 1993).

In Chapter 3, mixing is presented as a pervasive process operating in a representative arc magma chamber in the lower crust to mid-crust of the Hidaka Metamorphic Belt – the OGC. The OGC is emplaced within richly graphitic metasediments, now migmatites, of the Nakanogawa Group, a Palaeocene sequence of turbidites (Nanayama et al., 1993). The Nakanogawa Group is part of the Hidaka Supergroup, which is in turn an accretionary wedge complex (Chapter 2). Therefore, it is suggested that mixing of arc magmas at depth

with graphitic partial melts or assimilation of graphitic metasediments in MASH zones are important processes mediating oxygen fugacity in these magmas.

Melting at depth in arcs was once thought to result mostly from direct melting of the downgoing slab through frictional heating (e.g. Molnar and England, 1995). Although there are rare instances where direct melting is still considered to be the case (e.g. Defant and Drummond, 1990), melting is now thought to take place in a two stage process: (i) dehydration of the downgoing slab at the blueschist-eclogite transition releases solute-rich aqueous fluids into the overlying mantle wedge; (ii) these fluids flux melting of the overlying mantle wedge (see Richards, 2003). Arc magmas are typically more oxidised than non-subduction zone magmas, but they are still generally within the sulfide stability field of fO_2 space (Parkinson and Arculus, 1999; Mungall, 2002b). However, many arc magmas have oxygen fugacities within the sulfate stability field (e.g. Carroll and Rutherford, 1987; Kress, 1997). In the ore generation model of Mungall (2002b), the development of sulfide melts at any time in the evolution of arc magmas will strip them of chalcophile elements. Consequently, Mungall (2002b) states that most are not prospective for ore deposits. In sufficiently oxidised magmas, however, sulfides are not stable and the sequestration of chalcophile elements cannot occur. Therefore, Mungull (2002b) posits that oxidised magmas that have always been oxidised and sulfate stable will have higher chalcophile metal content than their reduced and sulfide stable counterparts. In any case, magmas that can both retain their chalcophile metal content and make it available to later ore concentration processes can become large tonnage porphyry Cu deposits [e.g. Chuquicamata, La Escondida, and El Teniente in South America; Freida River and Ok Tedi in Papua New Guinea – see Singer (2005)]. For magmas to retain their chalcophile metal content, they must remain sulfide undersaturated. If they do saturate and produce a sulfide liquid, that sulfide liquid, containing chalcophile metals, must be retained.

Experimental Rationale

Existing sulfur solubility models (e.g. Li and Naldrett, 1993; Li and Ripley, 2005; Liu et al., 2007) adequately describe the sulfur content of magmas, but do not address redox in mixing magmas as a potentially important mechanism to produce sulfur oversaturation. Li and Naldrett (1993) developed a model to describe the sulfide capacity of silicate magmas to which Li and Ripley (2005) and then Liu et al. (2007) updated with more extensive data sets. In these studies, the sulfur content at sulfide saturation (SCSS) was used to describe how mixing of mantle-derived mafic melt with crustal partial melt lowers sulfide solubility in the hybrid. The model's sulfide solubility curve is concave upward. A bimodal mixing line drawn between mafic and felsic endmembers in such a system shows the potential for mixing to generate sulfide oversaturation (Fig. 4.2). However, the data used throughout the development of the SCSS empirical model were for sulfide-stable experiments only; therefore, these models are only useful in magmatic systems where redox-controlled sulfate-to-sulfide stability is not a consideration.

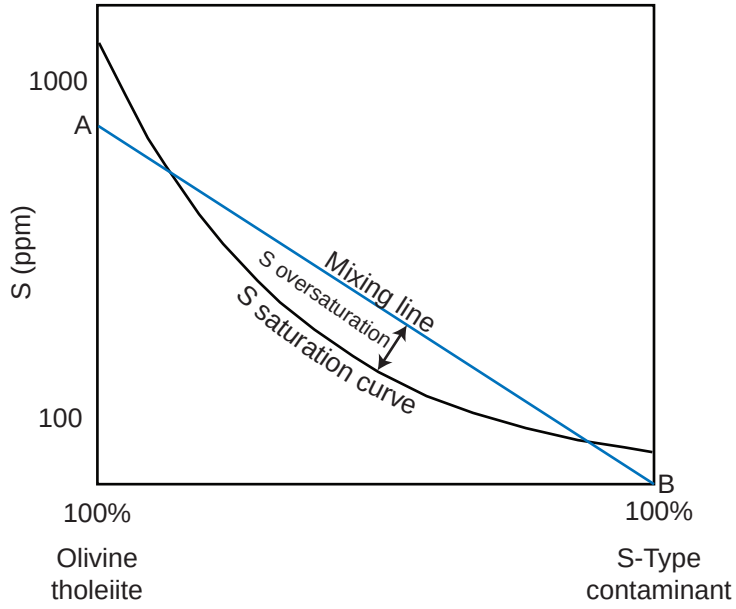

Figure 4.2: The sulfur saturation curve in black is a schematic after Figure 11 of Li and Ripley (2005). These authors calculated the curve for an olivine tholeiite being progressively contaminated with an S-type felsic partial melt. When a mafic melt of composition A (~1000 ppm S) is mixed (blue line) with a sulfur-free S-type contaminant of composition B, the sulfur content of the hybrid will exceed its sulfur solubility and it will become oversaturated. Oversaturation in S will cause the exsolution of a sulfide liquid.

To better explore sulfur solubility mechanisms in MASH zones, and the generation of immiscible sulfide melts by mixing-induced sulfur oversaturation, a set of piston cylinder experiments was designed to simulate the mixing of an oxidised gabbroic melt and a reduced felsic melt. The experiments are specifically undertaken to incorporate the oxidised/reduced sulfur saturation behaviour found by Jugo et al. (2005), and aim to propose a new sulfur solubility model that accounts for the order-of-magnitude difference in solubility between sulfate and sulfide.

Buffers

Representations of the redox state of magmas rely on the idea of fO_2 buffers, which though mostly not found in nature, do adequately describe the position in fO_2 space of silicate magmas (Frost, 1991). Mungall (2002b) presented the SSO buffer to describe the position in fO_2 space of the sulfide-sulfate transition with the equilibrium reaction:

$$FeS_{(liq)} + CaFeSi_2O_{6(Cpx)} + 2O_{2(fluid)} = CaSO_{4(Anh)} + 2FeSiO_{3(Opx)}$$

which occurs slightly above the NNO buffer at NNO + 1 (Fig. 4.3). Mungall (2002b) used FeS as the sulfide species and $CaSO_4$ as the sulfate species because these are the most abundant phases found in natural magmas. Figure 4.3 clearly shows that the CCO buffer, to which a melt would be buffered if assimilating or mixing with excess graphitic metasediments, is at least 2.5 log units below the NNO buffer and 3.5 log units below SSO.

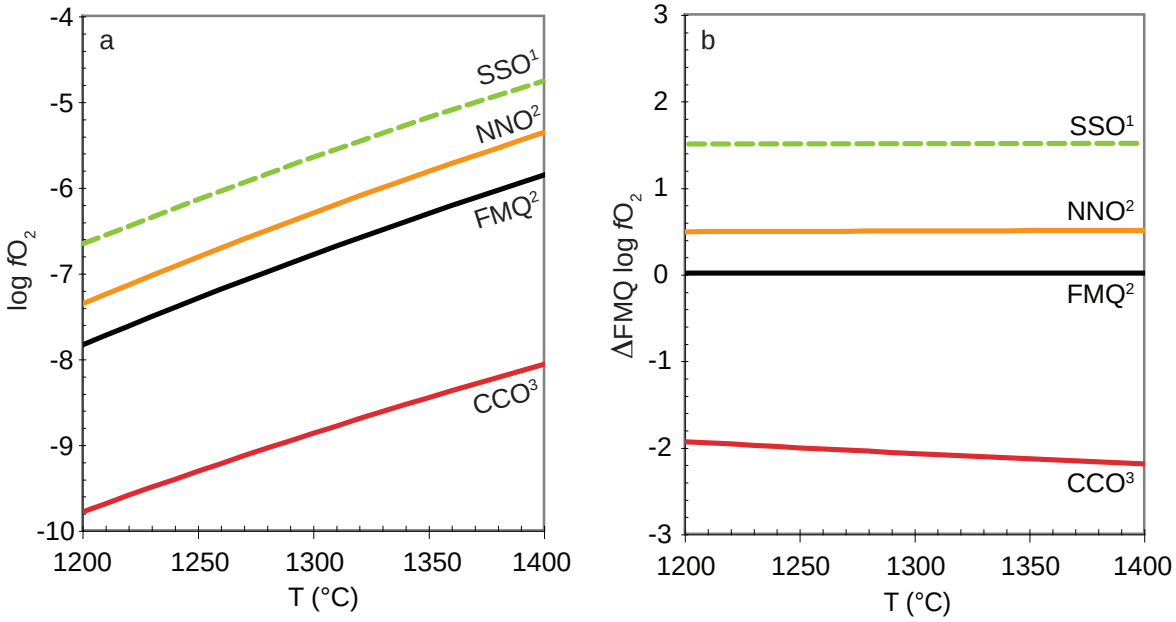

Figure 4.3: (a) Oxygen fugacity buffer curves at 6 kb for SSO (sulfur-sulfur oxide), NiNiO (nickel-nickel oxide), FMQ (fayalite-magnetite-quartz), and CCO (carbon-carbon oxide). (b) Buffer curves at 6 kb relative to FMQ. [1]SSO curve is estimated from Figure 1 of Mungall (2002). [2]NNO and FMQ curves calculated from equations of Frost (1991). [3]CCO curve calculated from equation of Ulmer and Luth (1991).

Experimental starting materials

A dredged sample of arc basalt, provided by Richard Arculus, and a graphitic S-type tonalite collected during fieldwork in southeastern Hokkaido, Japan (Chapter 3) were chosen as the endmembers for the mixing experiments. These samples were milled to powders in tungsten-carbide shaker mills. Two weight percent sulfur as anhydrite was added to the batches of basalt powder used for the experiments, ensuring that the basalt was both saturated in sulfur and highly oxidised. The tonalite was kept natural as it is highly enriched in graphite, attributable to its parent magma being sourced from and assimilating Nakanogawa migmatite (Fig. 3.13).

By weighing out the basalt and tonalite powders to different proportions for each experiment (see Table 4.1), the set of experiments together represent progressive mixing of the endmembers. Just enough sample powder to produce each experiment was weighed out ensuring optimal sample capture for each run. Scales accurate to four decimal places were used, so that weighing uncertainty is estimated to be ± 5 x 10^{-5} gm.

TABLE 4.1
Experimental run conditions

Tonalite / Basalt Proportion	Buffer Discs	Capsule	Run Conditions P (kb)	Run Conditions T (°C)
50/50	Hematite	BN in Pt	6	1300
40/60	Hematite	BN in Pt	6	1310
30/70	Hematite	BN in Pt	6	1320
20/80	Hematite	BN in Pt	6	1330
10/90	Hematite	BN in Pt	6	1340
5/95	Hematite	BN in Pt	6	1350
20/80	Hematite	Pt	6	1330
10/90	Hematite	Pt	6	1340
5/95	Hematite	Pt	6	1350
5/95	None	Pt	6	1350

Notes:

BN = Boron nitride.

All Pt tubing was 5 mm outer diameter, 0.5 mm wall thickness.

The sample aliquots were mixed in small clean sample vials to mechanically homogenise the starting material for each experiment.

For simplicity, no water was added to the experiments. The only source of water is that released through the breakdown of biotite in the tonalite powder, which contains approximately 10% biotite. The ~ 4% water content of biotite implies that the tonalite in each experiment released a maximum of about 0.4% water and for this reason they are considered to be essentially anhydrous.

Experimental run conditions and rationale

The OGC is interpreted to have been uplifted from a depth of ~ 23 km (see Chapters 2 and 3). For this study, pressure at that depth was estimated to be ~ 6 kbar (kb), which assumes normal continental crust and lithostatic conditions. For this reason, 6 kb was chosen as the run pressure for the experiments to represent the pressure conditions experienced by the melts originally plumbing the paleo-Kuril Arc. The temperature of the runs was chosen to be between 1350°C for the most mafic mixture and 1300°C for the most felsic mixture. This temperature range was chosen based on the liquidus estimate of the MELTS modelling software (Ghiorso and Sack, 1995) for the bulk compositions of the most mafic and most felsic experimental mixtures. The high liquidus temperature is required because the experiments were anhydrous. Approximately 50°C was added to the MELTS estimate to guarantee liquidus conditions in case of temperature measurement inaccuracies in the piston cylinder thermocouple set-up.

Experimental equilibrium

The super-liquidus temperatures employed in these experiments and small sample volume are thought to encourage rapid equilibration throughout the melt volume. Experiments run for the shortest and longest duration were produced first, and analysed by electron microscope to check for crystalline phases and then to check for chemical homogeneity by energy dispersive spectroscopy (EDS) spot analysis and x-ray element maps. At this early stage in the experimental runs, there were no inhomogeneities larger than the errors inherent in EDS. After the complete set of experiments was run, microprobe analysis (see below) revealed that the sulfur concentrations, significant to two digits, were homogenous throughout the sample.

Capsule materials

The choice of capsule is fraught with problems, especially when sulfide is expected to be a run product. The high temperature and run time complicates the choice further. For runs in the sulfate stability field, $Au_{\leq 25}Pd_{\geq 75}$ alloys would have acceptably high melting temperatures, but for these experiments Pt was chosen, because in addition to a high melting temperature (≥

1750°C) it has lower hydrogen permeability than AgPd (see Holloway and Wood, 1988). At 6 kb, copper, gold, and silver melt at temperatures too low for these experiments: ~1110°C, 1095°C, and 1000°C, respectively (Cohen et al., 1966). For runs in the sulfide stability field, boron nitride (BN) was chosen as a sub-capsule to contain the melt and any sulfide melts. The BN sub-capsule was then placed inside Pt (see below), which prevented reaction between the Pt and sulfides in the melt. BN consumes free oxygen in the piston cylinder atmosphere to form boron oxides, establishing log $fO_2 \leq -12$ (3.2 log units below CCO) at P ≈ 6 kb, T ≈ 1300°C, which is below the iron-wustite buffer (Wendlandt and Huebner, 1982). This reaction establishes a suitably reducing atmosphere that allows sulfide stability in the melt. It is unclear how soluble boron oxides are in silicate melt or to what extent that affects sulfur solubility, but for reasons explained later, it is not thought to have dissolved substantially in the experimental melts.

Experimental Methods

Piston cylinder apparatus

Experiments were conducted using 150 and 200 ton end-loaded piston cylinders, based on the Boyd and England (1960) design, housed at the high-pressure equipment laboratory in the Research School of Earth Sciences at the Australian National University in Canberra, Australia.

Capsule preparation and furnace assembly

Two different capsule designs were used in the experimental runs (Fig. 4.4): (i) a 5 mm OD Pt (Fig. 4.4a) and (ii) a 4.5 mm OD machined, lidded BN (boron nitride) sub-capsule (Fig. 4.4b) inserted into 5 mm OD Pt. After loading the sample powder directly into the Pt tube, or into a BN sub-capsule then into Pt, the Pt was triple crimped and welded shut using a graphite electrode continuous-arc microwelder. The welded experiment was then inserted into a 5 mm die and compressed to flatten the top and bottom welds. Hematite buffer discs (~1 mm thickness) were placed above and below the capsule to minimise hydrogen diffusion (Fig. 4.4a). The experiments were run at 6 kb (0.6 GPa) and between 1300°C and 1350°C, depending on the composition of the mixture (see Table 4.1), using a 5/8 inch (~15 mm) high temperature NaCl-pyrex and graphite furnace cell (after Bohlen, 1984). An MgO sleeve was machined to slide around the experiment capsule, extending above and below it to contain the hematite buffer discs, to protect the capsule and buffer material from interaction with the graphite furnace. Machined MgO tubes replaced the NaCl packing used in the Bohlen (1984) cell and an MgO disc was inserted between the experiment and the thermocouple to protect against poisoning of the thermocouple bead and penetration into the capsule. Figure 4.4c shows an assembled experiment including the NaCl-pyrex-graphite furnace assembly (see Bohlen, 1984). Finally, the entire assembly was wrapped in mylar, for ease of later extraction, before insertion into a 5/8 inch tungsten carbide pressure vessel for the experimental run.

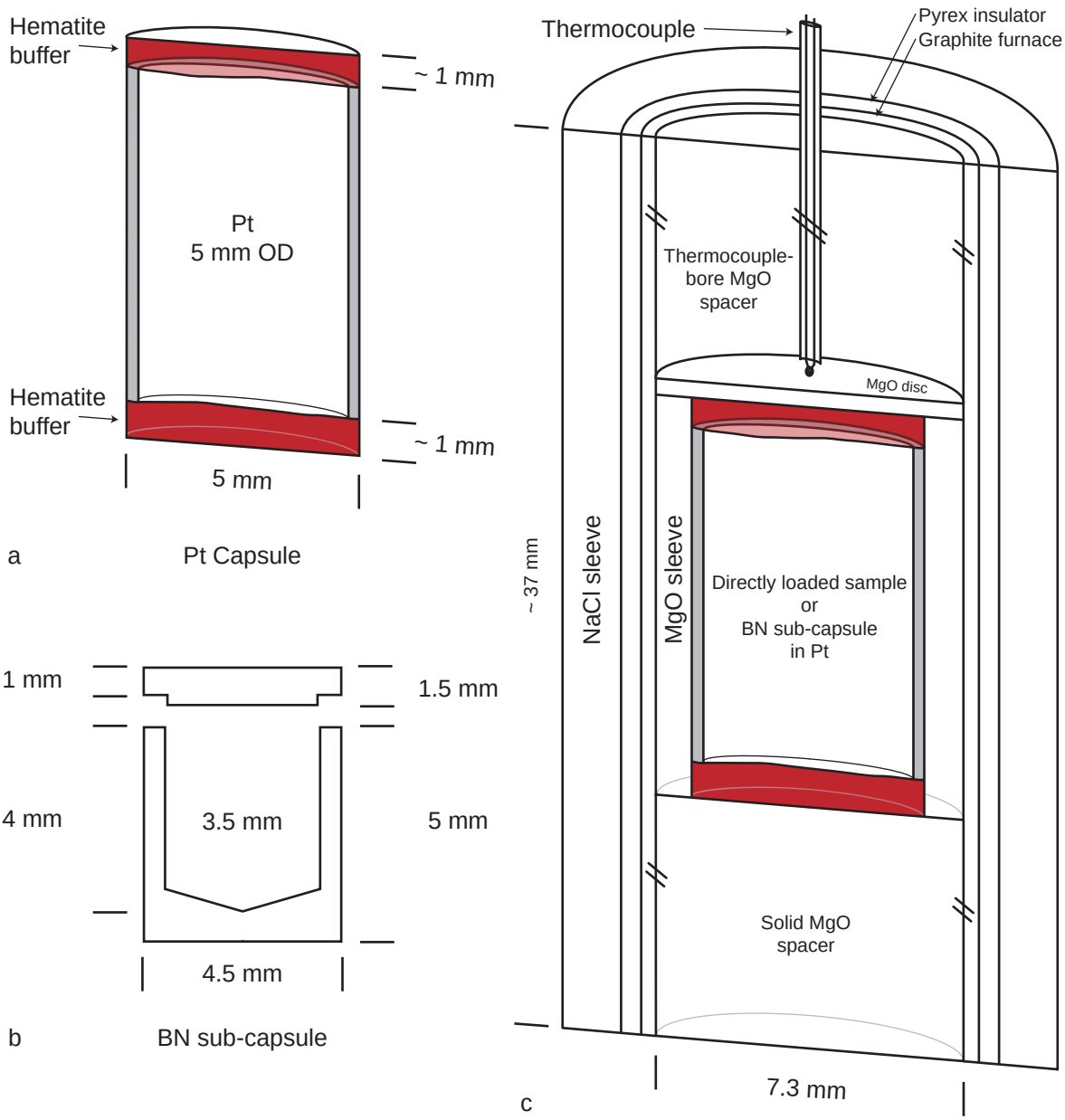

Figure 4.4: Schematic longitudinal sections through the experimental capsule and packing set up. (a) Pt capsule used in all experiments: 5 mm outer diameter (OD), 4.5 mm inner diameter (ID). Note hematite buffer discs placed above and below to limit hydrogen diffusion into the capsule. (b) BN sub-capsule placed inside Pt (above) for experiments under reducing conditions. (c) Complete furnace assembly setup.

Experimental runs

After initial pressurisation to ~ 1 kb to seal the furnace assembly in the pressure vessel, the experiment was brought to run conditions by simultaneously increasing the pressure and temperature after an initial isobaric heating to > 600°C to start melting the NaCl sleeve (the 'hot piston-in' technique). Temperature was monitored with a Type B thermocouple [Pt-6%Rh (+ leg) / Pt-30%Rh (- leg)], which was welded prior to insertion to form a bead (see Fig. 4.4c). Temperature was maintained to ± 1°C precision by Eurotherm temperature controllers after a brief (< 30 second) overshoot of up to 8°C above the target temperature during the temperature ramp. Thermocouple accuracy is estimated to be ± 10°C and no pressure correction was applied to the emf output of the thermocouple. Power output was

stable, varying by one or two percent during the length of the runs, which implies that the thermocouples were sufficiently protected from poisoning.

Above the melting temperature of the salt sleeve (~900°C at 6 kb, see Akella et al., 1969), it is virtually frictionless (Johannes, 1978; Boettcher et al., 1981; Bohlen, 1984). All experiments were run well in excess of this temperature (≥ 1300°C), therefore no pressure correction was applied to the hydraulic load as read by Heise pressure gauges attached to the piston cylinder apparatus. Furthermore, pressure was closely monitored during shorter experimental runs (less than ten hours) and no change was found to occur over the last few hours leading up to quench, implying that even for runs of less than a day, internal friction in the system rapidly decayed to zero. Pressure accuracy is estimated to be ± 0.04 kb.

The experiments were quenched non-isobarically at the end of each run. However, the quench is in excess of 200°C per second, which is thought to capture the equilibrium melt composition at run conditions. The experimental capsule was then extracted from the pressure vessel and furnace components, mounted in epoxy resin, dry-ground to expose the experimental glass, dry polished, carbon coated, and analysed by electron microprobe. Table 4.1 lists the starting powder proportions, capsule components, and run conditions for all experiments presented in this chapter.

Analyses

The rock powders used to prepare the starting material for each experiment were analysed for the major elements Na, Mg, Al, Si, P, S, K, Ca, Ti, Mn, Fe, F and Cl by XRF with a Phillips (PANalytical) PW2400 X-ray fluorescence spectrometer housed at the X-ray analysis facility in the Research School of Earth Sciences, ANU. Lithium borate discs were prepared by fusion of 0.27 g of dried sample powder and 1.72 g of '12-22' eutectic lithium metaborate-lithium tetraborate. The major elements were calibrated against 28 international standard rock powders. Total carbon and sulfur analyses were performed by elemental analyser mass spectrometry at ALS Chemex in Brisbane, Australia. The compositions are detailed in Table 4.2.

TABLE 4.2
Composition of endmember powders

	Arc Basalt	SE	Tonalite	SE
SiO_2	55.683	0.128	62.937	0.143
Al_2O_3	15.402	0.039	16.536	0.041
CaO	10.491	0.028	2.360	0.010
MgO	5.700	0.018	2.476	0.010
MnO	0.173	0.005	0.073	0.005
Na_2O	1.501	0.008	3.222	0.012
K_2O	0.398	0.006	2.865	0.011
TiO_2	0.475	0.006	0.804	0.007
P_2O_5	0.093	0.005	0.180	0.005
SO_3	bd	0.005	0.760	0.007
Fe_2O_3	10.263	0.028	6.503	0.019
F (ppm)	bd	99	bd	98
Cl (ppm)	1877	4	bd	3
Total	100.355		98.801	
Total C	0.02		0.28	
Total S	0.01		0.40	

Notes:
All data in wt. % except where noted.
SE = one standard error; bd = below detection limit.

The mounted silicate glasses (the run products) were analysed for major elements and sulfur by wavelength dispersive spectroscopy (WDS) on

TABLE 4.3
Sulfur contents of experimental glasses and microprobe beam conditions

Experiment (Tonalite/Basalt)	S (wt. %)	S (ppm)	σ	SiO_2 (oxide wt%)	σ	beam size (μm)	n
Reduced							
5/95	0.24	2400	0.041	53.76	0.323	50	20
10/90	0.14	1400	0.019	56.28	0.524	20	20
20/80	0.11	1100	0.014	56.00	0.230	50	20
30/70	0.09	900	0.006	58.40	0.431	20	20
40/60	0.08	800	0.015	60.13	0.390	20	20
50/50	0.08	800	0.012	60.34	0.253	20	20
Oxidised							
5/95	0.86	8600	0.017	56.43	0.551	50	20
5/95[1]	0.85	8500	0.021	54.94	0.276	20	20
10/90	0.94	9400	0.022	55.01	0.209	20	20
20/80	0.69	6900	0.011	58.49	0.405	50	20

Notes:

[1] This experiment was run without hemataite buffer discs to determine the effect of the buffer, if any, on sulfur content of the glasses.

σ is one standard deviation in the analyses of each glass.

n is the number of analysis points on each glass.

the Cameca SX100 electron probe at the Research School of Earth Sciences, Australian National University (ANU). Analyses for sulfur were performed using the method of O'Neill and Mavrogenes (2002) with a few modifications. Sulfur counts were collected for ~120 seconds on one PET crystal to achieve a limit of detection (LOD) of ~500 ppm. Beam conditions of 15 kV accelerating voltage, 100 nA beam current, and mixed beam sizes of 20 μm and 50 μm were used (see Table 4.3). Each glass was analysed at 20 different spot locations and analyses that showed higher than expected variation were reanalysed. The data is reported as averages and is presented ± 1 standard deviation (σ) in Table 4.4 with major elements reported in weight percent oxide equivalent and sulfur reported in elemental weight percent. Complete data for all spot analyses, including standards, are presented in Appendix C.

The calibration of the microprobe was checked using VG-2 from the Smithsonian glass database (see Jarosewich et al., 1979). VG-2 was analysed at the beginning, end, and periodically during each analytical session to continuously check calibration and to monitor instrument performance. The average sulfur value obtained on VG-2 during the study period was 1432 ± 103 ppm, which agrees excellently with the reported values for this standard (see O'Neill and Mavrogenes, 2002).

RESULTS

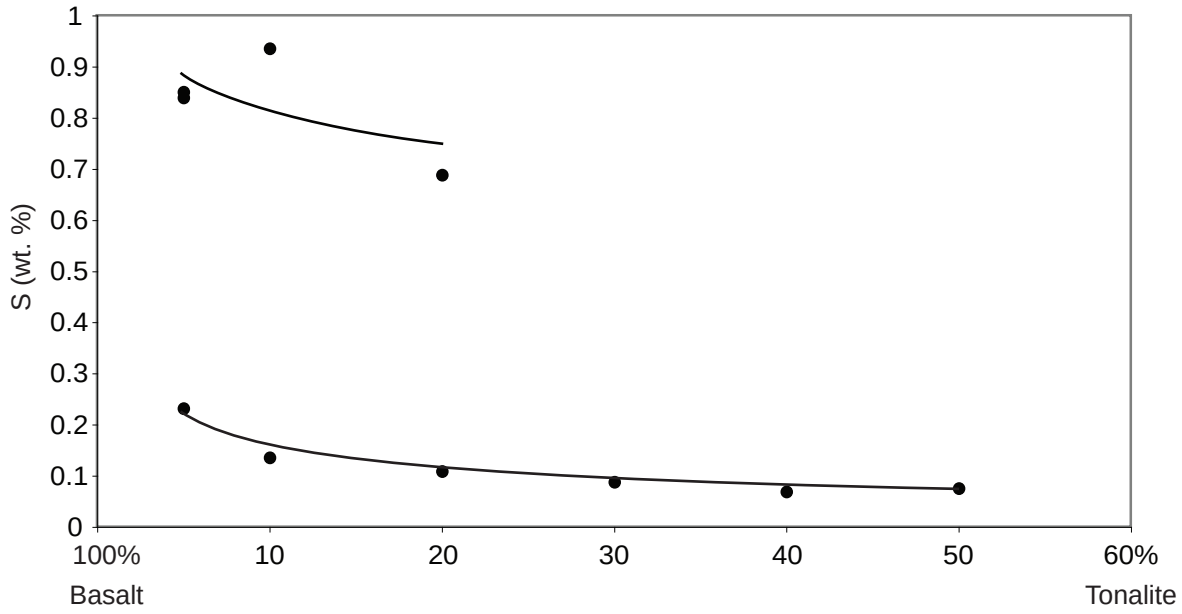

Figure 4.5: S content of glass vs. proportion of tonalite in experimental mixture. All points at < 0.3 wt. % S are from experiments in BN capsules and which are therefore sulfide stable. Points at > 0.6 wt. % S are from experiments in Pt-only capsules saturated in anhydrite and are therefore sulfate stable. An extra experiment at 0.05 mixing proportion was run without hematite buffer discs to determine if there is any effect on S solubility by the discs, for which it is apparent that there is no appreciable difference.

Major element data was modified slightly to account for Fe in different oxidation states. For samples in which sulfate is stable (i.e. those run in Pt only), total Fe is calculated as Fe_2O_3; for sulfide stable runs (i.e. those in BN), total Fe is calculated as FeO (Table 4.4). Plotting sulfur content as a function of mixing proportion (Fig. 4.5) clearly shows that the experiments fit into two sulfur solubility regimes: (i) glasses with sulfur content up to 0.9% S (9000 ppm) and (ii) glasses with sulfur content below ~0.1% S (1000 ppm).

High sulfur content: sulfate stable runs

Glasses with ~1% S content had anhydrite globules present as a stable phase at the bottom of the capsule (Fig. 4.6). The formation of these immiscible sulfate globules implies that the silicate melt was saturated in anhydrite, i.e. the melt was sulfate-stable. The average sulfur content in the silicate glass of these experiments is 0.83 ± 0.091%, reducing systematically with increasing tonalite proportion, but not as clearly as in the low sulfur experiments.

Low sulfur content: sulfide stable runs

The glasses with sulfur content ~0.1% S (1000 ppm) all have sulfide globules present in the capsule (Fig. 4.7), i.e. the melts were sulfide-stable. The average sulfur content in the glass is 0.12 ± 0.059% S, varying systematically with mixing proportion (Fig. 4.5). The globules are spherical in shape, implying that the sulfides were present as an immiscible phase in the silicate melt. The sulfide globules concentrate and are largest at the contact of the melt with the BN capsule; however, they are also present away from the edge of the capsule (Fig. 4.7). Wendlandt and Huebner (1982) noted similar behaviour during melting experiments at 35 kb and 1625°C on garnet lherzolite encapsulated in BN with native iron forming next to the

TABLE 4.4
Averaged major element contents of experimental glasses

	Oxidised experiments								Reduced experiments											
	5/95[1]	σ	5/95	σ	10/90	σ	20/80	σ	5/95	σ	10/90	σ	20/80	σ	30/70	σ	40/60	σ	50/50	σ
(wt. %)																				
Na_2O	1.31	0.023	1.13	0.035	1.39	0.023	1.08	0.027	1.62	0.034	1.18	0.073	1.68	0.023	1.33	0.068	2.00	0.017	2.20	0.028
MgO	5.67	0.079	5.49	0.176	5.90	0.077	4.70	0.033	5.46	0.068	5.06	0.047	4.90	0.042	4.44	0.054	4.01	0.043	3.91	0.027
Al_2O_3	15.58	0.098	15.49	0.165	15.56	0.056	15.70	0.129	15.34	0.093	15.58	0.140	15.71	0.076	15.72	0.139	16.46	0.114	16.45	0.071
SiO_2	54.94	0.276	56.43	0.551	55.01	0.209	58.49	0.405	53.76	0.323	56.28	0.524	56.00	0.230	58.40	0.431	60.13	0.390	60.34	0.253
K_2O	0.52	0.015	0.53	0.016	0.66	0.017	0.96	0.021	0.65	0.017	0.77	0.017	1.04	0.016	1.39	0.025	1.54	0.022	1.80	0.023
P_2O_5	0.09	0.017	0.09	0.014	0.10	0.014	0.11	0.021	0.04	0.017	0.01	0.010	0.02	0.012	0.01	0.013	0.00	0.013	0.01	0.013
CaO	11.57	0.107	11.94	0.085	11.59	0.083	10.63	0.055	12.83	0.145	12.10	0.068	11.06	0.010	10.14	0.073	8.77	0.070	7.71	0.061
MnO	0.16	0.007	0.17	0.013	0.15	0.009	0.16	0.013	0.12	0.010	0.13	0.009	0.11	0.013	0.12	0.001	0.11	0.012	0.11	0.011
FeO									1.40	0.489	2.44	0.034	2.33	0.040	1.86	0.060	1.82	0.032	1.75	0.030
[2]Fe_2O_3	8.67	0.040	7.97	0.206	7.88	0.065	6.82	0.209												
TiO_2	0.53	0.014	0.39	0.016	0.54	0.020	0.45	0.017	0.44	0.021	0.47	0.020	0.49	0.020	0.43	0.019	0.59	0.020	0.62	0.018
Total	99.04		99.63		98.86		99.01		91.67		94.02		93.33		93.83		95.52		94.91	
Mg/Fe	0.56		0.59		0.65		0.59		3.03		1.61		1.63		1.85		1.75		1.74	

Notes:

Mixing proportions are given as tonalite proportion/basalt proportion.

σ is one standard deviation

[1]This experiment was run without Fe_2O_3 buffer discs.

[2] Fe_2O_3 data calculated based on the relationship: Fe_2O_3 = FeO/0.8998 (from Winter, 2001).

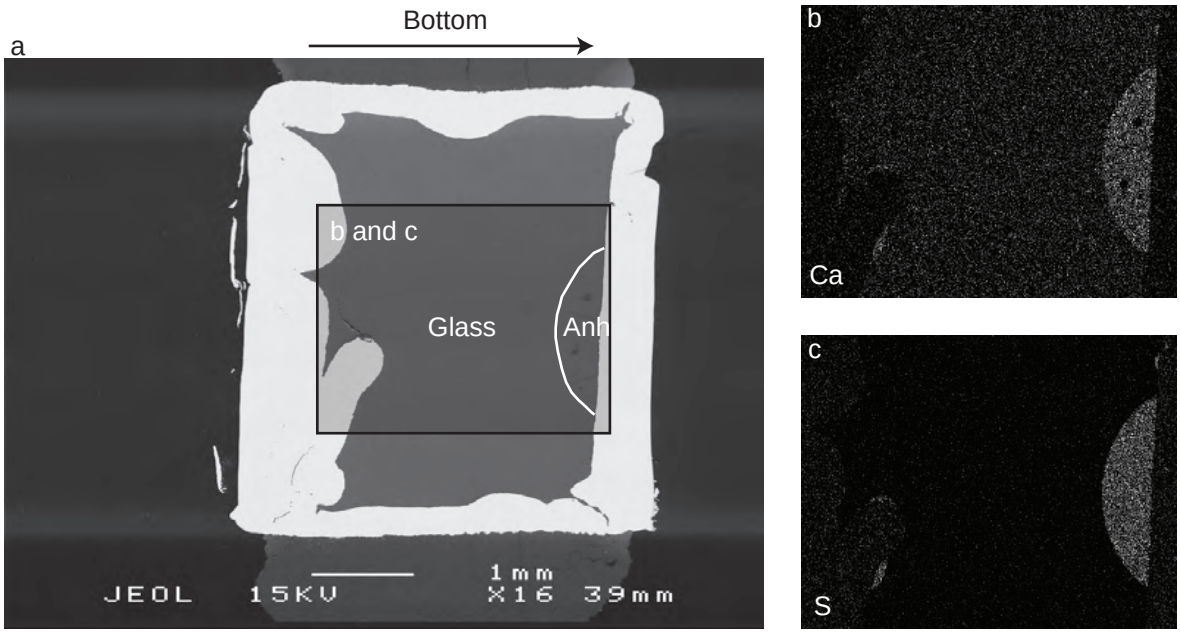

Figure 4.6: Anhydrite in glass. (a) Backscattered electron SEM image (bottom to the right) of an anhydrite saturated oxidised experiment (5% tonalite/95% basalt). Bright white around glass is Pt capsule. (b) and (c) X-ray element maps showing distribution of Ca and S (white speckling), respectively. Note inset in part (a) showing area of (b) and (c).

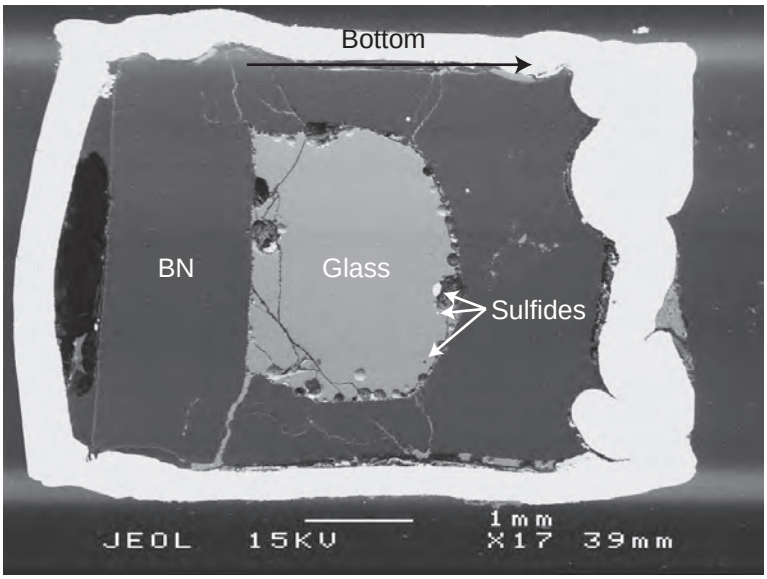

Figure 4.7: Whole capsule backscattered electron SEM image (bottom to the right) of a reduced experiment (50% tonalite/50% basalt). The development of sulfide globules is localised along the capsule wall, with the largest of the globules forming at the recess in the capsule bottom. Most globules were plucked during polishing, but bright-coloured remnants of sulfide material is clearly seen in the images. Note that the globules tend to concentrate at the bottom of the experiment and that the globules very rapidly decrease in size away from the capsule edge. This is thought to reflect settling of the globules to the bottom of the capsule and the relative lack of pervasive dissolution of BN into the glass.

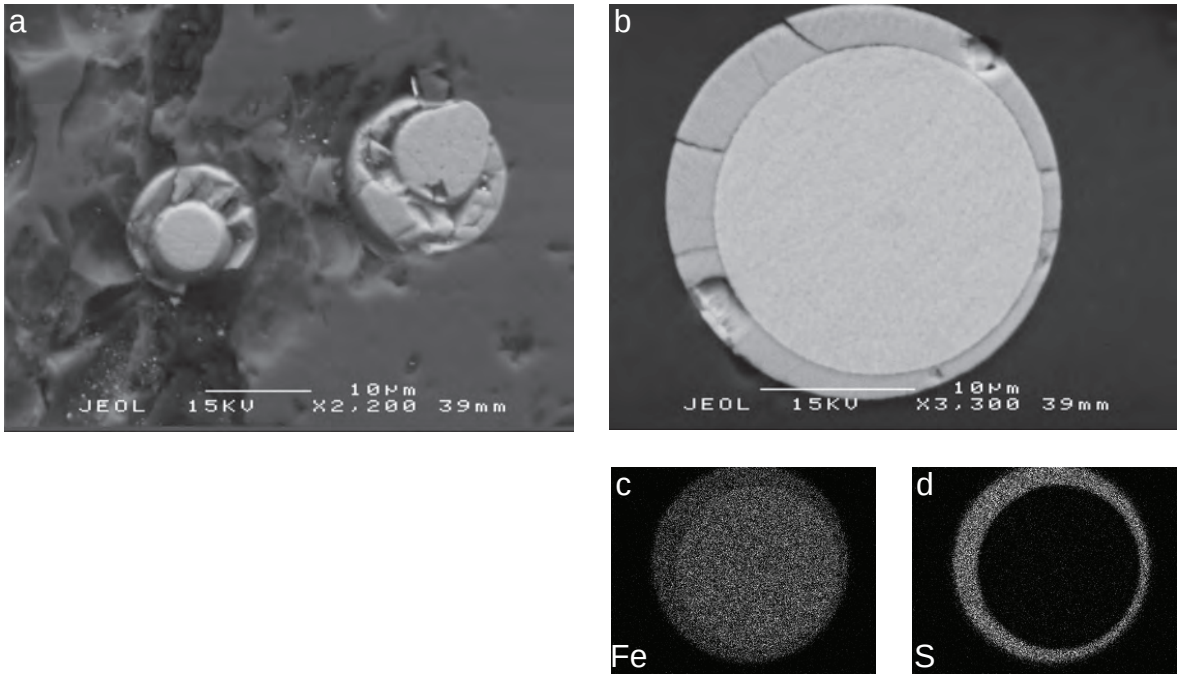

Figure 4.8: (a) Double bubble, two-phase Fe–S melt in reduced experiment (50% tonalite/50% basalt). (b) Second example of double-bubble phase with accompanying x-ray element maps for Fe (c) and S (d) showing a sulfur-rich rim around an almost sulfur-free core (white speckling).

capsule wall. They attributed the native iron formation to the strongly reducing environment created by BN. EDS performed on the immiscible globules formed in this study noted similar Fe-rich compositions, but these are part of a 'double bubble' phase (Fig. 4.8) that is probably related to the inability of sulfide melts to quench to glass as silicates can. The cores of the double bubbles are more Fe-rich (~70-80% Fe) than the rims (~40% Fe and ~30% S), with the rims pyrrhotitic in composition. However, the sulfur content of the experimental glass was consistently low throughout its entire volume. Therefore, the formation of sulfide globules, though concentrated at capsule edges, reflects a loss of sulfur from the whole silicate melt volume, not merely from that directly in contact with the BN. Also, the walls of the BN capsules are observed to be intact. For this reason, BN is not thought to have dissolved significantly into the silicate melt.

Discussion

The sulfur fence

The potential of mixing between reduced felsic melts and oxidised arc basalts to generate extreme sulfide oversaturation, even when the starting magmas may be sulfur-undersaturated, as shown by the results of this study, is a previously unrecognised means of sulfide production in arc settings. Figure 4.5 shows that the sulfur solubility of the melts is somewhat dependent on the bulk composition of the melts, in that the solubility curves decrease with increasing SiO_2, which agrees with the existing literature on sulfur solubility (e.g. Haughton et al., 1974; Li et al., 2001; O'Neill and Mavrogenes, 2002; Naldrett, 2004). However, the resulting change in sulfur solubility is only at the ppm level. From the most mafic to most felsic experiment at reducing conditions, the change in sulfur content of the glass is 1500 ppm. Between

equivalent mixtures of tonalite and basalt, equilibrated under oxidising versus reducing conditions, there is a much larger difference in sulfur content. The most mafic overlapping glasses (5% tonalite/95% basalt) have a 6000 ppm difference in sulfur content and the most felsic overlapping glasses (20% tonalite/80% basalt) a 5800 ppm difference (Table 4.3 and Fig. 4.5). The role that temperature, pressure, and bulk composition play in controlling sulfur solubility are normalised in these experiments by running equivalent mixtures at the same run conditions and using the same bulk endmember powders in preparing the mixtures. Considering that temperature, pressure, equilibration time, and composition are the same in runs with the same mixing proportions, it is argued here that by far the most important parameter controlling the sulfur content of these chemically equivalent, but redox separated glasses, is the redox state of the melt. This redox-controlled sulfur solubility gap is here termed the 'sulfur fence' (Fig. 4.9).

Sulfur oversaturation and the sulfur fence

The sulfur solubility curve of Li and Ripley (2005) shows a rapid, concave upward, decline with increasing contamination (Fig. 4.5). On this curve, Li and Ripley (2005) superimpose binary mixing lines between a sulfur-rich mafic endmember and a sulfur-free felsic endmember, implying that mixing alone can generate sulfur-oversaturation in a magma mixing system. The simple concave-upward shape of their curve implies that the amount of sulfur oversaturation generated through mixing of the endmember magmas is highly dependent on the mafic endmember's starting sulfur content.

In the sulfur fence model proposed here, the sensitivity of sulfur oversaturation to the original amount of sulfur in the mafic endmember is significantly reduced, implying that a wider range of sulfur contents in the unmixed magmas can still generate extensive sulfur oversaturation. In a mixing example in Fig. 4.9 (mixing line A), a sulfur-free felsic magma is mixed with a sulfur-undersaturated oxidised mafic magma; the redox-mediated solubility gap produced at the transition from sulfate to sulfide stability generates very high levels of sulfur oversaturation compared to those possible in the Li and Ripley (2005) model. Consider also that the same boundary conditions as the Li and Ripley (2005) model apply. A minimum sulfur content in the mafic endmember is required such that the mixing line between it and the felsic endmember must cross the sulfur fence (Fig. 4.9, mixing line B). At sulfur contents below this minimum, no oversaturation can be produced through mixing-induced sulfate reduction; however, the range in initial sulfur contents that can result in sulfur oversaturation and the amount of oversaturation that may be generated is greatly increased in the sulfur fence model.

Chalcophile metals undergo compatibility changes depending on silicate magma redox state. Capobianco et al. (1994) found that Rh and Ru behave compatibly and Pd incompatibly with oxide phases under sulfide-absent conditions. Jugo et al. (2005) interprets this to mean that magma generation under oxidising conditions will fractionate Pd from the other PGE.

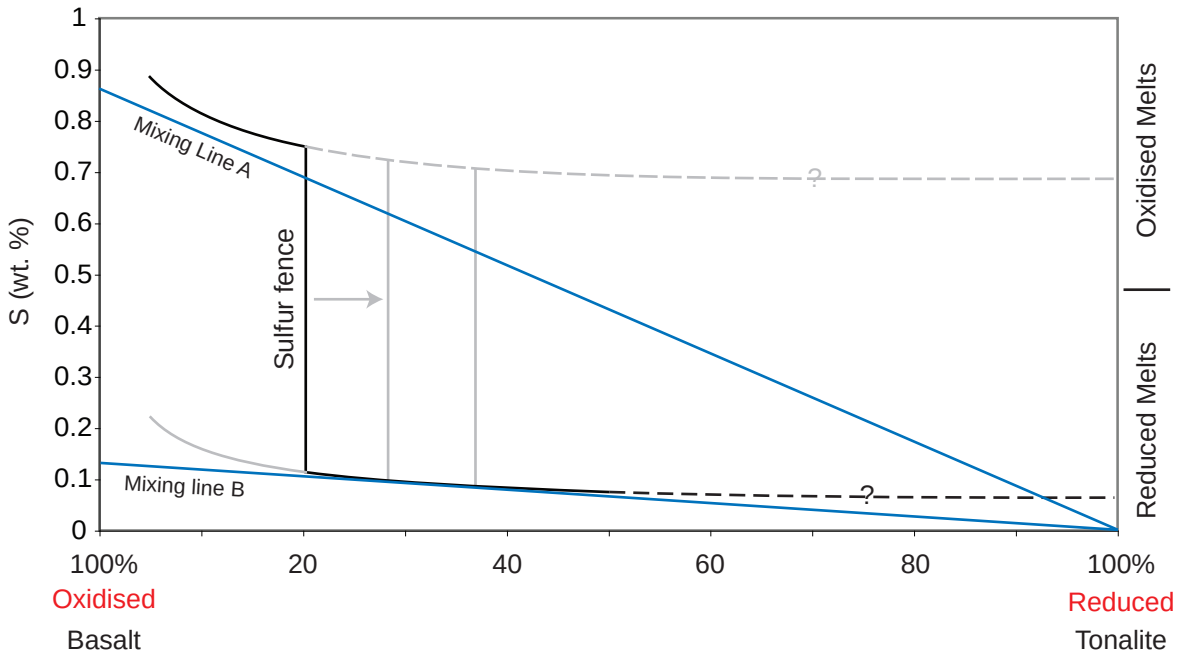

Figure 4.9: The sulfur fence. Curved black lines show the experimental sulfur solubility curve from experiments in this study. Oxidised melts, in which anhydrite is stable, have sulfur solubilities approaching 1 wt. % (top half of figure). Reduced melts, in which sulfide is stable, have sulfur solubilities of ~ 0.1 wt. %. The overlap between oxidised and reduced melts shows that there is an order of magnitude difference in sulfur solubility between melts with the same composition depending on overall redox state. The 'sulfur fence' represents the point at which graphite overcomes the melt's ability to remain oxidised and sulfate stable, becoming reduced and sulfide stable. The mixing line drawn between endmembers shows that a sulfur-undersaturated basaltic melt would experience massive sulfide-oversaturation once the melt goes to the reduced side of the fence.

Copper behaves compatibly over a wide range of sulfide-absent magmatic conditions (e.g. Pollard, 2006). Although it is clear that sulfur is much more soluble in oxidised melts than in reduced melts (see Jugo et al., 2005), there is little published data on the compatibility of sulfur in silicate melts. However, Jugo (2009) showed that low degrees of melting can produce sulfur-rich melts under oxidised conditions.

The greater the amount of fertile silicate magma that is brought within diffusive proximity of sulfide liquids, the greater the amount of metals that may be sequestered into the sulfide phase (the R-factor). The sulfide-silicate partition coefficients of some chalcophile metals such as Ni, Cu, and Au is typically 10^3 to 10^4; those of the platinum group elements, for example Pd, Ir, and Pt, exceed 10^3 and range up to 3.4×10^4 or higher (see Chapter 3 and references therein). Therefore, the development of sulfide melt at anytime in the evolution of a magmatic system will greatly affect its future metallogenic development. The metal-rich sulfide phase will essentially control the metal budget of the system and its physical loss will remove any ore potential from that magma.

The growth of individual sulfide globules is governed by the interplay between the absolute amount of sulfur in the system and the number density of sulfide globules, such that widely spaced globules in sulfur-rich magma will grow to reach larger sizes than more closely spaced globules. This is because closely spaced, high number-density globules will quickly develop sulfur diffusion haloes that interact with, and therefore compete with, their neighbours for

a finite supply of sulfur (see Mungall, 2002a). Since chalcophile metal sequestration relies principally on the R factor of individual sulfide globules and not on their size, it follows that the greater their number density, the greater the amount of metal that collectively becomes concentrated in the sulfide phase (although the metal tenor of the accumulated sulfide may be lower). The smaller average size of sulfide globules in magmas with pervasive sulfide globule nucleation will encourage their retention in migrating silicate magma phases because of their lower settling velocities (see Chapter 5). This has been implicated in the formation of important deposits such as Voisey's Bay in Newfoundland, Canada (Mungall, 2002a). Therefore, the solubility gap between sulfides and anhydrite, controlled by the melt fO_2 state and represented by the sulfur fence, is an important process in the generation of sulfur oversaturation and the development of metal-rich sulfide melts. Furthermore, the sulfur fence model provides a process by which mixing magmas with large ranges in sulfur content may still produce hybrids in which high levels of sulfur oversaturation can develop.

Positioning the fence: mass balance of graphite-driven sulfate reduction

The position of the sulfur fence is mobile and will depend both on the amount of graphite and the amount of sulfate that is present in the mixing magmas (at some proportion, the CCO buffer needs to overwhelm the SSO buffer during mixing). In an attempt to characterise the mass balance of graphite reduction of anhydrite, the following reaction was developed from the SSO buffer equation of Mungall (2002b):

$$CaSO_{4(Anh)} + 2C_{Gr} + 2FeSiO_{3(Opx)} = FeS_{(liq)} + CaFeSi_2O_{6(Cpx)} + 2CO_{2(fluid)} \quad (1)$$

From this equation, it is clear that two moles of graphite is required to reduce one mole of anhydrite to one mole of sulfide liquid in the presence of excess orthopyroxene. So, for example, assume a basaltic magma with 2% anhydrite mixes with a graphitic tonalite in the proportions 75% basalt and 25% tonalite, which is reasonable based on the estimates in Chapter 3. Working a simple example with molar weights and assuming a unit weight of 100 g, the calculation is as follows:

$$75\%\ \text{basalt} + 25\%\ \text{tonalite} \equiv 100\,\text{g} = 75\,\text{g basalt} + 25\,\text{g tonalite}$$

$$m_{Anh} = 75\,\text{g basalt} * 2\%\ \text{Anh} = 1.5\,\text{g}$$

$$n_{Anh} = \frac{m_{Anh}}{136.1396\,\text{g/mol}} = 0.0109$$

According to equation (1), two moles of graphite are required to reduce each mole of anhydrite, so:

$$n_{Gr} = 2 * n_{Anh} = 0.0218$$

Converting back into unit mass:

$$m_{Gr} = n_{Gr} * 12.0110\,g/mol = 0.2611\,g$$

$$\%_{Gr} = \frac{m_{Gr}}{25g_{tonalite}} * 100 \approx 1.0$$

In this case, the tonalite must have ~1% graphite to buffer the system at CCO, producing one mol of sulfide liquid. In a mixing environment, there will be natural variability in the amount of graphite present in the tonalite. Therefore, the proportion of tonalite required to cause sulfide saturation will also vary. Assuming that the total carbon of the natural tonalite sample used in the experiments (Table 4.2) is largely graphite, the required proportion of graphite is slightly higher than the amount present in samples used here. However, this amount of graphite is possible in natural rocks (e.g. Stein, 1990); therefore, these estimates are within the realm of compositions present in arc settings.

Epilogue: experimental failures with natural powders in Pt

The original goal of this study was to use the graphite content of the tonalite to internally buffer the oxygen fugacity of the mixing experiments. However, since the volumes of material used in piston cylinder experiments are so small, that control must be imposed on the system externally, which was done by using BN as a capsule material (for discussion on the oxygen fugacity control exerted by BN, see Wendlandt and Huebner, 1982). It is unfortunate that there is not yet a capsule material that is both suitably fO_2-neutral and unreactive to sulfide and silicate melts to use in sulfide exsolution experiments. However, it is worth noting that in determining the final run of experiments, several were attempted only in Pt with highly mixed powders (50% tonalite/50% basalt). These experiments invariably failed three to five hours into their runs. Most of these failures were due to capsule ruptures that could have resulted from abrasion and thinning of the capsule sidewalls during preparation. However, upon closer inspection of the last of these capsules, a rupture was found on its bottom, away from welds, and in a position free from any mechanical defect or thinning. This observation suggests that sulfide melt may have corroded the Pt capsule. In this case, it appears that the graphite content of the natural tonalite is indeed capable of buffering the mixtures from anhydrite-stable to sulfide-stable.

Other factors affecting sulfur solubility

As discussed above, temperature, pressure, SiO_2 content, and especially Fe^{2+} content are among the most well characterised parameters that affect the ability of a silicate melt to dissolve sulfur (Haughton et al., 1974; Li et al., 2001; O'Neill and Mavrogenes, 2002; Naldrett, 2004). In this study, temperature, pressure, SiO_2 content and Fe^{2+} content are normalised by running

the reduced/oxidised overlapping experiments with the same experimental run conditions and the same powder preparations. The low Fe content in the glasses of the reduced experiments (Table 4.4) can be explained by the presence of the Fe–S double-bubble globules in those capsules. The Fe is not lost from the system, but is concentrated in the immiscible liquid.

Establishing the redox state

The oxygen fugacity environment surrounding the capsule was not rigidly controlled in these experiments, but that level of control was not required. In the oxidising, anhydrite-stable, experiments, the presence of hematite next to the capsule and the excess anhydrite present in the experimental powder is enough to establish an oxygen fugacity at or above the SSO buffer, as evidenced by the presence of $CaSO_4$ in the experimental run product (Fig. 4.6). Hematite, at the temperatures of these experiments, is likely to have been a source of oxygen and there are suggestions that Pt is somewhat permeable to oxygen at the run temperatures in this study (Hugh O'Neill, pers. comm.). In the reducing, sulfide-stable experiments, the evidence from Wendlandt and Huebner (1982) clearly establishes that BN is highly reducing. The presence of Fe–S liquids at the glass-capsule contact confirms that these experiments were reduced.

Ore deposition in arcs

This study shows that the magma redox step from oxidised anhydrite- (or sulfate-) stable to reduced sulfide-stable conditions, produced by mixing mantle wedge-derived melts with graphite-rich felsic partial melts, is an important process capable of generating large degrees of sulfide oversaturation at the base of some arcs. The source of graphite in arcs is likely related to sediment accumulation at the nearby trench caused by the development of an accretionary wedge. Oceanic sediments have the potential to be highly enriched in organic carbon (see Emerson and Hedges, 1988), which will become graphite during metamorphism. Gabbroic complexes and migmatites in southeastern Hokkaido (e.g. the OGC and surrounds) clearly involve above-average accumulations of graphite (this study; Shibata et al., 1991; Tsuchiya et al., 1991). The apparent lack of major porphyry Cu ore deposits in the modern Japan-Kuril Arc may be related to this surfeit of carbon at depth. The assimilation of abundant carbon would favour the development of pervasive sulfide nucleation, which in turn favours efficient removal of chalcophile metals from the mixing magmas.

Sulfides at depth in graphitic terranes

The presence of massive and disseminated sulfides at depth is a key feature of the OGC (Chapters 2 and 3). In light of the sulfur fence model proposed in this study and the highly graphitic nature of the Nakanogawa Group, into which the OGC has intruded, it is suggested that the abundant graphite present in and around the OGC contributed to the development of these sulfides. It is also significant that no sulfide-related ore deposits occur in the near-

surface portion of the arc section. This implies that the development and the accumulation of massive to disseminated sulfides at depth inhibited the development of porphyry style mineralisation in the upper crust of the northern Japan Arc.

Although the mantle wedge underlying arcs is oxidised relative to normal oceanic mantle (Parkinson and Arculus, 1999), many arc magmas are still within the sulfide stability field in fO_2 space (typically up to FMQ + 2; see Carroll and Rutherford, 1987; Mungall, 2002b). Sulfate is also stable at $fO_2 \geq$ FMQ + 2 (Carroll and Rutherford, 1987) and the occurrence of anhydrite in recent eruptions at El Chichon (Carroll and Rutherford, 1987) and Mount Pinatubo (Pallister et al., 1996) show that sulfate-stable magma oxidation states are likely to be common in the upper crust of arcs.

Oxidised, chloride-rich mineralising brine fluids are widely accepted as playing a fundamental role in the development of porphyry Cu deposits. Burnham and Ohmoto (1980), for example, found that porphyry mineralising fluids ranged between the NNO and hematite-magnetite fO_2 buffers. In oxidised deposits, these fluids scavenge Cu, Mo, and Au from a large intrusion, subsequently circulate through an overlying fracture stockwork, and finally precipitate these metals as sulfide veins and disseminations in the stockwork (see Lowell and Guilbert, 1970). These processes were synthesised in the seminal description of the San Manuel-Kalamazoo deposit by Lowell and Guilbert (1970), which remains the type description of most porphyry Cu deposits around the world.

Rowins (2000) recently recognised a new class of reduced porphyry Cu deposits that involve mineralising fluids with $fO_2 <$ FMQ, well below the stability field of anhydrite. In deposits of this type, Cu and Au are fractionated from each other by the decreased solubility of Cu relative to Au in reduced fluids. Moreover, these metals are transported in a highly mobile, low density H_2S vapour phase rather than in the chloride brines assumed in typical, oxidised porphyry Cu mineralising systems (Rowins, 2000). The resulting signature of reduced porphyry Cu deposits is lower Cu and higher Au than their oxidised counterparts, and distal mineralisation from their causative porphyry intrusion. Since the generation of sulfide melt (Fe–S in this study) requires Fe, it may also be possible to see the effect of sulfide exsolution in reduced porphyry Cu systems as high silicate MgO/FeO* ratios. This is supported by the data (Table 4.4).

Does graphite play an important role in some porphyries?

The fundamental nature of sulfide nucleation when initiated by high levels of sulfur oversaturation, such as that generated in the (graphite-forced) sulfur fence model, is the formation of a high number density of sulfide globules. If pervasive throughout the hybridising magma, this in turn encourages scavenging of metals throughout the magma volume. Therefore, the development of MASH zones in the roots of arcs may play an integral role in

ore development primarily by generating felsic partial melts of graphitic accretionary wedge sediments and encouraging mixing of these melts with sulfur-rich oxidised mafic melts.

The exceptional association of porphyry deposits with arcs may be related in some instances to the reduction, by graphitic partial melts, of uncommonly sulfur-rich, oxidised basaltic melt (cf. Mungall, 2002b). However , sulfides produced in this way must then be prevented from settling out. Porphyry deposits in which this occurs are in addition to those interpreted to occur via the existing model where sulfide-saturation must be avoided to prevent metal depletion. The current porphyry Cu literature holds that the development of magmatic sulfide melts, before final emplacement depth, destroys ore potential (e.g. Mungall, 2002b). This study does not refute this; it is consistent with the existing model. Reduction from sulfate stability to sulfide stability will not occur if a graphitic felsic magma does not contain enough reductant to overcome the oxidised state of the magma it mixes with; therefore, in such cases, the oxidised porphyry model applies. Instead, in light of the findings in this study, a new model allowing certain, sulfide globule-bearing, magmas to participate in porphyry deposit genesis is presented next in Chapter 5. This new model describes dynamic magmatic conditions under which sulfide melt globules may be retained within ascending magmas. If sulfides remain entrained within these magmas (cf. the OGC or other gabbroic complexes), the development of major ore deposits in the upper crust may result. The accumulation of sulfides in the OGC implies that such entrainment did not occur at this locality.

Arc age and ore formation

Since a certain amount of graphite is required to overcome the oxidised sulfur-carrier species in a melt (equation 1 above), arcs in which significant accretionary wedges have accumulated may more commonly produce sulfide oversaturation via the sulfur fence model. Arcs with lower volumes of graphite-rich wedge material may not have the necessary reductant present to achieve a fully reduced, mixed melt. It is suggested that old arcs, given time to develop a thick accretionary wedge, or young arcs with above average sedimentary input to their trenches, are necessary for the sulfur fence mechanism to operate. Conversely, simple and young island arcs, containing little graphitic material or with small accretionary wedges, are unlikely to be settings where the sulfur fence model is relevant.

Porphyry Cu and magmatic Ni-Cu deposits: endmembers of the same system?

The study of magma mixing in MASH zones at the base of arcs may be a window on a new concept in porphyry Cu and magmatic Ni-Cu deposits. Both in arcs, these hitherto disparate deposit types could theoretically represent endmembers of the same ore system: one endmember where sulfides were extracted at depth (to form magmatic Ni-Cu deposits), and one endmember where sulfides either did not form or were retained, allowing formation of porphyry-Cu deposits in the upper crust. The key consideration in later producing a

porphyry-related ore-forming system is then a question of sulfide and metal retention, which is explored next in Chapter 5.

Conclusions

The experimental study of the sulfur content of mixtures of sulfate-saturated mafic melts with graphitic tonalite found the presence of a significant sulfur solubility gap between oxidised and reduced melts. This solubility gap is termed the sulfur fence and is a window on a new process responsible for generating sulfur oversaturation in mixing magmas, particularly applied to MASH zones in the roots of arcs.

Graphite is an ubiquitous reducing mineral species in accretionary wedge sediments, which are commonly associated with arc sequences. Graphite assimilation through mixing of anatectic accretionary wedge melts with sulfate-stable mafic melts in MASH zones can be expected to produce a hybrid melt in which sulfide is stable. The mass balance of a representative reduction reaction of anhydrite by graphite shows that one weight percent graphite is capable of reducing up to a few weight percent anhydrite in a mixture containing similar proportions of mafic and felsic magmas as interpreted for the sulfide-bearing gabbros of the OGC.

Applied to MASH zones, the sulfur fence may be an important process that allows large amounts of sulfur oversaturation to develop. Highly sulfur oversaturated melts produce immiscible sulfide globules pervasively and with high number density throughout the oversaturated part of the melt. High number density globules are expected to produce a metal-enriched sulfide melt. The metallogeny of such efficiently metal-depleted silicate melt is then controlled by the retention, or lack thereof, of the sulfide phase, a concept which is explored in Chapter 5.

References

Akella J., Vaidya S. N. and Kennedy G. C. (1969) Melting of Sodium Chloride at Pressures to 65 kbar. *Physical Review* **185**(3), 1135.

Boettcher A. L., Windom K. E., Bohlen S. R. and Luth R. W. (1981) Low-friction, anhydrous, low- to high-temperature furnace sample assembly for piston-cylinder apparatus. *Review of Scientific Instruments* **52**(12), 1903-1904.

Bohlen S. R. (1984) Equilibria for precise pressure calibration and a frictionless furnace assembly for the piston-cylinder apparatus. *Neues Jahrbuch fur Mineralogie-Monatshefte*(9), 404-412.

Boyd F. R. and England J. L. (1960) Apparatus for phase-equilibrium measurements at pressures up to 50 kilobars and temperatures up to 1750°C. *Journal of Geophysical Research* **65**(2), 741-748.

Brown D. and Spadea P. (1999) Processes of forearc and accretionary complex formation during arc-continent collision in the southern Ural Mountains. *Geology* **27**(7), 649-652.

Burnham C. W. and Ohmoto H. (1980) Late-stage processes of felsic magmatism. *Kozan Chishitsu = Mining Geology*(8), 1-11.

Campbell I. H. and Naldrett A. J. (1979) The influence of silicate:sulfide ratios on the geochemistry of magmatic sulfides. *Economic Geology* **74**(6), 1503-1506.

Capobianco C. J., Hervig R. L. and Drake M. J. (1994) Experiments on crystal/liquid partitioning of Ru, Rh and Pd for magnetite and hematite solid solutions crystallized from silicate melt. *Chemical Geology* **113**(1-2), 23-43.

Carroll M. R. and Rutherford M. J. (1987) The stability of igneous anhydrite: experimental results and implications for sulfur behavior in the 1982 El Chichon trachyandesite and other evolved magmas. *Journal of Petrology* **28**(5), 781-801.

Cohen L. H., Klement W. and Kennedy G. C. (1966) Melting of Copper, Silver, and Gold at High Pressures. *Physical Review* **145**(2), 519.

Defant M. J. and Drummond M. S. (1990) Derivation of some modern arc magmas by melting of young subducted lithosphere. *Nature* **347**(6294), 662-665.

Emerson S. and Hedges J. I. (1988) Processes controlling the organic carbon content of open ocean sediments. *Paleoceanography* **3**(5), 621-634.

Frost B. R. (1991) Introduction to oxygen fugacity and its petrologic importance. *Reviews in Mineralogy and Geochemistry* **25**(1), 1-9.

Ghiorso M. S. and Sack R. O. (1995) Chemical mass transfer in magmatic processes IV. A revised and internally consistent thermodynamic model for the interpolation and extrapolation of liquid-solid equilibria in magmatic systems at elevated temperatures and pressures. *Contributions to Mineralogy and Petrology* **119**(2), 197-212.

Goldschmidt V. M. (1937) The principles of distribution of chemical elements in minerals and rocks. *Journal of the Chemical Society*, 655-673.

Halter W. E., Heinrich C. A. and Pettke T. (2004) Laser-ablation ICP-MS analysis of silicate and sulfide melt inclusions in an andesitic complex II: evidence for magma mixing and magma chamber evolution. *Contributions to Mineralogy and Petrology* **147**(4), 397-412.

Halter W. E., Heinrich C. A. and Pettke T. (2005) Magma evolution and the formation of porphyry Cu-Au ore fluids: evidence from silicate and sulfide melt inclusions. *Mineralium Deposita* **39**(8), 845-863.

Halter W. E., Pettke T. and Heinrich C. A. (2002) The Origin of Cu/Au Ratios in Porphyry-Type Ore Deposits. *Science* **296**(5574), 1844-1846.

Haughton D. R., Roeder P. L. and Skinner B. J. (1974) Solubility of Sulfur in Mafic Magmas. *Economic Geology* **69**(4), 451-467.

Holloway J. R. and Wood B. J. (1988) *Simulating the Earth: Experimental Geochemistry*. HarperCollins Academic, London, UK. pp. 196.

Jarosewich E., Nelen J. A. and Norberg J. A. (1979) Electron microprobe reference samples for mineral analysis. *Smithsonian Contributions to Earth Sciences* **20**, 68-72.

Johannes W. (1978) Pressure comparing experiments with NaCl, AgCl, talc and pyrophyllite assemblies in a piston cylinder apparatus. *Neues Jahrbuch Fur Mineralogie-Monatshefte*(2), 84-92.

Jugo P. J. (2009) Sulfur content at sulfide saturation in oxidized magmas. *Geology* **37**(5), 415-418.

Jugo P. J., Luth R. W. and Richards J. P. (2005) An experimental study of the sulfur content in basaltic melts saturated with immiscible sulfide or sulfate liquids at 1300°C and 1.0 GPa. *Journal of Petrology* **46**(4), 783-798.

Keays R. R. (1995) The role of komatiitic and picritic magmatism and S-saturation in the formation of ore deposits. *Lithos* **34**(1-3), 1-18.

Keays R. R. and Davison R. M. (1976) Palladium, iridium, and gold in the ores and host rocks of nickel sulfide deposits in Western Australia. *Economic Geology* **71**(7), 1214-1228.

Keays R. R. and Lightfoot P. C. (2007) Siderophile and chalcophile metal variations in Tertiary picrites and basalts from West Greenland with implications for the sulphide saturation history of continental flood basalt magmas. *Mineralium Deposita* **42**(4), 319-336.

Kress V. (1997) Magma mixing as a source for Pinatubo sulphur. *Nature* **389**(6651), 591-593.

Li C., Maier W. D. and de Waal S. A. (2001) The role of magma mixing in the genesis of PGE mineralization of the Bushveld Complex; thermodynamic calculation and new interpretations. *Economic Geology* **96**(3), 653-662.

Li C. and Naldrett A. J. (1993) Sulfide capacity of magma: a quantitative model and its application to the formation of sulfide ores at Sudbury, Ontario. *Economic Geology* **88**(5), 1253-1260.

Li C. and Ripley E. M. (2005) Empirical equations to predict the sulfur content of mafic magmas at sulfide saturation and applications to magmatic sulfide deposits. *Mineralium Deposita* **40**, 218-230.

Liu Y., Samaha N.-T. and Baker D. R. (2007) Sulfur concentration at sulfide saturation (SCSS) in magmatic silicate melts. *Geochimica et Cosmochimica Acta* **71**(7), 1783-1799.

Lowell J. D. and Guilbert J. M. (1970) Lateral and vertical alteration-mineralization zoning in porphyry ore deposits. *Economic Geology* **65**(4), 373-408.

MacLean W. H. (1969) Liquidus phase relations in the FeS-FeO-Fe 3 O 4 -SiO 2 system, and their application in geology. *Economic Geology* **64**(8), 865-884.

Molnar P. and England P. (1995) Temperatures in zones of steady-state underthrusting of young oceanic lithosphere. *Earth and Planetary Science Letters* **131**(1-2), 57-70.

Moore J. C., Watkins J. S., Shipley T. H., McMillen K. J., Bachman S. B. and Lundberg N. (1982) Geology and tectonic evolution of a juvenile accretionary terrane along a truncated convergent margin: Synthesis of results from Leg 66 of the Deep Sea Drilling Project, southern Mexico. *Geological Society of America Bulletin* **93**(9), 847-861.

Mungall J. E. (2002a) Kinetic controls on the partitioning of trace elements between silicate and sulfide liquids. *Journal of Petrology* **43**(5), 749-768.

Mungall J. E. (2002b) Roasting the mantle: Slab melting and the genesis of major Au and Au-rich Cu deposits. *Geology* **30**(10), 915-918.

Naldrett A. J. (1992) A Model for the Ni-Cu-PGE Ores of the Noril'sk Region and Its Application to Other Areas of Flood Basalt. *Economic Geology* **87**(8), 1945-1962.

Naldrett A. J. (2004) *Magmatic Sulfide Deposits: Geology, Geochemistry, and Exploration*. Springer, Berlin. pp. 727.

Nanayama F., Kanamatsu T. and Fujiwara Y. (1993) Sedimentary petrology and paleotectonic analysis of the arc--arc junction: the Paleocene Nakanogawa Group in the Hidaka Belt, central Hokkaido, Japan. *Palaeogeography, Palaeoclimatology, Palaeoecology* **105**(1-2), 53-69.

O'Neill H. S. C. and Mavrogenes J. A. (2002) The sulfide capacity and the sulfur content at sulfide saturation of silicate melts at 1400°C and 1 bar. *Journal of Petrology* **43**(6), 1049-1087.

Pallister J. S., Hoblitt R. P., Meeker G. P., Knight R. J. and Siems D. F. (1996) Magma mixing at Mount Pinatubo: Petrographic and chemical evidence from the 1991 deposits. In *Fire and mud: Eruptions and lahars of Mount Pinatubo, Philippines* (eds. C. G. Newhall and R. S. Punongbayan), pp. 687-731. University of Washington Press, United States, Quezon City, Philippines.

Parkinson I. J. and Arculus R. J. (1999) The redox state of subduction zones: insights from arc-peridotites. *Chemical Geology* **160**(4), 409-423.

Pattison D. R. M. (2006) The fate of graphite in prograde metamorphism of pelites: An example from the Ballachulish aureole, Scotland. *Lithos* **88**(1-4), 85-99.

Peach C. L., Mathez E. A. and Keays R. R. (1990) Sulfide melt-silicate melt distribution coefficients for noble metals and other chalcophile elements as deduced from MORB: Implications for partial melting. *Geochimica et Cosmochimica Acta* **54**(12), 3379-3389.

Pollard P. (2006) An intrusion-related origin for Cu–Au mineralization in iron oxide–copper–gold (IOCG) provinces. *Mineralium Deposita* **41**(2), 179-187.

Richards J. P. (2003) Tectono-magmatic precursors for porphyry Cu-(Mo-Au) deposit formation. *Economic Geology* **98**(8), 1515-1533.

Rowins S. M. (2000) Reduced porphyry copper-gold deposits: A new variation on an old theme. *Geology* **28**(6), 491-494.

Shibata Y., Matsueda H. and Yui S. (1991) Texture and mineral paragenesis of orbicular graphite from Oshirabetsu, Hokkaido. *Mining Geology* **41**, 185.

Singer D. A., Berger V. I. and Moring B. C. (2005) Porphyry copper deposits of the world: database, map, and grade and tonnage models. United States Geological Survey.

Stavast W. J. A., Keith J. D., Christiansen E. H., Dorais M. J., Tingey D., Larocque A. and Evans N. (2006) The fate of magmatic sulfides during intrusion or eruption, Bingham and Tintic districts, Utah. *Economic Geology* **101**(2), 329-345.

Stein R. (1990) Organic carbon content/sedimentation rate relationship and its paleoenvironmental significance for marine sediments. *Geo-Marine Letters* **10**(1), 37-44.

Tsuchiya N., Suzuki S. and Chida T. (1991) Origin of graphite in the Oshirabetsu gabbroic body, Hokkaido, Japan. *Journal of Mineralogy, Petrology and Economic Geology* **86**(6), 264-272.

Wagner P. A. (1929) *The platinum deposits and mines of South Africa*. Oliver and Boyd, London. pp. 338.

Wendlandt R. F. and Huebner J. S. (1982) The redox potential of boron nitride and implications for its use as a crucible material in experimental petrology. *American Mineralogist* **67**(1, 2), 170-174.

Chapter 5: Magma chamber dynamics – sulfide melt formation and settling behaviour

Introduction

Previous chapters have discussed evidence for, and geochemical implications of, magma mixing in the Opirarukaomappu Gabbroic Complex (OGC) of southeastern Hokkaido, Japan. It was found that magma mixing likely played a critical role in the generation of metal-enriched sulfide melts in this region of the lower to middle arc crust. The next significant problem to address in understanding arc metallogeny is whether the metal enrichment and depletion processes resulting from sulfide saturation in the lower to middle crust can lead to formation of porphyry Cu mineralisation in the upper crust. Or, does deep sulfide melt formation always strip metals from silicate magmas, precluding porphyry-style mineralisation from developing? These processes may also be relevant to the generation of ores formed in association with felsic magmas developed away from arc settings, such as iron oxide copper-gold (IOCG) and intrusion related gold systems (IRGS), in that these magmas may also experience a stage of deep crustal magma mixing. It is argued in this chapter that entrainment of, or conversely, settling out of dense, metal-rich sulfide liquids is a controlling factor that may significantly influence the ore potential of magmas escaping from MASH zones (see Chapter 3).

This chapter firstly develops the conceptual framework to understand the importance of sulfide settling in the development of metal-rich silicate magmas. A mathematical model incorporating some of the newest melt viscosity equations is then developed to examine sulfide settling in silicate melts. The settling of sulfides through various magma mixtures is determined using bulk magma chemistry modelling by the MELTS software package (rev 1.8, Ghiorso and Sack, 1995), the viscosity calculation model of Giordano (2008), and the Hadamard-Rybczynski equation (Hadamard, 1911; Rybczynski, 1911). With this approach, I show that the settling velocities of sulfide globules with radii $\leq$ 1 cm in magmas that are $<$ 20% crystallised are exceeded by magma convection and escape velocities within the composition range representative of sulfide-bearing OGC (MASH) magmas. Progressively larger globule sizes are entrainable in magmas from which more crystallisation has occurred. Therefore, magmas escaping from a convecting magma chamber with globules $<$ 1 cm typically retain sulfides during their escape and for at least part of their journey to the near surface. Confinement and channelisation of migrating magmas are important constraints on the continuing suspension of sulfide phases once silicate magmas have left a magma chamber. This will be considered in the context of the Voisey's Bay deposit in Newfoundland, Canada.

Prologue: MELTS and model limitations

A few simplifications were made in the construction of the MELTS model (Ghiorso and Sack, 1995) and settling behaviour used for this chapter, which should be made clear before proceeding. Documentation provided with the MELTS software clearly states that phase relations are most highly calibrated at low pressures ($P < 2.0$ GPa) and MORB and alkaline mafic magma compositions. Modelling of more evolved systems is not recommended due to inaccuracies in phase equilibria of hornblende and biotite (Ghiorso and Sack, 1995). Modelling in this study is done at 0.8 GPa; intermediate and silica-rich compositions are also considered in this discussion and represented in figures. It is important to note that the most silica rich compositions may not be modelled as reliably as the most mafic ones. However, it will be shown that the most critical phase in sulfide production is in more mafic mixtures. Therefore, these are the most important parts of the model and Ghiorso and Sack (1995) indicate that MELTS is most reliable at these compositions.

Upon reaching highly evolved compositions, most of the sulfide history of the system, as well as any significant migration, will have already occurred. As the most sulfide-rich compositions in the OGC are relatively mafic ($SiO_2 \approx 53\%$), the settling behaviour during this most critical composition is likely accurate. Probably the most significant simplification is in determining the escape/migration velocities of mafic magmas and tonalites. Since the viscosity of a cooling and crystallising magma increases exponentially (refer to the Arrhenius equation and McBirney and Murase, 1984, respectively), and since magma migration velocity is inversely proportional to magma viscosity, an exponential decrease in migration velocity is assumed to be the case from 10^{-1} m/s in mafic melts (Klügel, 1998) to 10^{-9} m/s in felsic melts (Watt et al., 1996).

Sulfide Settling

Sulfide melts partition chalcophile metals (e.g. Goldschmidt, 1937; Peach et al., 1990). Therefore, a silicate melt will be depleted in these metals if sulfide melt exsolves and segregates from it. Retention of metal-rich sulfide melt in migrating silicate magmas, or even enrichment of sulfide in an escaping batch of magma, enhances the probability that magma evolution later leads to formation of an ore deposit. Whether or not sulfides remain in suspension depends principally on the settling velocity of sulfide globules through the silicate magma. These are calculated using settling equations based on Stokes' Law.

Hadamard (1911) and Rybczynski (1911) extended Stokes' Law of settling, which describes the settling of solid spheres through Newtonian fluids, to the settling of viscous spheres through Newtonian fluids with the Hadamard-Rybczynski Equation (see Weinberg and Podladchikov, 1994):

$$V = \frac{1}{3}\frac{\Delta\rho g r^2}{\mu_m}\left(\frac{\mu_m + \mu_{slf}}{\mu_m + \frac{3}{2}\mu_{slf}}\right) \quad (1),$$

where V is the settling velocity of sulfide globules (m s^{-1}), $\Delta\rho$ is the density difference between silicate melt and sulfide globule (kg m^{-3}), g is the value of gravitational acceleration (9.81 m s^{-2}), r is the radius of the sulfide globule (m), μ_m is the viscosity of the ambient magma, and μ_{slf} is the viscosity of the sulfide globule. Sulfide melts are typically very low viscosity (10^{-2} to 10^{-3} Pa s, see Dobson et al., 2000) and silicate liquidus viscosity ranges from 10^2 to 10^{12} Pa s (e.g. Marsh, 1981; Wickham, 1987). Sulfide liquids can therefore be assumed to be inviscid (i.e. $\mu_{slf} = 0$). In this case, equation (1) reduces simply to:

$$V = \frac{1}{3}\frac{\Delta\rho g r^2}{\mu_m} \qquad (2).$$

Newtonian versus non-Newtonian behaviour of magmas

Addressing Newtonian versus non-Newtonian behaviour of silicate magmas is critical in discussing sulfide settling. It must first be made clear that in this chapter, the term 'melt' refers to only the liquid portion of a magma. 'Magma' refers to melt + crystals. Crystallising silicate magmas are Newtonian fluids until suspended crystals form a touching network throughout the magma (Kerr and Lister, 1991; Saar et al., 2001; Walsh and Saar, 2008). Once a network is formed, the magma is non-Newtonian, but the behaviour of the interstitial melt is still Newtonian and this controls the settling of sulfide globules. The critical crystallinity at which the transition from Newtonian to non-Newtonian magma behaviour occurs depends on the total shear stress exerted on the magma and on crystal size, crystal shape, and crystal orientation distribution (Bottinga, 1994; Saar et al., 2001). Marsh (1981) determined this value to be between 50–60% crystallinity.

Magma composition has a strong control on viscosity; however, there is little evidence that crystal-free magmas have yield strength (e.g. McBirney and Murase, 1984), so bulk composition should not affect the Newtonian to non-Newtonian transition in super-liquidus magmas. At this point, the distinction between magma rheology (i.e. that of the melt + crystals) and melt rheology (i.e. that around a single sulfide globule) is important. It is here argued that the melt domain immediately surrounding a single sulfide globule is still Newtonian well past the transition at which the magma becomes non-Newtonian. In this case, sulfides continue to settle as long as there is a permeable path. On this small scale, and with a touching crystal network present, the rheology of the melt domains immediately surrounding sulfide globules controls settling; magma rheology does not. However, crystallinity does affect the settling rate of sulfide globules by increasing the tortuosity of the flow paths along which they move. It is likely that the low viscosity of sulfide melts allows them to percolate along and between the solid phases in a crystal mush. Therefore, further settling beyond magma lock-up is possible; however, the resulting settling velocity would be slower than that predicted by the Hadamard-Rybczynski equation. It is difficult to predict the actual value in this case because it depends on the complexities of the permeability network. For simplicity, melts in this study are taken to be always Newtonian and the settling paths of sulfide globules are taken to be

largely free of crystals. Therefore, the Hadamard-Rybczynski equation is broadly applicable and some downward settling through the magma occurs regardless of globule size.

The larger the density difference between the sulfide and silicate phases, the faster the settling velocity. Typical basaltic magmas have maximum densities of less than 2800 kg/m^3, whereas sulfide melts range in density between 4000 and 5500 kg/m^3 (Mungall and Su, 2005). The gravitational settling of sulfide melts with sequestered Cu, Ni, and PGE would need to be counteracted to avoid the stripping of these metals from melts escaping to the upper crust. The primary means of slowing or overcoming gravitational settling is by increasing the viscosity of the silicate melt or increasing the upward migration velocity of the magma. In a MASH zone setting (see Chapter 3 and Hildreth and Moorbath, 1988; Richards, 2003; Annen et al., 2006), changes in viscosity can be easily achieved through mixing.

Sulfide Settling in MASH Zones

Dynamical conditions affecting sulfide settling

Magma viscosity and silicate-sulfide density contrast affect the settling rate of sulfide globules in silicate magmas. Magma viscosity is most strongly influenced by temperature, SiO_2 content, crystallinity, and volatile content. Decreasing temperature increases viscosity by allowing more and stronger chemical bonding, particularly between Si and O, within the magma. Increasing SiO_2 content raises viscosity by increasing the number of framework Si-O tetrahedral bonds, similar to the effect caused by decreasing temperature. Crystallinity, or the fraction of suspended crystals in the magma, increases viscosity due to the interlocking of crystals with each other in the magma, which inhibits flow (see Marsh, 1981). Volatile content is an intrinsic chemical factor that is initially set by the source region of a silicate magma. Magmatic differentiation also causes increases in volatile content through removal of anhydrous crystals. The role of volatiles in controlling magma viscosity in various parts of the arc magmatic system has been the focus of much previous research (e.g. Spera, 1984; Shinohara et al., 1995; Melnik and Sparks, 1999; Wylie et al., 1999; Gonnermann and Manga, 2003), although little of this research has focussed on deep arc magma mixing systems. In this setting, temperature, SiO_2 content, and crystallinity changes are large, whereas volatile content changes are likely to be comparatively small (e.g. mixing arc basalt containing 3–4 % H_2O with tonalite containing 4–5 % H_2O). This section therefore focuses on the major controls on viscosity changes, and not on the role of volatiles, which are assumed to be retained in the magma.

Since it is clear that MASH zones have a significant role in setting the geochemical signatures of arc magmas (e.g. Hildreth and Moorbath, 1988; Richards, 2003; Annen et al., 2006), this chapter argues that mixing in MASH zones also plays a pivotal role in the metallogeny of magmas ascending to the surface. In these settings, magma mixing and assimilation cause dramatic changes in viscosity because the mixing endmembers have very different

temperatures and SiO_2 content. Futhermore, it is likely that convection is also a common process because relatively cool felsic partial melts from the lower crust coexist and mix with overwhelming amounts of high temperature, low viscosity mafic magma (Hildreth and Moorbath, 1988), and temperature contrast is a major driver of convection. Couch et al. (2001) showed that relatively rapid rates of magma convection (5–20 m/day) are possible within basaltic magma chambers. Such rapid convection would be expected to exert a controlling influence on sulfide globules suspended in a mixing silicate magma chamber; however, Martin and Nokes (1988) have shown that even in a vigorously convecting magma, the velocity gradient that exists between the wall of the chamber and the convection cells within the magma allows a net loss of suspended particles. Under these conditions, sulfide globules settle out from convecting magmas, though with a velocity much reduced from that predicted by the Hadamard-Rybczynski equation (cf. Martin and Nokes, 1988).

On a larger scale, the migration of magmas through the crust occurs at significantly lower velocities, between 10^{-9} to 10^{-10} m/s for granitic magmas (Watt et al., 1996), but up to 10^{-1} m/s for mafic magmas escaping the mantle into the lower crust (Klügel, 1998). Therefore, the viscosity of the silicate magmas, and thus migration velocities, are of key importance to the entrainment and removal of sulfides generated by mixing silicates in a MASH zone. Turner (2002) used U-series isotopes to infer rapid magma ascent rates (up to 10^{-5} m s^{-1}) and minimal lithospheric residence time above the downgoing slab in an arc setting. Furthermore, Turner (2002) determined that evolution from basalt to basaltic-andesite must also occur rapidly during ascent or, to reach more felsic compositions, in crustal magma reservoirs on time scales of $\leq 10^3$ years. Significantly greater values, up to 10^{-2} m s^{-1} (Blot, 1972), may occur in the shallow crust. It is therefore likely that migration velocities have the potential to exceed settling velocities in many instances.

Tectonic conditions affecting sulfide settling

The channelisation of magmas containing suspended sulfides is an important control on sulfide suspension and entrainment in migrating silicate magmas. Weinberg (1999), for example, showed that magmas migrating through the crust favour structurally-controlled pathways. The U-series data from Turner (2002) also support the role of chanellised flow in magma migration, particularly in arcs. Confinement in these pathways allows the flow to sustain higher energy and therefore a higher migration velocity. It is at structural 'widenings' (e.g. where a fault-controlled pathway opens into a magma chamber) that migrating magmas lose flow energy (velocity). This consequently reduces their ability to suspend denser phases. The Eastern Deeps section of the Voisey's Bay magmatic Ni-Cu deposit is a prime example of this happening to a migrating, sulfide-rich, basaltic magma (Li and Naldrett, 1999; Evans-Lamswood et al., 2000). Successive input pulses of magma into a lower chamber forced earlier sulfide-saturated magmas to migrate rapidly up along narrow structurally-controlled feeder pathways, and to then spread into a broad upper magma chamber. Upon entering the upper chamber, sulfides entrained in these rapidly migrating and channelised magma pulses

were introduced to a non-channelised environment with the consequence that the magma flow rate slowed dramatically. The reduction in flow rate allowed the denser, metal-rich sulfide phase to settle out of suspension. It is this settling out of sulfide phases that must be counteracted to retain the pre-concentrated metal content of the sulfides. Therefore, the key factors that allow sulfide phases to remain suspended in silicate magmas are elevated silicate viscosity, maintained channelised flow, and migration velocities exceeding sulfide settling velocities.

Results: Sulfide Settling Model

The calculations on settling of sulfides through silicate melts of varying compositions were done in a specific order. The result is Fig. 5.1, which establishes the interplay between silicate melt composition, melt viscosity, and sulfide globule size on the settling velocity of sulfides through silicate melt. Sulfide melt density is taken to be 4.5 g/cm^3.

Sulfide globule size

In figure 5.1, the globule radius is varied between 0.01 cm and 1.0 cm and the resulting settling velocity calculated for each size in four different mixtures between 10% OGC tonalite/90% IAB and 40% OGC tonalite/60% IAB (see Table 5.1 for compositions). These compositions were chosen because they reflect the likely range of mixed silicate, sulfide-bearing compositions in the OGC and may therefore be representative of mixing proportions in MASH zones in general. The mixtures were arithmetically calculated based on bulk XRF major element compositions of the endmembers (Table 5.1) to which 1% H_20 was included.

Table 5.1
Chemical composition of starting material and mixtures

	Starting materials		Mixtures (Tonalite/IAB)			
	IAB[1]	Tonalite (KR071)[2]	10/90	20/80	30/70	40/60
SiO_2	50.11	64.31	51.53	52.95	54.37	55.79
TiO_2	0.629	0.73	0.6391	0.6492	0.6593	0.6694
Al_2O_3	18.01	16.68	17.877	17.744	17.611	17.478
Fe_2O_3	2.28	5.94	2.646	3.012	3.378	3.744
MnO	8.07	0.08	7.271	6.472	5.673	4.874
MgO	7.77	2.36	7.229	6.688	6.147	5.606
CaO	11.21	2.25	10.314	9.418	8.522	7.626
Na_2O	1.41	2.7	1.539	1.668	1.797	1.926
K_2O	0.101	2.97	0.3879	0.6748	0.9617	1.2486
P_2O_5	0.069	0.15	0.0771	0.0852	0.0933	0.1014
SO_3		bd				

Notes:

[1]Kunashir Plateau IAB from Bailey et al. (1989); [2]XRF analysis as described in Appendix B.

Decimal places are maintained in the mixture calculations to reduce repetitive rounding errors.

bd = below detection limit

All data in wt. %

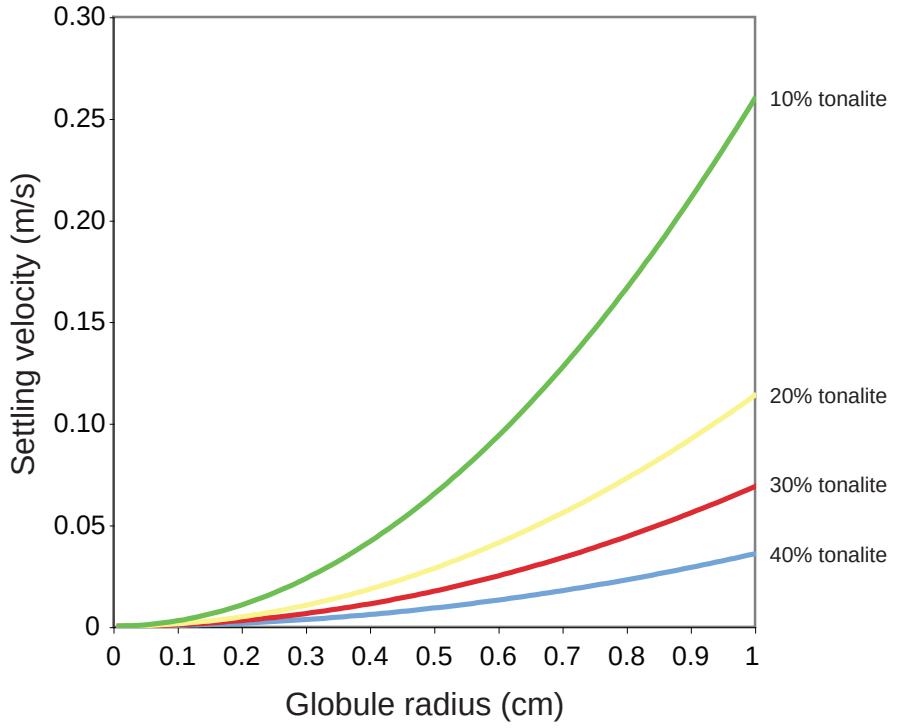

Figure 5.1: Calculated settling velocity (m/s) versus globule radius (cm) of a sulfide globule through silicate melt compositions of IAB and tonalite in varying mixing proportions.

MELTS (Ghiorso and Sack, 1995) was used to estimate the liquidus temperature and density of each mixture. The equations of Giordano (2008) were applied to the major element data to calculate the viscosity of the melt. With these values, the Hadamard-Rybczynski equation was used to calculate the settling viscosity of a sulfide globule of any given radius.

MELTS (Ghiorso and Sack, 1995) was then used to estimate the liquidus temperature and density of each mixture. The equations of Giordano (2008) were applied using these values and the major element data to calculate the viscosity of the melt. With all of these values, the Hadamard-Rybczynski equation was used to calculate the settling viscosity of sulfide globules of any given radius.

Controls on globule size

Upon exsolution in silicate magmas, suspended sulfide globules do not coalesce into progressively larger bodies because of their high surface tension. They must settle out and touch silicate crystals, which disrupt their surface tension, allowing individual globules to coalesce into a massive deposit and displace the crystals (see de Bremond d'Ars et al., 2001). Therefore, it follows that the primary control on globule size is their number density (number of globules per unit volume, see Chapter 4) and the sulfur diffusion rate. Sulfide globule nucleation is hindered by the high surface energy of incipient globules, which must be overcome with sufficient sulfur oversaturation (see Chapter 4 and Mungall and Su, 2005). Sulfur diffusion rate is reduced by low sulfur concentration and by high silica content (i.e. slower in more viscous magmas, cf. Baker and Rutherford, 1996; Freda et al., 2005). Therefore, high degrees of sulfur oversaturation and low silicate melt viscosities, or low silica content, are ideal conditions for pervasive globule nucleation and growth. However, the upper limit on globule size in any sulfide cloud is controlled by their number density. The

development of diffusion haloes that meet and compete for a finite supply of sulfur restricts the ultimate size reached by individual sulfide globules (Mungall, 2002). Chapter 4 details more completely the interplay between sulfide nucleation and growth.

Settling velocities

Figure 5.1 clearly shows that the settling velocities asymptote to zero as globule diameter shrinks toward zero, as expected. It also shows that as globule diameter increases, the settling velocity increases exponentially. However, sulfides settle through the most mafic mixture (green curve in Fig. 5.1) at velocities up to ten times faster than they settle through the most felsic mixture (blue curve in Fig. 5.1).

Discussion: Processes Affecting Extraction and Ore Development

Viscosity

Figure 5.2 is a viscosity model of a crystallising bulk mixture of 20% OGC tonalite and 80% IAB computed using MELTS (Ghiorso and Sack, 1995). The blue curve on this diagram shows that melt viscosity rapidly increases with progressive crystallisation. Importantly, this model considers only the viscosity of the melt and does not take into account the viscosity effects of progressively adding suspended crystals, which significantly increase magma viscosity (the viscosity increases because of increasing felsification of the melt driven by crystallisation of olivine, pyroxene, and calcic plagioclase – see Chapter 3). Upon reaching the critical crystallinity threshold of 50–60%, cessation of magma flow results in formation of intrusions (Marsh, 1981). Entrainment of suspended sulfides is highly dependent on the continuing ability of a magma to migrate. Therefore, magma viscosity conditions allowing both sulfide entrainment and migration must be attained with limited differentiation and crystallisation for sulfide-globule bearing magmas to escape from a sulfide saturated system. Specifically, sulfide globule-bearing magmas escaping from MASH zones must do so before critical crystallinity is reached if they are destined to reach the upper crust and participate in the formation of a mineralised deposit. Conversely, batches of magma could be extracted from crystal-rich mushes through gravitational compaction. However, such late-stage magma batches are likely to be sulfide-deficient, since buoyancy contrast is the driving mechanism. Escaping magmas with very low viscosity (i.e. basaltic magmas) may not have mixed or evolved sufficiently to reach sulfide saturation; therefore, they retain their metal and sulfur contents.

Migration and settling velocities in a crystallising intrusion

It is clear that settling velocities are highly dependent on globule size (Fig. 5.1). In the OGC, the maximum observed sulfide globule radius was ~0.25 cm (other sizes will be addressed later). The liquidus settling velocity of a 0.25 cm radius sulfide globule through a mixture

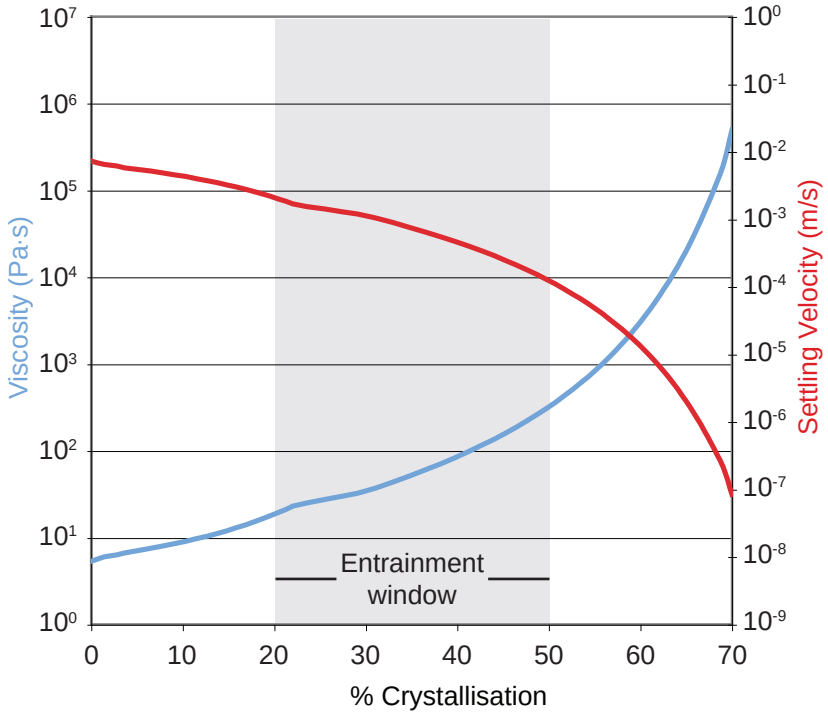

Figure 5.2: Viscosity model (melt only) of a crystallising silicate melt mixture of 80% IAB and 20% tonalite. Note the logarithmic scale on the y-axis. The blue curve is the modelled viscosity (Pa·s) of the silicate melt as it crystallises. The red curve is the settling velocity (m s^{-1}) of a sulfide globule, with a representative radius observed in the OGC (0.25 cm), through a silicate melt of the given composition. The grey extraction window on the left-hand side of the diagram represents the dynamical conditions under which the sustained suspension and extraction of sulfide globules would likely be possible (< 50% crystals – see text).

of 20% OGC tonalite/80% IAB is 7.1 x 10^{-3} m/s (Appendix D). Given that this mixture is relatively mafic (~53% SiO_2) with a modelled viscosity of 5.2 Pa·s (Fig. 5.2), its highest likely migration velocity is probably ~10^{-1} m/s (Turcotte, 1982; Klügel, 1998). Therefore, this size of sulfide globule is readily entrained in a silicate melt migrating at or near maximum velocity. Since melt migration velocity and sulfide globule settling velocity are inversely proportional to melt viscosity, progressing crystallisation will slow both equally.

Increasing viscosity slows chemical diffusion (Watt et al., 1996), inhibiting the sequestration of metals by circulating sulfide melt. In the example given above, two essential components needed for ore formation are retained in mixed magmas with progressing crystallisation beyond critical crystallinity: sulfur and pre-concentrated metals. Concentration of volatiles and incompatibles in the last, late phases of melt allows rapid element diffusion and faster sulfide globule settling through the last liquid domains (by lowering melt viscosity). However, with so much of the magma volume locked by high crystallinity, efficient sequestration of sulfide-rich melt into a single escaping phase is unlikely. Only with a pervasive fracture system permitting hydrothermal fluid flow would the metals and sulfur contained within the crystal-locked silicate magma be concentratable (as in porphyry Cu, see Lowell and Guilbert, 1970). However, the formation of a hydrothermal fluid that circulates through a fracture stockwork, such as in porphyry Cu, is only likely in the upper crust. This is because water saturation in a magma crystallising in the mid-crust (~6 kb) is suppressed, requiring significant crystallisation before fluid exsolution occurs. Conversely, magmas intruding

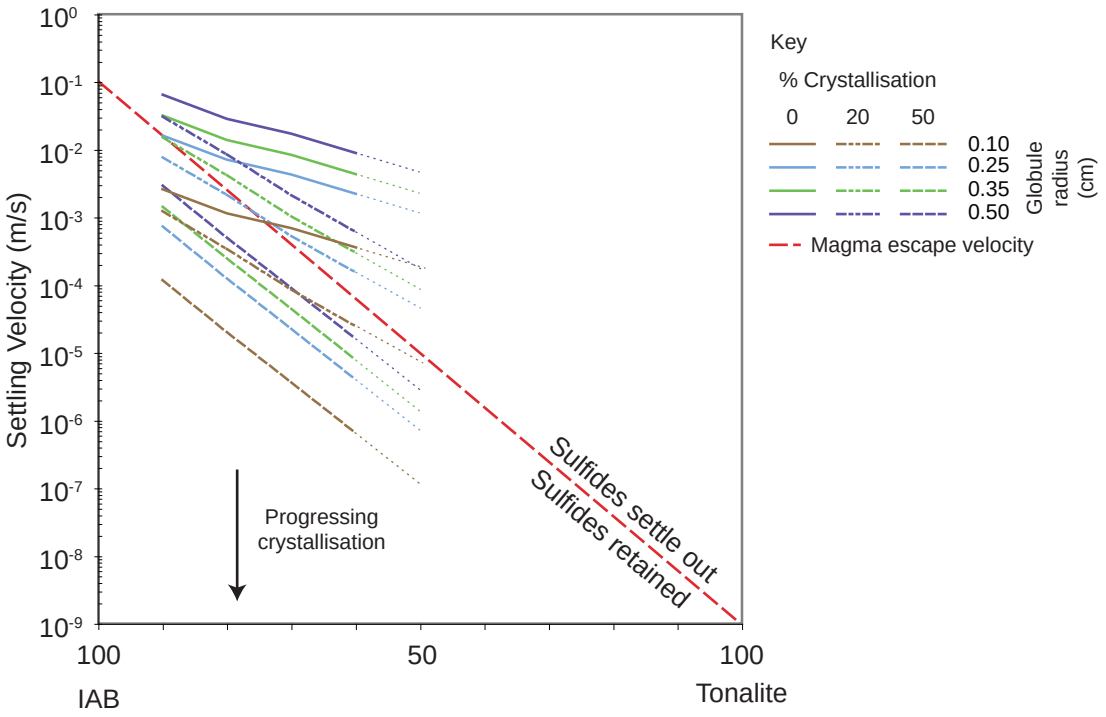

Figure 5.3: Settling velocity of sulfide globules of a given size (brown, blue, green, and purple lines) through crystal-free magma with bulk compositions between IAB and tonalite. Lines become dotted at compositions beyond MELTS capability and are speculative. Red dashed line is the estimated maximum escape velocity of magmas between IAB and tonalite. Migration velocities decrease exponentially with increasing silica content (see text) and the endpoints of the line were chosen to be 10^{-1} m/s for mafic melts (Klügel, 1998) and 10^{-9} m/s for felsic melts (Watt et al., 1996).

the shallow crust can exsolve a fluid phase before any crystallisation occurs (Holtz and Johannes, 1994; Holtz et al., 2001). Therefore, metal-rich sulfides generated in MASH zones are protected from magmatic fluids until upper crustal levels are reached.

Figure 5.3 compares sulfide globule settling velocities in liquidus magma to those in partially crystallised magma, as a function of globule radius and composition. The settling velocity of each globule size was calculated for each composition between 90% IAB and 60% IAB in 10% steps of increasing OGC tonalite. The major element composition of each mixture was calculated using the basic arithmetic method:

$$C_{ME} = X_{IAB} * C_{IAB}^{Element} + (1\text{-}X)_{Tonalite} * C_{Tonalite}^{Element}$$

where C_{ME} is the concentration of the major element (SiO_2, TiO_2, Al_2O_3, Fe_2O_3, MnO, MgO, CaO, Na_2O, K_2O, and P_2O_5) in the mixture, X_{IAB} is the proportion of IAB, $C_{IAB}^{Element}$ is the concentration of the major element in IAB; the remaining symbols are the equivalents for tonalite. The equations of Giordano (2008) were applied to each mixture composition to calculate its viscosity. The Hadamard-Rybczynski equation was then used to calculate the settling velocity of sulfide globules of a given radius through the appropriate mixture. The red dashed line represents the maximum migration velocity of each composition. It is an interpolation between the maximum migration velocity of granites suggested by Watt et al. (1996) and that for mafic melts suggested by Klügel (1998). Since the viscosity equations

of Giordano (2008) show that melt viscosity increases exponentially with SiO_2 content, it follows that the maximum migration velocity decreases exponentially with increasing SiO_2.

It is clear that for sulfide globule radii exceeding 0.25 cm, the liquidus settling velocities always exceed the maximum migration velocities and that some crystallisation is required to entrain sulfides. Conversely, globules with radii < 0.25 cm will escape with no crystallisation in mafic magmas. At 50% crystallinity, the melt component of a 20% OGC tonalite/80% IAB mixture has evolved to 56% SiO_2 and a viscosity of 300 Pa·s. The sulfide settling velocity of a 0.25 cm radius globule at this viscosity is 1.2×10^{-4} m/s (see Appendix D for all values) compared to a settling velocity of 7.1×10^{-3} m/s in the equivalent liquidus magma (Fig. 5.3). The liquidus settling velocity exceeds the migration velocity of the silicate magma, but the settling velocity in the evolved melt does not. Therefore, some crystallisation must occur for melts escaping MASH zones to be able to entrain sulfides. For example, the melt viscosity of the above mixture and globule size, after ~20% crystallisation, is adequate to allow entrainment (Fig. 5.3). In highly crystallised magmas (> 50%), the crystals form part of a touching network that locks the magma. It is suggested that sulfide globules, being certainly more mobile and perhaps smaller than the crystals, may still be able to be entrained in escaping melt if the crystal network acts like a sieve to other crystals (Fig. 5.4). In this case, the sulfides are mobile enough or small enough to slip through the crystal sieve and continue with the melt out of the magma chamber. This mechanism needs to be driven by a process other than gravity, as gravitational segregation would separate sulfide globules from

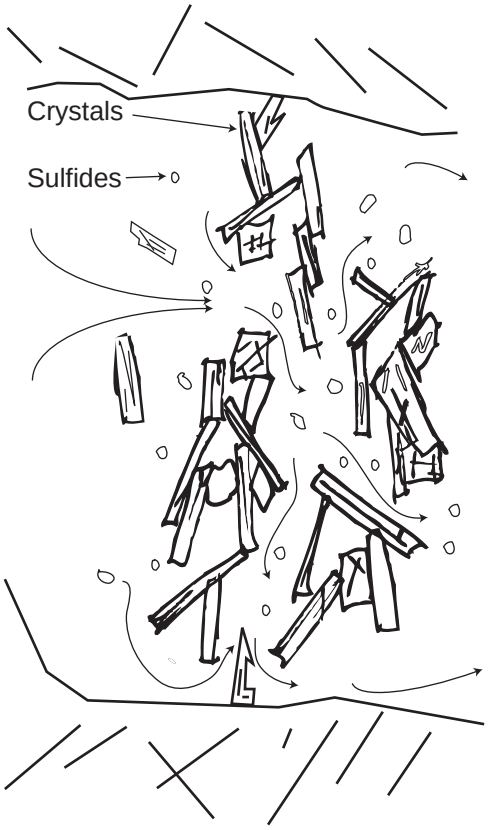

Figure 5.4: Schematic cross-section through touching, 3-D crystal network that acts like a 'crystal sieve'. Flow lines are possible paths for magma extraction from the highly crystallised magma. Sulfide globules could remain entrained in this melt if the melt component could migrate at sufficient velocities between the crystal network. Only the sulfide globules are able to fit through the gaps in the network.

melt. Therefore, sulfide 'filter pressing' requires large tectonic pressure differentials to drive rapid melt migration.

Buoyancy-related or structurally driven processes control melt migration in partially molten systems (Brown, 1994). Since deformational strain partitions into the melt component of such systems (Vigneresse and Tikoff, 1999), this suggests that areas under high stress, resulting in strain, would be ideal locations for melt conduits. Arcs are located along convergent plate boundaries, which are commonly transpressional or transtensional (i.e. undergoing slab roll-back) (Brown, 1994). In either case, the focussing of deformation along these boundaries likely favours development of melt conduits in the crust of arcs. Moreover, Turner (2002) determined that melt extraction by compression of porous matrices (i.e. melt-filled mushes), followed by a transition to chanellised flow, allows for rapid ascent of magmas (up to ~10^{-2} m/s) in these settings. Therefore, the necessary tectonic ingredients for high speed magma mobility are best available in arcs.

Sulfide retention

Not all batches of magma in the deep crust contain magmatic sulfides. Some are sulfide- and/or metal-depleted, some have never experienced sulfide saturation, still others contain sulfides, but only of low tenor. Some are enriched with high tenor sulfides, or are massive sulfides. One way to explain this diversity in sulfide abundance is by invoking heterogeneity in sulfide retention. Sulfide- and metal-depleted magmas may result when magmas migrate too slowly to counteract gravitational settling out of sulfide globules. Magmas with retained, but low tenor, sulfides may form in silicate magmas that are too viscous (too felsic) to allow the circulation of sulfides throughout the intrusion (i.e. low R-factor). Magmas enriched in high tenor sulfides may have had just the right viscosity conditions and migration velocities to allow both continued sulfide globule circulation (i.e. high R-factor) and retention of these sulfides. Massive sulfide is the sulfide-rich endmember in this continuum, representing sulfide globule cumulate, which is incapable of migrating upwards.

Upward migrating magmas that have undergone sulfide loss will be sulfur and metal depleted, and therefore unable to provide metals to any later-forming hydrothermal system. Those with low tenor sulfide may retain their metals dispersed in the magma. Those with retained, high tenor sulfides may form metal-enriched intrusions in the upper crust, which may later contribute metals to porphyry-type deposits. Sulfide accumulation and retention in the deep crust results in the formation of magmatic Ni-Cu deposits.

Entrainment window

The window of dynamic conditions where migration velocity exceeds settling velocity is comparatively wide. In this model, MASH zone magmas that mix sufficiently to reach mafic to mafic-intermediate silica contents (~53% SiO_2 in this example melt of 20% OGC

tonalite/80% IAB) are capable of entraining sulfides during migration, after no crystallisation for sulfide globule radii < 0.1 cm, or 20% crystallisation for globule radii < 0.25 cm . This entrainment window is marked on Fig. 5.2. Therefore the question of whether sulfides can be entrained in MASH zone-derived magmas has been answered in the affirmative. The process of suspension and entrainment of sulfide melt in mixing MASH-zone magma is likely to be a precursor process to porphyry Cu-related ore generation in some settings. This is supported by the observations that some porphyry Cu deposits appear to be PGE-rich (Tarkian and Stribrny, 1999; Auge et al., 2005), in that PGE would be concentrated in an exsolved sulfide melt phase. The important constraints on ore potential then become escape from the MASH zone before crystalline lockup (i.e. within the entrainment window) and maintenance of migration velocities high enough to prevent globule settling.

Other compositions and globule sizes

The preceding discussion addressed the dynamics of sulfide globule settling in only one mixture. Increasing sulfide globule size and increasing the tonalite proportion produces a small but important increase in the settling velocity profiles (Fig. 5.3). At large radius (0.5 cm), the settling velocity of sulfide globules always exceeds the maximum liquidus escape velocity of their host magma. Significant crystallisation (> 20%), at any composition, must take place for globules of this size to be entrained. Even at smaller radii (0.25 cm), the maximum liquidus escape velocity is always exceeded; however, much less crystallisation needs to occur (<< 20%) for maximum escape velocities to exceed settling velocity. Doubling the size of sulfide globules increases the sulfide settling velocity four-fold, as expected from the Hadamard-Rybczynski equation.

Sulfur oversaturation tends to be greater when it is generated by a mixing event (e.g. the redox mechanism described in Chapter 4). Large oversaturation in turn encourages pervasive nucleation of small sulfide globules (see Mungall, 2002). Therefore, where mixing of graphitic anatectic melts and sulfate-saturated mafic melts occurs in MASH zones, sulfide entrainment is favoured in low mixing, highly oversaturated melts. These are the types of mixtures that were observed to exist in the OGC, with one critical difference – the sulfides were present at depth. A significant amount of sulfide did not make it to the upper crust, although some may well have, since unsettled sulfide globules were observed in many bulk compositions (Chapter 2).

Massive sulfides in the OGC – Evidence for sulfide fall-out at depth

Apparently at odds with the sulfide settling behaviour suggested by the modelling presented above is the observation of massive sulfides in the OGC. These are evidence of sulfide melt settling out at depth. The explanation lies in a consideration of the confinement state of the magma migration conduit and the conduit tortuosity, suggested earlier in the discussion of the Voisey's Bay deposit in Newfoundland.

The foregoing discussion on settling behaviour only considered the settling of sulfide globules in essentially unconfined magmas free to flow and convect. Once magmas have escaped from their sites of generation, the maintenance of sufficient flow velocity becomes the critical factor in retaining suspended sulfides. A migrating flow meeting a larger conduit or a magma chamber loses energy and consequently some of its ability to retain suspended sulfides. These sulfides fall out of suspension and accumulate near the entrance to this lower energy environment, as interpreted at Voisey's Bay (Li and Naldrett, 1999). Such dynamic behaviour accounts for the presence of massive sulfides at depth, but also maintains consistency with the model discussed above. It is therefore likely that the massive sulfides in the OGC settled out from melts unable to migrate further or which stalled temporarily at this depth. The presence of tonalitic and dioritic melts outcropping within the OGC supports the interpretation that a large volume of intermediate magma was unable to escape to a higher crustal level. Stalling of these magmas ultimately would have led to the settling out of the suspended sulfides, represented in the field by the massive sulfide bodies in the OGC.

Tortuosity

As discussed, the relative level of confinement of melts migrating through the crust has a strong effect on the ability of melts to retain suspended sulfides. The level of convolution of the magma migration path also has a strong effect on the ability of a migrating magma in maintaining its flow energy. In simple terms, migration paths with more bends, constrictions, and surface roughness increase frictional energy losses from a migrating flow (Spera, 1984; Clennell, 1997). More direct paths between magma source and sink allow for higher sustained migration velocities and therefore retention of suspended sulfides. Tortuous, indirect, and complex migration paths have the opposite effect and encourage settling out and possibly magmatic Ni-Cu deposit formation.

Implications for ore development

MASH zones are fertile regions for sulfide production. Modelling of magma viscosity versus sulfide globule size and settling velocity suggests that melts generally need to crystallise at least ~10–20% of their original liquidus mass before sulfide entrainment and extraction can occur. The viscosity of silicate magmas, dependent mostly on temperature, silica content, and crystallinity, favours entrainment of sulfides between a 10–20% crystallinity up to critical crystallinity (50 to 60% crystallinity). Therefore, MASH zones in the lower to middle crust could be important for the generation of porphyry-Cu deposits in the overlying crust because of their role in sulfide production and in generating batches of magma that are metal-enriched. Furthermore, ore generation is enhanced by the ability of escaping magmas to entrain sulfide globules and the continuous input of primitive, fertile magmas from the underlying mantle to upgrade the metal content of those magmas.

Enriched versus depleted magma pulses in ore deposition

Magmatic sulfide ore deposits may build sporadically (cf. Noril'sk, see Naldrett, 1992), alternating between metal-rich and metal-poor layers. Similarly, porphyry Cu-Au systems are typified by intrusion complexes where many intrusions are barren of metals and only one or two are associated with ore deposition (Halter et al., 2004; Stavast et al., 2006). It may be that in both settings, major phases of ore deposition are confined to particular pulses in which batches of sulfide-enriched magmas alternate with batches of sulfide-depleted ones. Sulfide settling through silicate magmas is a process by which two reservoirs could be produced within a single magma chamber: sulfide-enriched toward the bottom of the chamber and sulfide-depleted throughout the rest of the chamber. Since mixing probably causes magma chambers to convect at rapid rates, the development of an isolated sulfide globule-enriched zone at the bottom of such a magma chamber may seem unlikely. However, Martin and Nokes (1988) showed that the velocity gradient between convection cells in a magma chamber and the chamber walls allows for a net loss of suspended particles. These 'wall-captured' sulfides could conceivably collect at the base of convection cells, at the bottom of the chamber, producing an especially enriched sulfide-layer. However, there would likely always be some sulfides remaining in the convection cells and these could escape. This could lead to the generation of two very different magma pulses: one sourced from the sulfide-rich layer at the bottom of the chamber and thus very sulfide-enriched and one sourced from the main body of the chamber and thus less enriched (or even metal-depleted). This potentially explains the variability in metal content of ore-forming magmas. Further settling out of sulfide melt could occur during migration at conduit widenings, such as those discussed above, or at any stalling point *en route* to the near surface.

A new ore spectrum?

Magmatic Ni-Cu and porphyry Cu deposits could be endmembers of an ore deposit spectrum produced from MASH zones. In this idea, sulfide globule entrainment, from MASH zone to emplacement depth, is key. The porphyry Cu endmember results from migrating magmas being able to entrain metal-rich sulfide globules until reaching the upper crust. The magmatic Ni-Cu endmember results from the settling out of metal-enriched sulfide globules and accumulation at depth, consequently forming massive sulfide. Only barren magmas could then be extracted. However, if the metal-enriched disseminated-sulfide-rich layer were later intruded by stratigraphically lower, fresher magmas, subsequent entrainment of these previously produced sulfides could occur, adding their metals to those in the new magmas. The new ore spectrum idea will be addressed further in Chapter 6.

Conclusions

Depending on the size of sulfide globules, the silicate viscosity window in MASH zones allows entrainment of sulfides in a window of values up to the 50-60% critical crystallinity lock-up.

The lower bound of this window is determined by the liquidus composition of the magma. Silicate magma migration velocities can exceed typical sulfide settling velocities of small globules (~0.10–0.30 cm radius) only after some amount of crystallisation has occurred. The amount of required crystallisation decreases depending on the starting composition of the magma. This implies that given the right conditions for sulfur oversaturation and exsolution of sulfide globules during silicate mixing in a MASH zone, the generated sulfides would be available for extraction providing that magmas are free to migrate from the MASH zone.

Magma migration through confined structural passages, such as faults and shear zones, favours higher energy flows and, therefore, the retention of suspended sulfides. The retention of metal-rich sulfides is an important factor in producing a viable ore deposit through later magma modification or fluid processing in the upper crust. MASH zones are areas of probable sulfide-melt metal enrichment due to the continuous input of hot and primitive mafic magmas. The superheat provided by these mafic magmas encourages rapid convection and magma mixing within the MASH zone magma chamber. Mixing between oxidised arc basalts and reduced tonalites can result in high levels of sulfur oversaturation, which favours smaller globules. Small globules are more likely to remain suspended because they have lower settling velocities.

References

Annen C., Blundy J. D. and Sparks R. S. J. (2006) The genesis of intermediate and silicic magmas in deep crustal hot zones. *Journal of Petrology* **47**(3), 505-539.

Auge T., Petrunov R. and Bailly L. (2005) On the origin of the pge mineralization in the elatsite porphyry Cu-Au deposit, Bulgaria: Comparison with the Baula-Nuasahi complex, India, and other alkaline PGE-rich porphyries. *Canadian Mineralogist* **43**(4), 1355-1372.

Baker L. L. and Rutherford M. J. (1996) Sulfur diffusion in rhyolite melts. *Contributions to Mineralogy and Petrology* **123**(4), 335-344.

Bailey, J. C., Frolova, T. I. and Burikova, I. A. (1989) Mineralogy, geochemistry and petrogenesis of Kurile island-arc basalts. *Contributions to Mineralogy and Petrology* **102**(3), 265-280.

Blot C. (1972) Volcanisme et séismes du manteau supérieur dans l'Archipel des Nouvelles-Hébrides. *Bulletin of Volcanology* **36**(3), 446-461.

Bottinga Y. (1994) Rheology and rupture of homogeneous silicate liquids at magmatic temperatures. *Journal of Geophysical Research* **99**(B5), 9415-9422.

Brown M. (1994) The generation, segregation, ascent and emplacement of granite magma: the migmatite-to-crustally-derived granite connection in thickened orogens. *Earth-Science Reviews* **36**(1-2), 83-130.

Clennell M. B. (1997) Tortuosity: a guide through the maze. *Geological Society, London, Special Publications* **122**(1), 299-344.

Couch S., Sparks R. S. J. and Carroll M. R. (2001) Mineral disequilibrium in lavas explained by convective self-mixing in open magma chambers. *Nature* **411**(6841), 1037-1039.

de Bremond d'Ars J., Arndt N. T. and Hallot E. (2001) Analog experimental insights into the formation of magmatic sulfide deposits. *Earth and Planetary Science Letters* **186**(3-4), 371-381.

Dobson D. P., Crichton W. A., Vocadlo L., Jones A. P., Wang Y., Uchida T., Rivers M., Sutton S. and Brodholt J. P. (2000) In situ measurement of viscosity of liquids in the Fe-FeS system at high pressures and temperatures. *American Mineralogist* **85**(11-12), 1838-1842.

Evans-Lamswood D. M., Butt D. P., Jackson R. S., Lee D. V., Muggridge M. G., Wheeler R. I. and Wilton D. H. C. (2000) Physical controls assocaited with the distribution of sulfides in the Voisey's Bay Ni-Cu-Co deposit, Labrador. *Economic Geology* **95**, 749-769.

Freda C., Baker D. R. and Scarlato P. (2005) Sulfur diffusion in basaltic melts. *Geochimica et Cosmochimica Acta* **69**(21), 5061-5069.

Ghiorso M. S. and Sack R. O. (1995) Chemical mass transfer in magmatic processes IV. A revised and internally consistent thermodynamic model for the interpolation and extrapolation of liquid-solid equilibria in magmatic systems at elevated temperatures and pressures. *Contributions to Mineralogy and Petrology* **119**(2), 197-212.

Giordano D., Russell J. K. and Dingwell D. B. (2008) Viscosity of magmatic liquids: A model. *Earth and Planetary Science Letters* **271**(1-4), 123-134.

Goldschmidt V. M. (1937) The principles of distribution of chemical elements in minerals and rocks. *Journal of the Chemical Society*, 655-673.

Gonnermann H. M. and Manga M. (2003) Explosive volcanism may not be an inevitable consequence of magma fragmentation. *Nature* **426**(6965), 432-435.

Hadamard J. (1911) Mouvement permanent lent d'une sphere liquide et visqueuse dans un liquid visqueux. *Comptes Rendus Mathématique. Académie des Sciences. Paris* **152**, 1735-1738.

Halter W. E., Bain N., Becker K., Heinrich C. A., Landtwing M., VonQuadt A., Clark A. H., Sasso A. M., Bissig T. and Tosdal R. M. (2004) From andesitic volcanism to the

formation of a porphyry Cu-Au mineralizing magma chamber: the Farallon Negro Volcanic Complex, northwestern Argentina. *Journal of Volcanology and Geothermal Research* **136**(1-2), 1-30.

Hildreth W. and Moorbath S. (1988) Crustal contributions to arc magmatism in the Andes of Central Chile. *Contributions to Mineralogy and Petrology* **98**(4), 455-489.

Holtz F. and Johannes W. (1994) Maximum and minimum water contents of granitic melts: implications for chemical and physical properties of ascending magmas. *Lithos* **32**(1-2), 149-159.

Holtz F., Johannes W., Tamic N. and Behrens H. (2001) Maximum and minimum water contents of granitic melts generated in the crust: a reevaluation and implications. *Lithos* **56**(1), 1-14.

Kerr R. C. and Lister J. R. (1991) The effects of shape on crystal settling and on the rheology of magmas. *Journal of Geology* **99**(3), 457-467.

Klügel A. (1998) Reactions between mantle xenoliths and host magma beneath La Palma (Canary Islands): constraints on magma ascent rates and crustal reservoirs. *Contributions to Mineralogy and Petrology* **131**(2), 237-257.

Li C. and Naldrett A. J. (1999) Geology and petrology of the Voisey's Bay intrusion: reaction of olivine with sulfide and silicate liquids. *Lithos* **47**(1-2), 1-31.

Lowell J. D. and Guilbert J. M. (1970) Lateral and vertical alteration-mineralization zoning in porphyry ore deposits. *Economic Geology* **65**(4), 373-408.

Marsh B. D. (1981) On the crystallinity, probability of occurrence, and rheology of lava and magma. *Contributions to Mineralogy and Petrology* **78**(1), 85-98.

Martin D. and Nokes R. (1988) Crystal settling in a vigorously converting magma chamber. *Nature* **332**(6164), 534-536.

McBirney A. R. and Murase T. (1984) Rheological Properties of Magmas. *Annual Review of Earth and Planetary Sciences* **12**(1), 337-357.

Melnik O. and Sparks R. S. J. (1999) Nonlinear dynamics of lava dome extrusion. *Nature* **402**(6757), 37-41.

Mungall J. E. (2002) Kinetic controls on the partitioning of trace elements between silicate and sulfide liquids. *Journal of Petrology* **43**(5), 749-768.

Mungall J. E. and Su S. (2005) Interfacial tension between magmatic sulfide and silicate liquids: Constraints on kinetics of sulfide liquation and sulfide migration through silicate rocks. *Earth and Planetary Science Letters* **234**(1-2), 135-149.

Naldrett A. J. (1992) A Model for the Ni-Cu-PGE Ores of the Noril'sk Region and Its Application to Other Areas of Flood Basalt. *Economic Geology* **87**(8), 1945-1962.

Peach C. L., Mathez E. A. and Keays R. R. (1990) Sulfide melt-silicate melt distribution coefficients for noble metals and other chalcophile elements as deduced from MORB: Implications for partial melting. *Geochimica et Cosmochimica Acta* **54**(12), 3379-3389.

Richards J. P. (2003) Tectono-magmatic precursors for porphyry Cu-(Mo-Au) deposit formation. *Economic Geology* **98**(8), 1515-1533.

Rybczynski W. (1911) Uber die fortschreitende Bewegung einer flussigen Kugel in einen zahen Medium. *Bulletin of the Academy of Science, Krakow 1, 40-46, 1911.* (1), 40-46.

Saar M. O., Manga M., Cashman K. V. and Fremouw S. (2001) Numerical models of the onset of yield strength in crystal-melt suspensions. *Earth and Planetary Science Letters* **187**(3-4), 367-379.

Shinohara H., Kazahaya K. and Lowenstern J. B. (1995) Volatile transport in a convecting magma column; implications for porphyry Mo mineralization. *Geology* **23**(12), 1091-1094.

Spera F. J. (1984) Carbon dioxide in petrogenesis III: role of volatiles in the ascent of alkaline magma with special reference to xenolith-bearing mafic lavas. *Contributions to Mineralogy and Petrology* **88**(3), 217-232.

Stavast W. J. A., Keith J. D., Christiansen E. H., Dorais M. J., Tingey D., Larocque A. and Evans N. (2006) The fate of magmatic sulfides during intrusion or eruption, Bingham and Tintic districts, Utah. *Economic Geology* **101**(2), 329-345.

Tarkian M. and Stribrny B. (1999) Platinum-group elements in porphyry copper deposits: a reconnaissance study. *Mineralogy and Petrology* **65**(3), 161-183.

Turcotte D. L. (1982) Magma Migration. *Annual Review of Earth and Planetary Sciences* **10**(1), 397-408.

Turner S. P. (2002) On the time-scales of magmatism at island-arc volcanoes. *Philosophical Transactions: Mathematical, Physical and Engineering Sciences* **360**(1801), 2853-2871.

Vigneresse J. L. and Tikoff B. (1999) Strain partitioning during partial melting and crystallizing felsic magmas. *Tectonophysics* **312**(2-4), 117-132.

Walsh S. D. C. and Saar M. O. (2008) Numerical models of stiffness and yield stress growth in crystal-melt suspensions. *Earth and Planetary Science Letters* **267**(1-2), 32-44.

Watt G. R., Burns I. M. and Graham G. A. (1996) Chemical characteristics of migmatites: accessory phase distribution and evidence for fast melt segregation rates. *Contributions to Mineralogy and Petrology* **125**(1), 100-111.

Weinberg R. F. (1999) Mesoscale pervasive felsic magma migration: alternatives to dyking. *Lithos* **46**(3), 393-410.

Weinberg R. F. and Podladchikov Y. (1994) Diapiric ascent of magmas through power law crust and mantle. *Journal of Geophysical Research* **99**(B5).

Wickham S. M. (1987) The segregation and emplacement of granitic magmas. *Journal of the Geological Society* **144**(2), 281-297.

Wylie J. J., Voight B. and Whitehead J. A. (1999) Instability of Magma Flow from Volatile-Dependent Viscosity. *Science* **285**(5435), 1883-1885.

Chapter 6: Synthesis and conclusions – New models for magmatic Ni-Cu and porphyry-Cu genesis

This study has examined the role of mixing in continental arc MASH zones on ore development in felsic magma-related ore systems, such as porphyry Cu and epithermal Au. This has never been previously attempted because of the relative rarity of exposed arc crust sections and the difficulty of accurately modelling lower crustal magmatic processes. The results of this study consequently offer unique insights into arc metallogeny and deepen our understanding of crustal-scale magma fractionation in general, with several key findings relating to the source of metals in felsic-magma related ore deposits and the nature of the mechanisms that function during transport of these magmas to the near surface.

Magma Mixing in the Deep Crust of Arcs

In Chapter 3, magma mixing was proposed to account for the trace element and Nd isotope patterns observed in geochemical data from rocks in the OGC. The endmember magmas in the OGC were interpreted to be MORB-like gabbro and tonalite. Between 20–30% mixing of tonalite with MORB-like gabbro accounts for the geochemical signatures of the intermediate magmas. Accepting that the OGC represents a lower- to middle-crustal MASH zone, recognition in the field that magma mixing has led to development of heterogeneity in the distribution of metal-rich sulfides implies that this represents a significant process in arc metallogeny.

At the initial stages of mixing, excess heat is available because of the overwhelming input of hot mantle-sourced gabbroic magmas into the MASH zone (Hildreth and Moorbath, 1988). This external heat drives partial melting of the overlying crust (Richards, 2003) and the temperature differences between the magmas drive vigorous convection. The deep crustal, felsic partial melts then mix, at proportions of up to tens of percent, with the mafic magmas to produce a hybrid (Hildreth and Moorbath, 1988), which is confirmed by this study. However, should the mafic input to the MASH zone stop, continued mixing and crystallisation will cool the intrusion enough such that partial melting stops and felsification of gabbros ceases. Felsification is a key process in causing sulfide saturation, so that the cessation of mixing will have a negative effect on the likelihood of generating sulfide melts. Logically then, it follows that MASH zones with long-lasting, high volume input of mantle magmas will be best suited to the production of sulfide-bearing magmas.

The Role of Magma Mixing in Mediating Sulfide Saturation

It is well established that in a silicate magma, sulfide oversaturation will cause exsolution of sulfide melt (see Naldrett, 2004). However, sulfide melts only form in silicate magmas that are sufficiently reduced to stabilise them, typically with melt fO_2 < FMQ + 1–2 (see

Carroll and Rutherford, 1987). At oxygen fugacities greater than this, sulfate (i.e. anhydrite) is the stable sulfur phase, although there is some overlap in the range of fO_2 values in which both sulfide and sulfate are stable. The mantle wedge underlying arcs is oxidised relative to normal oceanic mantle (Parkinson and Arculus, 1999), which results in arc rocks commonly within the sulfide-sulfate fO_2 stabilility overlap (Carroll and Rutherford, 1987; Mungall, 2002; Jugo et al., 2005). This is important because, sulfur is up to an order of magnitude more soluble in mafic silicate magmas as sulfate (~ 1 wt. %) than as sulfide (~ 0.1 wt. %). Experiments in this study (Chapter 4) suggest that the sulfide-sulfate solubility gap exists at felsic bulk compositions as well; however, it is clear that the most effective way to transport large amounts of magmatic sulfur is in oxidised, sulfate-stable basaltic melts.

If sulfate-stable mantle-sourced magmas enter a MASH zone, they must become reduced in order to exsolve and stabilise sulfide melt. Therefore, they must mix with melts that contain an abundant reducing agent. The only abundant, multiply valent elements in the deep crust of arcs are C, H, S, and Fe (cf. Mungall, 2002). A lack of free oxygen and reaction kinetics limit the reducing ability of hydrogen in the deep crust. The addition of external sulfate or sulfide to a magma will move the melt toward the SSO buffer (if melt fO_2 is below or above SSO, respectively), in addition to increasing the sulfur content of the melt (see Mungall, 2002). This potentially makes other sulfur saturation mechanisms irrelevant, due to the overwhelming effect of addition a large amount of sulfur. Addition of hematite would oxidise melt toward the hematite-magnetite buffer; however, during high grade metamorphism, iron is released from non-magnetic minerals and scavenged to form magnetite (Mayhew et al., 1991) and magnetite is commonly observed in highly metamorphosed rocks (Shive et al., 1992). Therefore, there is likely to be relatively little hematite present in the deep crust. Since most arc magmas are below the hematite-magnetite buffer in fO_2 space (Carroll and Rutherford, 1987), the addition of magnetite would have no net redox effect. However, carbon is of particular interest in arc magmatism because exposures of arc crust sequences are commonly associated with accretionary wedge complexes (Chapter 2). Metasediments in these complexes are typically metamorphosed oceanic sediments, which in many cases contain graphite in low to moderate abundances (Chapters 2 and 4). Indeed, graphite is ubiquitous in the southern Hidaka Belt, being observed in the OGC, in neighbouring gabbroic complexes, and in surrounding metasedimentary rocks (Chapters 2 and 3).

Magma mixing, sulfide saturation, and entrainment

Mixing of graphite-bearing metasediment-derived partial melts with oxidised, sulfur-rich mafic magmas is capable of producing highly sulfide-oversaturated hybrid magmas via the 'sulfur fence' model of Chapter 4. The sulfur fence model not only enlarges the range of initial sulfur contents that can result in mixing-induced oversaturation, but it also stipulates higher levels of sulfide oversaturation in hybrids than previous work (e.g. Li and Ripley, 2005). Continued mixing of graphitic felsic melts with mafic melts will cause large volume production of sulfide melts until the sulfur oversaturation is brought back to the saturation curve

(see Figs. 4.5 and 4.9). These sulfide melts will become metal-enriched through preferential partitioning of chalcophile metals, and their entrainment in migrating silicate magmas may allow formation of upper crustal ore deposits. Further addition of felsic material will only cause a small reduction in sulfide solubility (~100 ppm). This mostly increases viscosity and lowers temperature, which encourages magmas to stall. Conversely, hybrids produced by mixing oxidised mantle-sourced magmas with reductant- (i.e. graphite-) free anatectic melts are unlikely to experience sulfide oversaturation, precluding the possibility that metals could be stripped from the system by sulfide settling. Hybrid magmas produced in such a setting are thus likely to retain their metals and would also be able to become involved in porphyry-Cu deposit formation via the traditional hydrothermal porphyry model.

In Chapter 5, it was found that up to 40% mixing of OGC tonalite with IAB produces a hybrid magma with insufficient viscosity for liquidus melts to entrain sulfide globules in upwardly migrating magma. Some crystallisation is necessary to increase the viscosity of the residual melt, with the amount of required crystallisation dictated by the starting liquidus composition. At mixing percentages in the range typical of MASH zones (~20% to < 40%), ~ 20% crystallisation is sufficient to allow entrainment at sustained maximum migration velocities. However, more crystallisation will eventually lock-up the magma, stalling it at depth.

Favourable Migration Settings

Clearly, the migration of sulfide-bearing melts or magma is a key process that determines whether or not metals get to the upper crust in some arcs. In convergent settings, compressional stress will favour the formation of sill structures; in extensional settings, vertical dilational structures, such as dikes, will form (see Richards, 2003). Therefore, compression in arcs would tend to favour establishment of MASH zones, whereas extension would result in formation of highly permeable magma migration pathways. Plate tectonic theory stipulates that continental-oceanic plate convergence is associated with the development of arcs. Extensional regimes at these types of margins are likely related to slab roll-back and formation of back-arc basins; however, transpression is more common and the global association of magmatism and, importantly, related ore deposits with these settings is manifest (Richards, 2003).

Magma Mixing, Magma Migration, and Ore Metallogeny: Sulfide Entrainment and New Models for Magmatic Ni-Cu and Porphyry Cu Genesis

In this model, porphyry Cu deposits result from metal-bearing or metal-enriched magmas, which evolve through the deep crustal magma hybridisation discussed above, reaching the upper crust. For this to happen, hybrid magmas must retain any exsolved sulfide melt globules, so it is best if magmas migrate out of the deep-crustal mixing chamber soon after sulfide melt exsolution. Early migration, after a few tens of percent of mixing, would limit

the continuing reduction in migration velocities (caused by increasing viscosity) that could result in stalling and sulfide settling on the journey to the upper crust. The presence of transpression or extension, resulting in the formation of shear zones and pull-apart structures, establishes focussed ascent pathways for sulfide-bearing magmas to rapidly migrate upward. In magmas that do not reach sulfide-saturation at depth (and therefore maintain their metal content dissolved in the melt), rapid ascent would also inhibit sulfide saturation through the mechanisms discussed in this thesis. This would allow a fertile magma to reach the shallow upper crust to form porphyry mineralisation through the traditional hydrothermal porphyry model.

Magmatic Ni-Cu deposits form when exsolved sulfide melt globules settle, sequester metals, and accumulate in concentrations that are economic to mine. In many of the mixing scenarios modelled in Chapter 5, near-maximum migration velocities were required to keep entrained sulfide globules suspended. Thus, when sulfide-bearing magmas stall, or even just slow, their sulfide globules will settle out, potentially accumulating to form magmatic Ni-Cu deposits. Migration is dependent on the presence of suitable pathways and on magma viscosity. Therefore, magmatic Ni-Cu deposits would be expected in settings where the absence of rapid ascent pathways (pull-apart structures or shear zones, for example) cause migrating magmas to stall.

It is likely that the orientation of transpression is a key discriminant in determining the deposit type formed in arc settings. Formation of porphyry-Cu deposits results from establishment of magma ascent pathways that tap MASH zones and allow either rapid migration of metal-enriched, sulfide-bearing magmas or early escape of metal-enriched magmas before sulfide saturation is reached. Conversely, formation of magmatic Ni-Cu deposits results when sulfide-bearing magmas stall during migration or when compressional stress blocks the formation of dilational structures, leaving MASH zones untapped. In the context of this model, the massive sulfides near the base of the HMB sequence imply that the latter process occurred there. Loss of sulfides at depth also explains the lack of significant mineralisation in the upper crustal part of the HMB.

Synthesis

Magmatic Ni-Cu and porphyry-Cu deposits have been hitherto thought of as unrelated deposit types. Hedenquist and Lowenstern (1994), among others, indicate that porphyry-Cu deposits are the product of upper crustal hydrothermal scavenging of sulfur and chalcophile metals by Cl-rich brines. Magmatic Ni-Cu deposits, on the other hand, are inferred to form through development of immiscible sulfide liquids in silicate magmas, which interact with large amounts of magma to concentrate their siderophile and chalcophile metal content (e.g. Naldrett, 2004). These metal-rich sulfide melts then settle out at the base of a magma chamber and accumulate as massive sulfides.

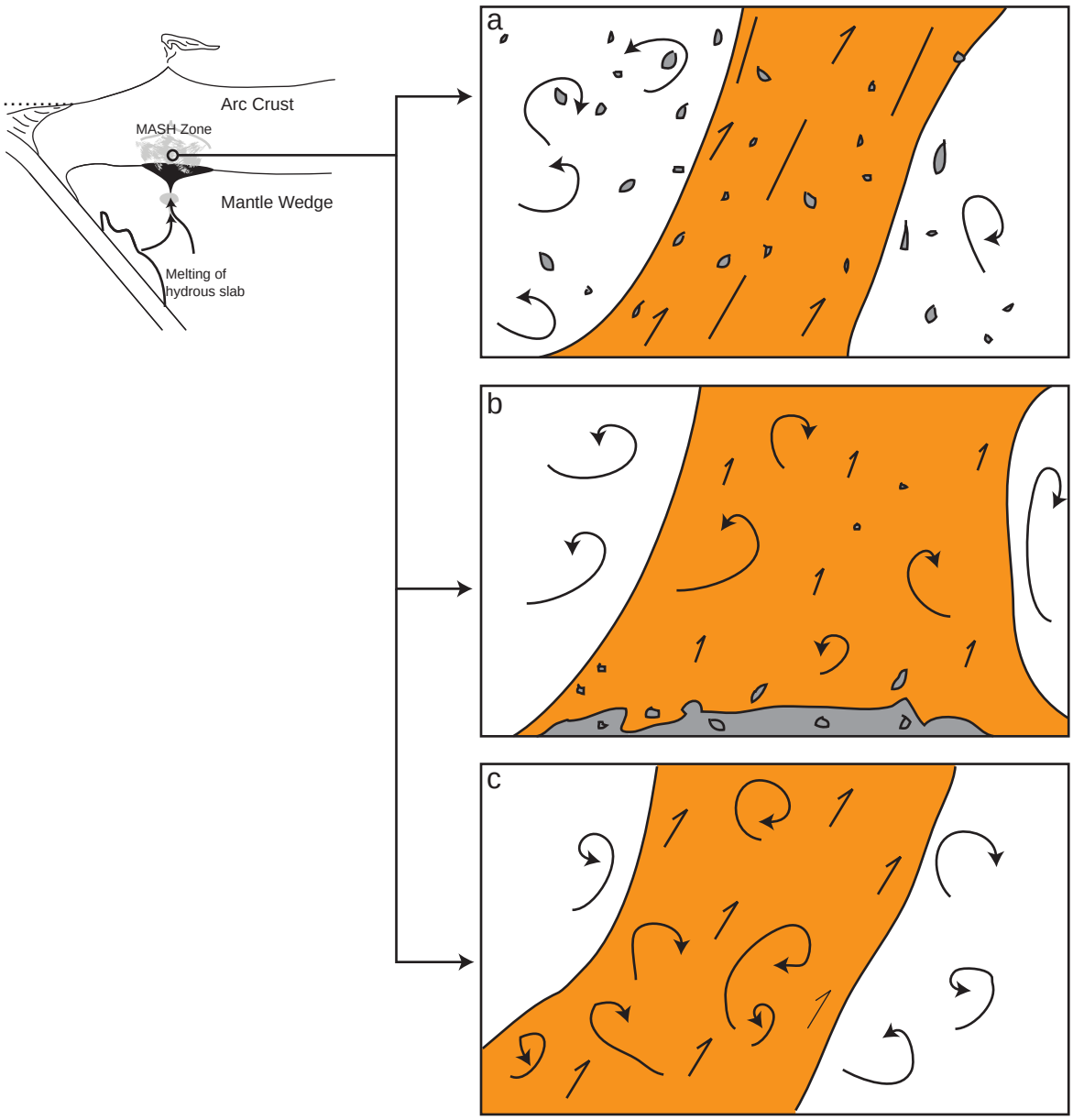

Figure 6.1: Schematic diagram of dynamic magma processes inside a MASH zone magma chamber. (a) Mixing induces sulfide melt globule generation (grey globules), which are entrained in an ascending batch of magma (in orange). (b) Mixing induces sulfide melt globule generation, but ascending magma is unable to entrain the sulfides. They settle downward and accumulate. (c) Mixing does not induce sulfide melt generation and a magma batch ascends without sulfide globules.

This study proposes that in arcs, these two disparate deposit types may be endmembers of a spectrum of magmatic processes, with immiscible sulfides playing the key role in discriminating the endmembers (Fig. 6.1). Immiscible sulfide melts may be generated during magma mixing in deep crustal MASH zones, sequestering metals from mantle-sourced magmas. However, if oxidised mafic magma is ineffectively reduced during mixing with felsic magma containing inadequate reducing material, sulfide melt exsolution is inhibited. This allows metal-rich oxidised magmas to escape to the upper crust, which is the basis of the current porphyry-Cu model that describes most deposits. In ore systems where sulfides are formed, entrainment or settling out of metal-enriched sulfides controls whether one endmember may evolve in preference to the other: (i) entrainment of sulfide globules, maintained to the upper crust, provides high concentrations of metals and sulfur for the formation of a porphyry-type deposit; (ii) settling out of sulfides at depth results in

the formation of magmatic Ni-Cu mineralisation. The observed scarcity of magmatic Ni-Cu deposits in arc settings is likely to be due to the rarity of exposures of the deeper parts of the arcs where these deposits form. Thus, if examples of deep arc sections can be found, these are considered to be highly prospective for Ni-Cu mineralisation.

Platinum group element concentrations may provide a means of testing the operation of this new model. An implication of deep crustal sulfide exsolution is that PGEs would be enriched in magmas that have undergone early (lower-crustal) sulfide exsolution because of the involvement of mantle-sourced magmas, which are thought to have elevated PGE concentrations (see Barnes et al., 1987). Magmas that entrained these sulfides, and that are later involved in porphyry Cu deposit genesis, would carry this signature into the deposit. Those not having undergone early sulfide saturation would be PGE-poor. Data collected from floatation concentrates of major porphyry deposits around the world show that PGE enrichment occurs in certain types of porphyries (Tarkian and Stribrny, 1999; Auge et al., 2005). These studies both hypothesise that mantle contributions may be responsible for providing precious metals during the development of porphyry magmas. MASH zone mixing of the type discussed here is one process by which fertile mantle magmas could contribute their precious metals to porphyry deposits, thereby accounting for these PGE enrichments.

Conclusions

Magma mixing is a prevalent process in the OGC of the northern Japan Arc, which is a MASH zone analogue. Mixing processes are likely related to the development of massive, but subeconomic sulfide mineralisation found there. The generation of felsic partial melts of graphite-rich Nakanogawa Group metasediments resulted from gabbroic underplating of the lower crust. These melts mixed with the gabbroic magmas, resulting in the hybrid compositions found throughout the OGC.

Graphite readily consumes oxygen, thereby affecting the oxygen fugacity of melts that contain it. Sulfide is much less soluble than sulfate in silicate melts and the solubility gap between sulfate and sulfide is termed the 'sulfide fence'. The reduction of an oxidised, sulfate-rich mafic melt by mixing in of graphite-rich felsic partial melts can result in large amounts of sulfide oversaturation by the change to sulfide stability across the sulfide fence. The exsolving sulfide melt concentrates chalcophile and siderophile metals, depleting the silicate magma.

Since the silicate melt itself no longer carries significant metal content, the retention of the metal-rich sulfide phase controls ore deposit formation. The retention of this phase is reliant on the ability of a magma to migrate more quickly than the sulfide melt is able to settle. Sulfide globule sizes typical of and larger than those observed in the OGC settle at velocities exceeding maximum migration velocities in liquidus magmas. Therefore, some crystallisation is necessary to evolve the melt component enough to allow sulfide retention. In melts representative of the sulfide-bearing compositions in the OGC, ~ 20% crystallisation is necessary to allow continuing sulfide retention if maximum migration velocities are sustained from MASH zone exit to final emplacement depth. Magmas that do not contain or do not mix with adequate reductant remain oxidised and metal-rich, and may then form ore deposits through the accepted porphyry model without ever developing sulfide melts.

Transpressive arc settings allow rapid ascent of magmas by favouring the development of vertical dilatational structures, such as dikes, and shear zones. Arc settings where compression dominates favour the development of horizontal dilatational structures, with vertical pathways to the upper crust sealed. This allows for long-lived, untapped MASH zones, but not the escape of magmas beyond their generation sites. In transpressive arcs, sulfide-bearing magmas from MASH zones may utilise permeable pathways to rapidly migrate upward. The sustained entrainment of sulfides allows metal-rich magmas to reach the upper crust. These magmas may then participate in porphyry Cu deposit genesis by releasing their metals to the pertinent mineralisation systems. Conversely, the lack of permeable translithospheric ascent pathways blocks sulfide-bearing magmas from migrating away from MASH zones. The stalling of these magmas in their generation sites allows the sulfides to settle out and accumulate at the bottom of the magma chamber. These massive sulfides constitute magmatic Ni-Cu deposits. Alternatively, sulfide-bearing magmas may escape MASH zones, but may

not have a suitably continuous path to the upper crust. Stalling at any point during ascent will allow sulfide globules to settle out and form a magmatic Ni-Cu deposit. Therefore, porphyry Cu and magmatic Ni-Cu deposits fall on the ends of a bimodal ore deposition spectrum mediated by MASH zone magma modification.

Directions for exploration and future research

The findings of this study imply an association between magmatic Ni-Cu and MASH zones in compressive arcs where graphitic sediments and deep crustal exposure are present. Porphyry Cu deposits are likely to be found in arcs where there is little graphitic sedimentary material to contribute to the development of sulfides and where tensional tectonic configurations allow for the development of translithospheric rapid magma ascent pathways. Future research should take into consideration the role that mantle-sourced magmas ultimately play at the beginning of the magma gestation process. This involvement should result in the presence of elevated PGE contents in porphyry Cu deposits if exsolved sulfide melts are involved in ore genesis, in addition to their elevated chalcophile content.

Considerable scope for research yet exists to determine timelines of mixing in MASH zones. The data used in this study were exclusively obtained from whole-rock powders. Although the whole rock samples used in this project were chosen and processed with care, microanalysis techniques on intact specimens would be the next step in refining the interpretations. This is especially the case in inhomogeneous settings, where several distinct components can contribute to final magma compositions. Considering the high resolution of new microanalysis techniques, magma mixing is a process that would greatly benefit from LA-ICP-MS or electron microprobe to determine not only mineral-specific trace element values, but also isotopic ratios, with a view to dating and to source composition determination.

There continues to be uncertainty in the factors that control sulfur solubility, particularly as sulfide. Metals will continue to be important for technological development, but rare metals like the PGE and several trace elements will become more and more valuable in advanced computing and electronic development. Understanding where these metals come from and their ultimate sources may assist in determining directions for exploration.

References

Auge T., Petrunov R. and Bailly L. (2005) On the origin of the pge mineralization in the elatsite porphyry Cu-Au deposit, Bulgaria: Comparison with the Baula-Nuasahi complex, India, and other alkaline PGE-rich porphyries. *Canadian Mineralogist* **43**(4), 1355-1372.

Barnes S.-J., Boyd R., Korneliussen A., Nilsson L.-P., Often M., Pedersen R. B. and Robins B. (1987) The use of mantle normalisation and metal ratios in discriminating between the effects of partial melting, crystal fractionation and sulphide segregation on platinum-group elements, gold, nickel, and copper: Examples from Norway. In *Geo-Platinum 87* (eds. H. M. Prichard, P. J. Potts, J. F. W. Bowles and S. J. Cribb), pp. 113-143. Elsevier Science Publishers Ltd. U.K.

Carroll M. R. and Rutherford M. J. (1987) The stability of igneous anhydrite: experimental results and implications for sulfur behavior in the 1982 El Chichon trachyandesite and other evolved magmas. *Journal of Petrology* **28**(5), 781-801.

Hedenquist J. W. and Lowenstern J. B. (1994) The role of magmas in the formation of hydrothermal ore deposits. *Nature* **370**(6490), 519-527.

Hildreth W. and Moorbath S. (1988) Crustal contributions to arc magmatism in the Andes of Central Chile. *Contributions to Mineralogy and Petrology* **98**(4), 455-489.

Jugo P. J., Luth R. W. and Richards J. P. (2005) An experimental study of the sulfur content in basaltic melts saturated with immiscible sulfide or sulfate liquids at 1300°C and 1.0 GPa. *Journal of Petrology* **46**(4), 783-798.

Li C. and Ripley E. M. (2005) Empirical equations to predict the sulfur content of mafic magmas at sulfide saturation and applications to magmatic sulfide deposits. *Mineralium Deposita* **40**, 218-230.

Mayhew M. A., Wasilewski P. J. and David Johnson B. (1991) Crustal magnetization and temperature at depth beneath the Yilgarn block, Western Australia inferred from Magsat data. *Earth and Planetary Science Letters* **107**(3-4), 515-522.

Mungall J. E. (2002) Roasting the mantle: Slab melting and the genesis of major Au and Au-rich Cu deposits. *Geology* **30**(10), 915-918.

Naldrett A. J. (2004) *Magmatic Sulfide Deposits: Geology, Geochemistry, and Exploration*. Springer, Berlin. pp. 727.

Parkinson I. J. and Arculus R. J. (1999) The redox state of subduction zones: insights from arc-peridotites. *Chemical Geology* **160**(4), 409-423.

Richards J. P. (2003) Tectono-magmatic precursors for porphyry Cu-(Mo-Au) deposit formation. *Economic Geology* **98**(8), 1515-1533.

Shive P. N., Blakely B. R., Frost B. R. and Fountain D. M. (1992) Magnetic properties of the lower crust. In *Continental Lower Crust* (eds. D. M. Fountain and R. J. Arculus), pp. 145-170. Elsevier, Amsterdam.

Tarkian M. and Stribrny B. (1999) Platinum-group elements in porphyry copper deposits: a reconnaissance study. *Mineralogy and Petrology* **65**(3), 161-183.

Appendix A: Sample localities, fieldbook notes, and sample map

The following pages detail sample numbers, GPS sample localities (taken at outcrop and based on the WGS 84 grid), and a scanned copy of the 1:50000 topographic field map with sample locations marked. Every sample mentioned in the thesis and extra samples taken, but not addressed in the text, are included for completeness. Next to each sample is the text from the field notebook used during the fieldwork. The abbreviations, as used in the book, are included to save space; an alphabetical listing to help decode the notes is provided as a footnote to the table.

Sample	Fieldbook Notes	Location (WGS 84)	
		Latitude	Longitude
HID12a	Nikambetsu tonalite	42° 05’ 24.8” N	143° 10’ 26.4” E
HID12c	Nikambetsu tonalite	Same as above	
OS1	migmatite w chiastolite porphyroblasts; oriented sample	42° 06’ 1.8” N	143° 08’ 23.5” E
KR001	Horoman Mine; disseminated S in metaseds		
KR002	Gabbro in creek bed. Sulphide spots in some regions.	42° 08’ 41” N	143° 10’ 19” E
KR003	sulphide boulder from creek - disseminated	42° 08’ 41.1” N	143° 10’ 23.6” E
KR004	sulphide boulder from creek - disseminated		
KR005	massive sulphide boulder near mine entrance		
KR006	crs grained gabbro w pegmatitic patches	42° 08’ 40.1” N	143° 10’ 8.2” E
KR007	leucogranite: fairly spotty location	42° 08’ 40.1” N	143° 10’ 9.8” E
KR008	gabbro nearing mine; upstream fm 007 ~150m; med–f grd gabbro	42° 08’ 39.4” N	143° 10’ 12.7” E
KR009	sluphide-rich sample for fractionation trend	42° 08’ 41.1” N	143° 10’ 14.2” E
KR010	Cu-rich (ccp) rock from large sulphide-rich enclave in creek bed	42° 08’ 41.6” N	143° 10’ 27.8” E
KR011	gabbro w/ abd felsic veins in narrow band	42° 08’ 41.3” N	143° 10’ 30.1” E
KR012	crs gabbro w/ abd sulphides	42° 08’ 41” N	143° 10’ 31.3” E
KR013	80-90% sulphide boulder in creek bed left of headwaters	42° 08’ 41.5” N	143° 10’ 32.6” E
KR014	crs grd gabbro, up feeder creek to left	42° 08’ 43.7” N	143° 10’ 33.9” E
KR015	disseminated sulphide in gabbro	42° 08’ 46.4” N	143° 10’ 35.5” E
KR016	f grd gabbro w abd felsic dykes as @ many other sites	+200m upstream	
KR017	pl-rich leucogabbro w abd micro dikes, crs grd & spotty	42° 08’ 39.3” N	143° 10’ 39.9” E
KR018	diorite?	+50m upstream	
KR019	disseminated sulphide in gabbro	42° 08’ 36.6” N	143° 10’ 43.2” E
KR020	metased? sheared granite? lose gabbro upstream from here	42° 08’ 34.2” N	143° 10’ 54.3” E
KR021	sheared granite (bt-rich); suspect mix of granite + metaseds @ 020	42° 08’ 35.3” N	143° 10’ 57” E
KR022	med grd gabbro pl rich fm below gabbro free zone	42° 08’ 33” N	143° 10’ 51.8” E
KR023	am/px gabbro crs grd	42° 09’ 1.3” N	143° 10’ 22” E
KR024	med bt, qz, fsp tonalite/granite(?)	42° 08’ 23.2” N	143° 09’ 35.5” E
KR025-1/-2	-1: med gabbro w S2- minerisation; -2: tonalite	42° 08’ 3.4” N	143° 09’ 50.5” E
KR026	med bt, qz, fsp tonalite like 024	42° 08’ 12.9” N	143° 10’ 14.2” E
KR027-1/-2	cntc b/w gabbro (-1) and tonalite (-2) shows S2-	42° 08’ 26.7” N	143° 09’ 48.7” E
KR028	f grd gabbro	42° 08’ 34.6” N	143° 09’ 1” E
KR029	px and ol gabbro - cumulate? V well zoned ol; v crs in some	42° 09’ 41.9” N	143° 07’ 3” E
KR030ABC	med grd cumulate + crs and megacrystic gabbros	42° 09’ 35.7” N	143° 07’ 5.6” E
KR031	granitic gneiss	42° 09’ 25.6” N	143° 05 39.1” E
KR032	two px gabbro	42° 09’ 20.9” N	143° 06’ 4.4” E
KR033	med cumulate	42° 09’ 20.2” N	143° 06’ 6.4” E
KR034-1/-2	-1: f grd gabbro in cG unit; -2: gneiss - partly melted	42° 08’ 5.7” N	143° 06’ 12.4” E
KR035	-1: melt vein material fm migmatite; -2: metased migmatite	42° 08’ 4.5” N	143° 06’ 12.6” E
KR036	psammitic segregation in migm	42° 07’ 55.8” N	143° 06’ 13.1” E
KR037-1/-2	-1: qztofldspthc migm from Nikambetsu; -2: tonalite @ same lcn	42° 06’ 2.7” N	143° 08’ 22” E
KR038	intermediate cmpsn intrusion in migm along Nikambetsugawa	42° 06’ 1.9” N	143° 08’ 39.8” E
KR039	porphyritic fsp-bt-am-ol gbro or diorite, metasomatised & w S2-	42° 07’ 6” N	143° 09’ 20.8” E
KR040	f–med gabbro in cG unit. Drkr variant.	42° 07’ 46.7” N	143° 06’ 55.6” E
KR041A	undeformed host	42° 12’ 19.8” N	143° 14’ 37.6” E
KR041B	graphitically alt host	Same as above	
KR041C1	nodules w sph pyrr	Same as above	
KR041C2	as C1	Same as above	
KR042	host rock alt gradually nearing gphtic vein. Bt fresher away fm vein.	Same as above	
KR043-1	f gr diorite intruded by -2	42° 07’ 1.9” N	143° 09’ 30.7” E

Sample	Fieldbook Notes	Location (WGS 84) Latitude	Longitude
KR043-2	crs grn diorite. Only -2 contains incls of -1	Same as above	
KR043-3	not recorded in Field Book. Prob from offcuts during t.s. processing	Same as above	
KR044-1	sulphide outcrop: -1 disseminated	42° 06’ 55.8” N	143° 09’ 40” E
KR044-2	massive S2-	Same as above	
KR044-3	crs grd host(?)	Same as above	
KR045-1/ -2/-3	intermediate cmpsn w crs and f phases in cntc	42° 06’ 55.1” N	143° 09’ 53” E
KR046-1/-2	-1: qz-bt-fsp diorite near creek headwall; -2: crsr grd region in o.c.	42° 06’ 50.5” N	143° 10’ 4.5” E
KR047	bt-rich intermediate	42° 07’ 1.3” N	143° 09’ 6.9” E
KR048	sulphide globule samples from Horoman River		
KR049a	sulphide globule samples from Nikambetsu River		
KR049	crs gabbro	42° 06’ 5.6” N	143° 08’ 40.1” E
KR050	bt-rich andalusite migm	42° 05’ 53.9” N	143° 07’ 53.4” E
KR057.2	sheared tonalite (?)	42° 09’ 8.8” N	143° 04’ 59.5” E
KR060.2	gabbro next to contact with tonalite	42° 06’ 4.5” N	143° 08’ 38.9” E
KR061	mafic tonalite (?) abd dsmntd sulfide	42° 06’ 7.2” N	143° 08’ 48.4” E
KR062	tonalite with sulfide	42° 06’ 33” N	143° 08’ 52.8” E
KR071	tonalite containing many enclaves; foliated 310/42°	42° 05’ 24.8” N	143° 10’ 26.4” E
KR091.2	tonalite/leucogabbro from o.c. with broken up gabbro veins next to leucogabbro; o.c. 20m to south in creek	42° 08’ 38.1” N	143° 09’ 56.0” E
KR092.2	S2- bearing gabbro; o.c. also veined as previous o.c’s; o.c. 20m downstream from given location	42° 08’ 37.4” N	143° 09’ 56.0” E
KR097	crd tonalite, sheared; foliation N/NW	42° 05’ 28.0” N	143° 10’ 27.1” E

Abbreviations:

abd = abundant; alt = altered; b/w = between; cG = coarse-grained metasomatic unit (See Chapter 2 for discussion of this unit); cmmn = common; cmpsn = composition; cntc = contact; crs(r) = coarse(r); drkr = darker; dsmntd = disseminated; f = fine; fm = from; gbro = gabbro; grd = grained; gpht(ic) = graphite(ic); ilm/mt = ilmenite/magnetite; incls = inclusions; intrstl = interstitial; lcn = location; med = medium; migm = migmatite; mnrlzn = mineralisation; mnrlgy = mineralogy; ndl = needle; o.c. = outcrop; qztofldspthc = quartzofeldspathic; S2- = sulphide; s.z. = shear zone; shrd = sheared; sig = significant; sphcl = spherical; v = very; w = with; wx = weathered. Mineral abbreviations are consistent with Siivola, J. and Schmid, R. 2007. Recommendations by the IUGS Subcommission on the Systematics of Metamorphic Rocks: Web version 01.02.07 <http://http://www.bgs.ac.uk/scmr/home.html> (Accessed 24.11.2008).

Appendix A

Sample Map

The map on the facing page is a high-resolution scan of the original 1:50000 topographical field map of southeastern Hokkaido, Japan. Contour interval is 20 m. Elevations marked along outside margin of map. Sample numbers and locations are written in pencil.

This map based on the 1:50,000 scale topographic map issued by the Geographical Survey Institute of Japan © Geographical Survey Institute, Government of Japan, used with permission.

Appendix B: Geochemical data

This appendix provides comprehensive tables of all geochemical data collected during the study. It is divided into three sections:

- Table B1-1: Major elements and total sulfur
- Table B2: Trace elements
  - Table B2-1: Trace elements (excluding rare earth elements)
  - Table B2-2: Rare earth elements
- Table B3: Platinum group elements
- Table B4: Isotopes
  - Table B4-1: Nd isotopes
  - Table B4-2: S isotopes

All analyses for major element, trace element, and Nd isotopes were collected from whole rock powders. Platinum group element and S isotope data were collected on whole rock powders and sulfide separates as indicated in the data tables.

Analytical Methods

Samples were milled to powders in a tungsten carbide mill for XRF major element analysis and in a zirconia mill for ICPMS-AES trace element and Nd isotope analysis. Powders for platinum group element analyses were milled to powders in zirconia or agate. Sulfide separates for platinum group element analyses and S isotopes were prepared by milling in agate followed by sieving for the desired size fraction ($180\,\mu m < \sigma < 220\,\mu m$).

Analyses for major elements were performed through lithium metaborate fusion-disc XRF at the James Cook University Advanced Analytical Centre (JCU-AAC) on whole-rock powders. For trace elements, combined nitric, perchloric, and hydroflouric acid sealed-bomb microwave-oven digestion was used to prepare whole-rock powders using ICPMS-AES. Analyses were performed using a Varian Liberty Series II ICP-MS housed at the JCU-AAC. Indium was used as an internal standard to check for instrument drift during analysis.

Total sulfur analysis was performed by infrared spectroscopy at GeoLabs. Each sample was combusted in an oxygen-rich environment to oxidise the sulphur in the sample matrix. The vapourised sulfur-containing stream was then analysed by infrared absorption.

Platinum group element analyses were performed by the nickel sulfide fire assay method at Geolabs in Ontario, Canada. Whole rock and sulfide separate powders were fused with a nickel and sulfur mixture to produce a sulfide button. This button was then dissolved in acid followed by coprecipitation with Te, producing a PGE concentrate containing Ru, Rh,

Pd, Pt, Ir, and Au tellurides. The concentrate was dissolved in aqua regia prior to analysis by ICP-MS.

Whole-rock Nd isotope analyses were carried out at the University of Melbourne School of Earth Sciences Multi-Collector ICP-MS Isotopic Analysis Facility. Sample preparation was completed using combined nitric and hydroflouric acid sealed-bomb digestion. Standards were analysed before and after each sample run and repeat analyses were performed during sample runs to check for instrumental calibration and drift.

Sulfur isotope data was obtained using a FiniganMAT elemental analyser-continuous flow isotope ratio mass spectrometer at Monash University. Whole rock powders were combined with ~ 0.5 gm of VO_5 in SnO_2 cups and combusted in an oxidising furnace column at 950°C. Standards were included preceding and following each sample run to allow for calibration and drift correction.

Detection Limits

Detection limits were provided by the relevant labs (Table B5). For major elements, only the detection limit of SO_3 is listed. The analyses of the rest of the elements exceeded the detection limits of the instrument by several orders of magnitude.

Table B1 Major elements and total S

Sample	SiO_2	TiO_2	Al_2O_3	Fe_2O_3	MnO	MgO	CaO	Na_2O	K_2O	P_2O_5	SO_3	LOI	SUM	Total S
HID12a	63.5	0.76	17.0	6.50	0.07	2.54	1.85	2.86	3.02	0.15	0.01	2.19	100.4	0.01
HID12c	63.5	0.81	16.7	6.92	0.07	2.67	2.38	3.30	2.96	0.22	0.02	1.42	100.9	0.40
OS1	63.2	0.87	17.2	7.31	0.08	2.71	2.46	2.25	2.38	0.16	bd	1.39	100.0	0.36
KR002	52.5	1.18	15.9	9.08	0.15	6.87	9.09	2.53	0.92	0.11	bd	2.00	100.3	0.01
KR005	sulfide separate													33.5
KR006	49.4	0.44	17.6	5.43	0.10	10.6	13.0	1.94	0.30	0.05	0.01	1.77	100.7	0.01
KR007	77.9	0.09	12.9	0.54	0.02	0.34	0.87	3.48	4.35	0.02	bd	0.27	100.8	bd
KR008	53.8	1.01	15.5	8.64	0.17	7.64	9.84	3.02	0.26	0.10	bd	0.99	101.0	0.01
KR011	56.4	0.68	15.8	7.17	0.14	6.36	8.80	3.25	0.95	0.10	0.02	1.32	101.0	0.10
KR017	57.7	0.92	17.0	6.48	0.11	5.43	7.10	3.21	1.07	0.15	0.01	1.76	100.9	0.02
KR018	58.5	1.26	16.0	8.11	0.14	4.24	6.26	3.30	0.89	0.19	bd	1.18	100.0	0.01
KR019	56.8	0.71	16.9	6.97	0.13	6.19	7.24	2.38	1.16	0.10	bd	1.98	100.6	0.04
KR020	64.9	0.68	16.3	5.99	0.27	2.43	2.38	2.66	2.90	0.11	0.01	1.95	100.6	0.21
KR021	62.5	0.72	18.0	5.78	0.11	2.44	2.75	2.89	3.30	0.09	0.02	2.35	100.9	0.23
KR023	52.3	0.61	14.6	6.79	0.12	9.99	10.5	1.95	1.92	0.05	0.01	2.11	100.0	bd
KR024	65.7	0.92	15.8	5.89	0.08	2.40	3.00	3.26	2.52	0.20	bd	0.70	100.5	0.19
KR025.1	54.0	1.15	16.2	8.71	0.14	6.10	8.58	2.64	1.71	0.15	bd	0.78	100.1	0.16
KR025.2	63.7	0.84	16.0	6.18	0.08	3.07	3.81	3.62	1.91	0.11	0.03	1.23	100.7	0.30
KR026	65.8	0.87	15.8	5.59	0.08	2.27	3.54	3.74	2.37	0.17	0.02	0.68	100.9	0.17
KR027.1	55.3	0.54	16.4	6.49	0.11	7.69	9.27	2.77	0.73	0.06	bd	0.90	100.2	0.12
KR027.2	72.1	0.48	15.2	2.11	0.02	1.28	4.03	3.82	1.11	0.14	0.02	0.50	100.8	bd
KR028	53.8	1.15	16.8	7.89	0.15	6.63	9.64	2.90	0.32	0.16	bd	1.07	100.5	0.01
KR030A	43.2	0.07	12.0	9.00	0.12	29.4	5.94	1.06	0.03	0.02	0.02	0.18	100.9	0.05
KR031	64.2	0.48	17.1	4.16	0.09	3.05	5.55	3.63	1.53	0.09	bd	0.71	100.6	0.01
KR035.2	69.6	0.53	14.4	4.50	0.06	2.33	3.32	3.51	1.04	0.09	bd	0.56	99.9	0.08
KR036	63.1	0.80	17.9	5.63	0.09	2.46	2.60	3.23	2.84	0.15	bd	1.74	100.6	0.03
KR037.1	65.0	0.69	15.9	5.69	0.07	2.34	3.53	2.98	2.17	0.15	bd	1.19	99.7	0.62
KR037.2	68.1	0.69	16.1	3.87	0.06	1.48	3.57	3.39	2.40	0.15	bd	0.62	100.4	0.05
KR039	51.4	0.73	20.2	5.83	0.10	6.28	10.5	3.03	0.59	0.09	0.01	1.43	100.1	0.01
KR043.1	54.2	0.97	16.6	7.48	0.13	6.90	9.10	2.97	0.91	0.11	bd	1.05	100.4	0.01
KR043.2	56.4	1.23	16.9	8.45	0.14	4.67	7.02	3.49	1.36	0.20	0.02	0.69	100.6	0.12
KR044.1	48.0	0.78	14.5	15.2	0.17	6.73	8.44	2.57	0.36	0.09	0.07	2.11	99.0	3.44
KR044.2	sulfide separate													31.8
KR044.3	50.6	0.75	17.4	8.58	0.13	8.61	10.2	2.69	0.29	0.09	0.04	1.42	100.8	2.77
KR045.1	56.7	0.84	16.9	7.45	0.13	6.41	7.43	2.57	0.72	0.12	bd	0.94	100.2	0.04
KR045.2	54.5	0.95	16.6	7.85	0.15	6.77	6.38	3.58	1.53	0.12	bd	2.01	100.4	0.10
KR046.1	54.2	0.93	17.7	6.81	0.13	7.07	9.36	2.45	0.82	0.11	bd	1.04	100.7	0.01
KR047	60.0	1.19	17.1	8.03	0.13	3.60	5.29	3.45	1.07	0.19	bd	0.64	100.7	0.30
KR049	48.1	0.80	21.3	6.74	0.11	9.72	10.8	2.31	0.05	0.07	bd	0.29	100.2	0.05
KR050	65.4	0.73	16.1	6.03	0.06	2.17	2.34	2.45	2.88	0.19	bd	1.63	100.0	0.34
KR057.2	61.8	0.40	18.3	4.59	0.10	3.71	5.82	3.98	0.72	0.07	bd	1.32	100.8	0.01
KR060.1	74.5	0.25	14.2	1.46	0.02	0.45	1.72	4.37	2.84	0.05	0.01	0.39	100.2	bd
KR060.2	59.4	0.96	16.7	8.49	0.12	3.83	4.47	2.90	1.82	0.07	bd	1.07	99.8	0.56
KR061	47.5	0.58	19.2	7.01	0.11	10.6	9.72	2.13	0.45	0.07	bd	2.66	99.9	0.05
KR062	58.8	1.09	17.6	5.93	0.10	4.55	6.76	3.21	1.37	0.14	bd	0.74	100.3	0.07
KR071	64.3	0.73	16.7	5.94	0.08	2.36	2.25	2.70	2.97	0.15	bd	1.53	99.7	0.32
KR091.2	76.8	0.43	12.3	1.05	0.01	0.29	0.85	1.84	5.92	0.05	bd	0.30	99.8	0.01
KR092.2	53.4	0.83	16.8	6.99	0.13	7.58	9.72	2.80	0.72	0.10	bd	1.08	100.1	0.01
KR097	64.7	0.69	16.6	5.79	0.07	2.31	2.34	2.75	2.80	0.16	bd	1.47	99.7	0.35

Notes: bd = below detection limit; all data in wt. %

Table B2 Trace elements (excluding rare earth elements)

Sample	Ag	Al	As	Ba	Bi	Cd	Co	Cr	Cu	Fe	Ga	Ge	Hf
HID12a	0.11	70400		559	0.22		24.1	59.1	43.6	40600	26.9	2.07	0.03
HID12c	0.14	71400		474	0.25		32.1	65.4	61.1	42300	25.6	2.02	bd
OS1	0.08	35600	bd	454	bd	0.08	31.6	366	76.0	27300	31.1	5.30	bd
KR002	0.06	63400	0.99	191	bd	0.01	37.5	202	32.1	51900	15.7	3.60	1.24
KR006	0.08	95400		21.7	0.11		43.6	682	47.7	37600	9.90	1.09	0.46
KR007	bd	60700		131	bd		33.7	1.75	2.71	3100	12.4	1.19	0.04
KR008	0.11	63000	0.76	63.7	bd	0.12	47.5	284	4.78	51400	13.3	3.84	2.13
KR011	0.12	74800		275	0.04		40.2	246	105	46600	17.5	1.76	0.38
KR017	0.07	81300		253	0.11		36.1	157	29.5	43000	18.4	1.80	2.18
KR018	0.21	60400	1.24	183	bd	0.16	29.0	134	26.5	45600	18.2	3.84	3.52
KR019	0.19	68300	2.49	220	bd	0.18	43.7	284	39.9	39900	18.9	3.68	2.43
KR020	0.59	39000	1.55	631	bd	0.17	33.1	132	111	32900	31.5	4.09	5.48
KR021	0.31	38400	0.73	720	bd	0.54	27.4	133	61.5	30000	35.4	3.95	3.25
KR023	0.09	71100		446	bd		46.2	553	20.7	45500	17.3	1.56	0.48
KR024	0.72	41600	4.52	458	bd	0.22	24.9	181	48.0	31800	29.3	4.33	8.94
KR025.1	0.26	64700	4.86	292	bd	0.17	49.8	505	43.2	50000	23.7	4.62	3.33
KR025.2	0.08	71800		667	0.04		32.2	106	53.2	40800	26.2	1.62	0.05
KR026	0.06	70900		914	bd		32.3	62.4	32.8	36200	31.4	1.86	0.05
KR027.1	0.20	30900	3.33	185	bd	0.27	64.5	662	142	39400	17.5	3.61	2.53
KR027.2	bd	68800		305	bd		47.0	7.65	6.87	13300	17.9	1.13	0.05
KR028	0.19	85500	1.90	72.7	bd	0.15	53.0	442	44.0	49800	17.1	4.18	2.54
KR030A	0.04	53900		2.14	bd		79.5	278	94.2	61200	4.61	1.17	0.03
KR031	0.26	65300	1.58	277	bd	0.14	21.5	139	17.5	46000	23.0	3.44	3.52
KR035.2	0.24	48500	1.11	263	bd	0.12	22.2	281	32.1	17800	21.7	3.44	3.00
KR036	0.09	58100	1.72	377	bd	0.07	12.4	248	51.7	28700	30.7	4.68	bd
KR037.1	0.08	61700	bd	370	bd	0.01	31.9	446	101	32100	26.6	4.61	bd
KR037.2	0.43	44000	bd	466	0.06	0.17	13.2	62.4	20.8	26900	29.5	3.36	5.58
KR039	0.07	96200		100	bd		40.5	237	44.4	37300	14.6	1.42	0.75
KR043.1	0.09	51900	8.89	216	bd	0.11	55.0	644	29.8	22700	20.8	4.17	1.26
KR043.2	0.05	77600		461	bd		41.9	110	29.4	51900	24.8	2.09	0.20
KR044.1	2.69	67700	3.03	97.5	2.20	1.38	320	613	8.60	44100	15.2	4.91	1.34
KR044.3	0.28	84200		66.5	0.87		97.4	442	483	56300	13.1	1.60	1.21
KR045.1	0.27	54700	6.81	255	bd	0.18	48.9	576	23.2	82300	21.5	3.93	3.35
KR045.2	0.11	63500	31.2	277	bd	0.15	63.0	59.7	592	41400	22.0	4.07	1.06
KR046.1	0.32	63300	2.54	138	bd	0.14	50.8	60.5	616	47300	17.4	3.32	3.65
KR047	0.15	53100	4.23	311	bd	0.13	39.8	244	73.7	30900	26.7	4.39	1.50
KR049	0.14	62200	bd	5.77	bd	0.11	81.0	110	101	51500	14.1	3.06	2.03
KR050	0.10	80400	bd	420	0.09	0.06	23.5	281	55.4	38400	28.1	4.46	bd
KR057.2	0.20	38100	bd	223	0.29	0.10	27.3	107	13.5	26300	21.8	3.18	1.83
KR060.1	bd	55500		584	bd		35.2	0.21	3.57	8530	23.0	1.25	0.20
KR060.2	0.22	60200	bd	443	bd	0.11	45.2	343	127	24900	30.2	4.75	1.70
KR061	0.14	57100	1.37	52.8	bd	0.20	88.7	257	107	49200	13.9	3.04	1.42
KR062	0.24	65700	1.83	274	bd	0.13	33.2	295	31.9	35100	25.1	3.90	3.22
KR071	0.35	54100	bd	592	0.09	0.15	26.9	158	66.7	28300	34.7	4.73	3.44
KR091.2	0.42	51700	bd	1640	bd	0.09	3.98	14.9	9.24	33100	54.7	1.98	5.27
KR092.2	0.12	41800	5.99	106	bd	0.12	57.1	880	73.5	6210	17.7	3.99	1.79
KR097	0.26	67200	bd	546	bd	0.01	27.6	162	76.1	42300	33.2	4.58	2.40

Notes:

bd = below detection limit; all data in ppm.

Table B2-1 Trace elements (excluding rare earth elements), cont'd

Mn	Nb	Ni	Pb	Rb	Sb	Se	Sn	Sr	Ta	Te	Ti	Tl	W	Zn
482	6.10	20.4	15.1	67.6	bd	bd	0.85		0.49	bd		0.44	134	100
541	6.81	48.5	14.9	69.0	bd	bd	0.95		0.55	bd		0.44	141	116
365	11.4	81.0	12.4	60.2	bd	5.54	1.23	277	0.76	0.14	3450	0.32	2.70	166
994	3.43	27.8	3.45	22.3	0.14	2.53	0.67	264	0.39	0.34	6910	0.11	1.27	100
760	0.50	92.6	1.08	11.2	0.28	bd	0.47		0.60	bd		0.05	88.6	35.0
28.5	1.58	1.08	23.1	76.9	bd	bd	0.15		0.16	bd		0.37	391	16.2
1050	2.48	61.5	3.78	3.50	bd	3.34	1.48	321	0.27	0.19	6220	bd	1.42	87.0
1070	2.27	62.2	7.12	29.8	bd	bd	0.76		0.25	bd		0.08	128	68.6
843	3.58	35.3	8.18	30.6	bd	bd	1.09		0.32	bd		0.15	126	71.0
862	6.31	29.5	4.97	23.6	bd	3.70	1.18	240	0.45	0.27	7280	0.13	2.03	121
766	4.77	96.3	18.0	36.1	bd	3.59	1.70	274	0.40	0.33	4370	0.17	3.27	103
1630	8.21	77.3	11.0	68.7	bd	4.13	1.36	256	0.41	0.17	3830	0.36	1.48	115
623	7.31	52.3	8.58	68.3	bd	3.98	1.59	246	0.33	0.08	4060	0.40	0.29	155
950	0.87	112	4.79	69.0	bd	bd	0.38		0.11	bd		0.28	76.9	57.0
484	9.86	57.1	10.9	69.5	bd	4.66	1.40	231	0.50	bd	5510	0.40	1.68	119
923	5.96	55.3	7.11	49.0	bd	5.13	1.21	272	0.43	bd	6750	0.25	9.45	133
590	5.23	69.3	9.52	61.0	bd	bd	0.85		0.38	bd		0.31	114	86.5
607	6.31	35.4	12.9	63.8	bd	bd	0.37		0.37	bd		0.33	177	89.9
185	2.54	357	7.04	17.1	bd	4.23	0.72	230	0.27	0.13	3010	0.08	4.44	84.5
145	3.27	37.6	9.47	41.2	bd	bd	0.64		0.27	bd		0.19	354	28.6
973	4.32	79.5	3.22	5.26	bd	5.55	0.80	239	0.27	bd	3990	bd	1.67	105
987	0.28	913	0.10	0.19	bd	bd	bd		0.12	bd		bd	162	40.7
943	4.22	45.3	9.39	32.2	bd	5.09	1.56	293	0.33	0.16	6920	0.19	4.11	78.8
392	5.85	65.1	7.76	18.9	bd	4.26	0.53	226	0.67	bd	0.10	2040	0.93	85.1
430	11.4	18.4	13.1	77.2	bd	4.98	2.56	394	0.87	bd	3620	0.39	5.47	151
506	10.2	120	10.2	67.6	bd	5.14	0.88	429	0.71	bd	4500	0.38	4.50	118
349	8.18	16.0	12.1	60.1	bd	4.45	2.85	180	0.57	bd	3510	0.33	0.30	91.7
767	2.04	106	4.20	15.3	bd	bd	1.01		0.27	bd		0.06	105	50.1
346	4.08	97.9	5.36	21.0	bd	5.09	1.28	265	0.30	0.31	4150	0.11	6.73	102
1030	4.94	30.4	8.07	34.3	bd	bd	0.16		0.33	bd		0.17	153	99.3
896	2.35	2660	14.1	5.52	bd	8.76	0.97	197	0.18	0.90	5750	bd	2.62	178
947	1.65	565	11.8	5.10	bd	bd	1.35		0.19	bd		bd	119	71.2
986	4.88	86.9	5.78	10.5	bd	4.10	0.42	275	0.34	0.37	4040	0.07	1.45	122
776	4.41	147	5.33	41.0	bd	4.98	2.50	265	0.35	0.28	4620	0.19	0.80	114
993	3.41	117	2.87	19.3	bd	5.03	1.18	206	0.25	0.32	5410	0.10	0.12	84.6
584	10.2	87.0	8.41	23.1	bd	4.24	0.95	384	0.68	0.25	4010	0.13	bd	150
867	1.29	334	0.15	0.54	bd	5.05	0.63	230	0.15	0.26	7910	bd	0.66	73.6
645	9.62	57.7	9.77	63.0	bd	4.93	2.56	251	0.68	bd	3980	0.34	bd	129
312	2.79	76.0	7.49	13.2	bd	4.42	1.90	364	0.26	0.13	5800	0.08	1.73	67.4
125	4.08	6.26	16.2	88.9	bd	bd	2.00		0.46	bd		0.40	295	24.1
500	9.18	159	9.08	44.7	bd	4.95	1.06	445	0.58	0.26	2030	0.26	2.15	165
630	1.84	262	2.56	10.7	bd	4.92	1.05	274	0.17	0.61	5230	bd	bd	90.0
598	7.06	29.9	6.91	37.7	bd	5.32	2.06	251	0.54	0.33	3070	0.20	0.98	96.2
507	10.9	66.6	14.1	76.8	bd	4.89	2.20	332	0.80	bd	5930	0.41	1.32	147
112	4.48	5.82	16.5	76.5	bd	4.66	0.09	170	0.22	bd	6720	0.37	bd	17.7
bd	3.14	144	5.27	16.8	bd	5.92	3.44	219	0.22	0.59	2480	0.09	3.82	99.3
798	10.2	72.5	13.9	59.1	bd	6.09	2.00	268	0.68	bd	4240	0.37	2.53	146

Notes:

bd = below detection limit; all data in ppm.

Table B2-2 Rare earth elements

Sample	Ce	Dy	Er	Eu	Gd	Ho	La	Lu	Nd	Pr	Sc	Sm	Tb	Tm	Y	Yb
HID12a	32.5	1.53	0.56	0.77	2.51	0.24	12.2	0.06	13.8	3.44	25.2	2.92	0.33	0.07	5.67	0.45
HID12c	41.3	2.01	0.69	0.92	3.57	0.31	17.0	0.06	18.7	4.66	26.2	4.05	0.45	0.08	7.56	0.51
OS1	44.5	2.21	0.85	1.21	3.46	0.35	20.5	0.08	21.0	5.32	25.7	4.33	0.47	0.01	9.21	0.63
KR002	15.8	4.22	2.60	1.26	3.67	0.84	6.33	0.38	10.5	2.20	37.6	3.12	0.64	0.35	23.1	2.54
KR006	3.64	1.65	1.03	0.66	1.46	0.35	1.27	0.14	3.16	0.60	46.8	1.05	0.25	0.15	10.0	0.96
KR007	34.1	1.88	0.83	0.11	2.74	0.32	14.3	0.08	14.4	3.94	2.90	3.24	0.38	0.11	9.28	0.65
KR008	13.1	4.27	2.65	1.06	3.71	0.87	4.99	0.38	9.71	1.95	42.6	3.05	0.64	0.36	24.6	2.57
KR011	18.8	4.09	2.40	0.97	3.99	0.83	7.95	0.34	12.0	2.57	51.2	3.39	0.64	0.35	23.9	2.28
KR017	27.2	4.27	2.53	1.03	4.32	0.88	11.6	0.36	15.0	3.45	35.0	3.79	0.69	0.37	26.2	2.41
KR018	30.1	5.23	3.16	1.24	4.90	1.05	12.5	0.47	17.5	3.94	29.9	4.58	0.82	0.44	29.9	3.13
KR019	27.3	3.40	1.97	1.19	3.42	0.67	12.2	0.28	14.1	3.38	31.0	3.41	0.55	0.27	19.2	1.91
KR020	58.0	3.84	2.48	1.08	4.28	0.76	25.5	0.51	25.8	6.65	17.3	5.27	0.65	0.39	22.2	3.25
KR021	74.6	1.97	0.95	1.06	3.75	0.35	33.3	0.13	32.1	8.48	17.4	5.58	0.44	0.12	9.36	0.82
KR023	4.95	2.68	1.65	0.63	2.33	0.57	1.84	0.23	4.60	0.84	66.3	1.65	0.40	0.23	16.7	1.50
KR024	50.4	3.63	1.85	1.04	4.40	0.66	22.2	0.22	23.5	5.94	19.7	5.01	0.65	0.24	18.7	1.59
KR025.1	29.9	5.44	3.20	1.33	5.00	1.07	12.6	0.46	17.5	3.95	43.6	4.67	0.85	0.44	31.0	3.07
KR025.2	25.3	1.42	0.84	1.18	1.87	0.29	13.1	0.15	10.5	2.73	27.4	1.95	0.26	0.13	8.64	0.91
KR026	52.8	3.42	1.71	1.08	4.67	0.65	24.7	0.20	24.2	6.05	23.9	4.80	0.64	0.23	18.8	1.43
KR027.1	19.5	3.66	2.14	0.87	3.32	0.73	8.18	0.31	11.2	2.58	37.2	3.13	0.58	0.30	20.7	2.06
KR027.2	13.2	1.95	1.14	0.76	2.08	0.40	6.14	0.15	6.98	1.61	8.32	1.82	0.32	0.16	12.2	1.04
KR028	21.0	5.19	3.09	1.31	4.73	1.03	8.17	0.43	14.4	3.03	41.0	4.18	0.83	0.42	29.9	2.93
KR030A	0.41	0.12	0.08	0.13	0.12	0.03	0.19	bd	0.31	0.06	11.0	0.09	bd	bd	0.79	0.01
KR031	24.1	3.84	2.35	0.85	3.37	0.76	9.20	0.39	12.0	2.81	23.7	3.35	0.59	0.34	22.8	2.52
KR035.2	29.9	2.45	1.40	0.97	2.68	0.47	13.4	0.23	13.6	3.54	15.7	3.07	0.43	0.21	13.5	1.59
KR036	52.4	1.92	0.61	1.08	3.49	0.27	23.1	0.05	23.1	5.98	22.7	4.69	0.44	0.06	6.95	0.40
KR037.1	47.2	2.42	1.08	1.06	3.36	0.42	22.3	0.12	20.7	5.43	20.5	4.22	0.47	0.14	11.5	0.87
KR037.2	32.8	3.93	2.10	0.92	3.84	0.73	13.1	0.26	15.7	3.84	13.4	3.98	0.65	0.28	20.9	1.86
KR039	12.0	3.19	1.96	0.80	2.98	0.68	4.86	0.28	8.00	1.70	36.5	2.35	0.50	0.29	20.4	1.92
KR043.1	22.1	4.59	2.77	1.14	4.21	0.91	8.97	0.40	13.3	2.95	39.5	3.68	0.71	0.38	27.2	2.71
KR043.2	30.6	5.61	3.24	1.40	5.69	1.13	13.3	0.44	18.3	4.06	47.9	4.93	0.91	0.45	32.6	3.03
KR044.1	14.5	3.52	2.10	1.12	3.16	0.70	5.83	0.31	9.49	2.04	35.2	2.76	0.55	0.29	20.1	2.04
KR044.3	12.3	3.31	2.01	0.85	3.05	0.70	4.80	0.29	8.27	1.74	47.9	2.43	0.51	0.29	20.5	1.92
KR045.1	25.3	4.16	2.54	1.24	3.96	0.83	11.0	0.38	14.1	3.24	36.0	3.70	0.65	0.35	24.4	2.55
KR045.2	22.2	4.22	2.51	1.08	3.95	0.85	9.31	0.36	12.9	2.95	38.9	3.52	0.66	0.35	24.9	2.44
KR046.1	17.6	3.60	2.18	0.97	3.36	0.72	7.69	0.32	10.6	2.36	32.7	2.94	0.56	0.30	21.4	2.15
KR047	35.2	3.45	2.12	1.65	3.86	0.71	16.3	0.35	17.0	4.15	30.3	3.87	0.57	0.31	20.4	2.28
KR049	6.15	2.63	1.60	0.80	2.39	0.53	1.81	0.23	5.83	1.07	18.3	1.92	0.40	0.22	15.5	1.55
KR050	44.1	2.03	0.75	1.00	3.25	0.32	20.0	0.07	19.4	5.03	19.2	4.06	0.44	0.09	8.38	0.54
KR057.2	21.4	3.03	1.85	0.86	2.87	0.61	9.41	0.29	11.1	2.66	19.2	2.79	0.48	0.27	18.2	1.91
KR060.1	34.4	2.49	1.27	0.41	2.98	0.47	15.1	0.15	14.3	3.82	6.75	3.17	0.45	0.17	14.2	1.13
KR060.2	37.6	2.53	1.63	1.51	2.70	0.51	18.0	0.28	15.6	4.04	32.1	3.01	0.42	0.24	14.9	1.83
KR061	6.51	2.09	1.25	0.78	1.91	0.43	2.39	0.18	5.09	1.00	20.8	1.58	0.33	0.17	12.4	1.22
KR062	30.4	4.37	2.48	1.30	4.28	0.85	12.5	0.33	16.3	3.80	26.6	4.12	0.71	0.33	25.3	2.30
KR071	51.5	1.83	0.61	1.03	3.58	0.28	23.4	0.06	23.2	6.15	21.0	4.74	0.45	0.07	6.83	0.48
KR091.2	14.3	0.95	0.46	0.76	1.29	0.17	6.52	0.04	6.74	1.63	3.78	1.41	0.18	0.05	4.89	0.33
KR092.2	16.9	3.89	2.39	1.01	3.47	0.79	7.01	0.34	10.4	2.33	40.3	3.00	0.61	0.33	23.5	2.32
KR097	41.7	1.72	0.57	0.88	3.08	0.25	18.0	0.06	19.3	4.86	17.5	4.02	0.39	0.07	6.34	0.47

Notes:

bd = below detection limit; all data in ppm.

Table B3 *Platinum group elements*

Sample	Au	Ir	Pd	Pt	Rh	Ru
HID12c	0.54	0.04	2.02	0.91	0.02	0.10
KR005	35.52	2.74	63.31	0.71	1.55	11.59
KR011	1.91	0.05	2.26	1.28	0.03	0.13
KR017	0.35	0.01	0.24	0.19	bd	bd
KR023	3.72	0.01	0.43	0.18	bd	bd
KR025.2	2.41	0.08	1.88	0.88	0.03	0.16
KR026	1.14	0.03	1.07	0.59	bd	bd
KR030A	1.42	0.23	1.46	2.02	0.1	0.50
KR031	0.32	0.02	0.27	0.43	bd	bd
KR044.1	13.85	0.57	7.69	2.60	1.03	1.11
KR044.2	7.18	11.02	17.28	0.88	7.68	47.03
KR044.3	15.94	0.48	18.58	1.98	0.39	0.98
KR045.1	0.68	0.01	0.23	0.73	bd	bd
KR045.2	0.72	0.02	0.77	0.70	bd	bd
KR047	1.78	0.05	1.77	0.95	0.03	0.11
KR049	0.23	0.01	0.29	bd	bd	bd
KR071	0.76	0.05	2.01	0.93	0.02	0.08
KR092.2	0.95	0.01	0.21	0.17	bd	bd

Notes:

bd = below detection limit; all data in ppb

Table B4-1 Nd isotopes

Sample	Rock type	Dissolution Method	Sm ppm	Nd ppm	$\frac{^{147}Sm}{^{144}Nd}$	$\frac{^{143}Nd}{^{144}Nd}$	εNd	Maximum Age	$\left(\frac{^{143}Nd}{^{144}Nd}\right)_i$	εNd_i
HID12C	S-type tonalite	high pressure	4.05	18.70	0.131	0.512610(8)	-0.5	51 ma	0.512566	-0.1
KR006	MORB-like gabbro	hotplate	1.05	3.16	0.201	0.513186(7)	10.7	51 ma	0.513119	10.7
KR008	px-hbl gabbro	hotplate	3.05	9.71	0.190	0.513044(8)	7.9	51 ma	0.512981	8.0
KR020	metasediment	high pressure	5.40	27.34	0.1193	0.512557(9)	-1.6	51 ma	0.512517	-1.1
KR020 repeat	metasediment	hotplate	5.07	25.42	0.1204	0.512566(16)	-1.4		0.512526	-0.9
KR021	metasediment	high pressure	5.58	35.01	0.0963	0.512683(8)	0.9	51 ma	0.512651	1.5
KR021 repeat	metasediment	hotplate	5.21	32.35	0.0972	0.512684(10)	0.9		0.512652	1.5
KR023	MORB-like gabbro	high pressure	1.65	4.60	0.217	0.513152(8)	10.0	51 ma	0.513073	9.8
KR023 repeat	MORB-like gabbro	high pressure				0.513137(8)	9.7			
KR024	I-type tonalite	high pressure	5.01	23.50	0.129	0.512714(8)	1.5	51 ma	0.512671	1.9
KR025.1	gabbro-diorite	high pressure	4.67	17.50	0.161	0.512874(9)	4.6	51 ma	0.512816	4.8
KR025.1 repeat	gabbro-diorite	high pressure				0.512867(9)	4.5			
KR025.2	tonalite	high pressure	1.95	10.50	0.112	0.512725(9)	1.7	51 ma	0.512688	2.2
KR026	tonalite	high pressure	4.80	24.20	0.120	0.512746(9)	2.1	51 ma	0.512706	2.6
KR031	I-type tonalite	high pressure	3.35	12.00	0.169	0.512759(7)	2.4	51 ma	0.512703	2.5
KR044.1	gabbro	hotplate	2.76	9.50	0.176	0.512982(9)	6.7	51 ma	0.512923	6.8
KR045.2	gabbro-diorite	hotplate	3.52	12.90	0.165	0.512908(8)	5.3	51 ma	0.512853	5.5
KR049	MORB-like gabbro	hotplate	1.92	5.80	0.200	0.513266(8)	12.3	51 ma	0.513199	12.2
KR061	MORB-like gabbro	hotplate	1.58	5.09	0.188	0.513149(9)	10.0	51 ma	0.513086	10.0
KR071	tonalite	high pressure	4.74	23.20	0.124	0.512597(7)	-0.8	51 ma	0.512556	-0.3
KR092.2	px-hbl gabbro	hotplate	3.00	10.40	0.174	0.512997(7)	7.0	51 ma	0.512939	7.1
KR097	S-type tonalite	high pressure	4.02	19.30	0.126	0.512611(9)	-0.5	51 ma	0.512569	-0.1

Standard	Agency	$^{143}Nd/^{144}Nd$	
		Accepted value	Measured value
BCR2	USGS	0.512640(20)	0.512640(9)
JNd-1	JGS	0.512117	0.512106(9)

Present-day CHUR	$^{143}Nd/^{144}Nd$	$^{147}Sm/^{144}Nd$
	0.512638	0.1967

Notes:

$^{143}Nd/^{144}Nd$ normalized to $^{146}Nd/^{145}Nd = 2.0719425$ (equivalent to $^{146}Nd/^{144}Nd = 0.7219$) and reported relative to LaJolla = 0.511860; internal precision (2se) ± ≤ 0.000014; external precision (2sd) ± ≤ 0.000020

External precision for $^{147}Sm/^{144}Nd$ = ± 0.2%

Decay constant ^{147}Sm = 6.54 x 10-12/yr

Concentrations for KR20 and KR21 were determined by isotope dilution with mixed ^{149}Sm-^{150}Nd tracer. These samples were dissolved in high pressure bombs with the repeats done using hotplate dissolution. This could make a difference as these likely are metasediment samples, but as it turns out the difference is not significant.

Numbers in brackets after $^{143}Nd/^{144}Nd$ values are internal precision values (±) of last digits(s) to 2 standard errors.

Table B4-2 *Sulfur isotopes*

Sample	Run 1 ‰ $\delta^{34}S$	Run 2 ‰ $\delta^{34}S$	Run 3 ‰ $\delta^{34}S$	Run 4 ‰ $\delta^{34}S$	Run 5 ‰ $\delta^{34}S$	Run 6 ‰ $\delta^{34}S$	Average ‰ $\delta^{34}S$
Blank	20.282	0	0	0	0	0	
NBS127	24.060	22.761	23.211	19.936	21.7020	24.7090	
NBS123	19.803	19.128	18.618				
HID12c	13.018	-5.248	-2.654	-4.842			-4.2735
HID12c repeat				-4.350			
KR005	-3.723	-5.124	-5.070			-10.3915	-6.2169
KR005 repeat	-6.235	-6.758					
KR013	-5.009	-8.690	-6.121			-10.5575	-6.8659
KR013 repeat	-5.703	-6.441	-5.540				
KR021	-2.133	-10.639	-6.315				-6.3623
KR024					-5.4375	-7.4375	-6.4375
KR025.2	-0.974		-4.841	-6.829		-7.7295	-5.0934
KR027.2		-5.873	2.676				-1.5985
KR030A	-3.658	10.587	18.945	0.230	4.2735	1.2085	0.7193
KR044.1						-7.5905	-7.5905
KR044.2	No data	-4.906	-5.759				-5.0470
KR044.2 repeat	-3.848	-6.553	-4.169				
KR044.3				-4.331	-5.3835	-5.6195	-5.0547
KR044.3 repeat				-4.498	-5.4415		
KR045.2					-0.6285	-0.4395	-0.5340
KR049	-5.421	4.085			6.0625	4.0345	2.1903
KR071					-7.9355	-9.7175	-8.8265
NBS127	0.898	-0.049	0.425	20.888	23.5890	24.086	

Standard	Agency	Accepted value
NBS127	NIST	20.3
NBS123	NIST	16.72

All data are ‰ $\delta^{34}S$.

Notes:

Matrix effects in residual ash affected the values in the first three runs, therefore no correction is available. Runs four to six are corrected to the NBS127 standard.

Table B5 *Detection limits*

Element	Detection Limit		Element	Detection Limit	
Majors			**PGE**		
S and SO_3	0.01	wt%	Au	0.75	ppb
			Ir	0.04	ppb
REE			Pd	0.11	ppb
Ce	0.1	ppm	Pt	0.14	ppb
Dy	0.1	ppm	Rh	0.08	ppb
Er	0.1	ppm	Ru	0.13	ppb
Eu	0.1	ppm			
Gd	0.1	ppm			
Ho	0.1	ppm			
La	0.1	ppm			
Lu	0.1	ppm			
Nd	0.1	ppm			
Pr	0.1	ppm			
Sc	0.1	ppm			
Sm	0.1	ppm			
Tb	0.1	ppm			
Tm	0.1	ppm			
Y	0.1	ppm			
Yb	0.1	ppm			
Trace Elements					
Ag	1	ppm			
Al	1	ppm			
As	2	ppm			
Ba	1	ppm			
Bi	1	ppm			
Cd	1	ppm			
Co	1	ppm			
Cr	1	ppm			
Cu	1	ppm			
Fe	1	ppm			
Ga	~5	ppm			
Ge	1	ppm			
Hf	1	ppm			
Mn	1	ppm			
Mo	1	ppm			
Nb	1	ppm			
Ni	1	ppm			
Pb	1	ppm			
Rb	1	ppm			
Sb	1	ppm			
Se	2	ppm			
Sn	1	ppm			
Sr	1	ppm			
Ta	1	ppm			
Te	1	ppm			
Ti	1	ppm			
Tl	1	ppm			
W	1	ppm			
Zn	5	ppm			

Appendix C: Electron microprobe spot analyses

Piston cylinder experiments in Chapter 4 were used to produce a set of homogenous quenched glasses. After mounting in epoxy discs, they were analysed for major elements and sulfur by wavelength dispersive spectroscopy (WDS) on the Cameca SX100 electron probe at the Research School of Earth Sciences, Australian National University (ANU). Analyses for sulfur were performed using the method of O'Neill and Mavrogenes (2002) with a few modifications. Sulfur counts were collected for ~120 seconds on one PET crystal to achieve a limit of detection (LOD) of ~500 ppm. Beam conditions of 15 kV accelerating voltage, 100 nA beam current, and mixed beam sizes of 20 μm and 50 μm were used (see Table 2 in Chapter 4). Each glass was analysed at 20 different spot locations and analyses that showed higher than expected variation were reanalysed. The data acquired for each spot analysis is reported in this appendix with major elements in weight percent oxide equivalent and sulfur in elemental weight percent.

The data was collected over three sessions, which are marked at the appropriate location in the data tables. Italics are used for standard (VG-2) analyses. The notation used in the tables represents an experiment index number followed by the spot analysis number, thus: XX-xx. A key table to link experiment numbers to mixing ratios is provided below (Table C1).

Table C1 Key to experiment index numbers and mixing proportions

Index number	Tonalite/(IAB + 2% S) Proportion	Capsule
7	5/95	Pt
12	20/80	Pt
18	50/50	BN in Pt
20	40/60	BN in Pt
23	20/80	BN in Pt
24	30/70	BN in Pt
25	10/90	BN in Pt
26	5/95	BN in Pt
28	10/90	Pt
29	5/95	Pt, no buffer

Table C2 *Microprobe spot analyses*

Sample	Na_2O (wt. %)	MgO (wt. %)	Al_2O_3 (wt. %)	SiO_2 (wt. %)	K_2O (wt. %)	P_2O_5 (wt. %)	CaO (wt. %)	MnO (wt. %)	FeO (wt. %)	TiO_2 (wt. %)	S Element %	Total
Session 1												
VG2-1	*2.4779*	*6.6331*	*14.3526*	*50.3511*	*0.2185*	*0.1729*	*10.9769*	*0.2075*	*11.7453*	*1.8998*	*0.1396*	*99.3144*
VG2-2	*2.4787*	*6.7257*	*14.3684*	*50.7664*	*0.2104*	*0.1833*	*11.0907*	*0.2002*	*11.862*	*1.9587*	*0.1429*	*100.13*
VG2-3	*2.4416*	*6.6019*	*14.2274*	*50.919*	*0.2358*	*0.1929*	*11.0526*	*0.2085*	*11.6222*	*1.8722*	*0.1465*	*99.6668*
20-1	2.0089	4.1759	16.6697	60.1907	1.5255	-0.0011	8.7544	0.1052	1.8048	0.6019	0.0707	95.9782
20-2	1.9959	4.069	16.2917	59.2043	1.5437	0.0086	8.8849	0.1117	1.8894	0.5904	0.084	94.7575
20-3	1.9868	4.1438	16.4428	60.1733	1.566	0.0184	8.8968	0.1201	1.7929	0.5823	0.0906	95.9043
20-4	2.0063	4.0404	16.5799	59.7998	1.4958	-0.0054	8.8527	0.1084	1.8265	0.5756	0.063	95.4111
20-5	1.9796	4.1677	16.6293	60.3716	1.528	-0.0162	8.8214	0.1065	1.8365	0.5818	0.09	96.2023
20-6	2.0007	4.1245	16.4452	59.7947	1.5285	-0.0323	8.8696	0.1192	1.8391	0.5808	0.0746	95.4515
20-7	1.9913	4.0649	16.3716	59.8677	1.5219	0.0097	8.7851	0.1076	1.7969	0.5971	0.0645	95.2426
20-8	1.9771	4.1186	16.411	60.3746	1.5544	0.0054	8.7677	0.1174	1.8602	0.57	0.0636	95.8836
20-9	1.9866	4.1209	16.3692	60.0728	1.5298	0.0011	8.7414	0.13	1.7917	0.5757	0.055	95.429
20-10	1.9858	4.1232	16.3048	59.9382	1.5324	-0.0032	8.8164	0.105	1.8193	0.576	0.1056	95.4122
20-11	1.9701	4.1231	16.5337	60.4613	1.5482	0.0227	8.7444	0.1154	1.7608	0.6071	0.0725	96.0318
20-12	2.0024	4.1068	16.5006	60.2629	1.5525	0.0054	8.7316	0.1225	1.8247	0.6091	0.0716	95.8617
VG2-4	*2.5403*	*6.8071*	*14.5391*	*50.945*	*0.2149*	*0.1881*	*11.0779*	*0.2338*	*11.6625*	*1.8778*	*0.1594*	*100.4049*
VG2-5	*2.4876*	*6.7806*	*14.2188*	*50.5965*	*0.2201*	*0.1997*	*11.1066*	*0.2307*	*11.6342*	*1.9721*	*0.1312*	*99.7091*
20-13	1.9716	4.1138	16.5552	60.5734	1.563	0.0108	8.6497	0.1018	1.7642	0.5707	0.0847	96.0435
20-14	1.9952	4.1212	16.6407	60.5491	1.5528	0.0011	8.7434	0.0881	1.8413	0.6152	0.0769	96.3017
20-15	2.0181	4.0731	16.4676	60.4792	1.5457	0.0076	8.741	0.132	1.8283	0.5883	-0.3284	95.8808
20-16	1.9793	4.0842	16.4125	60.1777	1.5228	-0.0183	8.7315	0.1148	1.786	0.6025	0.09	95.5911
20-17	2.0212	4.0716	16.4844	60.6083	1.5711	0.0173	8.7142	0.0931	1.777	0.6094	0.0556	96.0788
20-18	2.0222	4.029	16.2798	59.3706	1.588	0.0184	8.7796	0.1334	1.8218	0.6369	0.0431	94.7657
20-19	2.0226	4.0218	16.3944	59.8493	1.5711	0.0054	8.7162	0.1163	1.8464	0.6272	0.0844	95.3392
20-20	2.0055	4.0656	16.461	60.4069	1.5564	0.0065	8.6505	0.115	1.8221	0.5678	0.0884	95.8339
VG2-6	*2.5077*	*6.8246*	*14.3228*	*50.7741*	*0.2065*	*0.1555*	*11.0628*	*0.2205*	*11.803*	*1.9284*	*0.1318*	*100.0693*
VG2-7	*2.5632*	*6.7568*	*14.2303*	*50.967*	*0.2121*	*0.2028*	*10.9339*	*0.2122*	*11.7253*	*1.866*	*0.1284*	*99.9262*

Table C2 *Microprobe spot analyses*

Sample	Na_2O (wt. %)	MgO (wt. %)	Al_2O_3 (wt. %)	SiO_2 (wt. %)	K_2O (wt. %)	P_2O_5 (wt. %)	CaO (wt. %)	MnO (wt. %)	FeO (wt. %)	TiO_2 (wt. %)	S Element %	Total
VG2-8	*2.4757*	*6.8587*	*14.3882*	*51.0746*	*0.1968*	*0.1708*	*11.1635*	*0.2032*	*11.6887*	*1.8878*	*0.1489*	*100.4055*
Session 2												
VG2-1	*1.6165*	*7.4208*	*14.1773*	*50.8347*	*0.2145*	*0.1895*	*10.1291*	*0.2115*	*11.9344*	*1.6197*	*0.1431*	*98.6341*
VG2-2	*2.4141*	*6.736*	*14.1783*	*50.8478*	*0.2205*	*0.2239*	*11.1877*	*0.2119*	*11.3889*	*1.684*	*0.155*	*99.403*
7-1	1.0629	5.4701	15.6927	56.6731	0.5244	0.0812	11.9319	0.1714	7.3227	0.4179	0.8733	101.0931
7-2	1.1228	5.4496	15.5797	57.0718	0.5138	0.1011	11.8902	0.1679	7.2095	0.3898	0.8532	101.2011
7-3	1.1737	5.4727	15.6165	56.921	0.5096	0.0697	11.8884	0.1555	7.2577	0.4251	0.8224	101.133
7-4	1.1143	5.4283	15.4224	55.8143	0.5239	0.0798	11.7934	0.1742	7.1383	0.3955	0.843	99.5689
7-5	1.1191	5.4094	15.5684	56.9767	0.5058	0.0953	11.9224	0.1945	7.333	0.4137	0.8555	101.2477
7-6	1.1182	5.4118	15.4992	56.2802	0.5393	0.0927	12.0135	0.1871	7.2139	0.3881	0.8771	100.4966
7-7	1.1537	5.4133	15.6945	57.0598	0.5339	0.1100	12.0463	0.153	7.3454	0.4026	0.848	101.6068
7-8	1.0875	5.365	15.5519	56.7027	0.5318	0.0811	11.8655	0.152	7.1314	0.4096	0.8608	100.5984
7-9	1.1242	5.4051	15.5653	56.6529	0.5175	0.1046	11.9906	0.1757	7.3268	0.373	0.8583	100.9506
7-10	1.1069	5.4201	15.7044	57.0954	0.5333	0.107	11.9792	0.1693	7.4815	0.4070	0.8603	101.723
VG2-3	*2.3935*	*6.7477*	*14.2089*	*51.3864*	*0.2383*	*0.1727*	*11.2188*	*0.2081*	*11.4916*	*1.6718*	*0.1511*	*100.0396*
VG2-4	*2.444*	*6.772*	*14.1285*	*51.3088*	*0.2283*	*0.198*	*11.1809*	*0.2289*	*11.3226*	*1.6474*	*0.151*	*99.7612*
7-11	1.1353	5.3222	15.5362	56.4314	0.5403	0.0982	11.9958	0.1663	7.0897	0.3993	0.8677	100.4484
7-12	1.0962	5.373	15.3996	56.4846	0.5446	0.0906	12.0504	0.1661	7.252	0.3749	0.8497	100.5298
7-13	1.1884	5.4073	15.6571	56.8977	0.5106	0.1143	12.0427	0.1619	7.2539	0.3918	0.8472	101.3187
7-14	1.1796	5.3543	15.4123	55.7333	0.5385	0.0753	11.9592	0.1666	6.7764	0.3892	0.8298	99.2427
7-15	1.1877	5.346	15.5225	56.8112	0.5633	0.0731	11.9645	0.1665	7.213	0.3935	0.8494	100.9384
7-16	1.1036	5.6098	15.4000	56.1593	0.5382	0.0719	11.9008	0.141	7.1562	0.3898	0.8517	100.1724
7-17	1.1076	5.6834	15.4276	55.9217	0.5481	0.0976	11.8102	0.1746	7.0842	0.377	0.8491	99.9287
7-18	1.1565	5.9161	15.2535	56.0089	0.5123	0.0803	11.7602	0.1486	7.0318	0.3914	0.8633	99.9844
7-19	1.0877	5.8975	15.0645	55.2253	0.5087	0.1049	11.9255	0.1624	6.6884	0.3585	0.8883	98.7983
7-20	1.1326	5.7142	15.2672	55.6749	0.5216	0.0825	12.0097	0.1654	7.1643	0.3867	0.8903	99.8979
VG2-5	2.3684	6.8541	14.2882	51.6738	0.2217	0.2452	11.209	0.2062	11.4393	1.6854	0.1385	100.468
VG2-6	2.3654	6.8032	14.199	51.643	0.2227	0.1904	11.232	0.2108	11.2576	1.6616	0.131	100.0473

Table C2 *Microprobe spot analyses*

Sample	Na_2O (wt. %)	MgO (wt. %)	Al_2O_3 (wt. %)	SiO_2 (wt. %)	K_2O (wt. %)	P_2O_5 (wt. %)	CaO (wt. %)	MnO (wt. %)	FeO (wt. %)	TiO_2 (wt. %)	S Element %	Total
VG2-7	2.4352	6.8093	14.2325	51.3841	0.2194	0.2347	11.3124	0.2229	11.2419	1.6331	0.1329	99.991
12-1	1.0296	4.7404	15.8783	59.0965	0.9296	0.1089	10.6197	0.1673	6.6144	0.4658	0.6952	101.0396
12-2	1.0783	4.6835	15.7799	58.5965	0.9378	0.0885	10.6779	0.1545	6.3146	0.4598	0.7027	100.1754
12-3	1.0954	4.6906	15.5401	58.4536	0.9929	0.1183	10.6037	0.1694	6.1071	0.4259	0.6979	99.5915
12-4	1.1117	4.753	15.8552	58.9418	0.9805	0.1111	10.6063	0.1354	6.1563	0.4377	0.6931	100.4739
12-5	1.1134	4.7425	15.6815	58.5001	0.9433	0.1086	10.7598	0.1651	6.1307	0.4503	0.6735	99.941
12-6	1.0362	4.7033	15.74	58.5794	0.9749	0.1372	10.6109	0.1723	6.1684	0.4573	0.7185	100.0156
12-7	1.0544	4.7193	15.7617	58.6599	0.9387	0.1078	10.6998	0.1559	6.1761	0.4483	0.6834	100.0874
12-8	1.0387	4.717	15.6761	58.3565	0.9669	0.0854	10.6223	0.1589	6.0289	0.4477	0.7006	99.4983
12-9	1.0971	4.6702	15.6424	58.4504	0.9994	0.1003	10.5837	0.1461	6.0909	0.4699	0.6943	99.6377
12-10	1.0597	4.7051	15.7413	58.4928	0.9838	0.0683	10.6259	0.1528	5.9471	0.4433	0.6801	99.5792
VG2-8	*2.3352*	*6.8018*	*14.1896*	*51.4634*	*0.242*	*0.2001*	*11.3602*	*0.2244*	*11.0869*	*1.6255*	*0.1439*	*99.8166*
VG2-9	*2.4041*	*6.6742*	*14.3816*	*51.9804*	*0.2245*	*0.1805*	*11.2604*	*0.2165*	*11.2307*	*1.642*	*0.1314*	*100.4575*
12-11	1.0908	4.6796	15.6055	57.8434	0.9708	0.1332	10.6059	0.1654	5.9449	0.4352	0.6961	98.8654
12-12	1.0789	4.659	15.5491	58.0575	0.9367	0.1117	10.5911	0.1664	6.076	0.437	0.6961	99.0542
12-13	1.0961	4.7391	15.8411	58.9643	0.9677	0.0544	10.6294	0.1274	6.2145	0.4475	0.7017	100.4837
12-14	1.0452	4.7331	15.8173	58.5312	0.9674	0.1225	10.5377	0.1621	6.115	0.4152	0.6934	99.8322
12-15	1.0826	4.7446	15.8684	58.6542	0.9658	0.1205	10.6075	0.1594	6.3171	0.4797	0.7098	100.4182
12-16	1.1155	4.6727	15.6734	57.951	0.9821	0.1053	10.6857	0.1617	6.0094	0.4539	0.6759	99.1611
12-17	1.1057	4.6638	15.4785	58.1472	0.9788	0.1	10.5801	0.1474	5.9256	0.4253	0.695	98.941
12-18	1.0804	4.6544	15.6757	58.782	0.9493	0.1388	10.6802	0.1335	6.2502	0.4168	0.6956	100.1511
12-19	1.092	4.6569	15.4546	57.6703	0.9828	0.1198	10.5395	0.1511	5.7359	0.4399	0.6886	98.2189
12-20	1.1018	4.7101	15.8038	59.1639	0.9466	0.1208	10.6708	0.1645	6.3479	0.4445	0.6969	100.8673
VG2-10	*2.4262*	*6.7967*	*14.0888*	*51.3091*	*0.2159*	*0.2158*	*11.3494*	*0.2023*	*10.9438*	*1.6142*	*0.148*	*99.4578*
VG2-11	*2.4263*	*6.7696*	*14.1333*	*51.6341*	*0.2273*	*0.1861*	*11.2772*	*0.209*	*10.9047*	*1.5849*	*0.1374*	*99.627*
24-1	1.4907	4.4685	15.5239	57.6993	1.4128	0.0064	10.0457	0.1143	1.7967	0.4549	0.0951	93.2033
24-2	1.3081	4.3743	15.4665	57.7632	1.3748	0.014	10.1401	0.1209	1.8486	0.4119	0.0918	93.0059
24-3	1.3563	4.5009	15.7688	58.5226	1.4087	-0.0032	10.114	0.1258	1.9181	0.4289	0.0925	94.3289

Table C2 *Microprobe spot analyses*

Sample	Na_2O (wt. %)	MgO (wt. %)	Al_2O_3 (wt. %)	SiO_2 (wt. %)	K_2O (wt. %)	P_2O_5 (wt. %)	CaO (wt. %)	MnO (wt. %)	FeO (wt. %)	TiO_2 (wt. %)	S Element %	Total
24-4	1.3565	4.4399	15.6494	58.0257	1.3888	0.0248	10.0542	0.1142	1.953	0.4306	0.088	93.6128
24-5	1.2413	4.4676	15.7727	58.568	1.3194	0.0022	10.1516	0.114	1.8883	0.4188	0.0958	94.1351
24-6	1.2872	4.465	15.6647	58.2074	1.3755	0.0215	10.1878	0.1105	1.8325	0.4209	0.0889	93.7509
24-7	1.2792	4.4161	15.6274	58.0718	1.3904	0.0119	10.2054	0.1003	1.7927	0.4179	0.0955	93.5041
24-8	1.281	4.438	15.7455	58.6262	1.4154	0	10.267	0.1402	1.7865	0.4352	0.0857	94.3063
24-9	1.3103	4.4776	15.9348	59.1769	1.3795	-0.0108	10.121	0.1047	1.8611	0.4472	0.1048	95.0225
24-10	1.3396	4.4694	15.9187	58.8738	1.4189	0.0065	10.174	0.1204	1.8502	0.4584	0.0997	94.829
VG2-12	*2.3813*	*6.6735*	*13.9782*	*51.0659*	*0.2484*	*0.2031*	*11.2157*	*0.2293*	*10.8711*	*1.5676*	*0.1357*	*98.7053*
VG2-13	*2.4187*	*6.7757*	*14.2344*	*51.5126*	*0.2379*	*0.2046*	*11.2894*	*0.228*	*11.0553*	*1.6772*	*0.1455*	*99.9246*
24-11	1.4731	4.3802	15.5558	58.0726	1.434	0.0172	10.1314	0.1323	1.8136	0.4372	0.0939	93.635
24-12	1.308	4.4033	15.8825	58.741	1.3991	-0.0161	10.158	0.1332	1.9361	0.4615	0.091	94.6047
24-13	1.2287	4.4703	15.6817	58.4157	1.4251	-0.0022	10.1659	0.114	1.9248	0.418	0.0918	94.0276
24-14	1.305	4.5267	15.6966	58.1698	1.3872	-0.0108	10.2301	0.1147	1.9042	0.3969	0.0968	93.9246
24-15	1.3674	4.4898	15.709	58.2222	1.3943	0.0022	10.0742	0.1199	1.8715	0.4295	0.0981	93.8761
24-16	1.2879	4.3988	15.712	58.4519	1.39	0.0129	10.1453	0.1194	1.9063	0.4091	0.0811	93.9956
24-17	1.4153	4.4999	16.0101	59.3353	1.3842	-0.0129	10.2053	0.118	1.8416	0.4098	0.1015	95.4223
24-18	1.2879	4.4051	15.6812	58.1724	1.3779	0.0043	10.0695	0.1195	1.8925	0.4023	0.0936	93.5995
24-19	1.3117	4.3704	15.7493	58.7516	1.4027	0.014	10.1571	0.1301	1.8625	0.4414	0.0896	94.37
24-20	1.3111	4.3197	15.5939	58.1348	1.4125	0.0291	9.9509	0.1234	1.7112	0.4113	0.1053	93.2084
VG2-14	2.2939	6.721	14.1008	51.5803	0.2389	0.2031	11.2587	0.2074	10.8805	1.5845	0.1453	99.3593
VG2-15	2.4357	6.7074	14.0149	51.3321	0.2223	0.2435	11.1515	0.2033	10.9478	1.6337	0.1434	99.1788
Session 3												
VG2-1	*0.3679*	*6.7597*	*14.6287*	*51.7724*	*0.2091*	*0.1962*	*11.2091*	*0.2035*	*12.507*	*2.0814*	*0.1351*	*100.2048*
VG2-2	*1.6201*	*7.1261*	*14.6839*	*51.8066*	*0.2476*	*0.194*	*11.0201*	*0.2161*	*12.1634*	*1.9201*	*0.1359*	*101.2695*
VG2-3	*2.4159*	*6.9508*	*14.4613*	*51.0374*	*0.2277*	*0.2394*	*11.1838*	*0.2107*	*11.6753*	*1.9059*	*0.1438*	*100.5956*
25-1	1.2262	5.1902	15.7133	56.2294	0.7398	0.0192	12.1471	0.1375	2.3734	0.4633	0.156	94.5511
25-2	1.2818	5.0616	15.4391	55.6361	0.7543	0.0106	12.2133	0.1562	2.4436	0.4867	0.1542	93.7913

Table C2 *Microprobe spot analyses*

Sample	Na_2O (wt. %)	MgO (wt. %)	Al_2O_3 (wt. %)	SiO_2 (wt. %)	K_2O (wt. %)	P_2O_5 (wt. %)	CaO (wt. %)	MnO (wt. %)	FeO (wt. %)	TiO_2 (wt. %)	S Element %	Total
25-3	1.2115	5.0615	15.6517	56.4596	0.7597	0.0085	12.1401	0.1376	2.479	0.46	0.1538	94.6765
25-4	1.174	5.0222	15.398	55.9063	0.8011	0.018	12.0878	0.1279	2.442	0.4867	0.1451	93.7541
25-5	1.1308	5.0485	15.4828	56.2711	0.7707	0.0191	12.181	0.1319	2.483	0.4596	0.1463	94.2708
25-6	1.1357	5.0909	15.5905	56.2621	0.7687	0.0074	12.2539	0.1299	2.3883	0.4672	0.1614	94.4171
25-7	1.1975	5.0355	15.6166	56.5942	0.7856	0.0234	12.1629	0.1336	2.4207	0.4857	0.1181	94.6915
25-8	1.1592	5.0147	15.6159	56.3054	0.7596	0.0276	12.0942	0.1205	2.4218	0.444	0.1498	94.2622
25-9	1.0934	5.087	15.651	56.6	0.7805	0.0032	11.9891	0.129	2.4673	0.4702	0.163	94.5965
25-10	1.1805	5.062	15.6518	56.4148	0.7392	0.0117	12.0308	0.1299	2.4041	0.5011	0.1401	94.4059
VG2-4	*0.33*	*6.6597*	*14.754*	*51.9523*	*0.3395*	*0.2208*	*11.129*	*0.2164*	*12.3116*	*1.9979*	*0.1359*	*100.1827*
VG2-5	*2.3722*	*6.9508*	*14.4191*	*51.3675*	*0.2198*	*0.2389*	*11.1474*	*0.2212*	*11.8403*	*1.9066*	*0.1534*	*100.9903*
25-11	1.3897	4.9995	15.1047	54.4501	0.7535	0.0265	12.0982	0.1261	2.4829	0.486	0.1444	92.2058
25-12	1.2425	5.0725	15.6079	55.9195	0.77	0.0074	12.088	0.1385	2.4742	0.4838	0.1299	94.0639
25-13	1.1592	5.0795	15.5676	56.4962	0.7715	0.0202	12.0669	0.1189	2.4627	0.4465	0.166	94.5208
25-14	1.2019	5.0974	15.6117	56.5489	0.7499	0.0149	12.0038	0.1148	2.3969	0.4646	0.1349	94.4744
25-15	1.2171	5.1012	15.6046	56.3712	0.7946	0.0212	12.1442	0.1367	2.4751	0.4723	0.1057	94.5493
25-16	1.1804	4.9696	15.609	56.65	0.7697	0.0276	12.0555	0.1248	2.4377	0.4642	0.1106	94.5092
25-17	1.1223	5.0617	15.6812	56.364	0.7532	-0.0117	12.0773	0.1324	2.4345	0.4548	0.1775	94.4362
25-18	1.0719	5.0561	15.6725	56.8963	0.7509	-0.0021	12.0557	0.1326	2.4712	0.4966	0.1163	94.8363
25-19	1.1113	5.0021	15.7288	56.6424	0.7556	0.0085	12.0759	0.1378	2.4317	0.4274	0.1421	94.6053
25-20	1.1063	5.045	15.6354	56.6512	0.7731	0.0149	12.0413	0.1256	2.4176	0.4362	0.1283	94.5029
VG2-6	*2.4407*	*6.866*	*14.061*	*49.7279*	*0.2146*	*0.1968*	*11.0521*	*0.2123*	*11.6955*	*1.9257*	*0.1373*	*98.667*
VG2-7	*2.4463*	*6.8792*	*14.2016*	*50.2276*	*0.2165*	*0.1715*	*10.9934*	*0.2034*	*11.4914*	*1.8273*	*0.1374*	*98.9327*
18-1	2.1972	3.8881	16.4257	60.2822	1.8166	0.0108	7.7607	0.112	1.747	0.628	0.0798	95.0277
18-2	2.1829	3.9269	16.57	60.6525	1.8222	0.0291	7.7102	0.1249	1.7419	0.6223	0.0711	95.5251
18-3	2.2254	3.9052	16.4488	60.2001	1.7756	0.0065	7.7674	0.1149	1.7597	0.6038	0.0712	94.9495
18-4	2.2069	3.9134	16.3572	60.1197	1.8196	0.0065	7.6839	0.1007	1.7769	0.5928	0.0793	94.7362
18-5	2.181	3.9053	16.3365	59.8273	1.806	0.0108	7.6828	0.0906	1.7353	0.6066	0.0556	94.2935
18-6	2.1611	3.8921	16.3805	60.3733	1.7968	0.0194	7.7113	0.1088	1.7703	0.5879	0.0891	94.9795

Table C2 *Microprobe spot analyses*

Sample	Na_2O (wt. %)	MgO (wt. %)	Al_2O_3 (wt. %)	SiO_2 (wt. %)	K_2O (wt. %)	P_2O_5 (wt. %)	CaO (wt. %)	MnO (wt. %)	FeO (wt. %)	TiO_2 (wt. %)	S Element %	Total
18-7	2.2523	3.9067	16.4872	60.4886	1.7807	0.0129	7.7643	0.0989	1.7806	0.6235	0.0875	95.3706
18-8	2.1801	3.8654	16.3585	60.2527	1.7759	-0.0108	7.6579	0.1172	1.7791	0.6254	0.0897	94.7915
18-9	2.1877	3.9348	16.4371	60.0275	1.802	-0.0076	7.6518	0.1175	1.7926	0.6234	0.0838	94.742
18-10	2.2085	3.8889	16.3554	60.1042	1.8342	0.0194	7.6682	0.1248	1.6931	0.6407	0.0905	94.7182
VG2-8	*2.4156*	*6.8268*	*14.0997*	*49.8533*	*0.2216*	*0.2018*	*11.0307*	*0.2204*	*11.5818*	*1.9308*	*0.1476*	*98.6773*
VG2-9	*2.4064*	*6.8403*	*14.0638*	*49.7634*	*0.2172*	*0.2122*	*10.8524*	*0.1993*	*11.5763*	*1.8544*	*0.1652*	*98.3158*
18-11	2.1678	3.9143	16.4401	60.7752	1.8023	0.0054	7.6381	0.1083	1.7089	0.6245	0.084	95.3529
18-12	2.2504	3.9232	16.4967	60.5896	1.8149	-0.0022	7.7783	0.1066	1.7569	0.6243	0.0665	95.4737
18-13	2.2163	3.9147	16.562	60.2336	1.7984	0.0151	7.7092	0.1111	1.7599	0.6484	0.0946	95.1578
18-14	2.1585	3.9186	16.5306	60.5016	1.7957	-0.014	7.6846	0.0953	1.7583	0.6217	0.088	95.2407
18-15	2.1996	3.9837	16.5021	60.3441	1.7663	-0.0022	7.7271	0.1154	1.74	0.593	0.0914	95.1541
18-16	2.2398	3.911	16.4419	60.0803	1.7889	0.0161	7.8401	0.1196	1.7777	0.636	0.0637	94.9787
18-17	2.206	3.8822	16.5339	60.7501	1.8324	0.0194	7.6095	0.1237	1.6901	0.6486	0.0896	95.4749
18-18	2.2345	3.946	16.4691	60.1948	1.7653	0.0322	7.6334	0.115	1.72	0.6478	0.0991	94.9561
18-19	2.219	3.8741	16.3957	60.5431	1.7758	0.0268	7.7232	0.1337	1.7049	0.6128	0.0961	95.2014
18-20	2.2151	3.9296	16.4831	60.4591	1.8429	0.0172	7.8054	0.1281	1.7589	0.6211	0.065	95.3904
VG2-10	*2.3934*	*6.9896*	*14.3131*	*50.6041*	*0.2219*	*0.2043*	*10.9107*	*0.209*	*11.6634*	*1.9182*	*0.1498*	*99.727*
VG2-11	*2.4102*	*6.9121*	*14.1897*	*50.3425*	*0.2177*	*0.1536*	*11.0178*	*0.2269*	*11.4874*	*1.9172*	*0.1417*	*99.1583*
*VG2-12**	*2.3547*	*6.8887*	*14.3829*	*50.4866*	*0.2232*	*0.2289*	*11.0401*	*0.2116*	*12.0288*	*2.0502*	*0.1591*	*100.2136*
VG2-13	*2.4095*	*6.8868*	*14.3565*	*50.9233*	*0.2307*	*0.2054*	*11.0788*	*0.2314*	*12.1897*	*2.1224*	*0.144*	*100.9222*
26-1	1.6393	5.6085	15.5347	54.2922	0.6715	0.0224	13.0642	0.1278	0.388	0.4188	0.2838	92.3344
26-2	1.6199	5.4258	15.3048	53.7393	0.6608	0.0778	12.7414	0.1371	1.4667	0.477	0.2074	92.0649
26-3	1.6019	5.4672	15.4064	53.8571	0.6462	0.0075	12.8916	0.1317	1.5431	0.4555	0.2017	92.4111
26-4	1.596	5.4969	15.3212	53.6416	0.6504	0.0298	12.7746	0.1315	1.5598	0.4485	0.2144	92.0789
26-5	1.6484	5.4913	15.251	53.586	0.6505	0.0393	12.808	0.1125	1.3552	0.428	0.2593	91.8884
26-6	1.6597	5.4952	15.3467	53.8584	0.6689	0.0149	13.0066	0.122	0.6042	0.4547	0.307	91.8444
26-7	1.6878	5.5337	15.4987	54.2791	0.6121	0.0267	13.1335	0.1229	0.3332	0.4244	0.2322	92.1162
26-8	1.6237	5.5243	15.4552	54.1349	0.642	0.0246	13.1105	0.1172	0.6197	0.4129	0.2369	92.1384

Table C2 *Microprobe spot analyses*

Sample	Na_2O (wt. %)	MgO (wt. %)	Al_2O_3 (wt. %)	SiO_2 (wt. %)	K_2O (wt. %)	P_2O_5 (wt. %)	CaO (wt. %)	MnO (wt. %)	FeO (wt. %)	TiO_2 (wt. %)	S Element %	Total
VG2-13	*2.3537*	*6.9469*	*14.4447*	*50.8101*	*0.2139*	*0.2312*	*11.1075*	*0.2001*	*12.3362*	*2.048*	*0.1534*	*100.9988*
VG2-14	*2.4216*	*6.938*	*14.2999*	*50.9962*	*0.2199*	*0.2092*	*11.1659*	*0.1967*	*12.2413*	*2.0406*	*0.1324*	*100.9938*
26-9	1.5952	5.4818	15.4391	53.3812	0.6344	0.0448	12.8387	0.1302	1.7505	0.4466	0.2073	92.1569
26-10	1.61	5.4617	15.274	53.7687	0.6405	0.0632	12.8696	0.1057	1.6305	0.4604	0.2392	92.3623
26-11	1.5977	5.4672	15.3114	53.0009	0.6495	0.0499	12.7785	0.1446	1.7721	0.4416	0.3322	91.8774
26-12	1.6887	5.5159	15.3481	53.6876	0.6494	0.0427	12.7579	0.1247	1.7634	0.4505	0.2228	92.4741
26-13	1.5598	5.4694	15.3818	53.5482	0.6388	0.0491	12.7981	0.1159	1.7208	0.4489	0.2305	92.1913
26-14	1.5623	5.4213	15.257	53.4452	0.6266	0.05	12.7555	0.1233	1.7283	0.427	0.2277	91.8514
26-15	1.6399	5.3845	15.217	53.7776	0.6712	0.0459	12.7715	0.1146	1.6158	0.453	0.2334	92.1573
26-16	1.6287	5.3302	15.3663	54.216	0.6556	0.0364	12.764	0.1232	1.4038	0.4466	0.3129	92.5961
26-17	1.6282	5.3837	15.4147	53.7015	0.6473	0.0405	12.8025	0.1376	1.4933	0.456	0.2109	92.1268
26-18	1.6216	5.4938	15.2804	53.693	0.6314	0.0458	12.7312	0.1188	1.828	0.4772	0.1797	92.2805
26-19	1.6476	5.3483	15.2937	54.036	0.6797	0.0193	12.6192	0.1078	1.6657	0.4036	0.2293	92.279
26-20	1.63	5.3905	15.1839	53.5143	0.6671	0.048	12.6043	0.123	1.7545	0.4031	0.189	91.6964
VG2-15	*2.4405*	*6.8467*	*14.3479*	*50.8432*	*0.2123*	*0.2131*	*11.0368*	*0.2214*	*12.247*	*2.052*	*0.1581*	*100.7769*
VG2-16	*2.4813*	*6.9346*	*14.4367*	*50.6369*	*0.2408*	*0.2471*	*11.009*	*0.2068*	*12.3327*	*2.1321*	*0.1328*	*100.9233*
23-1	1.6874	4.8956	15.7253	55.8499	1.0236	0.0021	11.0598	0.1224	2.3146	0.5221	0.1262	93.4549
23-2	1.693	4.8685	15.6361	56.0626	1.067	0.0161	11.0643	0.1355	2.3324	0.4747	0.108	93.5658
23-3	1.684	4.8997	15.5196	55.9252	1.0093	0.0214	11.0277	0.1216	2.3157	0.4913	0.1102	93.2357
23-4	1.6732	4.872	15.7145	55.8267	1.03	0.0268	10.8938	0.1193	2.3613	0.4843	0.1368	93.2752
23-5	1.6982	4.8462	15.7181	56.1689	1.0703	0.0032	11.0061	0.126	2.3668	0.4819	0.1362	93.7579
23-6	1.6428	4.8916	15.8753	55.739	1.0256	0.044	10.995	0.084	2.3402	0.5166	0.1229	93.3998
23-7	1.6805	4.9027	15.7809	56.1492	1.0335	0.0129	11.0804	0.1163	2.3658	0.5164	0.1165	93.8713
23-8	1.6625	4.839	15.6239	56.278	1.0418	0.0203	10.8712	0.112	2.3553	0.4767	0.114	93.5087
23-9	1.6594	4.8808	15.6842	56.1389	1.0329	0.0118	10.9946	0.1131	2.2814	0.5089	0.0921	93.4901
23-10	1.6771	4.8297	15.6678	56.105	1.0424	0.0139	11.0155	0.1076	2.25	0.5107	0.1112	93.4419
VG2-17	*2.4195*	*6.8839*	*14.3709*	*50.573*	*0.2263*	*0.2061*	*11.0507*	*0.2311*	*12.3691*	*2.1018*	*0.1268*	*100.6859*
VG2-18	*2.4072*	*6.9658*	*14.3262*	*50.5187*	*0.2125*	*0.212*	*11.0744*	*0.2308*	*12.4611*	*2.1121*	*0.1645*	*100.8495*

Table C2 *Microprobe spot analyses*

Sample	Na_2O (wt. %)	MgO (wt. %)	Al_2O_3 (wt. %)	SiO_2 (wt. %)	K_2O (wt. %)	P_2O_5 (wt. %)	CaO (wt. %)	MnO (wt. %)	FeO (wt. %)	TiO_2 (wt. %)	S Element %	Total
23-11	1.6775	4.9101	15.7262	56.0183	1.0242	0.0214	11.0169	0.1279	2.3917	0.5051	0.0957	93.6106
23-12	1.6834	4.8828	15.7747	56.1236	1.0391	0.0193	11.1259	0.1064	2.3356	0.4561	0.1154	93.7775
23-13	1.6517	4.8339	15.6027	55.8227	1.0377	0.0235	10.9462	0.1073	2.3453	0.4903	0.1076	93.0762
23-14	1.6996	4.9421	15.6615	56.0191	1.022	0.0032	11.1341	0.1117	2.308	0.5115	0.1219	93.6564
23-15	1.6698	4.9042	15.72	56.1874	1.0504	0.0118	11.2243	0.0997	2.3773	0.4657	0.1191	93.9487
23-16	1.6618	4.9299	15.7407	56.0267	1.0221	-0.0011	11.1034	0.1239	2.3315	0.471	0.1141	93.639
23-17	1.7434	4.9373	15.7705	56.2514	1.0529	0.0097	11.1526	0.1121	2.3078	0.4674	0.1361	94.0768
23-18	1.6577	4.933	15.7513	56.2718	1.0545	0.0032	11.1829	0.0923	2.2369	0.4703	0.0895	93.8328
23-19	1.6955	4.9988	15.705	55.539	1.0239	0.0386	11.2321	0.1037	2.3382	0.4684	0.1209	93.3848
23-20	1.7021	4.932	15.7254	55.4709	1.0416	0.015	11.1257	0.0966	2.3622	0.4834	0.1037	93.1619
VG2-19	*2.3534*	*6.8726*	*14.4149*	*50.6216*	*0.2201*	*0.2152*	*10.9957*	*0.2239*	*12.416*	*2.0805*	*0.1474*	*100.7086*
VG2-20	*2.414*	*6.9044*	*14.3272*	*50.4217*	*0.2287*	*0.1868*	*10.9855*	*0.1988*	*12.4277*	*2.1005*	*0.1481*	*100.4911*
28-1	1.416	5.8851	15.5023	55.3352	0.6451	0.1028	11.651	0.1594	7.0359	0.5033	0.9692	100.1727
28-2	1.3813	5.8994	15.5062	55.0894	0.6339	0.1211	11.4956	0.1531	7.0772	0.5235	0.8918	99.6628
28-3	1.4252	5.9174	15.5885	54.7736	0.6405	0.1103	11.5476	0.1585	7.0111	0.5291	0.9557	99.6114
28-4	1.3749	6.0708	15.5541	54.9781	0.6509	0.0815	11.6562	0.1503	7.0158	0.5275	0.951	99.9603
28-5	1.4012	5.9142	15.5428	54.9256	0.6488	0.1059	11.6736	0.1528	6.9759	0.5242	0.9605	99.7842
28-6	1.3851	5.9902	15.5507	55.246	0.6529	0.0973	11.7344	0.1518	7.0277	0.5416	0.9538	100.2833
28-7	1.4039	5.9689	15.5613	55.2809	0.6578	0.1114	11.5445	0.1541	7.0776	0.57	0.9295	100.1876
28-8	1.3791	5.8632	15.6538	54.8314	0.6615	0.1068	11.5161	0.1529	7.127	0.5712	0.9271	99.7152
28-9	1.4007	5.8816	15.604	55.0065	0.6555	0.0943	11.4801	0.173	7.1487	0.5134	0.9299	99.8158
28-10	1.4137	6.0104	15.5547	55.2616	0.6896	0.0839	11.609	0.1441	7.1344	0.5235	0.9248	100.2728
VG2-21	*2.3944*	*6.9247*	*14.3785*	*50.6967*	*0.1913*	*0.1848*	*10.9651*	*0.2357*	*12.4144*	*2.0354*	*0.1264*	*100.6736*
VG2-22	*2.4546*	*6.8936*	*14.3068*	*50.1536*	*0.2222*	*0.2138*	*10.9916*	*0.2165*	*12.3925*	*2.1613*	*0.1564*	*100.3189*
28-11	1.4154	5.9963	15.565	54.8387	0.6682	0.1093	11.6414	0.1529	7.1156	0.5463	0.9451	99.9374
28-12	1.3865	5.8824	15.5723	55.0003	0.6736	0.0805	11.6058	0.1552	7.2012	0.5393	0.9298	99.955
28-13	1.3746	5.7881	15.491	54.8938	0.6586	0.0931	11.4817	0.1567	7.0647	0.5429	0.9005	99.3445
28-14	1.366	5.8316	15.617	54.8827	0.6996	0.088	11.6601	0.162	7.0886	0.5522	0.9353	99.8166

Table C2 *Microprobe spot analyses*

Sample	Na_2O (wt. %)	MgO (wt. %)	Al_2O_3 (wt. %)	SiO_2 (wt. %)	K_2O (wt. %)	P_2O_5 (wt. %)	CaO (wt. %)	MnO (wt. %)	FeO (wt. %)	TiO_2 (wt. %)	S Element %	Total
28-15	1.3375	5.7994	15.6393	55.1732	0.6292	0.1166	11.6713	0.1327	7.0368	0.5462	0.9532	99.987
28-16	1.3513	5.8648	15.5404	55.3354	0.6582	0.1179	11.6209	0.1575	7.0959	0.5386	0.9538	100.1869
28-17	1.3627	5.8008	15.6384	55.0715	0.657	0.109	11.6414	0.1476	7.1417	0.5658	0.9611	100.0564
28-18	1.3859	5.8375	15.5594	55.5198	0.6523	0.1175	11.5448	0.1623	7.0962	0.5066	0.9833	100.3471
28-19	1.3962	5.8827	15.4289	55.3247	0.6407	0.0858	11.4069	0.1436	7.1309	0.5289	0.9231	99.8136
28-20	1.3907	5.8455	15.4989	55.1447	0.6589	0.0742	11.6127	0.1724	7.1675	0.5694	0.9551	100.0434
VG2-23	*2.4215*	*6.939*	*14.3432*	*50.7101*	*0.2223*	*0.186*	*10.8848*	*0.2195*	*12.3806*	*2.095*	*0.146*	*100.6939*
VG2-24	*2.421*	*6.9096*	*14.353*	*50.8112*	*0.2202*	*0.2038*	*10.9739*	*0.2234*	*12.4515*	*2.1027*	*0.136*	*100.9419*
29-1	1.3536	5.6515	15.4035	54.2799	0.5063	0.11	11.4729	0.1571	7.8499	0.5308	0.8373	98.9886
29-2	1.2835	5.6116	15.6271	54.6484	0.5262	0.0886	11.4743	0.1574	7.8111	0.5282	0.856	99.4667
29-3	1.335	5.5664	15.7168	55.1608	0.5451	0.0952	11.6408	0.1489	7.8216	0.5389	0.8479	100.2638
29-4	1.3392	5.5136	15.6587	54.9401	0.5282	0.0953	11.5515	0.1628	7.8036	0.5449	0.8155	99.7673
29-5	1.2982	5.5706	15.6505	55.0241	0.5168	0.1237	11.6055	0.1502	7.844	0.5223	0.8753	100.0548
29-6	1.2982	5.6534	15.562	55.2377	0.5156	0.0635	11.707	0.1483	7.8264	0.518	0.8204	100.1693
29-7	1.3006	5.6023	15.6614	55.1263	0.5073	0.0938	11.653	0.1552	7.8332	0.5213	0.8757	100.2042
29-8	1.3023	5.656	15.6815	54.9903	0.5337	0.1112	11.5391	0.1613	7.7811	0.4906	0.8366	99.9188
29-9	1.3162	5.6483	15.6797	55.1395	0.5435	0.0847	11.6733	0.175	7.7899	0.5167	0.8601	100.2854
29-10	1.2938	5.7704	15.7384	54.9344	0.5282	0.0977	11.7481	0.1504	7.8142	0.5093	0.855	100.2933
VG2-25	*2.4167*	*6.9855*	*14.2949*	*50.8214*	*0.2023*	*0.2182*	*10.9724*	*0.1927*	*12.4394*	*2.0795*	*0.135*	*100.8926*
VG2-26	*2.6585*	*7.2747*	*14.4364*	*51.0276*	*0.2341*	*0.1965*	*10.4235*	*0.2186*	*12.5492*	*2.1111*	*0.1624*	*101.4547*
29-11	1.3027	5.7052	15.4948	54.9909	0.5422	0.1015	11.4309	0.1592	7.7798	0.5099	0.8383	99.6922
29-12	1.3094	5.7023	15.5147	54.9995	0.5279	0.1088	11.7215	0.161	7.7716	0.5374	0.8244	100.0013
29-13	1.2765	5.77	15.5668	55.1555	0.5057	0.0655	11.6112	0.1664	7.7416	0.532	0.8144	100.0185
29-14	1.3154	5.7793	15.379	54.2331	0.4942	0.087	11.3396	0.1635	7.7543	0.5381	0.846	98.7739
29-15	1.3123	5.7597	15.5692	54.7838	0.5168	0.125	11.5682	0.1662	7.8664	0.5258	0.8508	99.8936
29-16	1.3371	5.5943	15.6242	55.0123	0.5355	0.0805	11.5411	0.1686	7.7534	0.5341	0.8229	99.8255
29-17	1.2915	5.7822	15.5571	55.1099	0.5091	0.0858	11.594	0.1592	7.8123	0.5389	0.8344	100.1072
29-18	1.3572	5.7024	15.5524	55.0838	0.534	0.1086	11.5768	0.1517	7.7917	0.5296	0.8682	100.123

Table C2 *Microprobe spot analyses*

Sample	Na_2O (wt. %)	MgO (wt. %)	Al_2O_3 (wt. %)	SiO_2 (wt. %)	K_2O (wt. %)	P_2O_5 (wt. %)	CaO (wt. %)	MnO (wt. %)	FeO (wt. %)	TiO_2 (wt. %)	S Element %	Total
29-19	1.3138	5.6564	15.5293	55.132	0.5189	0.0709	11.5522	0.1569	7.8075	0.5021	0.8913	100.021
29-20	1.2839	5.6215	15.4895	54.7539	0.5052	0.0845	11.4118	0.158	7.7381	0.536	0.8387	99.2583
VG2-27	*2.4711*	*6.9063*	*14.361*	*50.769*	*0.22*	*0.1784*	*10.989*	*0.2296*	*12.5762*	*2.1182*	*0.1253*	*101.0692*
VG2-28	*2.458*	*6.8213*	*14.3555*	*50.7059*	*0.2201*	*0.2114*	*10.977*	*0.2178*	*12.5599*	*2.117*	*0.1544*	*100.9523*
VG2-29	*2.4535*	*6.868*	*14.2426*	*50.1088*	*0.2279*	*0.1961*	*10.9117*	*0.2109*	*12.5197*	*2.0771*	*0.1407*	*100.0974*

Notes:

'*' denotes sample change during session

Appendix D: MELTS models and Hadamard-Rybczynski equation calculations

The following sets of tables provide each line of each MELTS (Ghiorsi and Sack, 1995) model used in Chapter 5 and the Hadamard-Rybczynski equation (H-R) settling velocity calculations for the various models. MELTS revision 1.8 was used to run the models and to determine liquidus temperatures. This data was collected from the unformatted data table output after each successful MELTS run and slightly modified to fit into appropriate space. Data columns that were not used or had '0' in every line were deleted. The viscosity equations of Giordano (1998) were then applied to the chemical composition data provided by the MELTS models.

There are four sets of tables, presented in increasing tonalite percentage. Each set comprises two tables: one detailing the MELTS modelled chemical composition of remaining melt and one detailing the H-R settling velocity calculations for the relevant compositions. Each H-R settling velocity table follows immediately after the appropriate MELTS data table.

Table D1-1 10% tonalite/90% IAB mixture MELTS model output

T (°C)	P (kb)	liquid mass (gm)	liquid ρ (gm/cc)	SiO_2 (wt. %)	TiO_2 (wt. %)	Al_2O_3 (wt. %)	Fe_2O_3 (wt. %)	FeO (wt. %)	MnO (wt. %)	MgO (wt. %)	CaO (wt. %)	Na_2O (wt. %)	K_2O (wt. %)	P_2O_5 (wt. %)	H_2O (wt. %)	solid mass (gm)	Viscosity (Pa s)
1245.51	8	100.2538	2.7065	51.3950	0.6375	17.8315	0.1697	2.2216	7.2526	7.2080	10.2877	1.5351	0.3869	0.0769	0.9975	0.0081	2.26E+0
1240.51	8	99.6849	2.7071	51.3681	0.6408	17.9168	0.1681	2.2033	7.2940	7.0593	10.3363	1.5437	0.3891	0.0773	1.0032	0.5771	2.37E+0
1235.51	8	99.1259	2.7078	51.3418	0.6440	18.0013	0.1665	2.1844	7.3351	6.9128	10.3839	1.5522	0.3913	0.0778	1.0088	1.1361	2.49E+0
1230.51	8	97.7849	2.7079	51.3197	0.6511	18.1875	0.1593	2.1662	7.4357	6.7321	10.2800	1.5702	0.3967	0.0788	1.0227	2.4771	2.58E+0
1225.51	8	96.1402	2.7077	51.3015	0.6596	18.4161	0.1497	2.1478	7.5629	6.5391	10.1073	1.5922	0.4035	0.0802	1.0401	4.1217	2.66E+0
1220.51	8	94.5670	2.7075	51.2856	0.6677	18.6387	0.1407	2.1286	7.6887	6.3509	9.9362	1.6137	0.4102	0.0815	1.0575	5.6949	2.74E+0
1215.51	8	93.0608	2.7073	51.2720	0.6755	18.8553	0.1322	2.1085	7.8132	6.1676	9.7667	1.6347	0.4168	0.0828	1.0746	7.2011	2.84E+0
1210.51	8	91.6176	2.7072	51.2607	0.6830	19.0662	0.1241	2.0876	7.9363	5.9890	9.5989	1.6552	0.4234	0.0842	1.0915	8.6444	2.94E+0
1205.51	8	90.2334	2.7071	51.2516	0.6901	19.2712	0.1165	2.0659	8.0580	5.8151	9.4328	1.6751	0.4299	0.0854	1.1082	10.0285	3.06E+0
1200.51	8	88.9047	2.7069	51.2447	0.6969	19.4706	0.1094	2.0436	8.1784	5.6457	9.2683	1.6945	0.4363	0.0867	1.1248	11.3573	3.19E+0
1195.51	8	87.6281	2.7068	51.2399	0.7032	19.6645	0.1027	2.0205	8.2976	5.4808	9.1055	1.7135	0.4427	0.0880	1.1412	12.6339	3.33E+0
1190.51	8	86.4006	2.7067	51.2372	0.7093	19.8530	0.0964	1.9968	8.4155	5.3202	8.9444	1.7318	0.4490	0.0892	1.1574	13.8614	3.48E+0
1185.51	8	85.2195	2.7067	51.2364	0.7149	20.0360	0.0906	1.9724	8.5321	5.1638	8.7850	1.7497	0.4552	0.0905	1.1734	15.0425	3.65E+0
1180.51	8	84.0822	2.7066	51.2377	0.7202	20.2137	0.0851	1.9474	8.6475	5.0116	8.6273	1.7670	0.4613	0.0917	1.1893	16.1798	3.83E+0
1175.51	8	82.9864	2.7066	51.2410	0.7251	20.3863	0.0800	1.9219	8.7617	4.8635	8.4714	1.7838	0.4674	0.0929	1.2050	17.2756	4.04E+0
1170.51	8	81.9298	2.7066	51.2461	0.7297	20.5536	0.0752	1.8959	8.8747	4.7195	8.3172	1.8000	0.4735	0.0941	1.2206	18.3322	4.26E+0
1165.51	8	80.9103	2.7065	51.2531	0.7339	20.7160	0.0708	1.8693	8.9865	4.5794	8.1648	1.8157	0.4794	0.0953	1.2359	19.3517	4.50E+0
1160.51	8	79.9261	2.7066	51.2619	0.7377	20.8733	0.0667	1.8423	9.0972	4.4431	8.0141	1.8308	0.4853	0.0965	1.2512	20.3359	4.77E+0
1155.51	8	78.9753	2.7066	51.2724	0.7411	21.0258	0.0629	1.8148	9.2067	4.3106	7.8653	1.8454	0.4912	0.0976	1.2662	21.2866	5.06E+0
1150.51	8	78.0563	2.7066	51.2847	0.7442	21.1735	0.0593	1.7870	9.3151	4.1818	7.7182	1.8593	0.4969	0.0988	1.2811	22.2057	5.38E+0
1145.51	8	77.1675	2.7067	51.2987	0.7469	21.3165	0.0560	1.7587	9.4224	4.0566	7.5730	1.8728	0.5027	0.0999	1.2959	23.0945	5.73E+0
1140.51	8	76.3073	2.7067	51.3143	0.7493	21.4548	0.0529	1.7301	9.5286	3.9350	7.4296	1.8856	0.5083	0.1010	1.3105	23.9547	6.11E+0
1135.51	8	75.4247	2.7069	51.3302	0.7519	21.5807	0.0501	1.7019	9.6401	3.8176	7.2889	1.8965	0.5142	0.1022	1.3258	24.8373	6.54E+0
1130.51	8	73.2862	2.7073	51.3680	0.7698	21.5110	0.0499	1.6809	9.8616	3.7159	7.1750	1.8709	0.5274	0.1052	1.3645	26.9757	7.13E+0
1125.51	8	70.9480	2.7050	51.5518	0.7915	21.4373	0.0509	1.6338	9.9604	3.6042	7.0724	1.8372	0.5424	0.1087	1.4095	29.3140	8.24E+0
1120.51	8	68.7442	2.7028	51.7314	0.8128	21.3679	0.0517	1.5864	10.0545	3.4970	6.9719	1.8022	0.5573	0.1122	1.4547	31.5178	9.50E+0
1115.51	8	66.6659	2.7006	51.9069	0.8338	21.3025	0.0525	1.5387	10.1441	3.3940	6.8733	1.7663	0.5722	0.1157	1.5000	33.5961	1.09E+1
1110.51	8	64.7045	2.6984	52.0790	0.8544	21.2408	0.0532	1.4910	10.2291	3.2948	6.7763	1.7297	0.5870	0.1192	1.5455	35.5575	1.26E+1

Table D1-1 10% tonalite/90% IAB mixture MELTS model output

T (°C)	P (kb)	liquid mass (gm)	liquid ρ (gm/cc)	SiO_2 (wt. %)	TiO_2 (wt. %)	Al_2O_3 (wt. %)	Fe_2O_3 (wt. %)	FeO (wt. %)	MnO (wt. %)	MgO (wt. %)	CaO (wt. %)	Na_2O (wt. %)	K_2O (wt. %)	P_2O_5 (wt. %)	H_2O (wt. %)	solid mass (gm)	Viscosity (Pa s)
1105.51	8	62.8520	2.6962	52.2480	0.8745	21.1824	0.0539	1.4434	10.3098	3.1993	6.6808	1.6926	0.6017	0.1227	1.5910	37.4100	1.45E+1
1100.51	8	61.1008	2.6940	52.4142	0.8942	21.1270	0.0545	1.3962	10.3862	3.1071	6.5866	1.6551	0.6162	0.1262	1.6366	39.1611	1.66E+1
1095.51	8	59.4440	2.6919	52.5781	0.9133	21.0743	0.0550	1.3494	10.4582	3.0181	6.4935	1.6175	0.6307	0.1297	1.6823	40.8180	1.91E+1
1090.51	8	57.8749	2.6897	52.7399	0.9319	21.0241	0.0554	1.3031	10.5260	2.9321	6.4015	1.5798	0.6451	0.1332	1.7279	42.3871	2.19E+1
1085.51	8	56.3876	2.6876	52.9001	0.9499	20.9762	0.0559	1.2575	10.5896	2.8489	6.3104	1.5422	0.6593	0.1367	1.7734	43.8744	2.52E+1
1080.51	8	54.9763	2.6855	53.0588	0.9672	20.9303	0.0562	1.2126	10.6489	2.7684	6.2202	1.5048	0.6734	0.1402	1.8190	45.2856	2.89E+1
1075.51	8	53.6360	2.6834	53.2164	0.9839	20.8862	0.0566	1.1686	10.7040	2.6904	6.1307	1.4676	0.6874	0.1437	1.8644	46.6259	3.33E+1
1070.51	8	52.3619	2.6813	53.3731	0.9999	20.8439	0.0568	1.1254	10.7549	2.6147	6.0420	1.4309	0.7013	0.1472	1.9098	47.9001	3.83E+1
1065.51	8	51.1495	2.6793	53.5291	1.0152	20.8031	0.0571	1.0832	10.8016	2.5414	5.9540	1.3945	0.7151	0.1507	1.9551	49.1125	4.41E+1
1060.51	8	49.9947	2.6772	53.6847	1.0298	20.7636	0.0573	1.0419	10.8441	2.4702	5.8666	1.3586	0.7287	0.1542	2.0002	50.2673	5.08E+1
1055.51	8	48.8937	2.6751	53.8400	1.0436	20.7255	0.0575	1.0016	10.8824	2.4011	5.7798	1.3232	0.7423	0.1577	2.0453	51.3682	5.86E+1
1050.51	8	47.8432	2.6730	53.9953	1.0566	20.6884	0.0577	0.9624	10.9165	2.3340	5.6937	1.2884	0.7557	0.1612	2.0902	52.4188	6.76E+1
1045.51	8	46.8397	2.6710	54.1507	1.0688	20.6524	0.0578	0.9242	10.9465	2.2687	5.6080	1.2542	0.7690	0.1646	2.1349	53.4222	7.82E+1
1040.51	8	45.8805	2.6689	54.3064	1.0802	20.6174	0.0579	0.8871	10.9723	2.2053	5.5230	1.2206	0.7822	0.1680	2.1796	54.3815	9.06E+1
1035.51	8	44.9626	2.6668	54.4626	1.0906	20.5831	0.0580	0.8511	10.9940	2.1437	5.4385	1.1876	0.7953	0.1715	2.2241	55.2993	1.05E+2
1030.51	8	44.0837	2.6647	54.6192	1.1002	20.5497	0.0581	0.8161	11.0115	2.0837	5.3545	1.1554	0.8082	0.1749	2.2684	56.1783	1.22E+2
1025.51	8	43.2412	2.6627	54.7766	1.1089	20.5170	0.0581	0.7822	11.0249	2.0254	5.2711	1.1238	0.8211	0.1783	2.3126	57.0208	1.42E+2
1020.51	8	42.4330	2.6606	54.9348	1.1166	20.4849	0.0582	0.7494	11.0343	1.9686	5.1882	1.0928	0.8339	0.1817	2.3567	57.8289	1.65E+2
1015.51	8	41.6559	2.6585	55.0936	1.1234	20.4531	0.0582	0.7177	11.0399	1.9134	5.1060	1.0624	0.8466	0.1851	2.4006	58.6060	1.93E+2
1010.51	8	40.9102	2.6564	55.2536	1.1292	20.4221	0.0582	0.6870	11.0413	1.8596	5.0243	1.0328	0.8592	0.1885	2.4444	59.3518	2.26E+2
1005.51	8	40.1930	2.6543	55.4146	1.1339	20.3915	0.0582	0.6574	11.0387	1.8073	4.9431	1.0039	0.8717	0.1918	2.4880	60.0689	2.64E+2
1000.51	8	39.5029	2.6522	55.5768	1.1377	20.3613	0.0582	0.6288	11.0321	1.7563	4.8625	0.9756	0.8841	0.1952	2.5315	60.7590	3.01E+2
995.51	8	38.8384	2.6500	55.7402	1.1403	20.3314	0.0582	0.6012	11.0216	1.7067	4.7826	0.9481	0.8964	0.1985	2.5748	61.4236	3.64E+2
990.51	8	38.1979	2.6479	55.9049	1.1420	20.3020	0.0582	0.5746	11.0073	1.6583	4.7032	0.9212	0.9086	0.2018	2.6179	62.0640	4.29E+2
985.51	8	37.5803	2.6457	56.0708	1.1425	20.2728	0.0582	0.5489	10.9892	1.6113	4.6245	0.8949	0.9208	0.2052	2.6610	62.6816	5.06E+2
980.51	8	36.9844	2.6436	56.2381	1.1420	20.2439	0.0582	0.5243	10.9673	1.5654	4.5463	0.8694	0.9329	0.2085	2.7038	63.2776	5.98E+2
975.51	8	36.4089	2.6414	56.4068	1.1403	20.2152	0.0581	0.5005	10.9417	1.5208	4.4689	0.8445	0.9449	0.2118	2.7466	63.8531	7.08E+2
970.51	8	35.8529	2.6392	56.5769	1.1376	20.1867	0.0581	0.4777	10.9124	1.4773	4.3921	0.8202	0.9568	0.2150	2.7892	64.4091	8.40E+2

Table D1-1 *10% tonalite/90% IAB mixture MELTS model output*

T (°C)	P (kb)	liquid mass (gm)	liquid ρ (gm/cc)	SiO_2 (wt. %)	TiO_2 (wt. %)	Al_2O_3 (wt. %)	Fe_2O_3 (wt. %)	FeO (wt. %)	MnO (wt. %)	MgO (wt. %)	CaO (wt. %)	Na_2O (wt. %)	K_2O (wt. %)	P_2O_5 (wt. %)	H_2O (wt. %)	solid mass (gm)	Viscosity (Pa s)
965.51	8	35.3154	2.6371	56.7484	1.1337	20.1584	0.0581	0.4557	10.8795	1.4350	4.3160	0.7965	0.9687	0.2183	2.8316	64.9466	9.99E+2
960.51	8	34.7954	2.6349	56.9213	1.1288	20.1303	0.0580	0.4346	10.8432	1.3937	4.2406	0.7735	0.9805	0.2216	2.8739	65.4666	1.19E+3
955.51	8	34.2921	2.6326	57.0955	1.1227	20.1023	0.0580	0.4144	10.8034	1.3536	4.1660	0.7510	0.9922	0.2248	2.9161	65.9698	1.42E+3
950.51	8	33.8048	2.6304	57.2712	1.1155	20.0744	0.0579	0.3950	10.7602	1.3145	4.0921	0.7292	1.0039	0.2281	2.9582	66.4572	1.70E+3
945.51	8	33.3326	2.6282	57.4481	1.1073	20.0466	0.0579	0.3763	10.7137	1.2764	4.0189	0.7079	1.0155	0.2313	3.0001	66.9294	2.03E+3
940.51	8	32.8749	2.6260	57.6263	1.0980	20.0189	0.0578	0.3585	10.6640	1.2394	3.9466	0.6872	1.0270	0.2345	3.0418	67.3871	2.44E+3
935.51	8	32.4310	2.6237	57.8058	1.0876	19.9912	0.0578	0.3413	10.6112	1.2033	3.8750	0.6670	1.0385	0.2377	3.0835	67.8310	2.94E+3
930.51	8	32.0003	2.6215	57.9864	1.0763	19.9636	0.0578	0.3249	10.5554	1.1682	3.8043	0.6473	1.0499	0.2409	3.1250	68.2617	3.54E+3
925.51	8	31.5823	2.6192	58.1681	1.0639	19.9361	0.0577	0.3092	10.4966	1.1340	3.7343	0.6281	1.0613	0.2441	3.1663	68.6797	4.27E+3
920.51	8	31.1764	2.6169	58.3508	1.0506	19.9086	0.0577	0.2942	10.4351	1.1007	3.6653	0.6095	1.0726	0.2473	3.2076	69.0856	5.16E+3
915.51	8	30.7821	2.6147	58.5344	1.0364	19.8811	0.0577	0.2798	10.3708	1.0684	3.5971	0.5913	1.0839	0.2505	3.2486	69.4798	6.25E+3
910.51	8	30.3990	2.6124	58.7188	1.0214	19.8536	0.0577	0.2661	10.3039	1.0369	3.5298	0.5736	1.0950	0.2536	3.2896	69.8630	7.59E+3
905.51	8	30.0266	2.6101	58.9038	1.0055	19.8262	0.0577	0.2530	10.2344	1.0063	3.4634	0.5563	1.1062	0.2568	3.3304	70.2354	9.23E+3
900.51	8	29.6645	2.6079	59.0894	0.9889	19.7987	0.0577	0.2404	10.1626	0.9765	3.3980	0.5395	1.1172	0.2599	3.3710	70.5974	1.12E+4
895.51	8	29.3124	2.6056	59.2755	0.9716	19.7713	0.0577	0.2284	10.0886	0.9476	3.3334	0.5231	1.1282	0.2630	3.4115	70.9496	1.37E+4
890.51	8	28.9698	2.6033	59.4618	0.9536	19.7440	0.0578	0.2170	10.0123	0.9194	3.2698	0.5071	1.1392	0.2661	3.4519	71.2922	1.68E+4
885.51	8	28.6278	2.6007	59.6732	0.9233	19.7093	0.0581	0.2057	9.9267	0.8918	3.2071	0.4921	1.1504	0.2693	3.4931	71.6342	2.06E+4
880.51	8	28.2892	2.5979	59.9010	0.8849	19.6693	0.0586	0.1947	9.8343	0.8648	3.1454	0.4779	1.1616	0.2725	3.5349	71.9728	2.54E+4
875.51	8	27.9606	2.5952	60.1250	0.8478	19.6300	0.0591	0.1844	9.7414	0.8386	3.0848	0.4639	1.1728	0.2757	3.5765	72.3014	3.13E+4
870.51	8	27.6417	2.5925	60.3453	0.8121	19.5913	0.0597	0.1745	9.6479	0.8133	3.0253	0.4502	1.1839	0.2789	3.6177	72.6203	3.86E+4
865.51	8	27.3320	2.5899	60.5620	0.7777	19.5531	0.0603	0.1652	9.5538	0.7887	2.9669	0.4367	1.1949	0.2821	3.6587	72.9300	4.78E+4
860.51	8	27.0313	2.5873	60.7751	0.7445	19.5156	0.0609	0.1564	9.4593	0.7649	2.9095	0.4234	1.2058	0.2852	3.6994	73.2307	5.92E+4
855.51	8	26.7391	2.5848	60.9846	0.7125	19.4787	0.0615	0.1480	9.3644	0.7418	2.8533	0.4105	1.2166	0.2883	3.7398	73.5229	7.34E+4
850.51	8	26.4552	2.5824	61.1907	0.6817	19.4424	0.0622	0.1401	9.2691	0.7195	2.7981	0.3977	1.2272	0.2914	3.7800	73.8068	9.11E+4
845.51	8	26.1919	2.5801	61.4002	0.6525	19.4020	0.0630	0.1319	9.1737	0.6981	2.7433	0.3855	1.2374	0.2944	3.8180	74.0701	1.14E+5
840.51	8	25.9941	2.5779	61.6392	0.6267	19.3402	0.0640	0.1214	9.0790	0.6787	2.6870	0.3749	1.2455	0.2966	3.8470	74.2679	1.45E+5
835.51	8	25.8025	2.5758	61.8756	0.6017	19.2791	0.0650	0.1116	8.9833	0.6598	2.6317	0.3644	1.2534	0.2988	3.8756	74.4595	1.86E+5
830.51	8	25.6169	2.5737	62.1096	0.5775	19.2188	0.0661	0.1026	8.8867	0.6414	2.5774	0.3541	1.2612	0.3010	3.9037	74.6451	2.39E+5

Table D1-1 10% tonalite/90% IAB mixture MELTS model output

T (°C)	P (kb)	liquid mass (gm)	liquid ρ (gm/cc)	SiO_2 (wt. %)	TiO_2 (wt. %)	Al_2O_3 (wt. %)	Fe_2O_3 (wt. %)	FeO (wt. %)	MnO (wt. %)	MgO (wt. %)	CaO (wt. %)	Na_2O (wt. %)	K_2O (wt. %)	P_2O_5 (wt. %)	H_2O (wt. %)	solid mass (gm)	Viscosity (Pa s)
825.51	8	25.4371	2.5717	62.3410	0.5541	19.1592	0.0673	0.0942	8.7892	0.6236	2.5243	0.3439	1.2689	0.3031	3.9313	74.8249	3.06E+5
820.51	8	25.2628	2.5697	62.5699	0.5315	19.1004	0.0685	0.0864	8.6910	0.6062	2.4721	0.3339	1.2764	0.3052	3.9584	74.9992	3.94E+5
815.51	8	25.0940	2.5677	62.7965	0.5097	19.0424	0.0697	0.0793	8.5920	0.5893	2.4210	0.3240	1.2839	0.3072	3.9850	75.1680	5.09E+5
810.51	8	24.9304	2.5659	63.0205	0.4887	18.9851	0.0710	0.0727	8.4923	0.5729	2.3709	0.3143	1.2912	0.3093	4.0112	75.3316	6.57E+5
805.51	8	24.7719	2.5640	63.2422	0.4684	18.9286	0.0723	0.0666	8.3920	0.5569	2.3218	0.3048	1.2984	0.3112	4.0368	75.4900	8.52E+5
800.51	8	24.5172	2.5624	63.3780	0.4479	18.8977	0.0738	0.0609	8.3248	0.5424	2.2756	0.2961	1.3094	0.3145	4.0788	75.7448	1.06E+6
795.51	8	23.8270	2.5618	63.1334	0.4245	18.9781	0.0759	0.0557	8.4106	0.5325	2.2395	0.2910	1.3382	0.3236	4.1969	76.4350	1.06E+6
790.51	8	23.1569	2.5612	62.8740	0.4022	19.0601	0.0781	0.0509	8.5033	0.5227	2.2047	0.2857	1.3670	0.3329	4.3184	77.1051	1.07E+6
785.51	8	22.5051	2.5608	62.5986	0.3809	19.1437	0.0804	0.0465	8.6035	0.5130	2.1711	0.2803	1.3959	0.3426	4.4434	77.7568	1.06E+6
780.51	8	21.8700	2.5604	62.3059	0.3605	19.2291	0.0828	0.0425	8.7124	0.5034	2.1388	0.2748	1.4248	0.3525	4.5725	78.3920	1.06E+6
775.51	8	21.2497	2.5602	61.9940	0.3411	19.3163	0.0853	0.0388	8.8311	0.4939	2.1078	0.2691	1.4537	0.3628	4.7060	79.0123	1.04E+6
770.51	8	20.6424	2.5601	61.6610	0.3226	19.4056	0.0879	0.0355	8.9611	0.4846	2.0781	0.2633	1.4825	0.3735	4.8444	79.6195	1.02E+6
765.51	8	20.0464	2.5601	61.3043	0.3049	19.4971	0.0907	0.0324	9.1041	0.4753	2.0497	0.2572	1.5112	0.3846	4.9884	80.2156	9.84E+5
760.51	8	19.4928	2.5602	60.9695	0.2879	19.5661	0.0928	0.0302	9.2517	0.4627	2.0266	0.2493	1.5374	0.3955	5.1301	80.7691	9.66E+5
755.51	8	18.8342	2.5609	60.4613	0.2708	19.6682	0.0949	0.0284	9.4882	0.4505	2.0094	0.2414	1.5679	0.4094	5.3095	81.4277	8.67E+5
750.51	8	18.1788	2.5619	59.9011	0.2546	19.7748	0.0972	0.0267	9.7574	0.4387	1.9937	0.2331	1.5976	0.4241	5.5009	82.0832	7.60E+5
745.51	8	17.5218	2.5633	59.2769	0.2391	19.8867	0.0996	0.0252	10.0680	0.4272	1.9797	0.2245	1.6259	0.4400	5.7072	82.7402	6.47E+5
740.51	8	16.8568	2.5651	58.5709	0.2244	20.0047	0.1021	0.0238	10.4331	0.4160	1.9678	0.2152	1.6522	0.4574	5.9323	83.4052	5.29E+5
735.51	8	14.4414	2.5822	55.5433	0.2076	20.2499	0.1151	0.0259	12.5963	0.4156	2.0703	0.1944	1.3519	0.5339	6.6959	85.8206	9.54E+4
730.51	8	8.3045	2.7033	37.4748	0.1560	19.8577	0.1381	0.0408	27.4669	0.3771	2.2742	0.0733	0.3455	0.9284	10.8673	91.9574	3.20E+1
725.51	8	7.8528	2.7131	35.7015	0.1378	19.6548	0.1384	0.0389	28.9615	0.3528	2.2564	0.0648	0.2822	0.9818	11.4291	92.4092	2.55E+1
720.51	8	7.5243	2.7196	34.4197	0.1227	19.4898	0.1387	0.0366	30.0190	0.3319	2.2411	0.0590	0.2400	1.0247	11.8768	92.7377	2.45E+1
715.51	8	7.2595	2.7244	33.3903	0.1098	19.3465	0.1391	0.0342	30.8486	0.3132	2.2280	0.0547	0.2085	1.0621	12.2651	93.0025	2.59E+1
710.51	8	6.8659	2.7290	32.4856	0.0983	19.1825	0.1511	0.0329	31.5464	0.2930	2.2505	0.0503	0.1861	1.1229	12.6004	93.3961	2.97E+1
705.51	8	6.3502	2.7338	31.6572	0.0880	18.9861	0.1796	0.0325	32.1486	0.2715	2.3148	0.0459	0.1703	1.2141	12.8912	93.9118	3.65E+1
700.51	8	5.9040	2.7380	30.9161	0.0790	18.7961	0.2134	0.0319	32.6632	0.2521	2.3828	0.0422	0.1568	1.3059	13.1605	94.3580	4.66E+1
695.51	8	5.5165	2.7418	30.2434	0.0709	18.6133	0.2531	0.0312	33.1067	0.2345	2.4532	0.0392	0.1451	1.3976	13.4118	94.7455	6.16E+1
690.51	8	5.1793	2.7454	29.6264	0.0638	18.4385	0.2996	0.0303	33.4910	0.2186	2.5248	0.0365	0.1347	1.4886	13.6472	95.0827	8.34E+1

Table D1-1 10% tonalite/90% IAB mixture MELTS model output

T (°C)	P (kb)	liquid mass (gm)	liquid ρ (gm/cc)	SiO_2 (wt. %)	TiO_2 (wt. %)	Al_2O_3 (wt. %)	Fe_2O_3 (wt. %)	FeO (wt. %)	MnO (wt. %)	MgO (wt. %)	CaO (wt. %)	Na_2O (wt. %)	K_2O (wt. %)	P_2O_5 (wt. %)	H_2O (wt. %)	solid mass (gm)	Viscosity (Pa s)
685.51	8	4.8853	2.7488	29.0555	0.0575	18.2726	0.3537	0.0293	33.8246	0.2041	2.5967	0.0342	0.1253	1.5782	13.8684	95.3767	1.16E+2
680.51	8	4.6287	2.7521	28.5238	0.0519	18.1163	0.4162	0.0282	34.1140	0.1909	2.6676	0.0322	0.1168	1.6657	14.0764	95.6333	1.63E+2
675.51	8	4.4047	2.7554	28.0257	0.0469	17.9706	0.4879	0.0270	34.3644	0.1789	2.7366	0.0304	0.1090	1.7504	14.2722	95.8573	2.34E+2
670.51	8	4.2093	2.7587	27.5568	0.0424	17.8360	0.5698	0.0258	34.5798	0.1680	2.8029	0.0287	0.1018	1.8317	14.4563	96.0527	3.40E+2
665.51	8	4.0390	2.7621	27.1136	0.0385	17.7133	0.6624	0.0245	34.7635	0.1580	2.8657	0.0272	0.0952	1.9089	14.6292	96.2230	5.03E+2
660.51	8	3.8910	2.7656	26.6932	0.0349	17.6031	0.7665	0.0233	34.9185	0.1489	2.9240	0.0259	0.0889	1.9815	14.7913	96.3710	7.52E+2
655.51	8	3.7628	2.7693	26.2931	0.0318	17.5059	0.8823	0.0220	35.0473	0.1407	2.9773	0.0246	0.0831	2.0490	14.9431	96.4992	1.14E+3

Table D1-2 Hadamard-Rybczynski equation (H-R) settling velocity calculation for 10% tonalite/90% IAB mixture.

Solid/Liquid Proportion	Sulfide/Silicate Density Differential (kg/m^3)	Settling Velocity H-R (m/s)	Globule radius (cm)	Settling Velocity H-R (m/s)
0.00	1793.50	1.62E-2	0.01	5.21E-6
0.01	1792.90	1.54E-2	0.02	2.09E-5
0.01	1792.20	1.47E-2	0.03	4.69E-5
0.02	1792.10	1.42E-2	0.04	8.34E-5
0.04	1792.30	1.38E-2	0.05	1.30E-4
0.06	1792.50	1.34E-2	0.06	1.88E-4
0.07	1792.70	1.29E-2	0.07	2.55E-4
0.09	1792.80	1.25E-2	0.08	3.34E-4
0.10	1792.90	1.20E-2	0.09	4.22E-4
0.11	1793.10	1.15E-2	0.10	5.21E-4
0.13	1793.20	1.10E-2	0.11	6.31E-4
0.14	1793.30	1.05E-2	0.12	7.51E-4
0.15	1793.30	1.01E-2	0.13	8.81E-4
0.16	1793.40	9.56E-3	0.14	1.02E-3
0.17	1793.40	9.08E-3	0.15	1.17E-3
0.18	1793.40	8.61E-3	0.16	1.33E-3
0.19	1793.50	8.14E-3	0.17	1.51E-3
0.20	1793.40	7.69E-3	0.18	1.69E-3
0.21	1793.40	7.25E-3	0.19	1.88E-3
0.22	1793.40	6.82E-3	0.20	2.09E-3
0.23	1793.30	6.40E-3	0.21	2.30E-3
0.24	1793.30	5.99E-3	0.22	2.52E-3
0.25	1793.10	5.61E-3	0.23	2.76E-3
0.27	1792.70	5.14E-3	0.24	3.00E-3
0.29	1795.00	4.45E-3	0.25	3.26E-3
0.31	1797.20	3.86E-3	0.26	3.52E-3
0.34	1799.40	3.36E-3	0.27	3.80E-3
0.35	1801.60	2.92E-3	0.28	4.09E-3
0.37	1803.80	2.55E-3	0.29	4.38E-3
0.39	1806.00	2.22E-3	0.30	4.69E-3
0.41	1808.10	1.93E-3	0.31	5.01E-3
0.42	1810.30	1.69E-3	0.32	5.34E-3
0.44	1812.40	1.47E-3	0.33	5.68E-3
0.45	1814.50	1.28E-3	0.34	6.03E-3
0.47	1816.60	1.12E-3	0.35	6.39E-3
0.48	1818.70	9.71E-4	0.36	6.76E-3
0.49	1820.70	8.45E-4	0.37	7.14E-3
0.50	1822.80	7.34E-4	0.38	7.53E-3
0.51	1824.90	6.37E-4	0.39	7.93E-3
0.52	1827.00	5.52E-4	0.40	8.34E-3
0.53	1829.00	4.78E-4	0.41	8.76E-3
0.54	1831.10	4.13E-4	0.42	9.20E-3
0.55	1833.20	3.57E-4	0.43	9.64E-3
0.56	1835.30	3.08E-4	0.44	1.01E-2
0.57	1837.30	2.65E-4	0.45	1.06E-2
0.58	1839.40	2.27E-4	0.46	1.10E-2
0.58	1841.50	1.95E-4	0.47	1.15E-2
0.59	1843.60	1.67E-4	0.48	1.20E-2
0.60	1845.70	1.43E-4	0.49	1.25E-2
0.61	1847.80	1.22E-4	0.50	1.30E-2
0.61	1850.00	1.04E-4	0.51	1.36E-2

Table D1-2 Hadamard-Rybczynski equation (H-R) settling velocity calculation for 10% tonalite/90% IAB mixture.

Solid/Liquid Proportion	Sulfide/Silicate Density Differential (kg/m^3)	Settling Velocity H-R (m/s)	Globule radius (cm)	Settling Velocity H-R (m/s)
0.62	1852.10	8.82E-5	0.52	1.41E-2
0.63	1854.30	7.49E-5	0.53	1.46E-2
0.63	1856.40	6.34E-5	0.54	1.52E-2
0.64	1858.60	5.36E-5	0.55	1.58E-2
0.64	1860.80	4.53E-5	0.56	1.63E-2
0.65	1862.90	3.81E-5	0.57	1.69E-2
0.65	1865.10	3.20E-5	0.58	1.75E-2
0.66	1867.40	2.69E-5	0.59	1.81E-2
0.66	1869.60	2.25E-5	0.60	1.88E-2
0.67	1871.80	1.88E-5	0.61	1.94E-2
0.67	1874.00	1.57E-5	0.62	2.00E-2
0.68	1876.30	1.31E-5	0.63	2.07E-2
0.68	1878.50	1.09E-5	0.64	2.14E-2
0.69	1880.80	9.01E-6	0.65	2.20E-2
0.69	1883.10	7.46E-6	0.66	2.27E-2
0.69	1885.30	6.16E-6	0.67	2.34E-2
0.70	1887.60	5.08E-6	0.68	2.41E-2
0.70	1889.90	4.18E-6	0.69	2.48E-2
0.70	1892.10	3.44E-6	0.70	2.55E-2
0.71	1894.40	2.82E-6	0.71	2.63E-2
0.71	1896.70	2.31E-6	0.72	2.70E-2
0.71	1899.30	1.88E-6	0.73	2.78E-2
0.72	1902.10	1.53E-6	0.74	2.85E-2
0.72	1904.80	1.24E-6	0.75	2.93E-2
0.72	1907.50	1.01E-6	0.76	3.01E-2
0.73	1910.10	8.17E-7	0.77	3.09E-2
0.73	1912.70	6.61E-7	0.78	3.17E-2
0.73	1915.20	5.33E-7	0.79	3.25E-2
0.74	1917.60	4.30E-7	0.80	3.34E-2
0.74	1919.90	3.45E-7	0.81	3.42E-2
0.74	1922.10	2.70E-7	0.82	3.51E-2
0.74	1924.20	2.11E-7	0.83	3.59E-2
0.74	1926.30	1.65E-7	0.84	3.68E-2
0.75	1928.30	1.29E-7	0.85	3.77E-2
0.75	1930.30	1.00E-7	0.86	3.86E-2
0.75	1932.30	7.76E-8	0.87	3.95E-2
0.75	1934.10	6.01E-8	0.88	4.04E-2
0.75	1936.00	4.65E-8	0.89	4.13E-2
			0.90	4.22E-2
			0.91	4.32E-2
			0.92	4.41E-2
			0.93	4.51E-2
			0.94	4.61E-2
			0.95	4.70E-2
			0.96	4.80E-2
			0.97	4.90E-2
			0.98	5.01E-2
			0.99	5.11E-2
			1.00	5.21E-2

Table D2-1 20% tonalite/80% IAB mixture MELTS model output

T (°C)	P (kb)	liquid mass (gm)	liquid ρ (gm/cc)	SiO_2 (wt. %)	TiO_2 (wt. %)	Al_2O_3 (wt. %)	Fe_2O_3 (wt. %)	FeO (wt. %)	MnO (wt. %)	MgO (wt. %)	CaO (wt. %)	Na_2O (wt. %)	K_2O (wt. %)	P_2O_5 (wt. %)	H_2O (wt. %)	solid mass (gm)	Viscosity (Pa s)
1239.06	8	100.0562	2.6873	52.9079	0.6488	17.7333	0.1920	2.5342	6.4684	6.6777	9.4116	1.6670	0.6744	0.0852	0.9994	0.0225	5.23E+0
1234.06	8	99.3156	2.6875	52.8930	0.6532	17.8419	0.1894	2.5004	6.5166	6.5125	9.4422	1.6788	0.6795	0.0858	1.0069	0.7631	5.54E+0
1229.06	8	98.5484	2.6876	52.8794	0.6577	17.9550	0.1865	2.4648	6.5673	6.3467	9.4658	1.6909	0.6847	0.0865	1.0147	1.5302	5.88E+0
1224.06	8	97.2057	2.6873	52.8230	0.6660	18.1680	0.1834	2.4204	6.6580	5.9215	9.6342	1.7149	0.6942	0.0876	1.0287	2.8730	6.18E+0
1219.06	8	96.3453	2.6874	52.8179	0.6708	18.2929	0.1788	2.3979	6.7175	5.7721	9.5970	1.7284	0.7004	0.0884	1.0379	3.7334	6.57E+0
1214.06	8	94.8954	2.6869	52.8297	0.6784	18.4961	0.1692	2.3760	6.8201	5.5971	9.4286	1.7500	0.7111	0.0898	1.0538	5.1833	6.95E+0
1209.06	8	93.5060	2.6865	52.8433	0.6857	18.6936	0.1601	2.3533	6.9215	5.4271	9.2620	1.7711	0.7217	0.0911	1.0694	6.5726	7.37E+0
1204.06	8	92.1735	2.6860	52.8587	0.6926	18.8856	0.1514	2.3297	7.0215	5.2619	9.0973	1.7917	0.7321	0.0924	1.0849	7.9052	7.83E+0
1199.06	8	90.8941	2.6856	52.8758	0.6992	19.0722	0.1431	2.3053	7.1204	5.1014	8.9345	1.8118	0.7424	0.0937	1.1002	9.1846	8.34E+0
1194.06	8	89.6649	2.6852	52.8946	0.7055	19.2536	0.1353	2.2801	7.2180	4.9454	8.7735	1.8313	0.7526	0.0950	1.1153	10.4138	8.90E+0
1189.06	8	88.4828	2.6848	52.9150	0.7114	19.4297	0.1278	2.2541	7.3144	4.7938	8.6145	1.8503	0.7626	0.0963	1.1302	11.5958	9.52E+0
1184.06	8	87.3454	2.6844	52.9370	0.7169	19.6007	0.1208	2.2275	7.4097	4.6465	8.4572	1.8688	0.7726	0.0975	1.1449	12.7333	1.02E+1
1179.06	8	86.2500	2.6840	52.9605	0.7222	19.7666	0.1142	2.2001	7.5038	4.5035	8.3019	1.8867	0.7824	0.0988	1.1594	13.8287	1.01E+1
1174.06	8	85.1944	2.6837	52.9855	0.7270	19.9277	0.1079	2.1721	7.5967	4.3647	8.1484	1.9041	0.7921	0.1000	1.1738	14.8843	1.18E+1
1169.06	8	84.1764	2.6834	53.0120	0.7316	20.0839	0.1020	2.1435	7.6886	4.2298	7.9968	1.9209	0.8016	0.1012	1.1880	15.9023	1.27E+1
1164.06	8	83.1941	2.6831	53.0399	0.7357	20.2354	0.0965	2.1143	7.7794	4.0990	7.8471	1.9372	0.8111	0.1024	1.2020	16.8846	1.37E+1
1159.06	8	82.2455	2.6828	53.0691	0.7396	20.3821	0.0913	2.0846	7.8691	3.9719	7.6993	1.9530	0.8205	0.1036	1.2159	17.8332	1.48E+1
1154.06	8	81.3289	2.6825	53.0998	0.7431	20.5244	0.0864	2.0544	7.9578	3.8486	7.5533	1.9682	0.8297	0.1048	1.2296	18.7497	1.61E+1
1149.06	8	80.4428	2.6823	53.1317	0.7462	20.6621	0.0818	2.0237	8.0455	3.7290	7.4093	1.9829	0.8389	0.1059	1.2431	19.6359	1.74E+1
1144.06	8	79.5854	2.6820	53.1649	0.7490	20.7954	0.0774	1.9926	8.1321	3.6129	7.2671	1.9970	0.8479	0.1071	1.2565	20.4932	1.90E+1
1139.06	8	78.7555	2.6818	53.1994	0.7515	20.9244	0.0734	1.9610	8.2178	3.5004	7.1268	2.0106	0.8568	0.1082	1.2698	21.3232	2.07E+1
1134.06	8	77.9517	2.6816	53.2350	0.7536	21.0491	0.0696	1.9291	8.3026	3.3912	6.9885	2.0236	0.8657	0.1093	1.2828	22.1270	2.26E+1
1129.06	8	76.4306	2.6820	53.2652	0.7641	21.0529	0.0678	1.9075	8.4678	3.2936	6.8657	2.0143	0.8812	0.1115	1.3084	23.6481	2.47E+1
1124.06	8	74.5105	2.6827	53.2878	0.7801	20.9818	0.0671	1.8919	8.6860	3.2045	6.7544	1.9889	0.9010	0.1143	1.3421	25.5681	2.69E+1
1119.06	8	72.6786	2.6835	53.3062	0.7960	20.9124	0.0665	1.8750	8.9050	3.1183	6.6459	1.9609	0.9206	0.1172	1.3759	27.4001	2.92E+1
1114.06	8	70.9297	2.6844	53.3204	0.8117	20.8447	0.0659	1.8570	9.1245	3.0350	6.5401	1.9306	0.9401	0.1201	1.4098	29.1490	3.17E+1
1109.06	8	68.9939	2.6828	53.4681	0.8306	20.7774	0.0664	1.8119	9.2295	2.9448	6.4421	1.8939	0.9625	0.1235	1.4494	31.0847	3.64E+1
1104.06	8	67.0424	2.6801	53.6764	0.8507	20.7129	0.0674	1.7544	9.2770	2.8537	6.3481	1.8544	0.9862	0.1271	1.4916	33.0362	4.28E+1

Table D2-1 *20% tonalite/80% IAB mixture MELTS model output*

T (°C)	P (kb)	liquid mass (gm)	liquid ρ (gm/cc)	SiO_2 (wt. %)	TiO_2 (wt. %)	Al_2O_3 (wt. %)	Fe_2O_3 (wt. %)	FeO (wt. %)	MnO (wt. %)	MgO (wt. %)	CaO (wt. %)	Na_2O (wt. %)	K_2O (wt. %)	P_2O_5 (wt. %)	H_2O (wt. %)	solid mass (gm)	Viscosity (Pa s)
1099.06	8	65.1990	2.6774	53.8812	0.8704	20.6519	0.0683	1.6971	9.3207	2.7661	6.2556	1.8145	1.0097	0.1307	1.5338	34.8797	5.04E+1
1094.06	8	63.4562	2.6748	54.0827	0.8896	20.5939	0.0690	1.6402	9.3607	2.6820	6.1642	1.7744	1.0330	0.1343	1.5759	36.6224	5.92E+1
1089.06	8	61.8072	2.6722	54.2814	0.9082	20.5388	0.0697	1.5837	9.3970	2.6010	6.0740	1.7342	1.0561	0.1378	1.6179	38.2715	6.96E+1
1084.06	8	60.2455	2.6696	54.4774	0.9263	20.4862	0.0704	1.5280	9.4296	2.5229	5.9848	1.6941	1.0790	0.1414	1.6599	39.8332	8.17E+1
1079.06	8	58.7650	2.6670	54.6712	0.9438	20.4359	0.0709	1.4730	9.4587	2.4477	5.8965	1.6540	1.1016	0.1450	1.7017	41.3136	9.60E+1
1074.06	8	57.3604	2.6645	54.8628	0.9608	20.3877	0.0714	1.4190	9.4841	2.3751	5.8090	1.6142	1.1240	0.1485	1.7434	42.7182	1.13E+2
1069.06	8	56.0265	2.6620	55.0526	0.9771	20.3414	0.0718	1.3660	9.5060	2.3049	5.7224	1.5747	1.1462	0.1521	1.7849	44.0522	1.33E+2
1064.06	8	54.7585	2.6595	55.2408	0.9927	20.2969	0.0722	1.3141	9.5243	2.2371	5.6364	1.5356	1.1682	0.1556	1.8262	45.3202	1.56E+2
1059.06	8	53.5521	2.6571	55.4276	1.0076	20.2539	0.0725	1.2633	9.5391	2.1715	5.5512	1.4969	1.1899	0.1591	1.8673	46.5266	1.84E+2
1054.06	8	52.4031	2.6546	55.6132	1.0219	20.2123	0.0728	1.2138	9.5505	2.1080	5.4666	1.4587	1.2114	0.1626	1.9083	47.6755	2.16E+2
1049.06	8	51.3080	2.6522	55.7977	1.0354	20.1720	0.0731	1.1656	9.5583	2.0466	5.3827	1.4210	1.2327	0.1661	1.9490	48.7707	2.55E+2
1044.06	8	50.2632	2.6498	55.9813	1.0481	20.1329	0.0733	1.1186	9.5628	1.9871	5.2993	1.3838	1.2537	0.1695	1.9895	49.8155	3.01E+2
1039.06	8	49.2655	2.6475	56.1642	1.0601	20.0949	0.0734	1.0729	9.5638	1.9294	5.2166	1.3473	1.2745	0.1729	2.0298	50.8132	3.55E+2
1034.06	8	48.3120	2.6451	56.3466	1.0712	20.0579	0.0736	1.0286	9.5614	1.8734	5.1344	1.3114	1.2951	0.1764	2.0699	51.7667	4.20E+2
1029.06	8	47.3999	2.6428	56.5285	1.0815	20.0218	0.0737	0.9857	9.5557	1.8192	5.0529	1.2761	1.3155	0.1797	2.1097	52.6787	4.97E+2
1024.06	8	46.5268	2.6405	56.7100	1.0910	19.9865	0.0738	0.9440	9.5467	1.7665	4.9719	1.2415	1.3357	0.1831	2.1493	53.5519	5.89E+2
1019.06	8	45.6903	2.6382	56.8914	1.0996	19.9519	0.0738	0.9037	9.5343	1.7154	4.8915	1.2075	1.3557	0.1865	2.1886	54.3884	6.99E+2
1014.06	8	44.8865	2.6359	57.0724	1.1074	19.9178	0.0739	0.8648	9.5190	1.6659	4.8118	1.1740	1.3755	0.1898	2.2278	55.1922	8.31E+2
1009.06	8	44.1163	2.6336	57.2535	1.1142	19.8845	0.0739	0.8272	9.5003	1.6177	4.7326	1.1413	1.3951	0.1931	2.2667	55.9623	9.88E+2
1004.06	8	43.3766	2.6313	57.4347	1.1200	19.8517	0.0739	0.7909	9.4784	1.5709	4.6539	1.1093	1.4145	0.1964	2.3054	56.7020	1.18E+3
999.06	8	42.6657	2.6291	57.6160	1.1249	19.8195	0.0739	0.7558	9.4534	1.5254	4.5759	1.0780	1.4336	0.1997	2.3438	57.4130	1.40E+3
994.06	8	41.9820	2.6268	57.7976	1.1288	19.7877	0.0739	0.7221	9.4253	1.4812	4.4985	1.0473	1.4527	0.2029	2.3820	58.0967	1.68E+3
989.06	8	41.3238	2.6246	57.9794	1.1318	19.7563	0.0738	0.6895	9.3941	1.4383	4.4218	1.0173	1.4715	0.2062	2.4199	58.7548	2.01E+3
984.06	8	40.6900	2.6224	58.1616	1.1337	19.7254	0.0738	0.6582	9.3600	1.3965	4.3456	0.9880	1.4901	0.2094	2.4576	59.3887	2.41E+3
979.06	8	40.0791	2.6202	58.3441	1.1346	19.6948	0.0737	0.6281	9.3229	1.3560	4.2702	0.9594	1.5086	0.2126	2.4951	59.9995	2.89E+3
974.06	8	39.4900	2.6179	58.5271	1.1344	19.6645	0.0737	0.5992	9.2829	1.3165	4.1954	0.9314	1.5269	0.2158	2.5323	60.5887	3.47E+3
969.06	8	38.9215	2.6157	58.7106	1.1332	19.6345	0.0736	0.5713	9.2401	1.2781	4.1212	0.9041	1.5451	0.2189	2.5693	61.1571	4.17E+3
964.06	8	38.3727	2.6135	58.8945	1.1309	19.6048	0.0735	0.5446	9.1946	1.2408	4.0478	0.8774	1.5630	0.2220	2.6060	61.7060	5.03E+3

Table D2-1 20% tonalite/80% IAB mixture MELTS model output

T (°C)	P (kb)	liquid mass (gm)	liquid ρ (gm/cc)	SiO_2 (wt. %)	TiO_2 (wt. %)	Al_2O_3 (wt. %)	Fe_2O_3 (wt. %)	FeO (wt. %)	MnO (wt. %)	MgO (wt. %)	CaO (wt. %)	Na_2O (wt. %)	K_2O (wt. %)	P_2O_5 (wt. %)	H_2O (wt. %)	solid mass (gm)	Viscosity (Pa s)
959.06	8	37.8424	2.6114	59.0790	1.1276	19.5753	0.0734	0.5190	9.1463	1.2045	3.9751	0.8514	1.5809	0.2251	2.6425	62.2363	6.07E+3
954.06	8	37.3298	2.6092	59.2640	1.1232	19.5460	0.0733	0.4944	9.0954	1.1692	3.9031	0.8260	1.5985	0.2282	2.6788	62.7489	7.34E+3
949.06	8	36.8340	2.6070	59.4495	1.1177	19.5169	0.0732	0.4708	9.0419	1.1349	3.8318	0.8012	1.6160	0.2313	2.7149	63.2447	8.89E+3
944.06	8	36.3542	2.6048	59.6355	1.1111	19.4879	0.0731	0.4482	8.9859	1.1016	3.7614	0.7770	1.6334	0.2344	2.7507	63.7245	1.08E+4
939.06	8	35.8897	2.6026	59.8221	1.1035	19.4591	0.0730	0.4265	8.9275	1.0691	3.6917	0.7534	1.6506	0.2374	2.7863	64.1890	1.31E+4
934.06	8	35.4398	2.6005	60.0091	1.0948	19.4305	0.0729	0.4058	8.8667	1.0376	3.6227	0.7303	1.6676	0.2404	2.8217	64.6389	1.59E+4
929.06	8	35.0038	2.5983	60.1966	1.0851	19.4019	0.0728	0.3859	8.8036	1.0069	3.5547	0.7079	1.6845	0.2434	2.8568	65.0749	1.94E+4
924.06	8	34.5811	2.5962	60.3845	1.0743	19.3734	0.0727	0.3669	8.7384	0.9770	3.4874	0.6860	1.7012	0.2464	2.8918	65.4976	2.37E+4
919.06	8	34.1711	2.5940	60.5727	1.0626	19.3450	0.0726	0.3488	8.6710	0.9480	3.4210	0.6646	1.7179	0.2493	2.9264	65.9076	2.89E+4
914.06	8	33.7733	2.5919	60.7613	1.0499	19.3167	0.0725	0.3314	8.6017	0.9198	3.3554	0.6438	1.7343	0.2523	2.9609	66.3054	3.54E+4
909.06	8	33.3872	2.5898	60.9500	1.0363	19.2885	0.0724	0.3148	8.5304	0.8924	3.2907	0.6235	1.7506	0.2552	2.9952	66.6915	4.34E+4
904.06	8	33.0122	2.5876	61.1389	1.0218	19.2602	0.0723	0.2990	8.4572	0.8658	3.2270	0.6037	1.7668	0.2581	3.0292	67.0664	5.33E+4
899.06	8	32.6481	2.5855	61.3279	1.0064	19.2321	0.0723	0.2839	8.3824	0.8399	3.1641	0.5844	1.7828	0.2610	3.0630	67.4306	6.55E+4
894.06	8	32.2942	2.5834	61.5168	0.9903	19.2040	0.0722	0.2695	8.3058	0.8147	3.1022	0.5656	1.7987	0.2638	3.0965	67.7845	8.06E+4
889.06	8	31.9387	2.5809	61.7371	0.9577	19.1660	0.0725	0.2551	8.2201	0.7899	3.0410	0.5480	1.8149	0.2668	3.1310	68.1400	9.95E+4
884.06	8	31.5887	2.5783	61.9685	0.9189	19.1239	0.0730	0.2413	8.1302	0.7657	2.9808	0.5311	1.8312	0.2697	3.1657	68.4900	1.23E+5
879.06	8	31.2494	2.5758	62.1958	0.8815	19.0825	0.0735	0.2282	8.0400	0.7423	2.9217	0.5146	1.8472	0.2726	3.2001	68.8292	1.52E+5
874.06	8	30.9205	2.5733	62.4190	0.8453	19.0418	0.0741	0.2158	7.9495	0.7196	2.8638	0.4983	1.8631	0.2755	3.2341	69.1581	1.89E+5
869.06	8	30.6600	2.5709	62.6649	0.8133	18.9789	0.0750	0.2002	7.8641	0.6993	2.8044	0.4845	1.8760	0.2779	3.2616	69.4187	2.38E+5
864.06	8	30.4219	2.5687	62.9139	0.7830	18.9111	0.0759	0.1847	7.7794	0.6799	2.7455	0.4713	1.8880	0.2801	3.2871	69.6568	3.01E+5
859.06	8	30.1915	2.5665	63.1595	0.7537	18.8441	0.0769	0.1704	7.6940	0.6611	2.6877	0.4584	1.8998	0.2822	3.3122	69.8872	3.82E+5
854.06	8	29.9684	2.5644	63.4019	0.7253	18.7778	0.0780	0.1570	7.6080	0.6429	2.6311	0.4456	1.9114	0.2843	3.3368	70.1103	4.85E+5
849.06	8	29.7524	2.5623	63.6409	0.6977	18.7123	0.0790	0.1446	7.5215	0.6251	2.5756	0.4329	1.9227	0.2864	3.3611	70.3263	6.17E+5
844.06	8	29.5432	2.5603	63.8768	0.6710	18.6477	0.0802	0.1332	7.4345	0.6079	2.5212	0.4205	1.9339	0.2884	3.3849	70.5355	7.86E+5
839.06	8	29.3405	2.5584	64.1095	0.6452	18.5838	0.0813	0.1225	7.3469	0.5911	2.4680	0.4082	1.9448	0.2904	3.4083	70.7381	1.00E+6
834.06	8	29.1442	2.5565	64.3390	0.6202	18.5208	0.0825	0.1127	7.2590	0.5748	2.4158	0.3962	1.9554	0.2923	3.4312	70.9345	1.28E+6
829.06	8	28.9540	2.5547	64.5655	0.5960	18.4587	0.0838	0.1036	7.1708	0.5589	2.3646	0.3843	1.9659	0.2943	3.4538	71.1247	1.64E+6
824.06	8	28.7696	2.5529	64.7889	0.5726	18.3973	0.0851	0.0952	7.0821	0.5435	2.3146	0.3726	1.9761	0.2961	3.4759	71.3091	2.10E+6

Table D2-1 20% tonalite/80% IAB mixture MELTS model output

T (°C)	P (kb)	liquid mass (gm)	liquid ρ (gm/cc)	SiO_2 (wt. %)	TiO_2 (wt. %)	Al_2O_3 (wt. %)	Fe_2O_3 (wt. %)	FeO (wt. %)	MnO (wt. %)	MgO (wt. %)	CaO (wt. %)	Na_2O (wt. %)	K_2O (wt. %)	P_2O_5 (wt. %)	H_2O (wt. %)	solid mass (gm)	Viscosity (Pa s)
819.06	8	28.5910	2.5511	65.0093	0.5499	18.3368	0.0864	0.0874	6.9933	0.5285	2.2655	0.3611	1.9862	0.2980	3.4976	71.4877	2.70E+6
814.06	8	28.4179	2.5495	65.2267	0.5280	18.2772	0.0878	0.0801	6.9041	0.5139	2.2175	0.3498	1.9960	0.2998	3.5189	71.6608	3.47E+6
809.06	8	27.9123	2.5481	65.2268	0.5038	18.2924	0.0897	0.0733	6.8823	0.5023	2.1751	0.3418	2.0245	0.3052	3.5826	72.1664	4.00E+6
804.06	8	27.1893	2.5470	65.0682	0.4784	18.3608	0.0920	0.0670	6.9101	0.4927	2.1373	0.3360	2.0662	0.3134	3.6779	72.8894	4.26E+6
799.06	8	26.4905	2.5459	64.9013	0.4541	18.4301	0.0944	0.0612	6.9404	0.4832	2.1007	0.3301	2.1079	0.3216	3.7749	73.5882	4.53E+6
794.06	8	25.8142	2.5449	64.7257	0.4309	18.5003	0.0969	0.0558	6.9736	0.4738	2.0654	0.3241	2.1496	0.3301	3.8738	74.2645	4.81E+6
789.06	8	25.1588	2.5440	64.5410	0.4087	18.5716	0.0995	0.0509	7.0098	0.4645	2.0314	0.3181	2.1911	0.3386	3.9747	74.9198	5.09E+6
784.06	8	24.5228	2.5431	64.3467	0.3875	18.6439	0.1022	0.0465	7.0494	0.4553	1.9987	0.3121	2.2326	0.3474	4.0778	75.5559	5.39E+6
779.06	8	23.9046	2.5423	64.1423	0.3672	18.7173	0.1050	0.0424	7.0928	0.4463	1.9672	0.3060	2.2738	0.3564	4.1833	76.1741	5.70E+6
774.06	8	23.2920	2.5416	63.9208	0.3473	18.7854	0.1072	0.0392	7.1511	0.4347	1.9416	0.2983	2.3151	0.3658	4.2933	76.7866	5.97E+6
769.06	8	22.6907	2.5410	63.6844	0.3280	18.8524	0.1093	0.0366	7.2191	0.4223	1.9190	0.2901	2.3563	0.3755	4.4071	77.3880	6.24E+6
764.06	8	22.1931	2.5404	63.5195	0.3105	18.8969	0.1114	0.0340	7.2613	0.4099	1.8947	0.2812	2.3909	0.3839	4.5059	77.8856	6.77E+6
759.06	8	21.5634	2.5401	63.2035	0.2925	18.9826	0.1136	0.0318	7.3611	0.3984	1.8757	0.2733	2.4350	0.3951	4.6375	78.5152	6.83E+6
754.06	8	20.9455	2.5399	62.8661	0.2754	19.0712	0.1160	0.0297	7.4715	0.3871	1.8578	0.2655	2.4786	0.4068	4.7743	79.1331	6.83E+6
749.06	8	19.8463	2.5412	62.2920	0.2580	19.1753	0.1215	0.0286	7.7685	0.3775	1.8690	0.2582	2.4450	0.4293	4.9771	80.2324	5.69E+6
744.06	8	17.5714	2.5474	60.9477	0.2387	19.3229	0.1364	0.0299	8.6705	0.3724	1.9601	0.2516	2.1982	0.4849	5.3866	82.5073	2.65E+6
739.06	8	15.3246	2.5571	59.0383	0.2207	19.4989	0.1545	0.0319	9.9831	0.3695	2.0716	0.2412	1.9110	0.5560	5.9234	84.7541	8.92E+5
734.06	8	12.3184	2.5822	54.7065	0.2021	19.7721	0.1841	0.0375	13.1219	0.3726	2.2687	0.2114	1.4386	0.6916	6.9928	87.7603	7.63E+4
729.06	8	7.0657	2.7076	36.0123	0.1451	19.0213	0.2203	0.0591	28.6558	0.3279	2.5709	0.0761	0.3487	1.2058	11.3564	93.0130	3.90E+1
724.06	8	6.7405	2.7150	34.6046	0.1289	18.8301	0.2218	0.0559	29.8251	0.3078	2.5684	0.0689	0.2942	1.2640	11.8302	93.3382	3.66E+1
719.06	8	6.4856	2.7203	33.5094	0.1152	18.6681	0.2232	0.0525	30.7128	0.2900	2.5664	0.0637	0.2546	1.3137	12.2305	93.5931	3.85E+1
714.06	8	6.2727	2.7244	32.5978	0.1033	18.5250	0.2247	0.0490	31.4327	0.2739	2.5653	0.0594	0.2237	1.3583	12.5870	93.8060	4.33E+1
709.06	8	6.0884	2.7277	31.8094	0.0928	18.3956	0.2263	0.0457	32.0385	0.2591	2.5651	0.0559	0.1985	1.3994	12.9138	93.9903	5.11E+1
704.06	8	5.9253	2.7305	31.1104	0.0835	18.2771	0.2279	0.0424	32.5604	0.2455	2.5658	0.0528	0.1775	1.4379	13.2188	94.1534	6.24E+1
699.06	8	5.7786	2.7329	30.4797	0.0752	18.1676	0.2296	0.0393	33.0173	0.2328	2.5674	0.0501	0.1595	1.4744	13.5070	94.3001	7.86E+1
694.06	8	5.6451	2.7349	29.9032	0.0678	18.0658	0.2314	0.0364	33.4220	0.2209	2.5699	0.0477	0.1440	1.5093	13.7816	94.4335	1.02E+2
689.06	8	5.3506	2.7380	29.3260	0.0610	17.9079	0.2616	0.0348	33.7831	0.2064	2.6339	0.0446	0.1337	1.5923	14.0147	94.7281	1.39E+2
684.06	8	5.0617	2.7412	28.7811	0.0549	17.7453	0.3009	0.0335	34.1011	0.1925	2.7092	0.0417	0.1248	1.6832	14.2319	95.0170	1.95E+2

Table D2-2 Hadamard-Rybczynski equation (H-R) settling velocity calculation for 20% tonalite/80% IAB mixture.

Solid/Liquid Proportion	Sulfide/Silicate Density Differential (kg/m^3)	Settling Velocity H-R (m/s)	Globule radius (cm)	Settling Velocity H-R (m/s)
0.00	1812.70	7.09E-3	0.01	1.11E-6
0.01	1812.50	6.69E-3	0.02	4.43E-6
0.02	1812.40	6.30E-3	0.03	9.96E-6
0.03	1812.70	5.99E-3	0.04	1.77E-5
0.04	1812.60	5.64E-3	0.05	2.77E-5
0.05	1813.10	5.33E-3	0.06	3.98E-5
0.07	1813.50	5.03E-3	0.07	5.42E-5
0.08	1814.00	4.73E-3	0.08	7.08E-5
0.09	1814.40	4.45E-3	0.09	8.96E-5
0.10	1814.80	4.17E-3	0.1	1.11E-4
0.12	1815.20	3.90E-3	0.11	1.34E-4
0.13	1815.60	3.64E-3	0.12	1.59E-4
0.14	1816.00	3.39E-3	0.13	1.87E-4
0.15	1816.30	3.15E-3	0.14	2.17E-4
0.16	1816.60	2.92E-3	0.15	2.49E-4
0.17	1816.90	2.71E-3	0.16	2.83E-4
0.18	1817.20	2.50E-3	0.17	3.20E-4
0.19	1817.50	2.31E-3	0.18	3.58E-4
0.20	1817.70	2.13E-3	0.19	3.99E-4
0.20	1818.00	1.96E-3	0.2	4.43E-4
0.21	1818.20	1.80E-3	0.21	4.88E-4
0.22	1818.40	1.65E-3	0.22	5.35E-4
0.24	1818.00	1.51E-3	0.23	5.85E-4
0.26	1817.30	1.38E-3	0.24	6.37E-4
0.27	1816.50	1.27E-3	0.25	6.91E-4
0.29	1815.60	1.17E-3	0.26	7.48E-4
0.31	1817.20	1.02E-3	0.27	8.07E-4
0.33	1819.90	8.68E-4	0.28	8.67E-4
0.35	1822.60	7.39E-4	0.29	9.30E-4
0.37	1825.20	6.30E-4	0.3	9.96E-4
0.38	1827.80	5.37E-4	0.31	1.06E-3
0.40	1830.40	4.58E-4	0.32	1.13E-3
0.41	1833.00	3.90E-4	0.33	1.20E-3
0.43	1835.50	3.32E-4	0.34	1.28E-3
0.44	1838.00	2.83E-4	0.35	1.36E-3
0.45	1840.50	2.41E-4	0.36	1.43E-3
0.46	1842.90	2.05E-4	0.37	1.51E-3
0.48	1845.40	1.74E-4	0.38	1.60E-3
0.49	1847.80	1.48E-4	0.39	1.68E-3
0.50	1850.20	1.26E-4	0.4	1.77E-3
0.51	1852.50	1.07E-4	0.41	1.86E-3
0.52	1854.90	9.02E-5	0.42	1.95E-3
0.53	1857.20	7.63E-5	0.43	2.05E-3
0.54	1859.50	6.45E-5	0.44	2.14E-3
0.54	1861.80	5.44E-5	0.45	2.24E-3
0.55	1864.10	4.59E-5	0.46	2.34E-3
0.56	1866.40	3.86E-5	0.47	2.44E-3
0.57	1868.70	3.24E-5	0.48	2.55E-3
0.57	1870.90	2.72E-5	0.49	2.66E-3
0.58	1873.20	2.28E-5	0.5	2.77E-3
0.59	1875.40	1.91E-5	0.51	2.88E-3

Table D2-2 Hadamard-Rybczynski equation (H-R) settling velocity calculation for 20% tonalite/80% IAB mixture.

Solid/Liquid Proportion	Sulfide/Silicate Density Differential (kg/m^3)	Settling Velocity H-R (m/s)	Globule radius (cm)	Settling Velocity H-R (m/s)
0.59	1877.60	1.60E-5	0.52	2.99E-3
0.60	1879.80	1.33E-5	0.53	3.11E-3
0.61	1882.10	1.11E-5	0.54	3.23E-3
0.61	1884.30	9.22E-6	0.55	3.35E-3
0.62	1886.50	7.66E-6	0.56	3.47E-3
0.62	1888.60	6.35E-6	0.57	3.59E-3
0.63	1890.80	5.26E-6	0.58	3.72E-3
0.63	1893.00	4.35E-6	0.59	3.85E-3
0.64	1895.20	3.59E-6	0.6	3.98E-3
0.64	1897.40	2.96E-6	0.61	4.12E-3
0.65	1899.50	2.44E-6	0.62	4.25E-3
0.65	1901.70	2.00E-6	0.63	4.39E-3
0.65	1903.80	1.64E-6	0.64	4.53E-3
0.66	1906.00	1.35E-6	0.65	4.67E-3
0.66	1908.10	1.10E-6	0.66	4.82E-3
0.67	1910.20	8.99E-7	0.67	4.97E-3
0.67	1912.40	7.34E-7	0.68	5.12E-3
0.67	1914.50	5.97E-7	0.69	5.27E-3
0.68	1916.60	4.86E-7	0.7	5.42E-3
0.68	1919.10	3.94E-7	0.71	5.58E-3
0.68	1921.70	3.19E-7	0.72	5.74E-3
0.69	1924.20	2.58E-7	0.73	5.90E-3
0.69	1926.70	2.09E-7	0.74	6.06E-3
0.69	1929.10	1.66E-7	0.75	6.22E-3
0.70	1931.30	1.31E-7	0.76	6.39E-3
0.70	1933.50	1.03E-7	0.77	6.56E-3
0.70	1935.60	8.15E-8	0.78	6.73E-3
0.70	1937.70	6.42E-8	0.79	6.90E-3
0.70	1939.70	5.04E-8	0.8	7.08E-3
0.71	1941.60	3.96E-8	0.81	7.26E-3
0.71	1943.50	3.01E-8	0.82	7.44E-3
0.71	1945.30	2.42E-8	0.83	7.62E-3
0.71	1947.10	1.89E-8	0.84	7.81E-3
0.71	1948.90	1.47E-8	0.85	7.99E-3
0.72	1950.50	1.15E-8	0.86	8.18E-3
0.72	1951.90	9.96E-9	0.87	8.37E-3
0.73	1953.00	9.37E-9	0.88	8.57E-3
0.74	1954.10	8.82E-9	0.89	8.76E-3
0.74	1955.10	8.32E-9	0.9	8.96E-3
0.75	1956.00	7.85E-9	0.91	9.16E-3
0.75	1956.90	7.42E-9	0.92	9.36E-3
0.76	1957.70	7.02E-9	0.93	9.57E-3
0.77	1958.40	6.70E-9	0.94	9.78E-3
0.77	1959.00	6.42E-9	0.95	9.99E-3
0.78	1959.60	5.92E-9	0.96	1.02E-2
0.78	1959.90	5.87E-9	0.97	1.04E-2
0.79	1960.10	5.86E-9	0.98	1.06E-2
0.80	1958.80	7.04E-9	0.99	1.08E-2
0.82	1952.60	1.50E-8	1	1.11E-2
0.85	1942.90	4.45E-8		
0.88	1917.80	5.14E-7		

Table D2-2 Hadamard-Rybczynski equation (H-R) settling velocity calculation for 20% tonalite/80% IAB mixture.

Solid/Liquid Proportion	Sulfide/Silicate Density Differential (kg/m^3)	Settling Velocity H-R (m/s)	Globule radius (cm)	Settling Velocity H-R (m/s)
0.93	1792.40	9.40E-4		
0.93	1785.00	9.96E-4		
0.94	1779.70	9.44E-4		
0.94	1775.60	8.38E-4		
0.94	1772.30	7.09E-4		
0.94	1769.50	5.79E-4		
0.94	1767.10	4.60E-4		
0.94	1765.10	3.55E-4		
0.95	1762.00	2.60E-4		
0.95	1758.80	1.85E-4		

Table D3-1 *30% tonalite/70% IAB mixture MELTS model output*

T (°C)	P (kb)	liquid mass (gm)	liquid ρ (gm/cc)	SiO_2 (wt. %)	TiO_2 (wt. %)	Al_2O_3 (wt. %)	Fe_2O_3 (wt. %)	FeO (wt. %)	MnO (wt. %)	MgO (wt. %)	CaO (wt. %)	Na_2O (wt. %)	K_2O (wt. %)	P_2O_5 (wt. %)	H_2O (wt. %)	solid mass (gm)	Viscosity (Pa s)
1255.86	8	99.8893	2.6631	54.4271	0.6600	17.6304	0.2096	2.8540	5.6793	6.1520	8.5314	1.7990	0.9628	0.0934	1.0011	0.0055	8.75E+0
1250.86	8	99.3628	2.6635	54.4197	0.6632	17.7090	0.2080	2.8332	5.7094	6.0121	8.5689	1.8084	0.9679	0.0939	1.0064	0.5321	9.36E+0
1245.86	8	98.8463	2.6639	54.4128	0.6663	17.7867	0.2064	2.8117	5.7392	5.8746	8.6056	1.8176	0.9729	0.0944	1.0117	1.0486	1.00E+1
1240.86	8	98.3394	2.6642	54.4064	0.6694	17.8636	0.2048	2.7894	5.7688	5.7394	8.6416	1.8268	0.9779	0.0949	1.0169	1.5555	1.07E+1
1235.86	8	97.8418	2.6646	54.4006	0.6725	17.9397	0.2033	2.7663	5.7981	5.6066	8.6767	1.8359	0.9829	0.0954	1.0221	2.0531	1.15E+1
1230.86	8	97.3531	2.6650	54.3952	0.6755	18.0149	0.2017	2.7424	5.8272	5.4761	8.7111	1.8449	0.9878	0.0958	1.0272	2.5417	1.23E+1
1225.86	8	96.8731	2.6654	54.3903	0.6786	18.0895	0.2001	2.7177	5.8561	5.3479	8.7446	1.8539	0.9927	0.0963	1.0323	3.0218	1.32E+1
1220.86	8	96.4012	2.6657	54.3859	0.6816	18.1633	0.1986	2.6922	5.8848	5.2220	8.7772	1.8627	0.9976	0.0968	1.0373	3.4936	1.42E+1
1215.86	8	95.9373	2.6661	54.3820	0.6845	18.2364	0.1970	2.6659	5.9132	5.0984	8.8090	1.8715	1.0024	0.0973	1.0423	3.9575	1.53E+1
1210.86	8	95.4810	2.6665	54.3785	0.6875	18.3089	0.1955	2.6388	5.9415	4.9769	8.8399	1.8802	1.0072	0.0977	1.0473	4.4139	1.65E+1
1205.86	8	95.0319	2.6668	54.3755	0.6904	18.3808	0.1940	2.6109	5.9696	4.8576	8.8698	1.8889	1.0120	0.0982	1.0523	4.8630	1.78E+1
1200.86	8	93.7836	2.6662	54.4115	0.6970	18.5563	0.1846	2.5848	6.0490	4.7038	8.7122	1.9095	1.0254	0.0995	1.0663	6.1113	1.93E+1
1195.86	8	92.5654	2.6655	54.4497	0.7034	18.7293	0.1755	2.5579	6.1286	4.5536	8.5521	1.9298	1.0389	0.1008	1.0803	7.3294	2.09E+1
1190.86	8	91.3944	2.6648	54.4891	0.7094	18.8973	0.1668	2.5300	6.2072	4.4080	8.3941	1.9496	1.0523	0.1021	1.0942	8.5004	2.28E+1
1185.86	8	90.2679	2.6642	54.5296	0.7152	19.0604	0.1584	2.5014	6.2846	4.2669	8.2380	1.9689	1.0654	0.1034	1.1078	9.6270	2.48E+1
1180.86	8	89.1833	2.6635	54.5713	0.7206	19.2187	0.1504	2.4720	6.3611	4.1300	8.0840	1.9877	1.0783	0.1046	1.1213	10.7116	2.71E+1
1175.86	8	88.1383	2.6629	54.6142	0.7256	19.3723	0.1428	2.4418	6.4365	3.9974	7.9320	2.0059	1.0911	0.1059	1.1346	11.7565	2.96E+1
1170.86	8	87.1309	2.6624	54.6581	0.7304	19.5212	0.1356	2.4109	6.5109	3.8688	7.7820	2.0236	1.1037	0.1071	1.1477	12.7640	3.24E+1
1165.86	8	86.1588	2.6618	54.7030	0.7348	19.6657	0.1288	2.3794	6.5844	3.7442	7.6340	2.0407	1.1162	0.1083	1.1606	13.7360	3.55E+1
1160.86	8	85.2203	2.6613	54.7489	0.7389	19.8057	0.1222	2.3472	6.6569	3.6235	7.4879	2.0574	1.1285	0.1095	1.1734	14.6745	3.91E+1
1155.86	8	84.3137	2.6608	54.7958	0.7427	19.9414	0.1161	2.3144	6.7284	3.5065	7.3438	2.0735	1.1406	0.1107	1.1860	15.5812	4.30E+1
1150.86	8	83.4371	2.6603	54.8437	0.7462	20.0728	0.1102	2.2810	6.7991	3.3932	7.2017	2.0891	1.1526	0.1118	1.1985	16.4577	4.74E+1
1145.86	8	82.5892	2.6598	54.8925	0.7493	20.2000	0.1047	2.2471	6.8689	3.2834	7.0616	2.1041	1.1644	0.1130	1.2108	17.3057	5.24E+1
1140.86	8	81.7685	2.6593	54.9422	0.7521	20.3232	0.0995	2.2127	6.9379	3.1772	6.9234	2.1186	1.1761	0.1141	1.2230	18.1264	5.80E+1
1135.86	8	80.9735	2.6589	54.9927	0.7546	20.4424	0.0945	2.1779	7.0060	3.0742	6.7872	2.1326	1.1877	0.1152	1.2350	18.9213	6.42E+1
1130.86	8	80.2031	2.6585	55.0441	0.7568	20.5576	0.0899	2.1426	7.0733	2.9745	6.6529	2.1460	1.1991	0.1163	1.2468	19.6917	7.13E+1
1125.86	8	78.6647	2.6584	55.1029	0.7678	20.5474	0.0878	2.1183	7.2116	2.8844	6.5348	2.1350	1.2201	0.1186	1.2712	21.2302	7.94E+1
1120.86	8	76.7700	2.6586	55.1619	0.7836	20.4713	0.0871	2.0990	7.3896	2.8009	6.4273	2.1088	1.2463	0.1215	1.3026	23.1248	8.83E+1

Table D3-1 30% tonalite/70% IAB mixture MELTS model output

T (°C)	P (kb)	liquid mass (gm)	liquid ρ (gm/cc)	SiO_2 (wt. %)	TiO_2 (wt. %)	Al_2O_3 (wt. %)	Fe_2O_3 (wt. %)	FeO (wt. %)	MnO (wt. %)	MgO (wt. %)	CaO (wt. %)	Na_2O (wt. %)	K_2O (wt. %)	P_2O_5 (wt. %)	H_2O (wt. %)	solid mass (gm)	Viscosity (Pa s)
1115.86	8	74.9607	2.6588	55.2169	0.7994	20.3972	0.0865	2.0782	7.5680	2.7203	6.3225	2.0803	1.2722	0.1245	1.3340	24.9342	9.80E+1
1110.86	8	73.2317	2.6591	55.2680	0.8150	20.3252	0.0858	2.0561	7.7467	2.6426	6.2204	2.0495	1.2979	0.1274	1.3655	26.6632	1.09E+2
1105.86	8	71.5785	2.6595	55.3156	0.8304	20.2551	0.0852	2.0326	7.9256	2.5674	6.1207	2.0167	1.3233	0.1303	1.3971	28.3163	1.20E+2
1100.86	8	69.9972	2.6599	55.3597	0.8457	20.1870	0.0845	2.0079	8.1046	2.4949	6.0234	1.9821	1.3484	0.1333	1.4286	29.8977	1.33E+2
1095.86	8	68.4839	2.6603	55.4007	0.8608	20.1208	0.0839	1.9819	8.2837	2.4247	5.9282	1.9457	1.3731	0.1362	1.4602	31.4110	1.46E+2
1090.86	8	66.9090	2.6595	55.5093	0.8773	20.0574	0.0839	1.9400	8.4022	2.3532	5.8366	1.9062	1.3999	0.1394	1.4946	32.9859	1.66E+2
1085.86	8	65.2028	2.6565	55.7361	0.8961	19.9982	0.0848	1.8729	8.4144	2.2783	5.7487	1.8634	1.4304	0.1431	1.5337	34.6920	1.98E+2
1080.86	8	63.5881	2.6536	55.9593	0.9144	19.9417	0.0856	1.8065	8.4237	2.2064	5.6619	1.8207	1.4606	0.1467	1.5726	36.3067	2.37E+2
1075.86	8	62.0586	2.6507	56.1793	0.9321	19.8877	0.0864	1.7409	8.4301	2.1373	5.5760	1.7780	1.4904	0.1503	1.6114	37.8363	2.83E+2
1070.86	8	60.6085	2.6479	56.3963	0.9493	19.8359	0.0870	1.6765	8.4338	2.0708	5.4911	1.7355	1.5198	0.1539	1.6499	39.2864	3.38E+2
1065.86	8	59.2324	2.6451	56.6105	0.9660	19.7862	0.0876	1.6132	8.4347	2.0069	5.4069	1.6934	1.5489	0.1575	1.6883	40.6624	4.04E+2
1060.86	8	57.9255	2.6423	56.8221	0.9820	19.7383	0.0881	1.5512	8.4329	1.9452	5.3236	1.6515	1.5776	0.1611	1.7264	41.9694	4.83E+2
1055.86	8	56.6830	2.6396	57.0313	0.9973	19.6922	0.0885	1.4907	8.4284	1.8858	5.2409	1.6101	1.6060	0.1646	1.7642	43.2119	5.77E+2
1050.86	8	55.5008	2.6370	57.2383	1.0120	19.6476	0.0889	1.4315	8.4211	1.8285	5.1590	1.5691	1.6340	0.1681	1.8018	44.3941	6.89E+2
1045.86	8	54.3750	2.6343	57.4433	1.0261	19.6045	0.0892	1.3739	8.4112	1.7732	5.0777	1.5286	1.6616	0.1716	1.8391	45.5199	8.25E+2
1040.86	8	53.3019	2.6317	57.6464	1.0394	19.5626	0.0895	1.3179	8.3986	1.7198	4.9971	1.4886	1.6889	0.1750	1.8761	46.5930	9.87E+2
1035.86	8	52.2781	2.6292	57.8478	1.0520	19.5220	0.0897	1.2634	8.3834	1.6682	4.9171	1.4492	1.7158	0.1785	1.9128	47.6167	1.18E+3
1030.86	8	51.3007	2.6267	58.0476	1.0638	19.4824	0.0899	1.2105	8.3656	1.6182	4.8378	1.4104	1.7424	0.1819	1.9493	48.5942	1.42E+3
1025.86	8	50.3666	2.6242	58.2460	1.0749	19.4439	0.0900	1.1593	8.3453	1.5699	4.7590	1.3723	1.7687	0.1852	1.9854	49.5282	1.70E+3
1020.86	8	49.4733	2.6218	58.4431	1.0852	19.4063	0.0901	1.1097	8.3223	1.5232	4.6809	1.3347	1.7945	0.1886	2.0213	50.4215	2.04E+3
1015.86	8	48.6167	2.6193	58.6389	1.0947	19.3693	0.0902	1.0618	8.2971	1.4779	4.6035	1.2976	1.8201	0.1919	2.0569	51.2782	2.45E+3
1010.86	8	47.7972	2.6170	58.8336	1.1034	19.3333	0.0902	1.0154	8.2692	1.4341	4.5267	1.2613	1.8454	0.1952	2.0922	52.0977	2.95E+3
1005.86	8	47.0116	2.6146	59.0273	1.1112	19.2980	0.0902	0.9707	8.2389	1.3916	4.4504	1.2257	1.8703	0.1985	2.1271	52.8832	3.54E+3
1000.86	8	46.2579	2.6123	59.2202	1.1181	19.2634	0.0902	0.9275	8.2062	1.3504	4.3748	1.1908	1.8949	0.2017	2.1618	53.6369	4.27E+3
995.86	8	45.5344	2.6100	59.4123	1.1241	19.2294	0.0902	0.8859	8.1711	1.3105	4.2998	1.1565	1.9192	0.2049	2.1961	54.3605	5.15E+3
990.86	8	44.8392	2.6077	59.6037	1.1293	19.1960	0.0901	0.8458	8.1336	1.2717	4.2255	1.1229	1.9431	0.2081	2.2302	55.0557	6.22E+3
985.86	8	44.1709	2.6055	59.7944	1.1335	19.1631	0.0901	0.8072	8.0938	1.2342	4.1518	1.0900	1.9668	0.2112	2.2639	55.7240	7.51E+3
980.86	8	43.5279	2.6033	59.9846	1.1367	19.1307	0.0900	0.7701	8.0517	1.1977	4.0787	1.0578	1.9902	0.2143	2.2974	56.3669	9.09E+3

Table D3-1 *30% tonalite/70% IAB mixture MELTS model output*

T (°C)	P (kb)	liquid mass (gm)	liquid ρ (gm/cc)	SiO_2 (wt. %)	TiO_2 (wt. %)	Al_2O_3 (wt. %)	Fe_2O_3 (wt. %)	FeO (wt. %)	MnO (wt. %)	MgO (wt. %)	CaO (wt. %)	Na_2O (wt. %)	K_2O (wt. %)	P_2O_5 (wt. %)	H_2O (wt. %)	solid mass (gm)	Viscosity (Pa s)
975.86	8	42.9090	2.6011	60.1743	1.1389	19.0988	0.0899	0.7345	8.0075	1.1623	4.0063	1.0263	2.0132	0.2174	2.3305	56.9859	1.10E+4
970.86	8	42.3128	2.5989	60.3636	1.1402	19.0673	0.0897	0.7002	7.9610	1.1280	3.9346	0.9955	2.0360	0.2205	2.3634	57.5821	1.33E+4
965.86	8	41.7381	2.5968	60.5526	1.1404	19.0362	0.0896	0.6673	7.9124	1.0946	3.8636	0.9653	2.0585	0.2235	2.3959	58.1568	1.62E+4
960.86	8	41.1839	2.5947	60.7413	1.1397	19.0054	0.0894	0.6357	7.8618	1.0622	3.7933	0.9359	2.0807	0.2265	2.4281	58.7110	1.97E+4
955.86	8	40.6491	2.5926	60.9297	1.1378	18.9750	0.0893	0.6054	7.8090	1.0308	3.7237	0.9071	2.1027	0.2295	2.4601	59.2458	2.40E+4
950.86	8	40.1327	2.5905	61.1179	1.1349	18.9449	0.0891	0.5763	7.7544	1.0002	3.6548	0.8789	2.1244	0.2325	2.4917	59.7622	2.92E+4
945.86	8	39.6338	2.5884	61.3059	1.1310	18.9151	0.0889	0.5485	7.6977	0.9705	3.5866	0.8514	2.1458	0.2354	2.5231	60.2610	3.56E+4
940.86	8	39.1516	2.5863	61.4938	1.1260	18.8855	0.0888	0.5218	7.6392	0.9417	3.5193	0.8246	2.1669	0.2383	2.5542	60.7432	4.35E+4
935.86	8	38.6853	2.5843	61.6815	1.1199	18.8561	0.0886	0.4963	7.5789	0.9137	3.4527	0.7984	2.1878	0.2412	2.5850	61.2095	5.31E+4
930.86	8	38.2342	2.5823	61.8692	1.1127	18.8270	0.0884	0.4718	7.5168	0.8865	3.3868	0.7729	2.2084	0.2440	2.6155	61.6607	6.50E+4
925.86	8	37.7975	2.5803	62.0567	1.1044	18.7980	0.0882	0.4484	7.4531	0.8600	3.3218	0.7479	2.2288	0.2468	2.6457	62.0974	7.97E+4
920.86	8	37.3745	2.5783	62.2441	1.0951	18.7692	0.0880	0.4261	7.3877	0.8343	3.2576	0.7236	2.2489	0.2496	2.6756	62.5204	9.78E+4
915.86	8	36.9647	2.5763	62.4314	1.0847	18.7405	0.0878	0.4047	7.3207	0.8094	3.1943	0.6999	2.2688	0.2524	2.7053	62.9301	1.20E+5
910.86	8	36.5675	2.5743	62.6186	1.0733	18.7120	0.0876	0.3843	7.2523	0.7851	3.1317	0.6768	2.2884	0.2551	2.7347	63.3273	1.48E+5
905.86	8	36.1824	2.5724	62.8056	1.0608	18.6835	0.0875	0.3648	7.1824	0.7616	3.0701	0.6543	2.3078	0.2579	2.7638	63.7125	1.82E+5
900.86	8	35.8087	2.5705	62.9924	1.0474	18.6552	0.0873	0.3462	7.1112	0.7387	3.0093	0.6323	2.3269	0.2606	2.7926	64.0861	2.24E+5
895.86	8	35.4445	2.5685	63.1867	1.0292	18.6241	0.0872	0.3281	7.0373	0.7164	2.9493	0.6111	2.3459	0.2632	2.8213	64.4503	2.77E+5
890.86	8	35.1482	2.5660	63.4523	0.9935	18.5495	0.0880	0.3038	6.9624	0.6967	2.8866	0.5952	2.3615	0.2654	2.8451	64.7467	3.48E+5
885.86	8	34.8618	2.5637	63.7137	0.9587	18.4758	0.0889	0.2812	6.8868	0.6776	2.8251	0.5795	2.3767	0.2676	2.8685	65.0330	4.38E+5
880.86	8	34.5851	2.5614	63.9710	0.9250	18.4028	0.0898	0.2601	6.8108	0.6590	2.7649	0.5640	2.3916	0.2698	2.8914	65.3098	5.51E+5
875.86	8	34.3175	2.5592	64.2244	0.8922	18.3306	0.0907	0.2404	6.7342	0.6410	2.7059	0.5486	2.4061	0.2719	2.9140	65.5774	6.94E+5
870.86	8	34.0587	2.5570	64.4739	0.8604	18.2592	0.0917	0.2222	6.6573	0.6235	2.6481	0.5335	2.4203	0.2739	2.9361	65.8362	8.75E+5
865.86	8	33.8082	2.5549	64.7195	0.8295	18.1887	0.0927	0.2052	6.5800	0.6065	2.5915	0.5185	2.4341	0.2760	2.9579	66.0866	1.10E+6
860.86	8	33.5658	2.5529	64.9613	0.7995	18.1190	0.0937	0.1894	6.5023	0.5899	2.5360	0.5038	2.4477	0.2780	2.9792	66.3291	1.39E+6
855.86	8	33.3311	2.5510	65.1994	0.7705	18.0502	0.0949	0.1747	6.4244	0.5739	2.4817	0.4893	2.4609	0.2799	3.0002	66.5638	1.76E+6
850.86	8	33.1038	2.5491	65.4339	0.7422	17.9823	0.0960	0.1611	6.3462	0.5583	2.4285	0.4750	2.4738	0.2818	3.0208	66.7911	2.23E+6
845.86	8	32.8835	2.5472	65.6648	0.7149	17.9153	0.0972	0.1485	6.2678	0.5431	2.3764	0.4609	2.4864	0.2837	3.0410	67.0113	2.83E+6
840.86	8	32.6701	2.5455	65.8921	0.6883	17.8491	0.0985	0.1368	6.1892	0.5284	2.3254	0.4471	2.4986	0.2856	3.0609	67.2247	3.60E+6

Table D3-1 30% tonalite/70% IAB mixture MELTS model output

T (°C)	P (kb)	liquid mass (gm)	liquid ρ (gm/cc)	SiO_2 (wt. %)	TiO_2 (wt. %)	Al_2O_3 (wt. %)	Fe_2O_3 (wt. %)	FeO (wt. %)	MnO (wt. %)	MgO (wt. %)	CaO (wt. %)	Na_2O (wt. %)	K_2O (wt. %)	P_2O_5 (wt. %)	H_2O (wt. %)	solid mass (gm)	Viscosity (Pa s)
835.86	8	32.4633	2.5437	66.1160	0.6626	17.7839	0.0998	0.1260	6.1104	0.5140	2.2755	0.4334	2.5106	0.2874	3.0804	67.4315	4.57E+6
830.86	8	32.2629	2.5421	66.3364	0.6377	17.7196	0.1011	0.1159	6.0315	0.5001	2.2266	0.4200	2.5223	0.2892	3.0995	67.6320	5.82E+6
825.86	8	32.0686	2.5404	66.5535	0.6135	17.6561	0.1025	0.1066	5.9526	0.4865	2.1788	0.4069	2.5337	0.2909	3.1183	67.8263	7.42E+6
820.86	8	31.4814	2.5389	66.5639	0.5863	17.6710	0.1045	0.0977	5.9245	0.4758	2.1356	0.3977	2.5703	0.2964	3.1765	68.4134	8.56E+6
815.86	8	30.6892	2.5376	66.4509	0.5579	17.7312	0.1069	0.0893	5.9268	0.4666	2.0958	0.3908	2.6213	0.3040	3.2585	69.2056	9.32E+6
810.86	8	29.9256	2.5362	66.3317	0.5307	17.7919	0.1094	0.0816	5.9305	0.4576	2.0574	0.3838	2.6720	0.3118	3.3416	69.9693	1.01E+7
805.86	8	29.1886	2.5350	66.2060	0.5047	17.8533	0.1120	0.0746	5.9357	0.4486	2.0203	0.3767	2.7224	0.3196	3.4260	70.7063	1.10E+7
800.86	8	28.4763	2.5338	66.0737	0.4798	17.9153	0.1147	0.0681	5.9425	0.4398	1.9846	0.3697	2.7725	0.3276	3.5117	71.4186	1.20E+7
795.86	8	27.7869	2.5326	65.9347	0.4559	17.9779	0.1175	0.0622	5.9511	0.4311	1.9503	0.3626	2.8222	0.3358	3.5988	72.1079	1.31E+7
790.86	8	27.1189	2.5315	65.7885	0.4331	18.0413	0.1204	0.0568	5.9617	0.4225	1.9172	0.3555	2.8714	0.3440	3.6875	72.7760	1.42E+7
785.86	8	26.4706	2.5305	65.6351	0.4113	18.1056	0.1234	0.0518	5.9745	0.4140	1.8855	0.3484	2.9203	0.3525	3.7778	73.4243	1.54E+7
780.86	8	25.8344	2.5296	65.4684	0.3894	18.1660	0.1258	0.0480	5.9995	0.4026	1.8602	0.3392	2.9688	0.3611	3.8708	74.0604	1.67E+7
775.86	8	25.2142	2.5288	65.2918	0.3684	18.2264	0.1280	0.0447	6.0301	0.3908	1.8374	0.3296	3.0168	0.3700	3.9660	74.6807	1.80E+7
770.86	8	24.6103	2.5281	65.1064	0.3483	18.2881	0.1304	0.0415	6.0638	0.3793	1.8155	0.3200	3.0642	0.3791	4.0633	75.2846	1.94E+7
765.86	8	24.0214	2.5274	64.9115	0.3291	18.3513	0.1328	0.0386	6.1010	0.3681	1.7946	0.3106	3.1110	0.3884	4.1630	75.8735	2.09E+7
760.86	8	23.1997	2.5276	64.6037	0.3102	18.4165	0.1374	0.0364	6.2597	0.3611	1.7927	0.3054	3.0643	0.4022	4.3104	76.6952	1.98E+7
755.86	8	22.1092	2.5287	64.0674	0.2906	18.5248	0.1439	0.0347	6.5557	0.3570	1.8076	0.3037	2.9695	0.4220	4.5230	77.7856	1.61E+7
750.86	8	19.7063	2.5314	63.3409	0.2686	18.6080	0.1612	0.0360	6.9774	0.3404	1.8845	0.2908	2.8585	0.4735	4.7604	80.1886	1.18E+7
745.86	8	17.4678	2.5354	62.3539	0.2480	18.7026	0.1817	0.0375	7.5947	0.3290	1.9790	0.2825	2.6790	0.5341	5.0779	82.4271	7.20E+6
740.86	8	15.3965	2.5416	60.9615	0.2289	18.8247	0.2058	0.0394	8.5095	0.3229	2.0924	0.2763	2.4291	0.6060	5.5035	84.4984	3.37E+6
735.86	8	13.2755	2.5520	58.8609	0.2108	18.9765	0.2368	0.0427	9.9355	0.3193	2.2406	0.2651	2.1175	0.7028	6.0915	86.6194	1.06E+6
730.86	8	6.2448	2.7037	35.8538	0.1463	18.2381	0.3459	0.0863	28.6495	0.2913	2.9427	0.0865	0.4222	1.4941	11.4432	93.6501	6.04E+1
725.86	8	5.9400	2.7115	34.4027	0.1297	18.0194	0.3507	0.0819	29.8548	0.2727	2.9598	0.0783	0.3564	1.5707	11.9229	93.9549	5.79E+1
720.86	8	5.7033	2.7171	33.2909	0.1158	17.8364	0.3553	0.0771	30.7539	0.2564	2.9747	0.0723	0.3092	1.6359	12.3220	94.1916	6.20E+1
715.86	8	5.5064	2.7214	32.3719	0.1038	17.6757	0.3598	0.0722	31.4766	0.2418	2.9889	0.0676	0.2725	1.6944	12.6748	94.3885	7.01E+1
710.86	8	5.3364	2.7248	31.5801	0.0933	17.5309	0.3645	0.0674	32.0813	0.2284	3.0030	0.0636	0.2425	1.7484	12.9967	94.5584	8.49E+1
705.86	8	5.1863	2.7277	30.8798	0.0840	17.3985	0.3693	0.0627	32.5999	0.2161	3.0171	0.0602	0.2174	1.7990	13.2959	94.7086	1.05E+2
700.86	8	5.0515	2.7302	30.2490	0.0757	17.2764	0.3743	0.0582	33.0523	0.2047	3.0315	0.0572	0.1960	1.8470	13.5779	94.8434	1.34E+2

Table D3-1 30% tonalite/70% IAB mixture MELTS model output

T (°C)	P (kb)	liquid mass (gm)	liquid ρ (gm/cc)	SiO_2 (wt. %)	TiO_2 (wt. %)	Al_2O_3 (wt. %)	Fe_2O_3 (wt. %)	FeO (wt. %)	MnO (wt. %)	MgO (wt. %)	CaO (wt. %)	Na_2O (wt. %)	K_2O (wt. %)	P_2O_5 (wt. %)	H_2O (wt. %)	solid mass (gm)	Viscosity (Pa s)
695.86	8	4.9291	2.7324	29.6730	0.0683	17.1629	0.3795	0.0539	33.4517	0.1941	3.0462	0.0544	0.1774	1.8928	13.8459	94.9657	1.75E+2
690.86	8	4.8170	2.7344	29.1417	0.0616	17.0570	0.3849	0.0498	33.8074	0.1842	3.0612	0.0520	0.1611	1.9369	14.1025	95.0778	2.32E+2
685.86	8	4.7136	2.7362	28.6474	0.0557	16.9579	0.3905	0.0460	34.1261	0.1749	3.0765	0.0497	0.1466	1.9794	14.3494	95.1813	3.16E+2
680.86	8	4.6176	2.7378	28.1847	0.0503	16.8650	0.3965	0.0424	34.4131	0.1663	3.0921	0.0475	0.1338	2.0205	14.5880	95.2773	4.37E+2
675.86	8	4.5281	2.7393	27.7489	0.0454	16.7779	0.4027	0.0390	34.6725	0.1581	3.1080	0.0455	0.1222	2.0605	14.8193	95.3668	6.14E+2
670.86	8	4.4443	2.7407	27.3367	0.0410	16.6961	0.4092	0.0358	34.9074	0.1504	3.1242	0.0437	0.1119	2.0993	15.0442	95.4505	8.80E+2
665.86	8	4.3657	2.7420	26.9452	0.0371	16.6195	0.4161	0.0328	35.1205	0.1432	3.1406	0.0419	0.1025	2.1371	15.2634	95.5292	1.28E+3

Table D3-2 Hadamard-Rybczynski equation (H-R) settling velocity calculation for 30% tonalite/70% IAB mixture.

Solid/Liquid Proportion	Sulfide/Silicate Density Differential (kg/m^3)	Settling Velocity H-R (m/s)	Globule radius (cm)	Settling Velocity H-R (m/s)
0.00	1793.50	1.62E-2	0.01	5.21E-6
0.01	1792.90	1.54E-2	0.02	2.09E-5
0.01	1792.20	1.47E-2	0.03	4.69E-5
0.02	1792.10	1.42E-2	0.04	8.34E-5
0.04	1792.30	1.38E-2	0.05	1.30E-4
0.06	1792.50	1.34E-2	0.06	1.88E-4
0.07	1792.70	1.29E-2	0.07	2.55E-4
0.09	1792.80	1.25E-2	0.08	3.34E-4
0.10	1792.90	1.20E-2	0.09	4.22E-4
0.11	1793.10	1.15E-2	0.10	5.21E-4
0.13	1793.20	1.10E-2	0.11	6.31E-4
0.14	1793.30	1.05E-2	0.12	7.51E-4
0.15	1793.30	1.01E-2	0.13	8.81E-4
0.16	1793.40	9.56E-3	0.14	1.02E-3
0.17	1793.40	9.08E-3	0.15	1.17E-3
0.18	1793.40	8.61E-3	0.16	1.33E-3
0.19	1793.50	8.14E-3	0.17	1.51E-3
0.20	1793.40	7.69E-3	0.18	1.69E-3
0.21	1793.40	7.25E-3	0.19	1.88E-3
0.22	1793.40	6.82E-3	0.20	2.09E-3
0.23	1793.30	6.40E-3	0.21	2.30E-3
0.24	1793.30	5.99E-3	0.22	2.52E-3
0.25	1793.10	5.61E-3	0.23	2.76E-3
0.27	1792.70	5.14E-3	0.24	3.00E-3
0.29	1795.00	4.45E-3	0.25	3.26E-3
0.31	1797.20	3.86E-3	0.26	3.52E-3
0.34	1799.40	3.36E-3	0.27	3.80E-3
0.35	1801.60	2.92E-3	0.28	4.09E-3
0.37	1803.80	2.55E-3	0.29	4.38E-3
0.39	1806.00	2.22E-3	0.30	4.69E-3
0.41	1808.10	1.93E-3	0.31	5.01E-3
0.42	1810.30	1.69E-3	0.32	5.34E-3
0.44	1812.40	1.47E-3	0.33	5.68E-3
0.45	1814.50	1.28E-3	0.34	6.03E-3
0.47	1816.60	1.12E-3	0.35	6.39E-3
0.48	1818.70	9.71E-4	0.36	6.76E-3
0.49	1820.70	8.45E-4	0.37	7.14E-3
0.50	1822.80	7.34E-4	0.38	7.53E-3
0.51	1824.90	6.37E-4	0.39	7.93E-3
0.52	1827.00	5.52E-4	0.40	8.34E-3
0.53	1829.00	4.78E-4	0.41	8.76E-3
0.54	1831.10	4.13E-4	0.42	9.20E-3
0.55	1833.20	3.57E-4	0.43	9.64E-3
0.56	1835.30	3.08E-4	0.44	1.01E-2
0.57	1837.30	2.65E-4	0.45	1.06E-2
0.58	1839.40	2.27E-4	0.46	1.10E-2
0.58	1841.50	1.95E-4	0.47	1.15E-2
0.59	1843.60	1.67E-4	0.48	1.20E-2
0.60	1845.70	1.43E-4	0.49	1.25E-2
0.61	1847.80	1.22E-4	0.50	1.30E-2
0.61	1850.00	1.04E-4	0.51	1.36E-2

Table D3-2 Hadamard-Rybczynski equation (H-R) settling velocity calculation for 30% tonalite/70% IAB mixture.

Solid/Liquid Proportion	Sulfide/Silicate Density Differential (kg/m^3)	Settling Velocity H-R (m/s)	Globule radius (cm)	Settling Velocity H-R (m/s)
0.62	1852.10	8.82E-5	0.52	1.41E-2
0.63	1854.30	7.49E-5	0.53	1.46E-2
0.63	1856.40	6.34E-5	0.54	1.52E-2
0.64	1858.60	5.36E-5	0.55	1.58E-2
0.64	1860.80	4.53E-5	0.56	1.63E-2
0.65	1862.90	3.81E-5	0.57	1.69E-2
0.65	1865.10	3.20E-5	0.58	1.75E-2
0.66	1867.40	2.69E-5	0.59	1.81E-2
0.66	1869.60	2.25E-5	0.60	1.88E-2
0.67	1871.80	1.88E-5	0.61	1.94E-2
0.67	1874.00	1.57E-5	0.62	2.00E-2
0.68	1876.30	1.31E-5	0.63	2.07E-2
0.68	1878.50	1.09E-5	0.64	2.14E-2
0.69	1880.80	9.01E-6	0.65	2.20E-2
0.69	1883.10	7.46E-6	0.66	2.27E-2
0.69	1885.30	6.16E-6	0.67	2.34E-2
0.70	1887.60	5.08E-6	0.68	2.41E-2
0.70	1889.90	4.18E-6	0.69	2.48E-2
0.70	1892.10	3.44E-6	0.70	2.55E-2
0.71	1894.40	2.82E-6	0.71	2.63E-2
0.71	1896.70	2.31E-6	0.72	2.70E-2
0.71	1899.30	1.88E-6	0.73	2.78E-2
0.72	1902.10	1.53E-6	0.74	2.85E-2
0.72	1904.80	1.24E-6	0.75	2.93E-2
0.72	1907.50	1.01E-6	0.76	3.01E-2
0.73	1910.10	8.17E-7	0.77	3.09E-2
0.73	1912.70	6.61E-7	0.78	3.17E-2
0.73	1915.20	5.33E-7	0.79	3.25E-2
0.74	1917.60	4.30E-7	0.80	3.34E-2
0.74	1919.90	3.45E-7	0.81	3.42E-2
0.74	1922.10	2.70E-7	0.82	3.51E-2
0.74	1924.20	2.11E-7	0.83	3.59E-2
0.74	1926.30	1.65E-7	0.84	3.68E-2
0.75	1928.30	1.29E-7	0.85	3.77E-2
0.75	1930.30	1.00E-7	0.86	3.86E-2
0.75	1932.30	7.76E-8	0.87	3.95E-2
0.75	1934.10	6.01E-8	0.88	4.04E-2
0.75	1936.00	4.65E-8	0.89	4.13E-2
			0.90	4.22E-2
			0.91	4.32E-2
			0.92	4.41E-2
			0.93	4.51E-2
			0.94	4.61E-2
			0.95	4.70E-2
			0.96	4.80E-2
			0.97	4.90E-2
			0.98	5.01E-2
			0.99	5.11E-2
			1.00	5.21E-2

Table D4-1 40% tonalite/60% IAB mixture MELTS model output

T (°C)	P (kb)	liquid mass (gm)	liquid ρ (gm/cc)	SiO_2 (wt. %)	TiO_2 (wt. %)	Al_2O_3 (wt. %)	Fe_2O3 (wt. %)	FeO (wt. %)	MnO (wt. %)	MgO (wt. %)	CaO (wt. %)	Na_2O (wt. %)	K_2O (wt. %)	P_2O_5 (wt. %)	H_2O (wt. %)	solid mass (gm)	Viscosity (Pa s)
1259.18	8	99.6962	2.6422	55.9516	0.6714	17.5308	0.2288	3.1722	4.8888	5.6183	7.6490	1.9319	1.2524	0.1017	1.0030	0.0149	1.71E+1
1254.18	8	99.1942	2.6425	55.9532	0.6745	17.6056	0.2272	3.1500	4.9136	5.4842	7.6811	1.9415	1.2587	0.1022	1.0081	0.5169	1.84E+1
1249.18	8	98.7020	2.6427	55.9551	0.6775	17.6794	0.2256	3.1271	4.9381	5.3526	7.7125	1.9510	1.2650	0.1027	1.0132	1.0092	1.98E+1
1244.18	8	98.2192	2.6430	55.9576	0.6806	17.7524	0.2241	3.1033	4.9624	5.2234	7.7433	1.9604	1.2712	0.1032	1.0181	1.4920	2.14E+1
1239.18	8	97.7455	2.6433	55.9604	0.6835	17.8244	0.2225	3.0787	4.9864	5.0967	7.7733	1.9697	1.2774	0.1037	1.0231	1.9657	2.31E+1
1234.18	8	97.2806	2.6435	55.9638	0.6865	17.8957	0.2209	3.0532	5.0102	4.9724	7.8026	1.9790	1.2835	0.1042	1.0280	2.4306	2.50E+1
1229.18	8	96.8241	2.6438	55.9675	0.6894	17.9661	0.2194	3.0269	5.0339	4.8504	7.8313	1.9881	1.2896	0.1047	1.0328	2.8870	2.71E+1
1224.18	8	96.3758	2.6441	55.9717	0.6923	18.0357	0.2178	2.9998	5.0573	4.7307	7.8592	1.9972	1.2956	0.1052	1.0376	3.3354	2.93E+1
1219.18	8	95.9353	2.6443	55.9764	0.6951	18.1045	0.2163	2.9718	5.0805	4.6134	7.8863	2.0061	1.3015	0.1057	1.0424	3.7759	3.18E+1
1214.18	8	95.5024	2.6446	55.9814	0.6980	18.1727	0.2147	2.9429	5.1035	4.4983	7.9127	2.0150	1.3074	0.1062	1.0471	4.2088	3.46E+1
1209.18	8	95.0766	2.6448	55.9869	0.7008	18.2402	0.2132	2.9132	5.1264	4.3855	7.9384	2.0238	1.3133	0.1067	1.0518	4.6345	3.76E+1
1204.18	8	94.6578	2.6451	55.9928	0.7036	18.3070	0.2117	2.8826	5.1491	4.2749	7.9632	2.0325	1.3191	0.1071	1.0564	5.0533	4.09E+1
1199.18	8	94.2455	2.6453	55.9991	0.7064	18.3732	0.2102	2.8511	5.1716	4.1665	7.9873	2.0412	1.3248	0.1076	1.0611	5.4656	4.46E+1
1194.18	8	93.8394	2.6456	56.0058	0.7091	18.4389	0.2087	2.8188	5.1940	4.0602	8.0105	2.0498	1.3306	0.1081	1.0657	5.8718	4.86E+1
1189.18	8	93.4392	2.6458	56.0130	0.7119	18.5040	0.2072	2.7856	5.2162	3.9560	8.0328	2.0583	1.3363	0.1085	1.0702	6.2720	5.31E+1
1184.18	8	92.5018	2.6452	56.0597	0.7169	18.6374	0.1995	2.7537	5.2691	3.8303	7.9174	2.0755	1.3498	0.1096	1.0811	7.2094	5.86E+1
1179.18	8	91.4522	2.6444	56.1180	0.7223	18.7854	0.1904	2.7215	5.3296	3.7023	7.7664	2.0946	1.3653	0.1109	1.0935	8.2589	6.49E+1
1174.18	8	90.4406	2.6436	56.1769	0.7274	18.9291	0.1817	2.6885	5.3892	3.5784	7.6174	2.1131	1.3806	0.1121	1.1057	9.2705	7.19E+1
1169.18	8	89.4650	2.6428	56.2366	0.7322	19.0684	0.1733	2.6547	5.4479	3.4585	7.4706	2.1312	1.3956	0.1133	1.1178	10.2462	7.99E+1
1164.18	8	88.5233	2.6420	56.2969	0.7366	19.2034	0.1652	2.6201	5.5059	3.3425	7.3259	2.1487	1.4105	0.1145	1.1296	11.1878	8.89E+1
1159.18	8	87.6139	2.6413	56.3578	0.7408	19.3343	0.1575	2.5849	5.5630	3.2304	7.1832	2.1657	1.4251	0.1157	1.1414	12.0973	9.91E+1
1154.18	8	86.7349	2.6406	56.4194	0.7447	19.4612	0.1501	2.5490	5.6194	3.1218	7.0426	2.1822	1.4396	0.1169	1.1529	12.9763	1.11E+2
1149.18	8	85.8848	2.6399	56.4816	0.7483	19.5841	0.1431	2.5124	5.6750	3.0169	6.9041	2.1982	1.4538	0.1181	1.1643	13.8263	1.24E+2
1144.18	8	85.0622	2.6392	56.5444	0.7516	19.7031	0.1364	2.4753	5.7299	2.9154	6.7675	2.2137	1.4679	0.1192	1.1756	14.6489	1.38E+2
1139.18	8	84.2657	2.6386	56.6077	0.7546	19.8184	0.1300	2.4375	5.7841	2.8173	6.6330	2.2286	1.4817	0.1203	1.1867	15.4455	1.55E+2
1134.18	8	83.4939	2.6379	56.6716	0.7572	19.9299	0.1239	2.3993	5.8376	2.7224	6.5005	2.2431	1.4954	0.1214	1.1977	16.2173	1.74E+2
1129.18	8	82.7457	2.6373	56.7360	0.7596	20.0378	0.1181	2.3605	5.8903	2.6307	6.3699	2.2570	1.5090	0.1225	1.2085	16.9655	1.96E+2
1124.18	8	81.4261	2.6369	56.8150	0.7683	20.0534	0.1148	2.3297	5.9858	2.5452	6.2515	2.2524	1.5312	0.1245	1.2281	18.2851	2.21E+2

Table D4-1 40% tonalite/60% IAB mixture MELTS model output

T (°C)	P (kb)	liquid mass (gm)	liquid ρ (gm/cc)	SiO_2 (wt. %)	TiO_2 (wt. %)	Al_2O_3 (wt. %)	Fe_2O3 (wt. %)	FeO (wt. %)	MnO (wt. %)	MgO (wt. %)	CaO (wt. %)	Na_2O (wt. %)	K_2O (wt. %)	P_2O_5 (wt. %)	H_2O (wt. %)	solid mass (gm)	Viscosity (Pa s)
1119.18	8	79.5207	2.6365	56.9070	0.7843	19.9716	0.1142	2.3067	6.1292	2.4664	6.1468	2.2257	1.5631	0.1275	1.2575	20.1904	2.50E+2
1114.18	8	77.6998	2.6363	56.9949	0.8001	19.8922	0.1135	2.2821	6.2729	2.3905	6.0449	2.1969	1.5946	0.1305	1.2870	22.0113	2.82E+2
1109.18	8	75.9586	2.6361	57.0791	0.8157	19.8150	0.1128	2.2558	6.4167	2.3174	5.9456	2.1660	1.6258	0.1335	1.3165	23.7526	3.18E+2
1104.18	8	74.2926	2.6359	57.1599	0.8313	19.7401	0.1122	2.2280	6.5605	2.2470	5.8488	2.1331	1.6567	0.1365	1.3460	25.4186	3.58E+2
1099.18	8	72.6978	2.6358	57.2372	0.8467	19.6674	0.1115	2.1987	6.7045	2.1791	5.7543	2.0984	1.6872	0.1395	1.3756	27.0133	4.03E+2
1094.18	8	71.1707	2.6358	57.3115	0.8619	19.5968	0.1108	2.1679	6.8483	2.1137	5.6620	2.0621	1.7173	0.1425	1.4051	28.5405	4.52E+2
1089.18	8	69.7076	2.6357	57.3828	0.8769	19.5284	0.1101	2.1359	6.9921	2.0506	5.5717	2.0244	1.7470	0.1455	1.4346	30.0035	5.07E+2
1084.18	8	68.3055	2.6357	57.4514	0.8917	19.4621	0.1094	2.1026	7.1356	1.9898	5.4834	1.9852	1.7763	0.1485	1.4640	31.4056	5.68E+2
1079.18	8	66.9614	2.6358	57.5175	0.9063	19.3978	0.1087	2.0681	7.2788	1.9310	5.3969	1.9449	1.8052	0.1514	1.4934	32.7498	6.37E+2
1074.18	8	65.6724	2.6359	57.5811	0.9207	19.3354	0.1079	2.0326	7.4217	1.8743	5.3121	1.9035	1.8336	0.1544	1.5227	34.0387	7.13E+2
1069.18	8	64.3370	2.6349	57.7046	0.9361	19.2766	0.1078	1.9823	7.5098	1.8173	5.2290	1.8604	1.8642	0.1576	1.5543	35.3742	8.20E+2
1064.18	8	62.8898	2.6318	57.9386	0.9534	19.2230	0.1086	1.9074	7.4971	1.7585	5.1474	1.8155	1.8992	0.1612	1.5901	36.8214	9.91E+2
1059.18	8	61.5168	2.6288	58.1689	0.9702	19.1714	0.1093	1.8340	7.4825	1.7022	5.0666	1.7709	1.9337	0.1648	1.6256	38.1944	1.20E+3
1054.18	8	60.2131	2.6259	58.3958	0.9864	19.1217	0.1099	1.7621	7.4660	1.6481	4.9865	1.7266	1.9677	0.1684	1.6608	39.4981	1.45E+3
1049.18	8	58.9740	2.6231	58.6194	1.0020	19.0738	0.1105	1.6920	7.4475	1.5960	4.9072	1.6828	2.0012	0.1719	1.6957	40.7371	1.75E+3
1044.18	8	57.7955	2.6203	58.8400	1.0169	19.0275	0.1109	1.6236	7.4271	1.5460	4.8287	1.6393	2.0342	0.1754	1.7302	41.9157	2.11E+3
1039.18	8	56.6735	2.6176	59.0578	1.0313	18.9826	0.1113	1.5571	7.4048	1.4978	4.7508	1.5964	2.0667	0.1789	1.7645	43.0377	2.55E+3
1034.18	8	55.6044	2.6149	59.2728	1.0449	18.9391	0.1116	1.4924	7.3806	1.4513	4.6736	1.5541	2.0987	0.1824	1.7984	44.1067	3.09E+3
1029.18	8	54.5850	2.6122	59.4853	1.0579	18.8969	0.1119	1.4296	7.3546	1.4066	4.5971	1.5123	2.1301	0.1858	1.8320	45.1262	3.73E+3
1024.18	8	53.6120	2.6097	59.6953	1.0702	18.8559	0.1121	1.3688	7.3266	1.3634	4.5212	1.4710	2.1611	0.1891	1.8653	46.0991	4.52E+3
1019.18	8	52.6827	2.6072	59.9030	1.0817	18.8159	0.1123	1.3099	7.2968	1.3217	4.4460	1.4305	2.1916	0.1925	1.8982	47.0285	5.47E+3
1014.18	8	51.7923	2.6047	60.1085	1.0926	18.7767	0.1124	1.2529	7.2654	1.2815	4.3716	1.3902	2.2217	0.1958	1.9308	47.9189	6.62E+3
1009.18	8	50.9419	2.6023	60.3121	1.1027	18.7386	0.1124	1.1979	7.2319	1.2426	4.2976	1.3509	2.2513	0.1991	1.9630	48.7692	8.02E+3
1004.18	8	50.1278	2.5999	60.5137	1.1120	18.7014	0.1125	1.1448	7.1967	1.2050	4.2244	1.3122	2.2803	0.2023	1.9949	49.5834	9.73E+3
999.18	8	49.3477	2.5976	60.7135	1.1205	18.6650	0.1125	1.0935	7.1597	1.1686	4.1517	1.2742	2.3090	0.2055	2.0264	50.3634	1.18E+4
994.18	8	48.5998	2.5953	60.9117	1.1282	18.6293	0.1124	1.0441	7.1209	1.1334	4.0798	1.2368	2.3371	0.2086	2.0576	51.1113	1.43E+4
989.18	8	47.8822	2.5930	61.1083	1.1350	18.5944	0.1123	0.9966	7.0803	1.0994	4.0084	1.2002	2.3649	0.2118	2.0885	51.8289	1.74E+4
984.18	8	47.1933	2.5908	61.3034	1.1409	18.5602	0.1122	0.9508	7.0381	1.0664	3.9377	1.1643	2.3922	0.2149	2.1189	52.5179	2.12E+4

Table D4-1 40% tonalite/60% IAB mixture MELTS model output

T (°C)	P (kb)	liquid mass (gm)	liquid ρ (gm/cc)	SiO_2 (wt. %)	TiO_2 (wt. %)	Al_2O_3 (wt. %)	Fe_2O3 (wt. %)	FeO (wt. %)	MnO (wt. %)	MgO (wt. %)	CaO (wt. %)	Na_2O (wt. %)	K_2O (wt. %)	P_2O_5 (wt. %)	H_2O (wt. %)	solid mass (gm)	Viscosity (Pa s)
979.18	8	46.5314	2.5886	61.4971	1.1460	18.5266	0.1121	0.9068	6.9942	1.0344	3.8677	1.1291	2.4190	0.2179	2.1491	53.1798	2.57E+4
974.18	8	45.8951	2.5865	61.6896	1.1501	18.4936	0.1120	0.8645	6.9486	1.0035	3.7983	1.0946	2.4454	0.2209	2.1789	53.8161	3.13E+4
969.18	8	45.2830	2.5844	61.8809	1.1533	18.4611	0.1118	0.8239	6.9013	0.9735	3.7296	1.0608	2.4714	0.2239	2.2083	54.4282	3.82E+4
964.18	8	44.6938	2.5823	62.0711	1.1556	18.4292	0.1116	0.7849	6.8525	0.9444	3.6616	1.0277	2.4970	0.2269	2.2374	55.0174	4.66E+4
959.18	8	44.1264	2.5803	62.2603	1.1568	18.3978	0.1114	0.7475	6.8021	0.9162	3.5943	0.9954	2.5222	0.2298	2.2662	55.5848	5.69E+4
954.18	8	43.5795	2.5783	62.4486	1.1570	18.3668	0.1112	0.7116	6.7502	0.8888	3.5277	0.9638	2.5470	0.2327	2.2947	56.1316	6.95E+4
949.18	8	43.0523	2.5763	62.6360	1.1562	18.3362	0.1109	0.6772	6.6968	0.8623	3.4618	0.9328	2.5714	0.2355	2.3228	56.6589	8.50E+4
944.18	8	42.5436	2.5744	62.8226	1.1544	18.3061	0.1107	0.6443	6.6419	0.8366	3.3966	0.9026	2.5954	0.2383	2.3505	57.1676	1.04E+5
939.18	8	42.0525	2.5725	63.0086	1.1514	18.2763	0.1104	0.6127	6.5856	0.8116	3.3321	0.8731	2.6190	0.2411	2.3780	57.6586	1.27E+5
934.18	8	41.5783	2.5706	63.1939	1.1474	18.2468	0.1101	0.5825	6.5280	0.7873	3.2684	0.8444	2.6423	0.2439	2.4051	58.1328	1.56E+5
929.18	8	41.1201	2.5687	63.3786	1.1422	18.2176	0.1098	0.5536	6.4690	0.7638	3.2055	0.8163	2.6651	0.2466	2.4319	58.5911	1.92E+5
924.18	8	40.6771	2.5668	63.5628	1.1359	18.1888	0.1095	0.5259	6.4087	0.7409	3.1433	0.7888	2.6876	0.2493	2.4584	59.0341	2.36E+5
899.18	8	38.8777	2.5576	64.6099	1.0837	17.9342	0.1100	0.3819	6.1106	0.6436	2.8330	0.6777	2.7824	0.2608	2.5722	60.8335	7.03E+5
894.18	8	38.5739	2.5555	64.8551	1.0594	17.8612	0.1106	0.3541	6.0472	0.6266	2.7720	0.6596	2.7988	0.2629	2.5924	61.1372	8.82E+5
889.18	8	38.2674	2.5532	65.1157	1.0239	17.7843	0.1115	0.3281	5.9790	0.6097	2.7124	0.6420	2.8153	0.2650	2.6132	61.4437	1.10E+6
884.18	8	37.9712	2.5511	65.3718	0.9893	17.7082	0.1124	0.3039	5.9104	0.5933	2.6540	0.6245	2.8314	0.2670	2.6336	61.7399	1.38E+6
879.18	8	37.6849	2.5489	65.6237	0.9557	17.6331	0.1134	0.2814	5.8415	0.5774	2.5968	0.6073	2.8470	0.2691	2.6536	62.0263	1.73E+6
874.18	8	37.4080	2.5469	65.8714	0.9230	17.5588	0.1144	0.2604	5.7724	0.5619	2.5408	0.5903	2.8622	0.2711	2.6732	62.3032	2.18E+6
869.18	8	37.1400	2.5449	66.1149	0.8913	17.4854	0.1155	0.2408	5.7031	0.5469	2.4860	0.5736	2.8769	0.2730	2.6925	62.5711	2.73E+6
864.18	8	36.8807	2.5430	66.3544	0.8604	17.4129	0.1166	0.2226	5.6336	0.5323	2.4324	0.5571	2.8913	0.2749	2.7114	62.8305	3.43E+6
859.18	8	36.6295	2.5412	66.5900	0.8304	17.3413	0.1178	0.2057	5.5640	0.5182	2.3798	0.5409	2.9052	0.2768	2.7300	63.0816	4.32E+6
854.18	8	36.3863	2.5394	66.8216	0.8012	17.2706	0.1191	0.1900	5.4942	0.5044	2.3284	0.5249	2.9187	0.2787	2.7483	63.3249	5.44E+6
849.18	8	36.1505	2.5376	67.0494	0.7729	17.2009	0.1203	0.1754	5.4244	0.4910	2.2782	0.5091	2.9318	0.2805	2.7662	63.5606	6.85E+6
844.18	8	35.9220	2.5360	67.2734	0.7453	17.1322	0.1217	0.1618	5.3545	0.4780	2.2289	0.4936	2.9445	0.2823	2.7838	63.7891	8.65E+6
839.18	8	35.7005	2.5344	67.4937	0.7186	17.0644	0.1231	0.1492	5.2846	0.4653	2.1808	0.4784	2.9568	0.2840	2.8011	64.0106	1.09E+7
834.18	8	35.2019	2.5328	67.5907	0.6898	17.0462	0.1250	0.1372	5.2388	0.4545	2.1352	0.4662	2.9876	0.2881	2.8408	64.5093	1.31E+7
829.18	8	34.3125	2.5312	67.5065	0.6579	17.1003	0.1276	0.1257	5.2294	0.4460	2.0931	0.4579	3.0457	0.2955	2.9144	65.3986	1.43E+7
824.18	8	33.4571	2.5297	67.4167	0.6272	17.1548	0.1303	0.1151	5.2209	0.4377	2.0526	0.4497	3.1032	0.3031	2.9889	66.2541	1.57E+7

Table D4-1 40% tonalite/60% IAB mixture MELTS model output

T (°C)	P (kb)	liquid mass (gm)	liquid ρ (gm/cc)	SiO_2 (wt. %)	TiO_2 (wt. %)	Al_2O_3 (wt. %)	Fe_2O3 (wt. %)	FeO (wt. %)	MnO (wt. %)	MgO (wt. %)	CaO (wt. %)	Na_2O (wt. %)	K_2O (wt. %)	P_2O_5 (wt. %)	H_2O (wt. %)	solid mass (gm)	Viscosity (Pa s)
819.18	8	32.6330	2.5283	67.3212	0.5978	17.2096	0.1331	0.1054	5.2135	0.4294	2.0136	0.4413	3.1600	0.3107	3.0644	67.0781	1.73E+7
814.18	8	31.8381	2.5269	67.2200	0.5696	17.2649	0.1360	0.0965	5.2074	0.4212	1.9761	0.4330	3.2161	0.3185	3.1409	67.8730	1.90E+7
809.18	8	31.0703	2.5256	67.1128	0.5426	17.3207	0.1390	0.0883	5.2026	0.4130	1.9400	0.4247	3.2714	0.3264	3.2185	68.6409	2.09E+7
804.18	8	30.3274	2.5243	66.9996	0.5166	17.3771	0.1422	0.0808	5.1993	0.4050	1.9055	0.4163	3.3259	0.3344	3.2973	69.3837	2.29E+7
799.18	8	29.6077	2.5231	66.8802	0.4917	17.4341	0.1454	0.0739	5.1978	0.3971	1.8723	0.4080	3.3795	0.3425	3.3775	70.1034	2.52E+7
794.18	8	28.9093	2.5220	66.7543	0.4678	17.4918	0.1488	0.0675	5.1981	0.3893	1.8406	0.3997	3.4322	0.3508	3.4591	70.8018	2.76E+7
789.18	8	28.1559	2.5210	66.6008	0.4445	17.5519	0.1528	0.0619	5.2215	0.3826	1.8145	0.3928	3.4650	0.3601	3.5517	71.5553	2.96E+7
784.18	8	27.0394	2.5209	66.3181	0.4194	17.6217	0.1593	0.0580	5.3685	0.3787	1.8148	0.3918	3.3964	0.3750	3.6983	72.6718	2.77E+7
779.18	8	25.9600	2.5210	66.0059	0.3947	17.6929	0.1656	0.0548	5.5360	0.3730	1.8202	0.3891	3.3251	0.3906	3.8521	73.7512	2.56E+7
774.18	8	24.9108	2.5212	65.6640	0.3713	17.7671	0.1724	0.0519	5.7208	0.3675	1.8272	0.3864	3.2501	0.4071	4.0143	74.8003	2.33E+7
769.18	8	23.8871	2.5215	65.2870	0.3490	17.8451	0.1797	0.0493	5.9263	0.3622	1.8360	0.3836	3.1709	0.4245	4.1864	75.8240	2.08E+7
764.18	8	23.0101	2.5219	64.9648	0.3289	17.9015	0.1869	0.0466	6.1159	0.3566	1.8416	0.3791	3.0914	0.4407	4.3459	76.7011	1.92E+7
759.18	8	21.9432	2.5228	64.4399	0.3081	18.0040	0.1957	0.0445	6.4018	0.3525	1.8582	0.3772	2.9987	0.4621	4.5572	77.7680	1.58E+7
754.18	8	20.7422	2.5243	63.8258	0.2879	18.1123	0.2070	0.0429	6.7451	0.3472	1.8850	0.3734	2.8962	0.4889	4.7884	78.9690	1.24E+7
749.18	8	18.5855	2.5276	62.9975	0.2656	18.2077	0.2325	0.0443	7.2266	0.3313	1.9694	0.3577	2.7741	0.5456	5.0476	81.1257	8.71E+6
744.18	8	16.5484	2.5319	61.9783	0.2451	18.3004	0.2629	0.0460	7.8387	0.3173	2.0685	0.3436	2.6281	0.6127	5.3584	83.1628	5.45E+6
739.18	8	14.5783	2.5379	60.6180	0.2258	18.3993	0.3003	0.0484	8.6903	0.3056	2.1899	0.3297	2.4414	0.6956	5.7556	85.1328	2.80E+6
734.18	8	12.4826	2.5491	58.3737	0.2072	18.5307	0.3513	0.0529	10.1818	0.2983	2.3611	0.3115	2.1541	0.8123	6.3650	87.2286	8.71E+5
729.18	8	6.2222	2.7021	34.9706	0.1392	17.6516	0.5022	0.0999	29.2884	0.2739	3.0526	0.1010	0.4001	1.6296	11.8908	93.4889	7.51E+1
724.18	8	5.8293	2.7092	33.7016	0.1237	17.3966	0.5258	0.0970	30.2955	0.2524	3.1213	0.0913	0.3536	1.7395	12.3017	93.8818	8.06E+1

Table D4-2 Hadamard-Rybczynski equation (H-R) settling velocity calculation for 40% tonalite/60% IAB mixture.

Solid/Liquid Proportion	Sulfide/Silicate Density Differential (kg/m^3)	Settling Velocity H-R (m/s)	Globule radius (cm)	Settling Velocity H-R (m/s)
0.00	1857.80	2.22E-3	0.01	5.41E-8
0.01	1857.50	2.06E-3	0.02	2.17E-7
0.01	1857.30	1.91E-3	0.03	4.87E-7
0.01	1857.00	1.77E-3	0.04	8.66E-7
0.02	1856.70	1.64E-3	0.05	1.35E-6
0.02	1856.50	1.52E-3	0.06	1.95E-6
0.03	1856.20	1.40E-3	0.07	2.65E-6
0.03	1855.90	1.29E-3	0.08	3.47E-6
0.04	1855.70	1.19E-3	0.09	4.39E-6
0.04	1855.40	1.01E-3	0.1	5.41E-6
0.05	1855.20	1.01E-3	0.11	6.55E-6
0.05	1854.90	9.27E-4	0.12	7.80E-6
0.05	1854.70	8.50E-4	0.13	9.15E-6
0.06	1854.40	7.79E-4	0.14	1.06E-5
0.06	1854.20	7.13E-4	0.15	1.22E-5
0.07	1854.80	6.47E-4	0.16	1.39E-5
0.08	1855.60	5.85E-4	0.17	1.56E-5
0.09	1856.40	5.27E-4	0.18	1.75E-5
0.10	1857.20	4.75E-4	0.19	1.95E-5
0.11	1858.00	4.27E-4	0.2	2.17E-5
0.12	1858.70	3.83E-4	0.21	2.39E-5
0.13	1859.40	3.44E-4	0.22	2.62E-5
0.14	1860.10	3.08E-4	0.23	2.86E-5
0.15	1860.80	2.75E-4	0.24	3.12E-5
0.15	1861.40	2.45E-4	0.25	3.38E-5
0.16	1862.10	2.18E-4	0.26	3.66E-5
0.17	1862.70	1.94E-4	0.27	3.95E-5
0.18	1863.10	1.72E-4	0.28	4.24E-5
0.20	1863.50	1.52E-4	0.29	4.55E-5
0.22	1863.70	1.35E-4	0.3	4.87E-5
0.24	1863.90	1.20E-4	0.31	5.20E-5
0.25	1864.10	1.06E-4	0.32	5.54E-5
0.27	1864.20	9.46E-5	0.33	5.90E-5
0.29	1864.20	8.42E-5	0.34	6.26E-5
0.30	1864.30	7.51E-5	0.35	6.63E-5
0.31	1864.30	6.70E-5	0.36	7.02E-5
0.33	1864.20	5.98E-5	0.37	7.41E-5
0.34	1864.10	5.35E-5	0.38	7.82E-5
0.35	1865.10	4.65E-5	0.39	8.24E-5
0.37	1868.20	3.85E-5	0.4	8.66E-5
0.38	1871.20	3.19E-5	0.41	9.10E-5
0.40	1874.10	2.65E-5	0.42	9.55E-5
0.41	1876.90	2.19E-5	0.43	1.00E-4
0.42	1879.70	1.82E-5	0.44	1.05E-4
0.43	1882.40	1.51E-5	0.45	1.01E-4
0.44	1885.10	1.25E-5	0.46	1.15E-4
0.45	1887.80	1.03E-5	0.47	1.20E-4
0.46	1890.30	8.55E-6	0.48	1.25E-4
0.47	1892.80	7.07E-6	0.49	1.30E-4
0.48	1895.30	5.85E-6	0.5	1.35E-4
0.49	1897.70	4.83E-6	0.51	1.41E-4

Table D4-2 Hadamard-Rybczynski equation (H-R) settling velocity calculation for 40% tonalite/60% IAB mixture.

Solid/Liquid Proportion	Sulfide/Silicate Density Differential (kg/m^3)	Settling Velocity H-R (m/s)	Globule radius (cm)	Settling Velocity H-R (m/s)
0.50	1900.10	3.99E-6	0.52	1.46E-4
0.51	1902.40	3.29E-6	0.53	1.52E-4
0.51	1904.70	2.72E-6	0.54	1.58E-4
0.52	1907.00	2.24E-6	0.55	1.64E-4
0.53	1909.20	1.84E-6	0.56	1.70E-4
0.53	1911.40	1.52E-6	0.57	1.76E-4
0.54	1913.50	1.25E-6	0.58	1.82E-4
0.55	1915.60	1.03E-6	0.59	1.88E-4
0.55	1917.70	8.41E-7	0.6	1.95E-4
0.56	1919.70	6.90E-7	0.61	2.01E-4
0.56	1921.70	5.65E-7	0.62	2.08E-4
0.57	1923.70	4.63E-7	0.63	2.15E-4
0.57	1925.60	3.78E-7	0.64	2.22E-4
0.58	1927.50	3.09E-7	0.65	2.29E-4
0.58	1929.40	2.52E-7	0.66	2.36E-4
0.59	1931.30	2.06E-7	0.67	2.43E-4
0.59	1933.20	1.68E-7	0.68	2.50E-4
0.61	1942.40	5.65E-8	0.69	2.58E-4
0.61	1944.50	4.51E-8	0.7	2.65E-4
0.62	1946.80	3.60E-8	0.71	2.73E-4
0.62	1948.90	2.88E-8	0.72	2.81E-4
0.62	1951.10	2.30E-8	0.73	2.89E-4
0.62	1953.10	1.84E-8	0.74	2.96E-4
0.63	1955.10	1.46E-8	0.75	3.05E-4
0.63	1957.00	1.17E-8	0.76	3.13E-4
0.63	1958.80	9.27E-9	0.77	3.21E-4
0.64	1960.60	7.37E-9	0.78	3.29E-4
0.64	1962.40	5.85E-9	0.79	3.38E-4
0.64	1964.00	4.64E-9	0.8	3.47E-4
0.64	1965.60	3.68E-9	0.81	3.55E-4
0.65	1967.20	3.08E-9	0.82	3.64E-4
0.66	1968.80	2.81E-9	0.83	3.73E-4
0.66	1970.30	2.56E-9	0.84	3.82E-4
0.67	1971.70	2.33E-9	0.85	3.91E-4
0.68	1973.10	2.12E-9	0.86	4.00E-4
0.69	1974.40	1.93E-9	0.87	4.01E-4
0.70	1975.70	1.76E-9	0.88	4.19E-4
0.70	1976.90	1.61E-9	0.89	4.29E-4
			0.9	4.39E-4
			0.91	4.48E-4
			0.92	4.58E-4
			0.93	4.68E-4
			0.94	4.78E-4
			0.95	4.89E-4
			0.96	4.99E-4
			0.97	5.09E-4
			0.98	5.20E-4
			0.99	5.31E-4
			1	5.41E-4